The ^{14}N(n,p) reaction cross-section measurement at n_TOF - CERN and its application to the design of a facility for neutron capture therapy

UNIVERSIDAD DE GRANADA

Tesis Doctoral

Diciembre 2022

Pablo Torres Sánchez

Departamento de Física Atómica, Molecular y Nuclear
Universidad de Granada

Programa de Doctorado en Física y Ciencias del Espacio

Directores:
Dr. Ignacio Porras Sánchez
Dr. Javier Praena Rodríguez

Editor: Universidad de Granada. Tesis Doctorales
Autor: Pablo Torres Sánchez
ISBN: 978-84-1117-624-8
URI: https://hdl.handle.net/10481/79145

A mis padres.
A mis abuelos, a todos ellos.

Agradecimientos
Acknowledgements

Quiero empezar los agradecimientos con una breve historia de cómo acabé por conocer a mis directores de tesis. Gracias a todos los que, tal vez inconscientemente, me llevaron a hacer una tesis como esta.

Muy de pequeño, quería ser médico. Me aprendí todos los órganos, todos los huesos y músculos con gran ilusión. Siempre me interesó el conocimiento en general, así que con el paso de los años fui saltando por varias disciplinas. Unas semanas después de llegar al Instituto en 1°de Bachillerato, mis nuevos profesores de Física y Química, Pedro Vera y Francisco Villoslada, me ofrecieron la posibilidad de participar en el Proyecto de Iniciación a la Investigación e Innovación para estudiantes de Secundaria en Andalucía (PIIISA). Como ya sabía que quería hacer la carrera de física, y me gustaba la atómica, elegí un proyecto sobre espectroscopía, de entre tantos otros sobre partículas o astrofísica. En el primer día del proyecto, el profesor Enrique Buendía (que años después me daría Física Cuántica, y a quien siempre consideraré como el mejor profesor que tuve en la carrera), nos mostró unos espectros de tubos de descarga de gases, y otro con el espectro de luz solar. Interesado por la forma de ese espectro, aprendí a integrar para comprender las leyes del cuerpo negro. En la segunda sesión, a los alumnos que participábamos en el proyecto nos repartieron entre varios profesores y yo fui asignado a Ignacio Porras, al que le mostré mis resultados, que después presenté en el Congreso PIIISA de 2012. Ahora sé que desde aquel momento Ignacio no se olvidó de mí. Años después, ya en la carrera, fui a su despacho para conocer su línea de investigación. Ignacio me contó que estaban haciendo experimentos con Javier Praena en el CERN para investigar el uso de neutrones en radioterapia contra el cáncer. Entonces se hizo una conexión con mi yo de pequeño. Supe que yo quería trabajar en eso.

Ahora sí,

Gracias Ignacio, por confiar en mí desde el principio. Por transmitirnos tus ilusiones con este proyecto de una forma única y que deja huella. Por ofrecerme siempre nuevos proyectos en los que contribuir. Por darme tanta libertad para trabajar de forma autónoma. Y por qué no, también por dejar que me llevara el ordenador a casa justo antes de la pandemia.

Gracias Javier, por enseñarme tantas cosas de física experimental. Por forzarme siempre a dar el siguiente paso. Por pensar que sería buena idea que participara en el commissionning de la NEAR, gracias de verdad. Por fijarte en tantos detalles que me puedan ayudar en esta larga carrera que es la investigación.

A todos los miembros del grupo de Física de Neutrones de la UGR. Muchas gracias a Fernando por estar siempre atento a todas las cuestiones administrativas, y por todo el trabajo de fondo en la gestión de las tareas docentes del contrato FPU durante los últimos cuatro años. A María, por los breves pero buenos momentos en los que hemos coincidido, siempre saltando de estancia en estancia. Por muchos buenos consejos sobre tu experiencia en el doctorado y como postdoc. Volverás cuando yo me vaya, y la historia se repetirá. A Nataliya, compañera en los primeros momentos de la tesis, por tantas simulaciones y cambios hasta que dimos con un buen diseño para la BSA. A Fran, por ser un buen compañero desde que empezamos la carrera. Al final te fuiste a Ginebra, gracias por echarme una mano cuando he estado allí. A las nuevas incorporaciones del grupo, por renovar la ilusión de los inicios de la tesis. En especial a Antònia, por esa capacidad de trabajo y esa buena sintonía en la tarea de mejorar y "generalizar" el planificador de tratamientos.

Al resto de miembros de nuestro grupo de investigación en terapia por captura de neutrones. A las biólogas, Mari Carmen y María José y las compañeras de biología, por enseñarnos mil cosas curiosas que ocurren cuando uno va más allá de la física. A Andrés, por sus útiles consejos en las reuniones del grupo.

Quiero también dar las gracias a José Expósito y al equipo de Radiofísicos del Hospital Universitario Virgen de las Nieves de Granada, por darnos acceso a imágenes simuladas de resonancia magnética de tumores cerebrales sobre los que construimos y probamos el Planificador de tratamientos.

Special thanks to the n_TOF Collaboration. Thanks to all the people that made the ^{14}N(n,p) Campaign possible, when I just arrived to the Collaboration as a graduate student. Un millón de gracias a Marta por el montaje de los MicroMegas, por apuntar en el Runbook toda la valiosa información que luego iba a necesitar y siempre resolver mis preguntas al inicio del análisis. Also to Claudia and the Edinburgh team (Sarah, Ruchi, Mirko...) for setting up the DSSSD. Thanks to the Collaboration for valuable comments and suggestions in the n_TOF Analysis and Collaboration Meetings through the years. Thanks also to all the young members (Massimo, Thanos, Veatriki, Zina, Sam, Aditya, Sebastian, Michi, Javi, Jorge, Simone, Alice, Adrià, Jose, Víctor, Elizabeth, and many others) for sharing your time during my stays at CERN, and in the n_TOF Meetings, which made them much more agreeable, specially before the pandemic. Thank you Alberto for being my tutor during my PhD stay in Sept-Dec 2021 for the NEAR commissioning, and to all the people involved in this work (Ana-Paula, Oliver, Oscar, the MAM-1 and Antilope teams). Special thanks to Elisso for setting up the HPGe detector that we both used to analyze the irradiated samples.

To the BNCT community, for being always welcoming and for creating many bonds through the congresses. Special thanks to Argentinians and Italians: Agus, Andre, Lucas, Ian, Chiara and Seta, who became friends year to year, and now having the CTF to join us with many other colleagues around the world to spread the news and milestones from the BNCT community.

Quiero dar las gracias a toda mi familia, cercana y lejana, por tantas experiencias y memorias que contar. Por conformar la historia de quien soy.

Hermi y Javier, por regalarme libros de física avanzada cuando todavía estaba en el colegio, sin dudar que les sabría sacar provecho.
Ova y Lidia, por estar siempre cerca y confiar en mí. Ova, sé que te habría gustado que hubiese sido médico. Con esta tesis he hecho lo posible por contribuir a la medicina.
Gustavo, por tus muchos buenos consejos y por enseñarme la importancia de la comunicación.
A mis padrinos, por mostrar lo que es tener los pies en la tierra y ser ejemplo del buen hacer, y por su especial interés en entender en qué estaba investigando.

A todos mis primos y tíos y resto de familiares que me habéis visto crecer, por todos los días que hemos pasado juntos y seguiremos pasando.

A tantos, por estar siempre pendientes y preguntarme cada vez por los últimos avances de mis investigaciones. A todos, por soportar mis explicaciones, muchas veces con palabrejas que nadie entiende.

Gracias a mi familia más cercana:

A mi hermana, por ser el ejemplo puro de la constancia y la persistencia.
A mi madre, por siempre escucharme. Por entenderme aunque no sepas de lo que hablo. Por estar pendiente de todo y de todos. Por enseñarme que con la verdad se puede ir a cualquier sitio.
A mi padre, por traerme libros, cintas de vídeo, programas y enciclopedias para el ordenador cuando era pequeño. Por buscar en todos los sitios para darme siempre lo mejor. Por enseñarme a cumplir las tareas con disciplina y en tiempo. Por enseñarme lo importante que es entender "cómo funcionan las cosas".

A los tres, por acompañarme tantas veces en mis viajes. Por hacerme echaros de menos cuando estaba por ahí. Soy como soy gracias a vosotros. Gracias por quererme tanto.

Gracias.

List of Acronyms

ACE: A Compact ENDF

AD: Advantage Depth

ADC: Analog-to-Digital Converter

ADDR: Advantage Depth Dose Rate

AR: Average treatment dose Ratio

BPA: Boronophenylalanine

BSA: Beam Shaping Assembly

BSA-UGR: Beam Shaping Assembly designed at the University of Granada

BSH: Sodium Borocaptate

BNCT: Boron Neutron Capture Therapy

CANS: Compact Accelerator-based Neutron Source

CASTOR: CERN Advanced STORage system

CERN: European Organization for Nuclear Research

C-BENS: Cyclotron-Based Epithermal Neutron Source

CNA: Centro Nacional de Aceleradores

CT: Computed Tomography

CTV: Clinical Tumor Volume

DAQ: Data Acquisition System

DICOM: Data Imaging and Communications in Medicine

DSSSD: Double-Sided Silicon Strip Detector

DVH: Dose Volume Histogram

EAR-1: Experimental Area 1

EAR-2: Experimental Area 2

ENDF: Evaluated Nuclear Data File

ENSDF: Evaluated Nuclear Structure Data File

EOI: End Of Irradiation

FWHM: Full Width at Half Maximum

FOM: Figure Of Merit

GBM: GlioBlastoma Multiforme

HPGe: High Purity Germanium detector

HU: Hounsfield Units

IBANDL: Ion Beam Analysis Nuclear Data Library

IAEA: International Atomic Energy Agency

ICRP: International Commission on Radiological Protection

ICRU: International Committee for Radiological Units

IGRT: Image-Guided Radiation Therapy

IMRT: Intensity-Modulated Radiation Therapy

INTC: ISOLDE and n_TOF Experiments Committee

JEFF: Joint Evaluated Fission and Fusion nuclear data library

JENDL: Japanese Evaluated Nuclear Data Library

KURRI: Kyoto University Research Reactor Institute

LET: Linear Energy Transfer

LS2: Long Shut-Down 2

MACS: Maxwellian Averaged Cross-Section

MCA: Multi-Channel Analyzer

MCMC: Markov Chain Monte Carlo

MCNP: Monte Carlo N-Particle

MRI: Magnetic Resonance Imaging

MTR: Maximum Therapeutic dose Ratio

n_TOF: neutron Time-Of-Flight

NCT: Neutron Capture Therapy

NEAR: New Experimental Area

NeMeSis: Neutrons for Medicine and Scientific applications

NIST: National Institute for Standards and Technology

OAR: Organs at Risk

PS: Proton Synchcrotron

PSA: Pulse Shape Analysis

PTV: Planning Tumor Volume

QUANTEC: Quantitative Analyses of Normal Tissue Effects in the Clinic

RBE: Relative Biological Effectiveness

RBS: Rutherford Back-Scattering

RF: Resolution Function

RMS: Root Mean Square

ROI: Region Of Interest

RRR: Resolved Resonance Region

RT: Radiation Therapy/Radiotherapy

SEE: Single Event Effect

SBRT: Stereotactic Body Radiation Therapy

SRS: Stereotactic RadioSurgery

T/N Ratio: Tumor to Normal tissue Ratio

TD: Treatable Depth

TENDL: TALYS-based Evaluated Nuclear Data Library

TOF: Time Of Flight

THOR: Tsing Hua Open-pool Reactor

TPS: Treatment Planning System

TR: Therapeutic dose Ratio

URR: Unresolved Resonance Region

VMAT: Volumetric Modulated Arch Therapy

YETS: Year-End Technical Shut-Down

List of Figures

List of Tables

Abstract

Experimental nuclear data and simulations are crucial for new radiotherapies of cancer. In Boron Neutron Capture Therapy (BNCT), an accurate knowledge of neutron interaction with the elements present in body tissues is key for dosimetry. At low neutron energies, the reaction between neutrons and nitrogen, ^{14}N(n,p), becomes a main component of the dose in most human tissues. There are several discrepancies in previous measurements of this reaction, which increase the uncertainty in dose estimations needed for treatment planning. Furthermore, Neutron Capture Therapy needs intense and clean neutron sources, suitable for therapy and with the possibility of being installed in hospital environments, getting over previous facilities at nuclear reactors. This thesis aims to contribute to these two topics.

The nuclear data from a new measurement of the ^{14}N(n,p) reaction, carried out at the n_TOF Facility at CERN will be shown. The new high-accuracy data span from 8 meV to 800 keV, covering the range of interest for BNCT, including the thermal point (25.3 meV), whose cross-section value was found to be at 1.809±0.045 b. The implications of this new nuclear data to BNCT dosimetry will be explored via Monte Carlo simulations.

A new Beam Shaping Assembly (BSA) will be proposed for a proton accelerator-based neutron source, using 30 mA of 2.1 MeV protons onto a lithium target. This BSA produces a high-intensity and well-collimated neutron field that also provides low contamination from gamma radiation and both thermal and fast neutrons. The spectrum of the beam coming out of the BSA aperture will be shown to be adequate for BNCT treatments, fullfilling all recommendations from the IAEA and also performing well in in-phantom dose simulations.

The new nuclear data and the proposed neutron beam will be put together as input in order to develop a Treatment Planning System (TPS). The TPS processes medical images (DICOM) and runs Monte Carlo simulations of neutron transport through the model of the patient, allowing to compute dose estimations in the tumor and surrounding tissues, including organs at risk. The TPS will be used to perform a pilot test simulation with a realistic case of a Glioblastoma patient.

Resumen en Español

El uso de datos nucleares experimentales y simulaciones es crucial para nuevas formas de radioterapia contra el cáncer. En la Terapia mediante Captura de Neutrones por Boro (BNCT, por sus siglas en inglés), un conocimiento preciso de la interacción de los neutrones con los elementos presentes en los tejidos corporales es clave para la dosimetría. La reacción de los neutrones con el nitrógeno, ^{14}N(n,p), es una componente muy importante de la dosis en la mayoría de tejidos humanos para neutrones de baja energía. Existen discrepancias entre varias medidas anteriores de esta reacción, lo que aumenta la incertidumbre en las estimaciones de dosis necesarias para planificar un tratamiento. Por otra parte, la Terapia por Captura de Neutrones necesita fuentes de neutrones intensas y limpias, adecuadas para terapia y que tengan la posibilidad de instalarse en el entorno hospitalario, a diferencia de las instalaciones anteriores que se han construido en reactores nucleares. Esta tesis pretende contribuir a resolver estos dos problemas.

Se mostrarán los datos nucleares obtenidos en una nueva medida de la reacción ^{14}N(n,p) realizada en las instalaciones de neutrones por tiempo de vuelo (n_TOF) del CERN. Los nuevos datos de alta precisión abarcan el rango entre 8 meV y 800 keV, cubriendo por completo el rango de interés para BNCT, lo que incluye el punto térmico (25.3 meV), para el cual se ha encontrado que la sección eficaz es 1.809 ± 0.045 b. Las repercusiones de estos nuevos datos nucleares para la dosimetría en BNCT serán exploradas usando simulación Monte Carlo.

Se propone un nuevo dispositivo conformador de haces (Beam Shaping Assembly, BSA), diseñado para una fuente de neutrones basada en acelerador, con 30 mA de protones a 2.1 MeV sobre un blanco de litio. Esta BSA produce un campo de neutrones colimado de alta intensidad que además presenta una contaminación baja por radiación gamma y neutrones rápidos o térmicos. Se mostrará que el espectro del haz de neutrones a la salida de la apertura de la BSA es adecuado para tratamientos de BNCT, cumpliendo todas las recomendaciones del Organismo Internacional para la Energía Atómica (OIEA) y además mostrando buenos resultados con simulaciones de dosis en maniquíes.

Tanto los nuevos datos nucleares como el haz de neutrones propuesto se combinarán como inputs en el desarrollo de un Sistema de Planificación de Tratamientos (TPS, por sus siglas en inglés). El TPS procesa imágenes médicas DICOM y ejecuta simulaciones Monte Carlo de transporte de neutrones en un modelo del paciente, lo que permite calcular la dosis en el tumor y los tejidos circundantes, incluyendo los órganos de riesgo. El TPS será usado para realizar una simulación de prueba piloto con un caso realista de paciente con Glioblastoma.

Outline

- Chapter 1 provides a general introduction of neutron capture therapy, and the main open questions of this experimental form of radiotherapy: the uncertainties in dose estimation and the needs of well suited neutron beams for treatment, will be presented.
- Chapter 2 addresses the need of reducing the uncertainties by measuring the cross-section of the ^{14}N(n,p)^{14}C reaction, which is the most relevant dose component delivered by low energy neutrons in human tissues. The analysis of the experiment, performed at the Experimental Area 2 (EAR2) of the n_TOF Facility at CERN, will be described, together with the results from the measurement.
- Chapter 3 will discuss the implications of the results of the measurement found in Chapter 2, including both the changes in the neutron transport and in neutron dose.
- Chapter 4 is devoted to the design of a Beam Shaping Assembly (BSA) that provides a novel neutron beam suitable for BNCT treatment that accomplishes the IAEA recommendations, based on the use of the ^{7}Li(p,n) reaction as a neutron source using a proton accelerator at a proton energy of 2.1 MeV.
- Chapter 5 will present the development of a Treatment Planning System (TPS) dedicated to simulate the performance of a treatment with the BSA designed in Chapter 4 and using the new nuclear data obtained in Chapter 2, for the case of a real Glioblastoma patient.
- The Conclusions will summarize the findings of this thesis.
- Additional appendices will include the nuclear data from the experiment described in Chapter 2 and Kerma Factors obtained in Chapter 3 (Appendix A); the MCNP inputs used in the TPS in Chapter 5 (Appendix B); and the measurement of the spectrum of the new NEAR station of the n_TOF Facility with the Multi-foil Activation Technique (Appendix C), which could be used in a similar manner to measure the spectrum coming out of the BSA designed in Chapter 4.

Contents

Chapter 1

Introduction

Experimental nuclear data and simulations are crucial for new radiotherapies of cancer. Realistic simulations of treatment planning using the most accurate input data are essential to provide safe and effective tools in the encouraging fight against cancer.

Cancer is a group of diseases in which some of the body cells grow uncontrollably and spread to other parts of the body [1]. According to the World Health Organization, cancer is one of the leading causes of death worldwide, accounting for 10 million deaths in 2020. The incidence of new cases was estimated around 19.4 million people. In light of the last estimates by the International Agency for Research on Cancer (IARC), one in five persons will get cancer in their lifetime and one in ten will die from the disease [2].

Treatments of cancer include surgery, chemotherapy, inmunotherapy and radiotherapy, among others. Radiotherapy (also called Radiation Therapy) uses large doses of radiation in order to kill cancer cells and shrink tumors. The physical mechanisms to deliver dose to the tumor vary broadly depending on the type of radiotherapy treatment. These include external beam radiotherapy and internal radiotherapy. Internal radiotherapy comprises brachytherapy, which is the implantation of seeds or capsules that contain a radiation source near the tumor area (commonly used for certain types of cancer as prostate cancer, cervical or endometrial cancer and some cancers of the eye), and also the administration of radio-pharmaceuticals targeting the tumor cells that are labelled with a radioactive isotope (e.g. ^{131}I for thyroid cancers, ^{177}Lu or ^{90}Y) [3]. External beam therapy uses different types of radiation fields generated from out-of-body beams. These beams can be comprised of ionizing radiation such as photons, electrons, protons or heavy ions, and also neutrons. The most common type of radiation is photon-based and uses either X-rays or Gamma rays to generate the dose. Several techniques use photons, including 3D Conformal radiation therapy, which is the most widely used type of external-beam radiotherapy. More recently developed techniques include Intensity-Modulated Radiation Therapy (IMRT), Image-Guided Radiation Therapy (IGRT) or Volumetric Modulated Arc Therapy (VMAT). These types of treatment use several fields and the dose is delivered following a large number of fractions spanning along weeks. Other photon-based techniques such as Stereotactic Radio-Surgery (SRS) and Stereotactic Body Radiation Therapy (SBRT) aim to reduce the number of fractions by increas-

ing the dose delivered in few sessions, as with the use of the Gamma-Knife [4]. Electrons are used in radiation therapy in cases of superficial tumors due to their short range in tissues. Hadrontherapy comprises protontherapy [5] and heavy-ion therapy [6], which use the corresponding ion beams in order to deliver very well shaped dose distributions thanks to the distinctive matter-radiation interaction of highly energetic ions (70-250 MeV). These ions deliver small amounts of energy along their path through the body and most of the energy is released in a short region where the Bragg peak is found. The energy of the particles in the beam is tuned to match its range in tissue with the position of the tumor, achieving large doses in the tumor while delivering small amount of dose in nearby tissues, in cases of well localized tumors without ramifications or branching. Neutrons have been used in experimental forms of radiotherapy in mainly two types: Fast Neutron Therapy and Neutron Capture Therapy (NCT). Fast Neutron Therapy makes use of highly energetic neutrons (50-70 MeV) targeting to the tumor. Its use achieved some development in the past but it has been discontinued lately due to the lack of support and funding, which was ultimately due to lower-than-expected clinical outcomes [7]. Neutron Capture Therapy will be described in the next section.

1.1 Neutron Capture Therapy of Cancer

Only four years after the discovery of the neutron by James Chadwick in 1932 [8], Gordon L. Locher proposed their use as a weapon against cancer [9]. Locher based its idea on the previously discovered large thermal neutron capture cross-section of the isotope ^{10}B, leading to the reaction:

$$ {n_{th}}^{1} + {}^{10}\mathrm{B} \rightarrow \begin{cases} {}^{7}\mathrm{Li}\ (1.01\ \mathrm{MeV}) + \alpha\ (1.77\ \mathrm{MeV}) & 6\% \\ {}^{7}\mathrm{Li}\ (0.84\ \mathrm{MeV}) + \alpha\ (1.47\ \mathrm{MeV}) + \gamma\ (0.478\ \mathrm{MeV}) & 94\% \end{cases} \tag{1.1} $$

This reaction produces two highly energetic charged particles that deliver their energy in a very small region of the size of a cell, and 94 % of the time it also generates a 478 keV gamma from the desexcitation of $^{7}\mathrm{Li}^{*}$. Then Locher hypothesized that tumors could be treated by irradiating them with thermal neutrons, provided that boron could be accumulated selectively in the tumor. This is the main mechanism underlying NCT, which in its most common practical applications uses ^{10}B as the target isotope, leading to Boron Neutron Capture Therapy (BNCT). Other isotopes have been proposed as an alternative basis for NCT, such as ^{157}Gd, or to act cooperatively with boron to enhance dose in certain regions, as ^{33}S [10].

1.1.1 The grounds of BNCT

BNCT is a mixed therapy in the sense that it combines the use of an irradiation with an external field (of neutrons) and the administration of a boron compound that is

[1] Thermal energy is defined as the one corresponding to the mean energy of neutrons in thermal equilibrium at 300 K, $kT = 25.3$ meV.

selectively uptaken by cancer cells. Both of these steps of the BNCT treatment are relatively harmless to the patient if performed alone, given the low dose delivered by neutrons in human tissues and the low toxicity of the boron compounds used in BNCT. However, their simultaneous administration triggers the nuclear reactions of neutrons with ^{10}B and hence the release of large amounts of energy through particles with high Linear Energy Transfer (LET). The emitted α particle and ^{7}Li nucleus have a range of 9 and 4 μm, respectively. This is less than the average size of human cells, for which most tissue types lie between 10-100 μm, hence all the damage occurs within the cell that contained the boron.

BNCT is a multidisciplinary research field, in which a diverse set of scientific and technical branches of science cooperate. In order to design, produce and adequate the neutron field for treatments, nuclear physicists and engineers are needed, and also for beam operation and quality management. Nuclear physicists also provide input on nuclear data for the dose computations. In order to develop and synthesize boron compounds that are selective and have low toxicity, chemists and pharmacists are also on board. Radiobiologists provide the essential input on the biological effects of neutron radiation on the various tissues in the body, which serve to better estimate the dose delivered in treatments. Medical physicists perform the treatment planning, integrating all the information generated by all previous scientific research, and monitor the dosimetric quantities during the treatment. All the healthcare labor is executed by hospital staff, coordinated by medical doctors who can best determine the adequacy of a patient for a BCNT treatment and its conditions to improve the patient quality of life and maximize the chances of cure.

Neutron field

In order to maximize the boron dose in the tumor, thermal neutrons have to reach the region. Thermal neutrons have low penetrability in human tissues, and hence only superficial tumors like melanoma with a depth around or below 3 cm can be treated as such. In order to increase the beam penetrability, the neutron energy has to be increased. This way, neutrons lose most of their initial energy by elastic collisions with atoms in the tissue and moderate through the tissue, reaching thermal energy much deeper in the body. This has a counterpart, as part of the dose deposited by neutrons during the moderation process is not related to boron and therefore affects equally the tumor and normal tissues. The larger the initial neutron energy, the higher the dose deposited due to this effect. There is a balance between these two effects that determines the upper limit of the energy of neutrons that are suitable for BNCT. This limit was traditionally set at 10 keV. Given all that, a neutron beam for BNCT in deep tumors should have an epithermal spectrum, avoiding the presence of thermal neutrons and fast neutrons (more than 10 keV). Other aspects of relevance in the neutron beam are the gamma contamination and the divergence of the beam, that shall be reduced within manageable limits. All these considerations were established as recommendations in a Technical Document of the International Atomic Energy Agency (IAEA) [11].

Boron compounds

Boron is not one of the most abundant elements in the human body. It does not accumulate in the tissues and is only found as a trace in certain tissues as the bones, nails and hair. ^{10}B is an stable isotope of boron, accounting for 19.65 % of natural boron. For this reasons, chemical compounds containing boron have to be synthesized in order to be used in BNCT. There are several types of boron carriers, ranging from small molecules (*e.g.* boron-labeled amino acids, as boronophenylalanine (BPA)) [12], to complex and larger molecules as mercapto-undecahydro-closo-dodecaborate (or sodium borocaptate, BSH), which contains 12 ^{10}B atoms ($Na_2B_{12}H_{11}SH$) [13], and more recently, the search has expanded to nanoparticles, boron cluster compounds and others [14]. Among these, only BSH and BPA have been used in clinical trials in the recent years, with BPA showing Tumor to Normal tissue concentration ratios (T/N ratio) around 3.5 and up to 6 in some patients [15]. In general, a T/N ratio over 2.5 is required as a pre-requisite for BNCT treatments, which is assessed in pre-irradiation analysis such as a ^{18}F-labelled-BPA PET scans [16].

Radiobiology and Dosimetry of BNCT

The working principle of BNCT is maximizing the damage to the tumor cells while not leaving the normal tissues impaired. In order to determine the effects of the neutrons in the cells and tissues, radiobiological and dosimetric studies have to be made. Dosimetry aims to determine the physical dose delivered to the tissues. Radiobiology studies the biological effects of the neutron irradiation in tissues and cells by examining different endpoints depending on the physical dose. A joint objective is the modeling of the biological effects of the dose. Several models have been proposed for this purpose, including the classical RBE model used as a standard in BNCT and described by Coderre and Morris [17]. In the recent years, the photon-isoeffective dose model has arisen as an alternative that provides doses that generate the same effect than a photon irradiation with that physical dose [18].

Clinical studies

The final goal of BNCT is to provide a tool for physicians to treat and cure cancers of bad prognosis. In order to do so, clinical trials have to be made in order to determine the safety, adequacy and benefits of BNCT, compared to state-of-the-art procedures in common clinical practice. BNCT was originally targeting brain tumors as Glioblastoma Multiforme (GBM) and other high-grade gliomas, and then its use has spread to head-and-neck cancers and melanoma. Some other types of cancers including liver cancer and lung cancer have also been treated or are under investigation to be treated with BNCT.

1.1.2 Historical and present developments in BNCT

During the 50's, the first clinical trials were performed under the supervision of Dr. W. Sweet in the Research Reactor of the Brookhaven National Laboratory. The results of these trials were poor due to the use of low-penetrating thermal neutrons and the limited selectivity of the compounds used to carry the boron to the tumor, with boric acid among them [19]. Few years later, H. Hatanaka developed

a BNCT program in Japan which lead to better results after the introduction of a more selective boron compound, BSH [20]. The posterior shift towards the use of epithermal neutrons to increase the neutron field penetrability (that thermalizes through the tissues and reaches thermal energy in the tumor region) and the use of a BPA, firstly used for melanoma by Y. Mishima [21], improved the outcome of the clinical trials. After that initial stages, during the 90's, a series of BNCT projects were developed in many countries around the world, including Argentina, Czech Republic, Finland [22, 23, 16], Italy [24], Japan [25, 26], the Netherlands [27], Sweden [28], Taiwan [29] and the US[30]. In all of these cases, the neutron source was obtained from a nuclear reactor, which has been historically the only neutron source with a neutron flux intense enough to allow treatments within a reasonable time. Most of protocols focused on brain tumors including high-grade gliomas such as Glioblastoma Multiforme and recurrent head-and-neck cancers [31]. Some other protocols explored the use of BNCT for melanoma or even the treatment of liver metastases using extra-corporeal BNCT [32, 33]. Some of these projects achieved promising results as described in the clinical trials [16] and the report from the NuPECC of 2014 [34]. In the last two decades, the BNCT field is suffering a process of metamorphosis due to the decommissioning of most of the nuclear reactors that served for BNCT treatments, being the reactors in Taiwan (epithermal beam for brain tumors and head and neck cancers) [35] and Argentina (thermal beam for melanoma) [36] the only nuclear reactors still in use for BNCT. This has led to a change of the technology used to produce the neutron fields, given the intense development of the particle accelerator technologies in the last decades [37, 38]. In the recent years, many projects have arisen and there is an ample list of facilities under development or construction. These projects aim to follow the guidelines and recommendations established in the Technical Document of the IAEA [11]. These projects comprise several centers in Japan [39], Finland [40], Italy [41, 42], Russia [43], Argentina [44] China and South Korea. The first accelerator-based BNCT facility, the C-BENS (Cyclotron-Based Epithermal Neutron Source) in Kyoto, Japan [45, 46], is already working and a couple of clinical trials have already shown their results recently [47, 48].

1.2 Current limitations of BNCT

The BNCT group at the University of Granada has been working on diminishing the uncertainties that have hampered the BNCT development and reduced its applicability in real clinical practice. These aspects are developed within the framework of the NeMeSis Project[49]. Among these sources of uncertainty, two main topics arise:

- Reliable and adequate neutron sources in hospital environments. The design of a neutron beam suitable for BNCT that can be produced using a Compact Accelerator-based Neutron Source (CANS) is needed to timely address the needs of patients and medical doctors.

- Dose estimates carried out during treatment planning. The reduction of the uncertainty in each step of the dose computations is needed to provide strength and reliability to this experimental form of radiotherapy.

Each of these two main topics generate a relatable objective in this thesis. The first of these objectives will be the design of a neutron beam using a 2.1 MeV - 30 mA proton accelerator. The second objective needs a further framing in what the scope is too wide to be covered by a single field of expertise. A dedicated section follows discussing the dosimetry in BNCT and the specific task on reducing uncertainties in dosimetry that will be handled in this thesis.

1.2.1 Dosimetry in BNCT

Dose in BNCT is computed based on the physical absorbed dose (total energy delivered per unit mass) and the use of Relative Biological Effectiveness (RBE) coefficients. These RBE weight the different physical dose components according to their biological effects. As it was previously mentioned, each type of radiation has a different LET and hence produce different kinds of damage, for the same absorbed dose. For instance, photon radiation, which has low LET, does generate partial damages that can be recovered by the cell repair mechanisms. Highly energetic charged particles like protons or heavy ions used in hadron therapy, and also the reaction products from the neutron-induced reactions have large LET, leading to damages that are much more difficult to repair (double-strand breaks in the DNA, for instance) culminating in cell death.

The physical dose is estimated using the close concept of Kerma, which is a close approximation of the dose in situations of transport equilibrium. The Kinetic Energy Released per unit Mass (Kerma, K) is defined as the initial kinetic energy of all secondary charged particles liberated per unit mass at a point of interest by uncharged radiation. For neutrons, the relevant magnitude is usually the flux, and hence neutron kerma factors, k_f, can be defined such that $K = \int k_f(E_n) \cdot \phi(E_n) dE_n$. Neutron kerma can be used as a good approximation of neutron dose (in most circumstances, where transport equilibrium is held), including BNCT [50].

In the dose estimation, each dose component has a different behaviour and hence different kerma factors. This way, each dose component is computed separately and then the total dose is found as a weighted sum using the corresponding RBE:

$$D_T = w_{th} \cdot D_{th} + w_f \cdot D_f + \chi_B w_B \cdot D_B + D_\gamma \tag{1.2}$$

Neutron dose is usually separated in two components, corresponding to the thermal neutron dose, D_{th} which is dominated by neutron capture on nitrogen, and fast neutron dose, D_f, dominated by neutron elastic scattering off hydrogen. The gamma dose, D_γ, accounts for the dose generated by all photon radiation interactions, including those gammas already present in the initial beam as contamination, but also mainly the gammas generated as secondary radiation due to neutron interaction, where the hydrogen capture (deuterium production) with subsequent emission of 2.24 MeV gammas is the main contributor. The boron-related dose, D_B is usually computed as a dose per unit boron concentration in tissue, typically in Gy/ppm of ^{10}B. Then the actual dose from this component is calculated by multiplying by the boron concentration, χ_B in the corresponding tissue.

The Photon iso-effective dose, modeled by González *et al.*[18], uses a more elaborate dependency (taking into account the Linear-Quadratic model for he biological

response) in order to obtain a dose that generates the same effect as photons. A simple approximation of this model for which the new RBE can be determined experimentally was proposed by the Granada Group in a paper by Pedrosa-Rivera *et al.* [51]:

$$D_0 + \frac{D_0^2}{\alpha/\beta} = w_{th}^* \cdot D_{th} + w_f^* \cdot D_f + \chi_B w_B^* \cdot D_B + w_\gamma^* \cdot \left(D_\gamma + \frac{D_\gamma^2}{\alpha/\beta} \right) \tag{1.3}$$

A more detailed analysis of the neutron dose can be made by examining the contribution to the kerma factors by each isotope present in the material or tissue of interest. If we consider brain tissue, with elemental composition shown in Table 1.1, then the kerma factor at each neutron energy is shown in Figure 1.1. All partial contributions by each isotope are also shown in the Figure.

Element	Fraction	Element	Fraction	Element	Fraction
O	0.737723	P	0.003540	Mg	0.000150
C	0.125420	K	0.003100	Ca	0.000090
H	0.110667	Cl	0.002360	Fe	0.000050
N	0.013280	Na	0.001840	Zn	0.000010
		S	0.001770		

Table 1.1: Elemental Composition of brain tissue, according to ICRP [52]. Concentration is given as mass percentage. Brain tissue density is 1.03 g/cm^3.

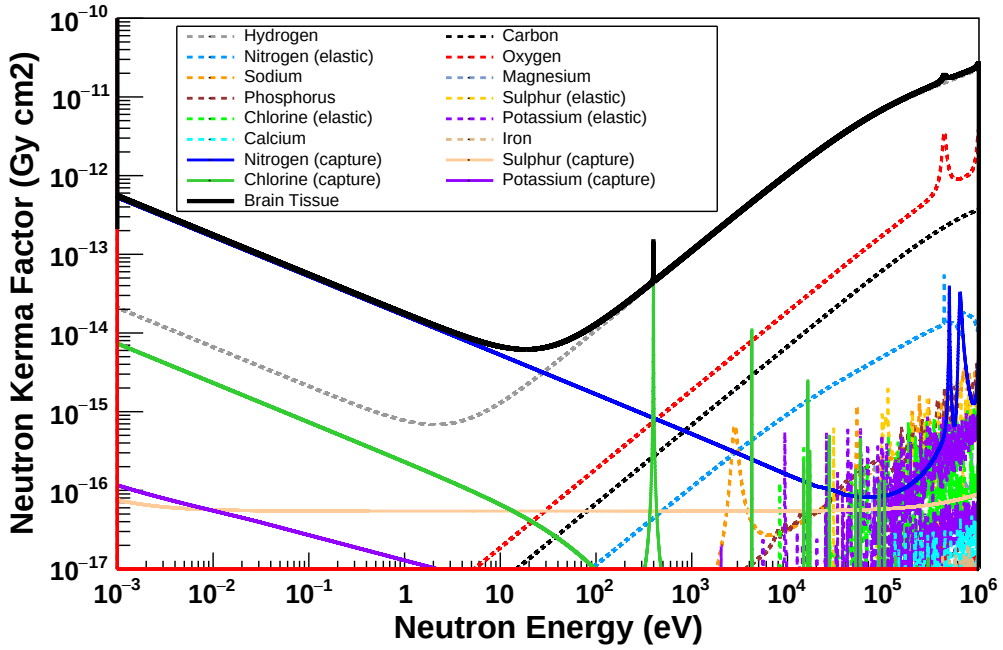

Figure 1.1: Neutron Kerma factor of brain tissue (black solid line) and partial kerma factors for every isotopic contribution. Neutron elastic scattering and subsequent recoils contributions are shown in dotted lines, and neutron captures with emission of charged particles are shown with solid lines. The kerma factors have been computed using the cross-section evaluated data from ENDF/B-VIII.0.

In brain tissue, the elastic scattering off hydrogen is the most relevant dose-generating interaction for high energy neutrons (above 10 eV), except for the presence of a strong resonance of the ^{35}Cl(n,p)^{35}S. Other minor contributions come from elastic scattering off oxygen (specially due to some resonances) and carbon, which are the most abundant elements in brain tissue. All other elements contribute to a much lesser extent.

The largest contribution at low neutron energy (below 10 eV) is the neutron capture on nitrogen, with subsequent proton emission. The second largest contribution comes from elastic scattering off hydrogen, but this contribution is 20 times less important. All other contributions at low energy are even less relevant. Therefore, around 95 % of the total neutron dose (excluding gammas) is related to nitrogen, specifically by the ^{14}N(n,p)^{14}C reaction. In this sense, the nitrogen content of a tissue does largely determine the neutron-related dose from low energy neutrons.

The nitrogen content is highly variable among human tissues. Table 1.2 shows a list for various general tissues. Brain has a relatively low nitrogen content of about one half of the reference standard ICRU-33 tissue, which is close to muscle tissue. Some tissues are specially affected by low energy neutrons through nitrogen, as the skin or the bones, which have around twice as much nitrogen as the standard tissue, or the lens of the eyes with an even larger nitrogen content.

Tissue	Fraction of N	Density g/cm^3
ICRU-33	0.026000	1.00
Brain Tissue	0.013280	1.03
Cortical Bone	0.041990	1.85
Adipose Tissue	0.007970	0.92
Muscle Tissue	0.027680	1.04
Skin	0.046420	1.10
Lens of the eye	0.053270	1.10

Table 1.2: Nitrogen fraction by weight for various human tissues Composition of brain tissue, according to ICRP [52]. Tissue densities are also given.

1.2.2 Uncertainties in dose estimations

There are several sources of uncertainty in dose estimation in BNCT, that can lead to inaccurate treatment plannings. For this reason, the precision margins used in this therapy are enlarged so as to maintain the principle of avoiding unintended overdosification of normal tissues. In a clinical trial by Kankaanranta *et al.* [53], two cohorts were compared based on the tumor dose. One group received an average dose at the tumor of 31 Gy-eq, while the other received a larger dose of 36 Gy-eq. The group with large dose showed better prognosis and larger survival after the treatment. Reducing uncertainties can lead to increasing the tumor dose at the patient by diminishing the safe margin applied. This can lead to a clear improvement on the therapeutic outcome.

Among the sources of uncertainty in dose estimation, three main domains can be identified:

- The Physical Dose calculation. This concerns the D_i in the total dose computation. This is dependent on the geometry of the model used to estimate the dose using a transport code such as MCNP [54], including the material definition and spatial precision of the model, which is usually CT-based. It is also very dependent on the nuclear data used by the transport code to simulate the neutron interactions and also to estimate the dose deposition via kerma factors. Concerning the nuclear data, some of the cross-section of the most relevant reactions, such as ^{14}N(n,p)^{14}C and ^{35}Cl(n,p)^{35}S show some discrepancies of relevance in the data that increase the uncertainty in the accuracy of previous measurements, which are used as reference for the dose estimates used in dose computations.
- The Radiobiological model of the effect of the dose. This is signified in the RBE, which are tissue-dependent and suffer from large uncertainties due to the difficulties in accessing experimentally to this data.
- The boron concentration in tumor and normal tissues. This is a relevant field in two main topics. The first one is the determination of the macroscopic boron distribution which can be at least partially accessed via PET studies. The second aspect is the microscopic or cell-to-cell boron uptake, where the amount of boron actually within the cells or the fraction left in the interstitial medium have to be taken into account. This information is specially relevant given the short-range effect of the neutron capture reaction by boron.

1.3 Objectives

This thesis aims to reduce the uncertainty in dose estimation in BNCT by measuring the neutron capture cross-section on ^{14}N in the range of interest of BNCT. Moreover, to design a neutron beam suitable for BNCT using the lowest energy possible accelerator-based neutron source. Finally, to create a Treatment Planning System that incorporates the previous results and also aims at providing an accurate estimation of the dose in the prescribed treatment plan.

Chapter 2

Measurement of the ^{14}N(n,p) reaction with MicroMegas detectors and DSSSD at n_TOF

2.1 The ^{14}N(n,p)^{14}C reaction

The ^{14}N(n,p) leading to the ground state of ^{14}C is an exothermic reaction with a Q-value of 626 keV. At thermal neutron energy (25.3 meV), the reaction is isotropic and the outgoing proton leaves with 584 keV, while the recoiling ^{14}C has 42 keV.

As it was already mentioned in the Introduction, the ^{14}N(n,p) reaction is the main contribution to the dose from thermal neutrons in most human tissues. This is of special relevance in BNCT given that neutron thermalization is needed for the therapy to perform well. The dose given to all tissues due to their nitrogen content can not be skipped and hence acts as a limiting factor that usually determines the maximum irradiation to a patient.

Apart from medical physics, this reaction is of key relevance in nuclear astrophysics, as nitrogen is one of the most important neutron poisons in s-process nucleosynthesis [55]. It is also related to the production of fluorine as the reaction acts as a proton feeder [56].

There are other fields in which this reaction plays a fair role. In cosmic astroparticle physics, the ^{14}N(n,p)^{14}C reaction is the main route for producing ^{14}C in the atmosphere through secondary neutrons from cosmic radiation [57]. Also nuclear bomb testing lead to significant ^{14}C production through this reaction. An increase in the ^{14}C content in the atmosphere was used as indicator of nuclear explosions and it is hence relevant for non-proliferation. Moreover, it is of interest in environmental science, since a large fraction of the ^{14}C produced in those events has already entered the life cycle and it is no longer in the atmosphere. The continued reduction of ^{14}C concentration in the atmosphere has hence been used for tracking the global dynamic cycle of carbon [58].

2.1.1 Current status of the cross-section data

There is a handful of previous measurements of the ^{14}N(n,p)^{14}C cross-section. However, there are still many discrepancies and these disparities lead to relevant uncertainties in their applications. There are no previous measurements that cover the full range of energy from thermal neutrons to the resonance region. The measurements are focused on specific energy regions, namely thermal neutron measurements, differential measurements in the 1/v region, integral measurements in the astrophysical range of interest and measurements in the resonance region. Figure 2.1 shows the previous experimental data available for this reaction, as found in the EXFOR Database [59].

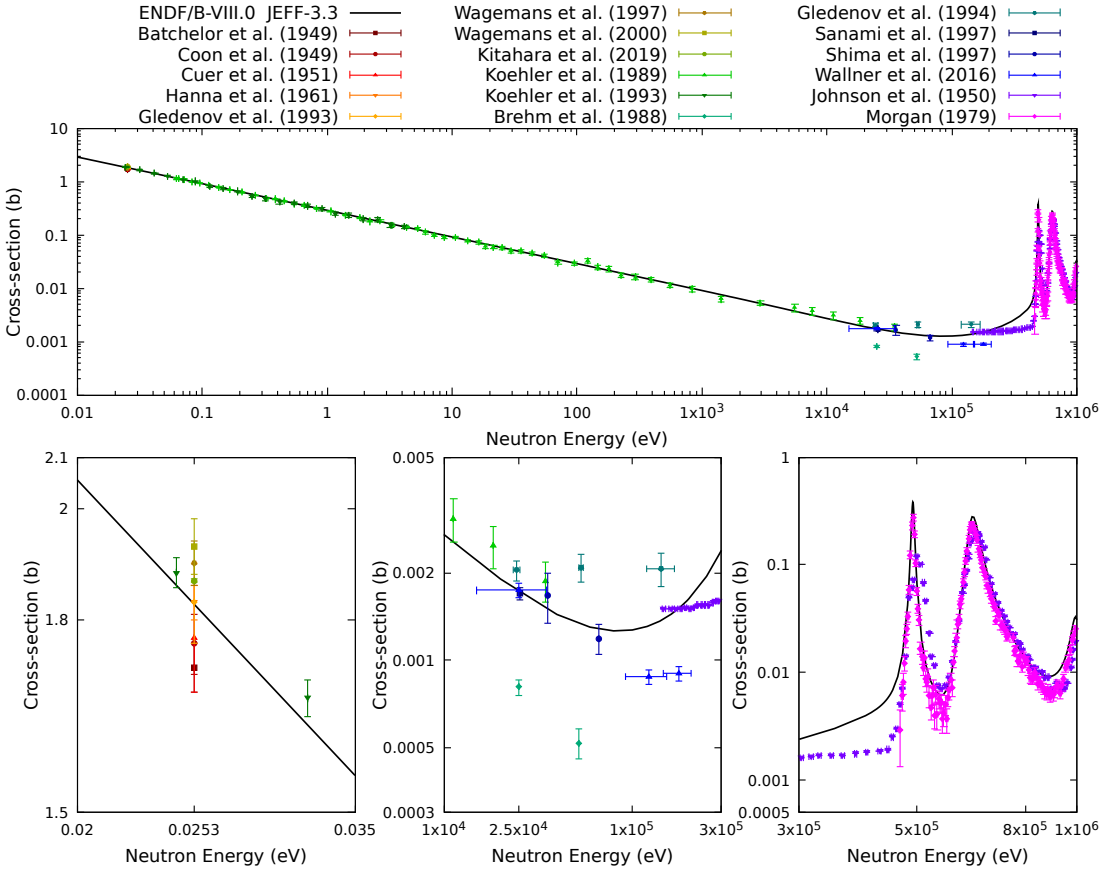

Figure 2.1: Status of the cross-section of the 14N(n,p) reaction as of the previous measurements. The last evaluation by ENDF/B-VIII.0 (same as JEFF-3.3) is also shown in a black solid line. The *top* figure shows the full picture of the cross-section from the thermal energy to 1 MeV. The *bottom* figures show the details in regions where there are discrepancies found. The *bottom-left* shows the thermal energy, the *bottom-center* shows the astrophysics range (10-300 keV), and the *bottom-right* shows the first resonances.

There are several measurements at the thermal point. All of the data are contained within 1.7 and 2.0 b [60, 61, 62, 63, 64, 65, 66]. The last measurements were performed by Wagemans *et al.* (2000), whose value for the thermal cross-section was 1.93 ± 0.05 b [65] and Kitahara *et al.*, who reported 1.868 ± 0.006 b [66]. These measurements were both higher than previous measurements around 1.83 b [63, 67, 64]. These were used as input for the last evaluation of this reaction by Chadwick *et al.* [68], which is included in the ENDF/B-VIII.0 and JEFF-3.3

Evaluations. Figure 2.1 (*bottom,left*) shows the detail of previous data around the thermal point.

There is one single measurement of the 1/v range by Koehler *et al.*, proving this behavior from 61 meV to 65 keV [69]. Its measurement was normalized by extrapolation from the thermal cross-section in the Nuclear Data Compilation by Ajzenberg-Selove *et al.* [70]. In a posterior measurement, Koehler *et al.* extended the range to include the thermal value, obtaining the same value (1.93 b) [67].

There are no differential data in the range 35-150 keV. This gap is located in the region of interest of nuclear astrophysics. In balance, there are several integral measurements in this region, including some quasi-maxwellian averaged cross-section measurements at 25 keV. The cross-section at 25 keV is well established with a close agreement between all measurements (Gledenov *et al.* [71], Sanami *et al.* [72] and Wallner *et al.* [55]) except Brehm *et al.*, who obtained a lower value of a factor of two. Some differences arise above 25 keV. Shima *et al.* [73] observed a reduction in the integral cross sections from 1.67 mb at 35.8 keV to 1.19 mb at 67.1 keV, while Gledenov *et al.* [71] saw a mostly flat behavior between 24.5 keV and 144 keV with values oscillating between 2.04 and 2.08 mb. The most recent measurement by Wallner *et al.* encountered a reduction above 25 keV, with values of 0.88 and 0.90 mb at 123 and 178 keV, respectively. Figure 2.1 (*bottom,center*) shows the detail of previous data in the keV range.

The first resonance is located closely below 500 keV. There are a few measurements examining the resonance region. Johnson *et al.* measured from 150 keV to 2.15 MeV and resolved the resonances using neutrons produced via the ^{7}Li(p,n) reaction, scanning at several points [74]. Later, Morgan measured the cross-section above 450 keV with better resolution using the time of flight technique [75]. Another measurement by Gabbard *et al.* [76] provides more data above 1.2 MeV. Others measured above 2 MeV [77, 76]. The data from Morgan has been taken as reference for the evaluations. More recently, Wallner *et al.* projected a reduction of a factor of 3.3 in the strength of the first resonance from a fitting of their integral measurements. Figure 2.1 (*bottom,right*) shows the detail of previous data in the resonance region.

The ENDF/B-VIII.0 evaluation does not provide data about the resonance parameters for this reaction. Information on the resonance parameters has been also obtained via reactions that lead to the same compound nucleus [78]. The ^{14}C(p,n)^{14}N reaction, whose threshold allows the observation of the first resonances, has been used for providing information on the J^{π} of the resonant states [79, 80, 81, 82]. Other reactions have higher thresholds above these states of ^{15}N [70]. Some measurements found an anisotropy in the first resonance [80], while others did not [81]. The neutron polarization measurement by Niecke *et al.* [82] found a positive parity for this state. On the contrary, negative parity was assigned in other measurement [79] and compilations [70, 83].

These discrepancies justify a new measurement of the cross-section, covering a broad range that connects all previous measurements in a common basis. For this reason, a measurement in the neutron Time-Of-Flight (n_TOF) Facility at CERN was proposed [84] and performed during a Campaign in September-October 2017. The next section will describe the features of the n_TOF Facility.

2.2 The Neutron Time Of Flight (n_TOF) facility at CERN

The n_TOF facility is the neutron beam facility at CERN and it is dedicated to measure the cross-section of neutron-induced nuclear reactions for reactor technology, nuclear astrophysics and medical physics [85]. It started operating in 2001 and since then, four main phases have determined its history. Phase-1 consisted of the original design promoted by Nobel Prize Carlo Rubbia among others, in the period from 2001 to 2004. Phase-2 included the design of a new target and lasted from 2009 to 2012. In Phase-3 (2014-2018), a second beam line and experimental area was added to the facility. The current Phase-4 has upgraded the Facility with a new target optimized to be used for two experimental areas and the addition of a irradiation/activation station close to the target, starting from 2021.

At n_TOF, neutrons are generated by means of a proton beam of 20 GeV/c momentum from the CERN Proton Synchrotron (PS) impinging onto a lead target of approximate dimensions of 40 cm in length and 60 cm in diameter. This generates a broad variety of particles by the process of spallation, including around 300 neutrons per initial proton. The CERN PS provides a proton beam in bunches of $7 \cdot 10^{12}$ particles with a low repetition rate of 0.8 Hz that allows no overlap between consecutive bunches. A water layer acts as a moderator that broadens the neutron spectrum up to a range from thermal neutrons to few GeV, allowing an almost isolethargic spectrum in the eV-keV range. Most of the charged particles generated in this process are deflected by means of sweeping or permanent magnets. Neutrons and gamma radiation, however, are allowed to fly freely towards two experimental areas located underground around 185 m in the horizontal direction, deviated 10º from the beam direction (Experimental Area 1, EAR-1) and 20 m above ground in the vertical direction (Experimental Area 2, EAR-2). Figure 2.2 shows a general diagram of the facility.

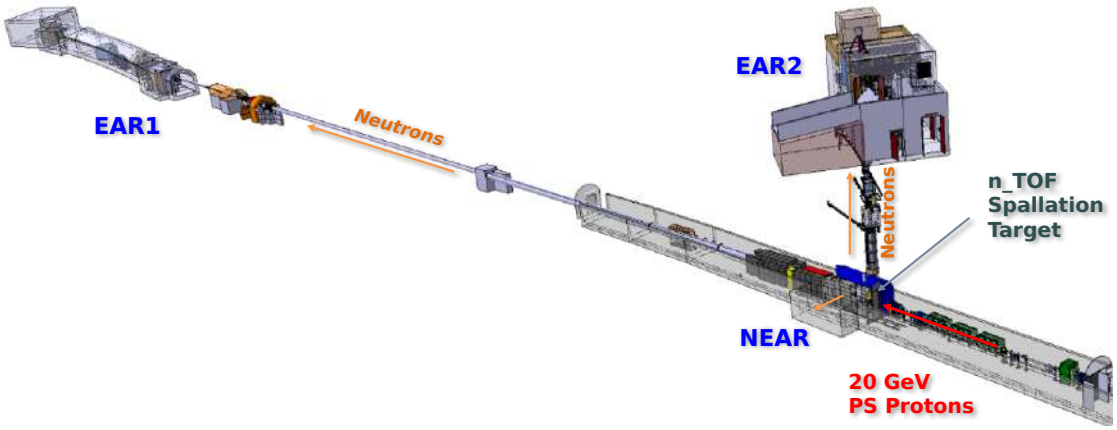

Figure 2.2: Diagram of the n_TOF Facility at CERN, including the underground location of the spallation target and EAR-1, EAR-2 above ground and the NEAR close to the target.

EAR-1, due to its long flight path, profits from a very good energy resolution ($\Delta E/E$ from 10^{-4} to 10^{-3}). EAR-2, located approximately 10-fold closer to the target, lacks this extremely good resolution but shows a much larger flux (30-40 times that of EAR-1) that allows, for instance, the measurement of very low reaction cross-sections. It is also well suited for measurements that need a high flux due to limited time for the measurement campaign as in short-lived isotopes. The measurement of the ^{7}Be(n,a) and ^{7}Be(n,p) reactions was a successful example of such case [86, 87].

A New Experimental Area (NEAR), located closely near the target, has been developed after the Long Shutdown 2 of CERN (2018-2020). Its characterization has been performed as part of the new Commissioning of the n_TOF Facility. Part of this characterization has been done within this thesis during a 3-month stay at CERN. The details of this work on the characterization of the NEAR neutron flux are described in Appendix C.

2.2.1 The Time Of Flight Technique

The Time-Of-Flight (TOF) Technique allows to measure the energy of particles by means of the time they take to travel a certain distance. It is specially adequate for neutrons, for which other techniques designed for charged particles are not available. The velocity of the neutron, v_n, is connected to the TOF by means of the distance, called the flight path length, L: $v_n = L/\text{TOF}$. Then the kinetic energy, E_n, can be obtained, using the relativistic relations:

$$E_n = E - m_n c^2 = (\gamma - 1)\, m_n c^2 \tag{2.1}$$

where E is the total neutron energy, m_n is the neutron mass at rest, c is the speed of light and $\gamma = 1/\sqrt{1 - v^2/c^2}$ is the Lorentz factor.

Combining all this, we obtain the relativistic relation between TOF and the kinetic energy of the neutron:

$$E_n = m_n c^2 \left(\frac{1}{\sqrt{1 - L^2/(TOF \cdot c)^2}} - 1 \right) \tag{2.2}$$

Below the tens of MeV, the relativistic effects are small and the relation can be reduced to the classical formula:

$$E_n \approx \frac{1}{2} m_n \left(\frac{L}{TOF} \right)^2 \tag{2.3}$$

The TOF can be accessed experimentally considering two times: the measured time-of-flight, t_m, and the so-called moderation or resolution time, t_{RF}. The resolution time depends on the structure of the original proton pulse, the spallation process and the subsequent moderation through the moderating layers of the target. This will be detailed in the following paragraphs. The measured time is the time of acquisition of an event minus the reference time, known as t_0:

$$TOF = t_m - t_{RF} = (t - t_0) - t_{RF} \tag{2.4}$$

The reference time is the timestamp at which the proton beam impinges onto the target. There are two ways to extract this at the n_TOF Facility. In general, the γ-flash is employed as the origin of time since it is the first signal observed in most types of detector systems. The γ-flash is composed of a huge amount of gamma radiation (and possibly other ultra-relativistic particles) is generated by hadronic interaction during the spallation process. The reference time is then the timestamp of the detection of the γ-flash, t_γ, from which the time needed by light to travel from target to detector (L/c) has to be substracted:

$$t_0 = t_\gamma - \frac{L}{c} \tag{2.5}$$

When the γ-flash signal can not be used as the time reference for whatever reason (for instance, not being present or not being a reliable signal), then the PKUP signal is used. The PKUP is a current monitor located just before the spallation target. An additional time offset t_{offset} has then to be used to calibrate the time references between the PKUP and any particular detector:

$$t_0 = (t_{PKUP} - t_{offset}) - \frac{L}{c} \tag{2.6}$$

The moderation time depends primarily on the track of the neutrons inside the target. For this reason, it is better treated as a distance, λ, through a conversion: $\lambda = v \cdot t_{RF} = L \cdot \frac{t_{RF}}{TOF}$. In reality, this is a stochastic quantity that can be described by means of a probability density which will depend on the outgoing neutron energy. For this reason, this is treated as a response function related to the resolution of the facility, and called the Resolution Function, relating the measured time of flight for any given neutron energy.

The energy distribution as a function of the measured time-of-flight is then:

$$E_n = m_n c^2 \left(\frac{1}{\sqrt{1 - \left(\frac{L+\lambda}{c_m}\right)^2}} - 1 \right) \tag{2.7}$$

The Resolution Function

The energy distribution can be described using the moderating distance. The neutrons arriving to the experimental area at a given TOF have an energy spread and hence the TOF to energy conversion can not be determined as an univocal constant. This distribution is also not easy to determine or parametrize by means of analytical functions, and therefore it has to be calculated via Monte Carlo simulations. These simulations have to take into account all the structure of the proton bunch, the physics of the spallation and subsequent moderating process, and are specially sensitive to the geometry of the target. Figure 2.3 shows the TOF to Energy distribution of EAR-2 at the distance of 19.75 m from the target.

The TOF to Energy distribution can be approximated by determining an effective flight path ($L + \lambda$), though this is not enough to capture the full information of the Resolution Function. It is therefore needed to use this information when fitting

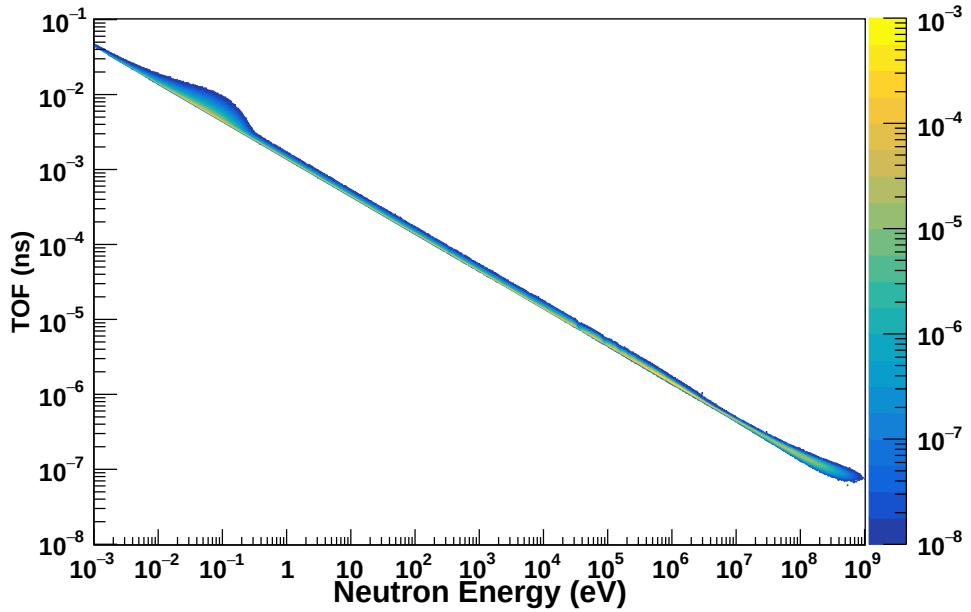

Figure 2.3: TOF distribution as a function of the energy of the neutron, for the EAR-2 at a position of 19.75 cm from the target and a sample size of 2.5 cm in diameter. A beam duration of 7 ns (R.M.S.) has also been included in the simulation.

the experimental data by means of resonance analysis codes as SAMMY or REFIT. The RF is dependent on the position and size of the samples. To extract such detailed numerical data from the simulations, among other utilities, the n_TOF Collaboration has developed a Transport Code. This code implements an optical transport of neutrons from a scoring plane located right after the target towards the EAR. A set of pre-recorded primaries from MCNP and FLUKA simulations of the spallation process in the target are used to feed the Transport Code. A selection of parameters allows to customize the simulation requests for the specific needs of each experiment. This includes the position and size of the sample (including misalignment), the possible layers of materials upstream (Al or kapton windows, backings, other samples, etc). The details of the procedures to obtain the Resolution Function for any experiment are described in Ref. [88].

2.2.2 EAR-2

The ^{14}N(n,p)^{14}C reaction was measured in 2017 within Phase-3. During that time, the 2nd Generation n_TOF Target was in place. That target was designed for operation when there was only one experimental area (EAR-1), and therefore it was not optimized for EAR-2. Considering this, here we will describe the features of this facility concerning that Target, even if after this, the 3rd Generation n_TOF Target, optimized for both EAR-1 and EAR-2, is now on duty.

Figure 2.4 shows the layout of the beam line and a photo of the experimental area inside the bunker. The technical features of the facility and the characteristics of the neutron beam are described in detail in Refs. [89, 90]. Here we will present the overall features that characterize EAR-2, including the flux, the beam profile and the Resolution Function.

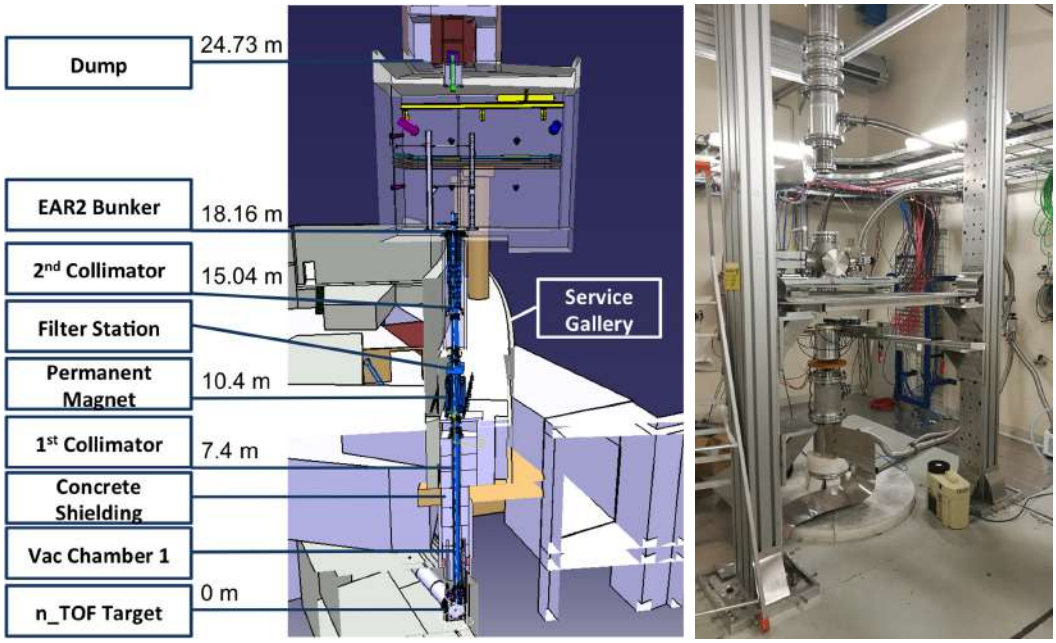

Figure 2.4: *Left:* Layout of the EAR-2 pipes and collimation system from the n_TOF Target (bottom) to the Experimental Area and the Beam Dump (top). The location of the magnet, collimator and auxiliary equipment are indicated. *Right:* Photo of the inside of the EAR-2 bunker at the time of the measurement of the ^{14}N(n,p) reaction. Neutrons come upstream from underground to reach the location where the samples and detectors are located, at the center of the image.

The EAR-2 Neutron Flux, Beam Profile and Resolution Function

The neutron flux of the n_TOF EAR-2 is comprised of several components that are defined depending on the target and moderator design. Neutrons from the spallation reactions are mainly generated by fission and evaporation processes, which develops into an *evaporation peak* centered around 1 MeV. There is an additional peak, called *spallation peak*, originated from neutrons coming from intra-nuclear cascade, around 100 MeV. The maximum energy of the spectrum is limited by the kinetic energy of the proton beam (20 GeV/c momentum), so the spectrum reaches up to a few GeV. The moderation system based on water (hydrogen-rich material) generates a long tail ending around a *thermal peak* centered at 25.3 meV. This tail is somewhat flat, leading to an iso-lethargic behavior of in the epithermal part the spectrum (from 1 eV to hundreds of keV). Moreover, the thermal peak can be removed by the use of borated water, that absorbs mostly thermal neutrons via the ^{10}B(n,α) reaction. This reduces the overall background by suppressing the gammas from the ^{1}H(n,γ) reaction generated in water by these neutrons. This is done for EAR-1, while at EAR-2, a pure water circuit is used for both target cooling and moderation. Thus, the thermal peak is not suppressed. Other features of the spectrum are related to the presence of materials along the beam line, such as oxygen and aluminum or contaminants as manganese, which generate the so-called dips in the spectrum.

Figure 2.5 shows the spectrum of EAR-2 in units of neutrons per nominal pulse, which is established as the one generated by a $7{\cdot}10^{12}$ proton bunch onto the n_TOF target, both as an energy spectrum (*left*) and as a TOF spectrum (*right*).

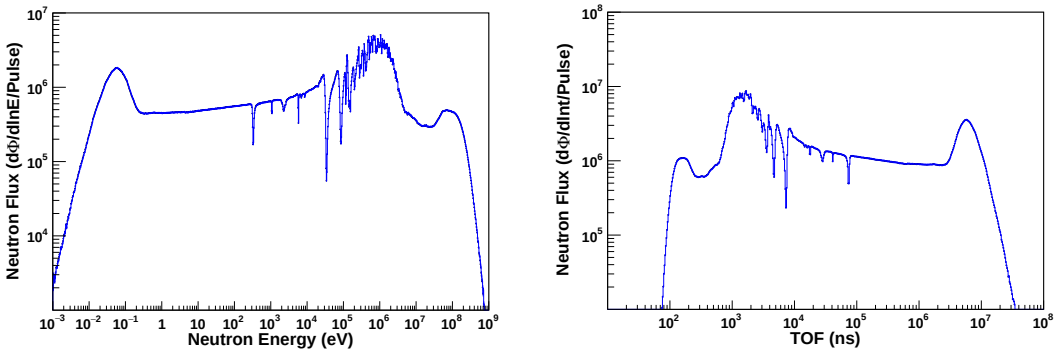

Figure 2.5: Nominal neutron flux at EAR-2 per pulse, at a distance of 19.5 m from the n_TOF Target. The *left* figure shows the energy spectrum. The *right* figure shows the TOF spectrum. Simulations from the n_TOF Transport Code.

The instantaneous flux of the EAR-2 can be computed by integrating the energy-dependent flux. From 3 meV to 100 MeV, the instantaneous flux for EAR-2 is $11.5{\cdot}10^5$ n/cm^2/pulse (compared to $1.5{\cdot}10^5$ n/cm^2/pulse at EAR-1). By converting to time by means of the average frequency of the proton pulse, the flux at EAR-2 becomes $9.58{\cdot}10^5$ n/cm^2/s (and $1.25{\cdot}10^5$ n/cm^2/s for EAR-1).

The EAR-2 beam profile depends on the features and distances to the target, collimators and entrance windows. Neutrons are produced at different positions within the spallation target and with a certain angular distribution. Besides this, the beam profile is dependent on the neutron energy, which has to be taken into account in simulations, specially in the case of position-sensitive detectors or small samples. Figure 2.6 shows the integral 2D beam profile at a distance of 19.5 m from the target, for the configuration used during the ^{14}N(n,p) measurement.

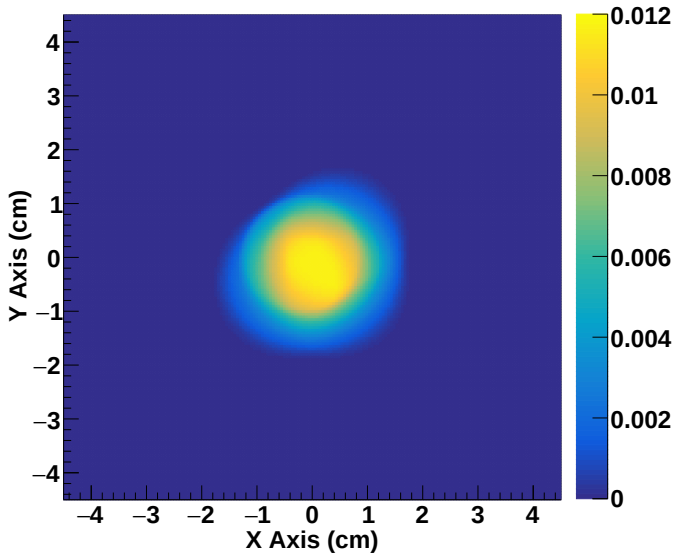

Figure 2.6: Beam profile at n_TOF EAR-2, 19.5 m from the target. Arbitrary units in the Z-axis. Simulations from the n_TOF Transport Code.

The EAR-2 Resolution Function

The EAR-2 Resolution Function is shown in terms of a λ distribution as a function of the real energy of the neutrons in the beam in Figure 2.7. It is clearly noticeable the effect of the size or duration of the initial proton bunch which generates the neutron beam, that dominates at the highest energies (low TOF) but also rapidly declines in influence and thus the width of the distribution is much reduced around the MeV range. The effect of neutron moderation enlarges the distribution and generates a long tail towards larger values of λ (larger moderation times imply a longer track inside the moderator, and thus an increased effective path length). This effect is much more increased at the thermal peak, where completely moderated neutrons can perform longer tracks without changing their energy. The color scale corresponds to the number of histories in the simulation, and thus the intensity is larger around the neutron energies where the flux is also the highest.

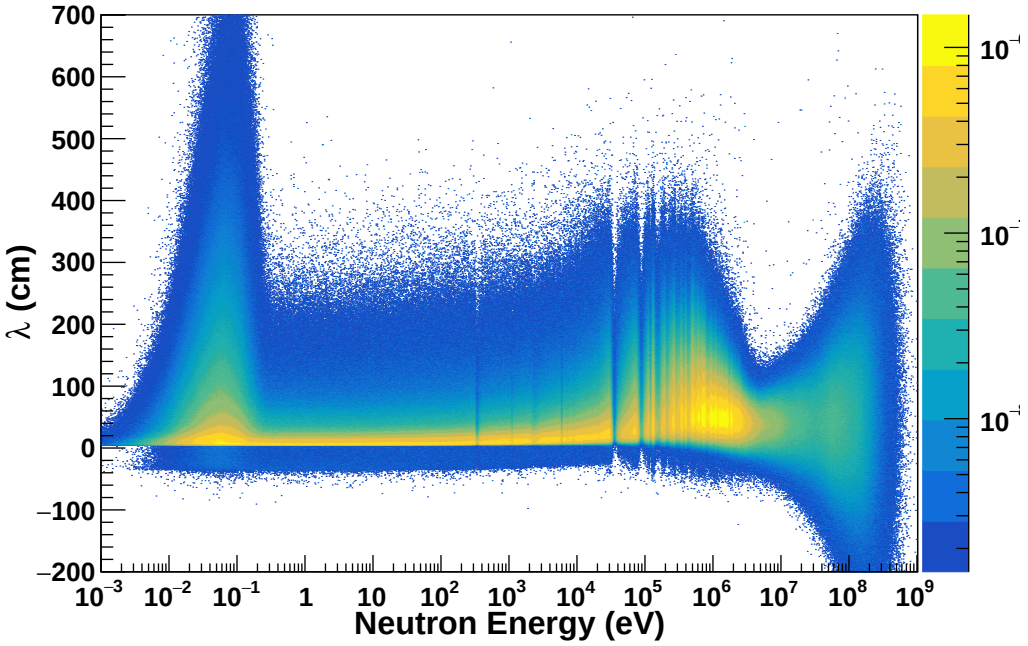

Figure 2.7: λ-2D distribution as a function of the energy of the neutron, for the EAR-2 at a position of 19.75 cm from the target and a sample size of 2.5 cm in diameter. A beam duration of 7 ns (r.m.s) has also been included in the simulation.

2.2.3 Data Acquisition and ROOT-file production

The n_TOF Data Acquisition System (DAQ) during Phase-3 was based on Signal Processing Devices (SPDevices), which offered a good combination of high sampling rate and amplitude resolution and a high dynamic range. ADQ412DC-3G cards were used, with a maximum sampling rate of 2GS/s, a resolution of 12 bits and 175 MB on-board memory. This combination allows to record the full time window in which neutrons travel from the target to the experimental area. Every detector was connected to a particular electronic chain based on the detector requirements and amplification needs. At n_TOF, a large amount of data is generated corresponding to each pulse, which requires a high data transfer, that further calls for sufficient

computer power to analyze and store data. In the aim to reduce the amount of data recorded per bunch, a *zero-suppression algorithm* is applied before transferring data to disk. This algorithm selects a number of samples before and after a signal has crossed a certain pre-defined threshold, while the rest of the data, which presumably contains only noise and low energy background, is rejected. This threshold has to be defined in a conservative way so as not to reject any real signal, but also to keep data storage within acceptable limits. The recorded data (RAW data) are saved and transferred to CASTOR (CERN Advanced STORage system), which can be retrieved later for analysis.

The trigger to start data acquisition is sent by CERN PS 10 μs before the proton bunch impinges onto the n_TOF Target. Since then, a movie of 100 ms maximum (with the fragments selected by the *zero-suppression algorithm*) is recorded. These movies contain information of the timestamps and amplitude at each time in terms of ADC channels (Analog-to-Digital Converters), which are saved in binary RAW files. These RAW files have to be further processed into ROOT files. These ROOT-files can be analyzed using the object-oriented data analysis framework ROOT, developed at CERN. To do so, the Pulse Shape Analysis (PSA) code was developed at n_TOF [91]. This code is designed for pulse recognition from the RAW-data movies. The code makes use of a set of parameters that allow to define the specific requirements for each type of detector and particle. The basic principle behind the code is the recognition of a signal if the derivative of the signal crosses several times a threshold defined as a multiple of the RMS (root mean square) in a broader neighborhood within the movie. Additional parameters define certain threshold for signal amplitude, area or width, or those for the identification of the γ-flash, which determine the reference time and thus the TOF of any signal. In order to test the performance of the PSA code, a *Signal Analyzer* Display was also developed at n_TOF in order to visualize the signal identification with actual RAW data. Figure 2.8 shows an example of pulse recognition by the PSA using the *Signal Analyzer*.

Once the set of parameters are optimized for signal recognition of a given detector type and particle, all the RAW data files are processed and converted into ROOT files. The data contained in these ROOT files is organized in *TTrees*, which register each event with a list of *TBranches*. Each of these refer to a relevant information of a pulse, *i.e.* the t_m, amplitude, area or FWHM of the signal, but also the arrival time of the γ-flash, t_γ, of the bunch in which this signal was recorded, so as to determine the TOF, and other pertinent data.

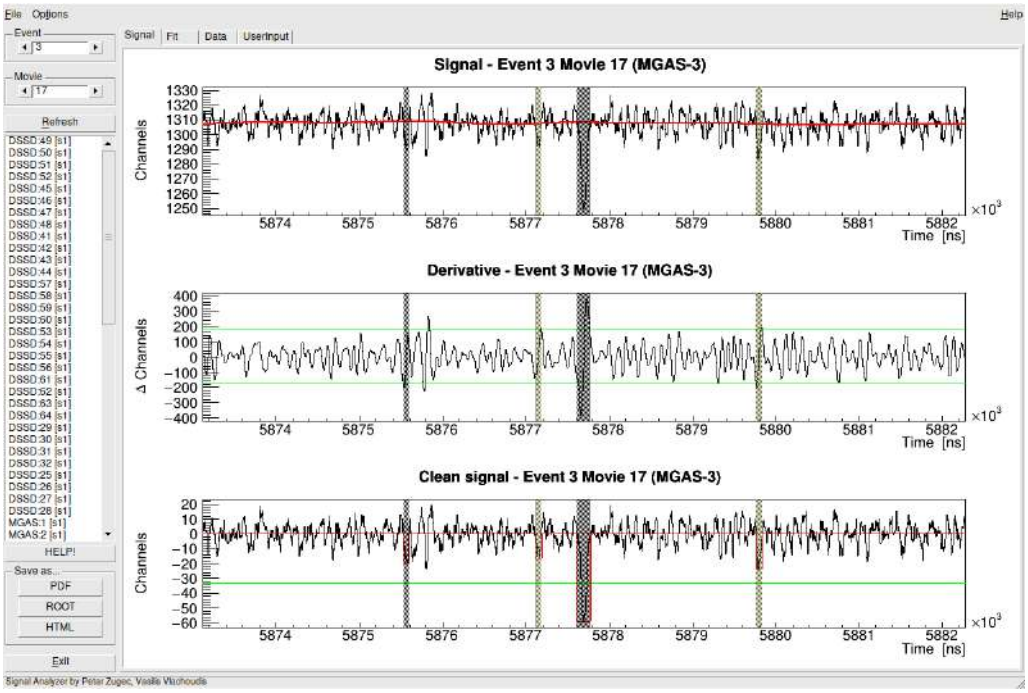

Figure 2.8: Screenshot of the *Signal Analyzer*. The image shows a movie from the MicroMegas Detector facing the backward adenine sample used in the measurement of the ^{14}N(n,p) reaction. The top panel shows the original signal (black) and the baseline (red). The central panel shows the derivative of the signal, and horizontal green lines indicate the threshold used as first criterion to identify pulses. The lower panel depicts the recognized signals and pulse shape fitting (not applied in this case). Recognized pulses are highlighted in grey.

2.3 The Experimental Campaign for the ^{14}N(n,p) reaction

The ^{14}N(n,p) reaction was measured at n_TOF during September-October 2017. The measurement was carried out in a joint Campaign together with the ^{35}Cl(n,p) reaction, which is not covered in this thesis. For both reactions, the energy range of interest was similar, and the out-going particle, a proton, has a similar kinetic energy, allowing to use the same type of detectors and set-ups.

The experimental setup consisted of a couple of separate detection system that worked in parallel. The first of them, (upstream) was based on a stack of micro mesh gaseous structure detectors (MicroMegas), while the second (downstream) used Double-Sided Silicon Strip Detectors (DSSSD).

The measurement was carried out relative to the ^{10}B(n,α) reaction. To this aim, $^{10}B_4C$ samples were used in both detection systems. For validation and in order to set the TOF-to-Energy calibration, an ^{235}U sample was included in the MicroMegas set-up. In order to measure the ^{14}N(n,p) reaction, adenine ($C_5N_5H_5$) samples were used. For the joint measurement of the ^{35}Cl(n,p) reaction, potassium chloride (KCl) samples were used.

MicroMegas Detectors

The MicroMegas detectors are a type of gaseous detectors based on microbulk technology, for which the low-mass, robustness and neutron and γ transparency allow the use of several detectors along the beam with a minimal perturbation of the neutron beam. Since the detectors are on-beam in front of the samples, the geometrical efficiency is close to 50 % [92]. This type of detector has been used regularly at n_TOF both for measurements [93] and beam characterization and monitoring [90].

A MicroMegas detector is divided in two gas volumes by a thin metallic plate with micro-holes in its surface (the micro-mesh, of $\approx$ 5 μm width). The first region is delimited between the cathode and the micromesh, which are separated by a few mm. The second region is defined between the micromesh and the anode, with a typical width of 25-100 μm. For neutron-induced reactions, the neutron-converting material is deposited onto the cathode, also called drift electrode. For that reason, the backing material of the samples has to be a conductive material, such as Al. The charged particles produced by the neutron interaction that enter the first volume (conversion region) generate ionization within the gas. The electrons produced are drifted through an electric field towards the micromesh. The voltage applied to the drift and mesh electrodes has to be determined to maximize the electric field lines that pass through the micro-holes so as to increase the detector transparency. Once the electrons arrive to the second volume (amplification gap), the number of electrons multiply by means of avalanche processes. The gain of the detector can be further controlled by the mesh voltage. An appropriate selection of the parameters generate a signal large enough to be detected, with other constraints being the resolution, controlled via the drift velocity and the time needed for charge collection, which controls the probability of having pile-up events.

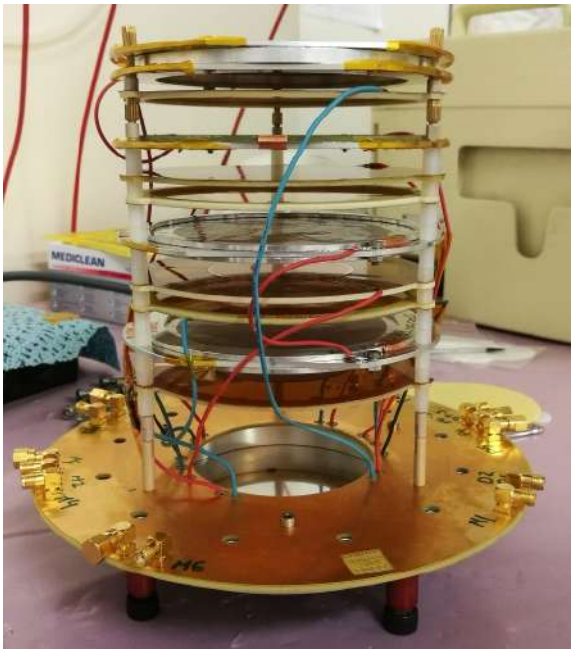

Figure 2.9: The MicroMegas setup, with the six samples and six MicroMegas detectors used in the measurement. Two additional samples of KCl were placed for the purpose of other measurement. From top to bottom, the uranium, boron, adenine and KCl samples are shown.

The MicroMegas setup consisted of a set of detectors mounted in a common vessel as shown in Figure 2.9. It was operated with a gas mixture of 90 % Ar and 10 % CF_4 at atmospheric pressure and room temperature. The MicroMegas detectors were 9.5 cm in diameter. The ^{235}U and ^{10}B samples were placed in forward direction, the two nitrogen samples were placed in a back-to-back configuration, and two KCl samples in the same configuration as the previous ones. Separate measurements with the samples and dummy samples (Al foils as substrate of the nitrogen samples) were carried out in order to determine the background and reduce systematic uncertainties.

Double-Sided Silicon Strip Detectors

The DSSSD are solid state detectors that provide position sensitivity and allow background subtraction by means of front-rear strip coincidence analysis. These detectors have to be placed off-beam where a lower beam background is found, at the cost of a lower geometrical efficiency. The DSSSD used in this experiment, model W1 by *Mirion Semiconductor Ltd.*, had a total active surface of 49.5×49.5 mm^2 and 16×16 strips, being each strip of 3.1 mm width. The nominal silicon thickness was 40 μm. Front and rear strips are aligned in transverse directions. Coincident pulse detection in one strip of each side allows the position identification of the particles.

The DSSSD setup consisted of a couple of detectors facing each one a sample of adenine (top sample) and KCl (bottom sample). These samples were replaced temporarily at the beginning and end of the measurement and replaced with ^{10}B samples for normalization. Additionally, the samples were replaced with an ^{241}Am source, and a mask was located in between the source and the detector, for calibration and testing purposes. Figure 2.10 shows the DSSSD setup.

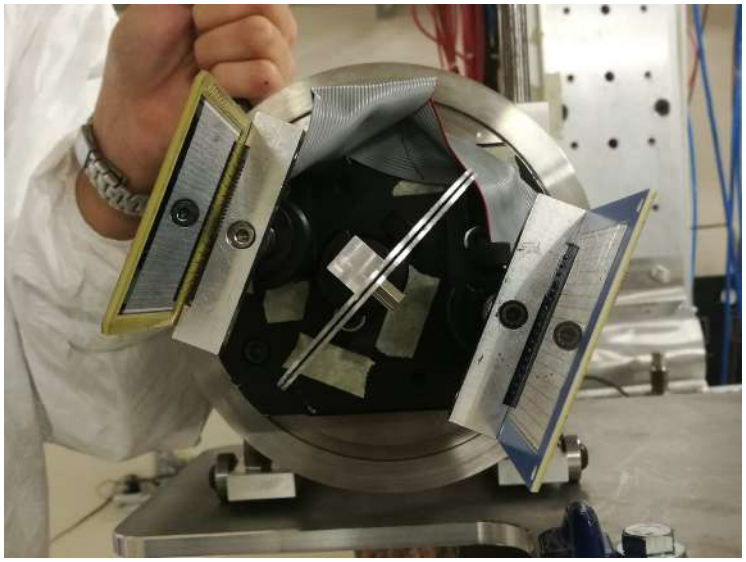

Figure 2.10: The DSSSD setup, with the two samples (adenine at the top and KCl at the bottom) and two DSSSD facing each sample. The position sensitivity of the DSSSD allows an angular distribution analysis of the reactions.

2.4 Preparation and characterization of the samples

For this measurement, one ^{235}U sample, one ^{10}B sample and two ^{14}N samples were used for the MicroMegas setup. For the DSSSD setup, one ^{10}B sample and one ^{14}N sample were used. All the sample deposits were 9 cm in diameter in the case of Micromegas, and 5 cm in diameter in the case of DSSSD, which is enough to cover the neutron beam.

The ^{235}U sample was prepared with the electrodeposition method and an areal density of 0.1176±0.0005 mg/cm2 with a 99.934 % ^{235}U enrichment onto 30 μm of Al. The boron sample was made of $^{10}B_4C$ by the sputtering method.

The nitrogen samples were made of adenine ($C_5H_5N_5$) and prepared by thermal evaporation at CERN by Mr. Wilhelmus Vollenberg. The use of adenine was a reliable choice following the large nitrogen composition and the low neutron cross section of carbon. The hydrogen present in the sample produces gamma radiation after neutron interaction that is not detected by the Micromegas. Also the proton recoils from elastic scattering of neutrons have lower energy than those from the ^{14}N(n,p) reaction produced by neutrons of the same incident energy, and can be identified and thus filtered out. The adenine samples were characterized via Rutherford Back-Scattering (RBS) at the Centro Nacional de Aceleradores (CNA) in Seville, Spain. Previous works showed excellent possibilities for sample characterization [94]. The energy of the H^+ was selected at 0.85 MeV.

In the simulations the Rutherford cross-section for the scattering of H^+ in Al was used. For C, N and H, the evaluated cross-section data from the IBANDL database were used [95]. The RBS spectra were analyzed using the SIMNRA package [96].

Considering the dimension of the samples (5 and 9 cm in diameter) and of the H^+ beam spot (3 mm) used for the sample characterization, several points were analyzed for each sample to provide a picture of the homogeneity. The samples were scanned from the edges to the center in three different directions. In order to perform an accurate and precise determination of the number of atoms of ^{14}N, few points outside the area coated with adenine were also analyzed by RBS. This allowed the determination of the cleanliness of the substrate reducing the free parameters of the SIMNRA fit of the experimental data. The overall thickness of adenine is revealed both by the presence of the peak and the reduction in energy of the edge from the Al substrate. A noticeable increase of the adenine thickness is found when comparing the center with respect to the edges of the sample.

Figure 2.11 shows an example of the fitting of the SIMNRA simulation with the experimental data. The contributions from each isotope present in the sample are also included in the figure, demonstrating the clear coincidence of the steps in the number of counts with the simulated curves. In order to estimate the accuracy of the measurement, several fits of the spectra varying the adenine thickness were carried out for each measured point, finding a good agreement for all measures within 1-2 % of uncertainty. This procedure was followed for each measured point in all samples.

Several points were measured over the samples in search for variations in the thickness. We found a smooth reduction of the mass density from the center to the edges.

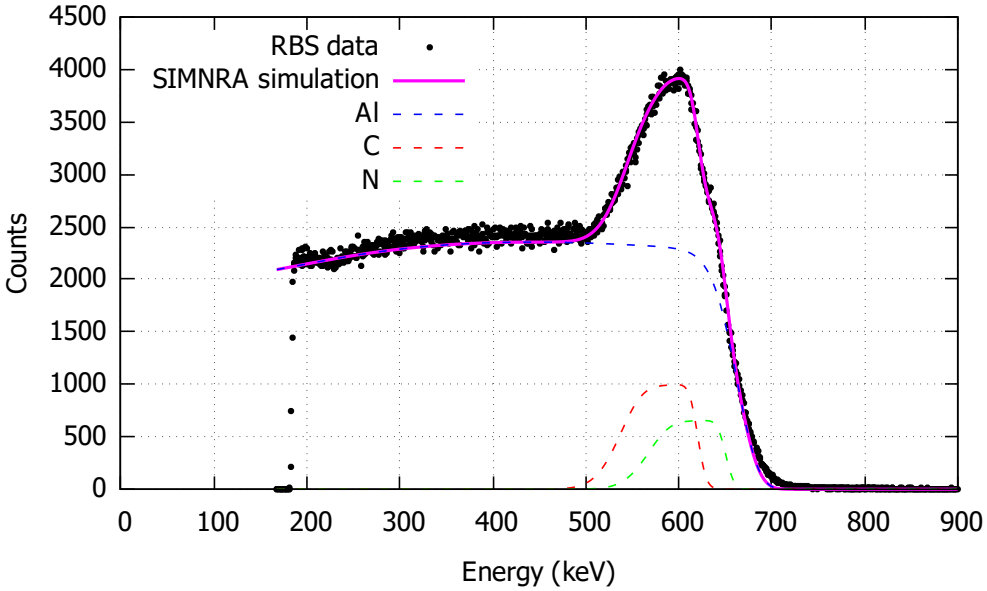

Figure 2.11: Example of a single RBS measurement and mass thickness determination through simulations. The results of the SIMNRA simulation, with the detailed contribution from each isotope also shown with dashed lines.

The same mass density was found for points at the same distance from the center, within uncertainties. Figure 2.12 reveals a parabolic pattern in the mass density, which was attained through the equation $m = m_0 - a \cdot r^2$. The parameter a is a measure of the mass distribution throughout the sample, quantified as the curvature of the quadratic fit, while m_0 is the mass density at the center of the samples. This behavior was shared for all samples. The fitting of the data including the spatial distribution aimed to reduce the uncertainty, which reduces to 1.2-1.5 % for the total mass in the samples.

Table 2.1 summarizes the results for all the samples. The mass at center corresponds to the peak surface density of atoms, and a is the mass distribution parameter. The total mass is computed as the integral of the mass density given by the above mentioned formula.

Sample	m_0 (at/b)	a ($at/b/cm^2$)	Total number of atoms ($10^{20} \cdot at$)
DSSSD	$6.88{\cdot}10^{-6}$	$7.24{\cdot}10^{-8}$	1.306±0.020
Backward MicroMegas	$1.382{\cdot}10^{-5}$	$2.18{\cdot}10^{-7}$	8.79±0.11
Forward MicroMegas	$1.958{\cdot}10^{-5}$	$3.91{\cdot}10^{-7}$	9.94±0.12

Table 2.1: Results of the characterization of the mass density for all the adenine samples.

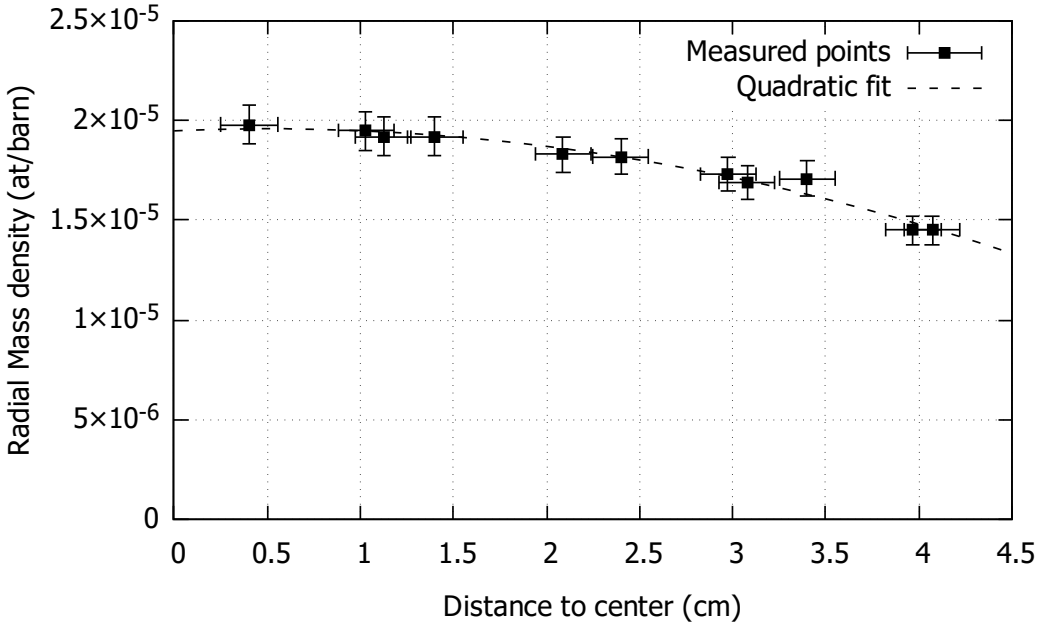

Figure 2.12: Mass density radial distribution for the Forward adenine sample in the MicroMegas setup. The horizontal error bars match with the size of the probe (3 mm). The adenine thickness gradually decreases to its edges following a quadratic function. The quadratic fit is shown with a dashed line.

2.5 Data Analysis

At n_TOF, two types of proton bunches are delivered to the target by the PS. Primary pulses are dedicated to n_TOF and have an intensity close to the nominal intensity ($7{\cdot}10^{12}$ protons per bunch). A second type of pulses, also called *Parasitic* pulses, have a lower intensity (2-3.5$\cdot 10^{12}$ protons per bunch).

In all cases, the analysis was done separately for high intensity and low intensity pulses. High intensity pulses allow larger statistics, but suffer from a most intense gamma flash. On the other hand, low intensity pulses profit from a reduced gamma flash which allows a better signal identification and cleaning, thus increasing the energy range of the measurement in the high energy region.

The count rate, C, in a certain detector can be computed as:

$$C = N\sigma\Phi\epsilon + B \tag{2.8}$$

where N is the number of atoms in the sample that faces the beam, or effective mass; σ is the reaction cross-section, Φ is the neutron flux impinging onto the sample and ϵ is the detection efficiency, which depends on the geometrical solid angle of the detector to the sample and the intrinsic detection efficiency. B is the background count rate, which is composed of all other detected radiation, including ambient background, beam-related and sample-related sources of radiation. The flux can be computed by means of another known reaction, such as standard reactions as ^{10}B(n,α) or ^{6}Li(n,t).

In our case, the cross-section of the ^{14}N(n,p) reaction will be computed relative to the ^{10}B(n,α) reaction:

$$\sigma_N = \frac{(C_N - B_N) \cdot N_B \cdot \epsilon_B}{(C_B - B_B) \cdot N_N \cdot \epsilon_N} \sigma_B \tag{2.9}$$

where subscripts X_N and X_B indicate nitrogen and boron, respectively.

Signal identification allows a filtering of a large fraction of fake signals, and thus serves as a first raw estimate of the count rate. However, this is a poor estimate and has to be corrected for several effects. For instance, dead-time and pile-up events have to be accounted. Pulse selection and thresholds always leave some undetermined pulses out, which need to be accounted and compensated. Background needs to be estimated and subtracted. Beam attenuation between and within samples has also to be accounted. This is specially relevant in case of thick samples, or when a stack of samples are placed on top of each other, as in the MicroMegas set-up. In order to calculate the detection efficiency, dedicated simulations of the set-up have to be performed. The next sections will describe the overall corrections performed in this analysis, separately for each detection system.

2.5.1 MicroMegas Analysis

Signal Identification

The signals from MicroMegas detectors were reconstructed off-line by means of a Pulse Shape Analysis routine described in a previous paragraph, from which information was extracted about the amplitude, area, timing and other features of the signals. Overall, pulse identification was clean and proton signals were properly accounted. The criteria were set so that any possible real proton signal were included, even if several fake signals were also identified as such. Posterior stages in the processing would reject all fake signals, most related to low energy noise structures. Pulse identification in the neighborhood of the γ-flash was greatly limited, due to the non-consistent behavior of the γ-flash recovery. This avoided the design of an average pulse shape for the γ-flash from where deviations could be interpreted as useful signals. Therefore, the maximum neutron energy accessible with this detection system was reduced to around 50-150 keV (depending on the baseline recovery, which was faster for parasitic proton pulses). Figure 2.13 shows two examples of such pulse identification displayed via the *Signal Analyzer*.

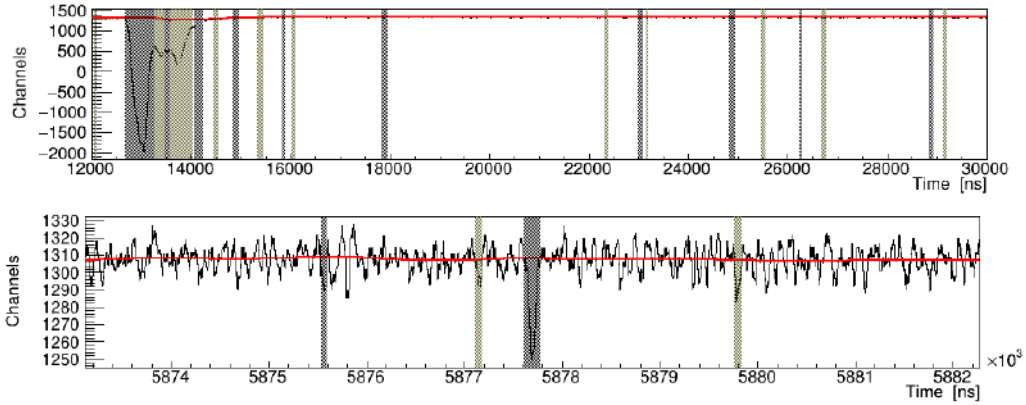

Figure 2.13: Two examples of pulse identification with the PSA routine using RAW data from a MicroMegas detector facing an adenine sample. The top movie shows the identification of the γ-flash structure and the slow recovery of the detector ($\tilde{2}$ μs), and also the identification of smaller amplitude signals later in time. The bottom movie shows the identification of a proton, together with three other fake signals (low energy noise) that would later be rejected.

Noise and background subtraction

In the case of nitrogen, the emitted proton has a low energy, which makes it complicate to separate the counts from the low energy noise and background. The adenine samples were replaced with dummy samples (i.e. only with the Al backing) during the last part of the measurement in order to measure the overall background. Dedicated fittings of the count distribution along the whole energy range were performed, in order to estimate the fraction of rejected counts outside the selection thresholds. Figure 2.14 shows the counts from the forward nitrogen sample in the MicroMegas detector. The signals from protons can be clearly distinguished above the background along the energy range, also noting an increase of the low energy noise in the detector at higher neutron energies towards the γ-flash, which limits the proton detection above 100-150 keV, considering also the lower proton production due to the decrease of the cross-section at these energies.

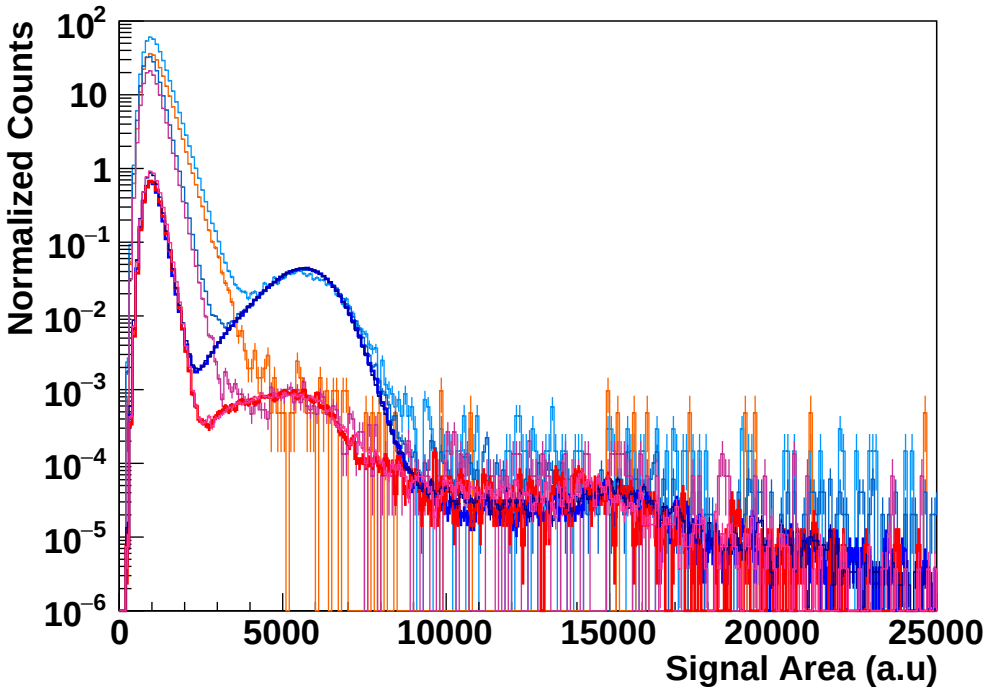

Figure 2.14: Energy deposition spectra for four neutron energy intervals (5-20 meV, 0.2-2 eV, 20-200 eV and 2-20 keV) in the MicroMegas detector facing the forward adenine sample. The blue-like colors correspond to the data with the adenine sample, while the red-like colors correspond to the Dummy sample (only Al backing). Thick lines correspond to the counts in the 0.2-2 eV neutron energy interval and Light blue/orange spectra correspond to the 2-20 keV one. The curves have been normalized to the same integral between 3700 and 10000.

A similar procedure was followed in the case of the boron and uranium samples. Figure 2.15 shows a scatter plot of the area of the signal versus their TOF for the MicroMegas detector facing the ^{10}B sample, where α signals are discriminated from the other reaction products, electronic noise and pile-up events. Similarly, a threshold in energy deposition has been used to separate the fission fragments from the signals from α decay and electronic noise for the detector with the ^{235}U sample as shown in Figure 2.18. In that Figure, the energy deposition curves for different energy ranges have been normalized to prove that the low energy tail is the same at all energies, hence the correction due to the fraction of fission events lost below the threshold is the same at all energies, evaluated as 0.972.

The residual background within the selection thresholds was measured by means of the dummy samples. The background at all the neutron energies was found well below 10^{-3} for the ^{235}U and ^{10}B samples with respect to the reaction count rates, therefore it was neglected in the analysis.

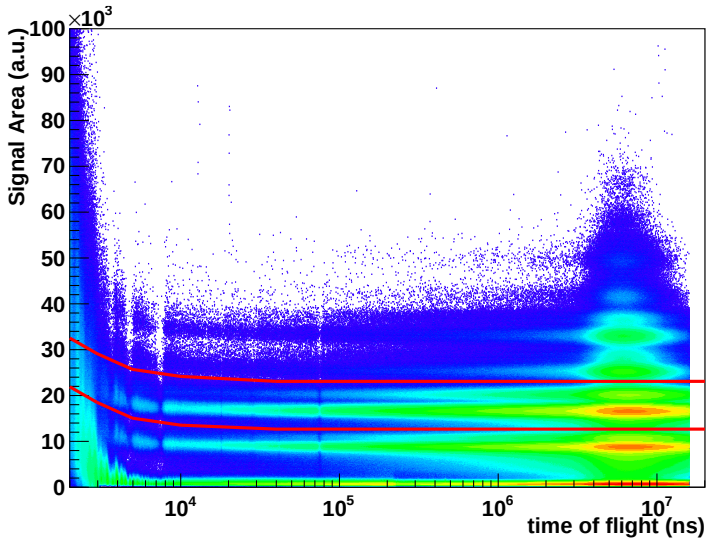

Figure 2.15: Scatter plot of deposited energy vs. time of flight for the detector in forward emission from ^{10}B. The two regions corresponding to the detection of α-particles and ^{7}Li are clearly distinguished (in the upper part also the higher energy α-particles from the (n, α_0) reaction are visible). The lines are the energy-dependent threshold applied to select the α-particles used in the analysis. Pile-up events can also be observed above the regular α signals. The behavior at low tof is related to the effect of the γ-flash.

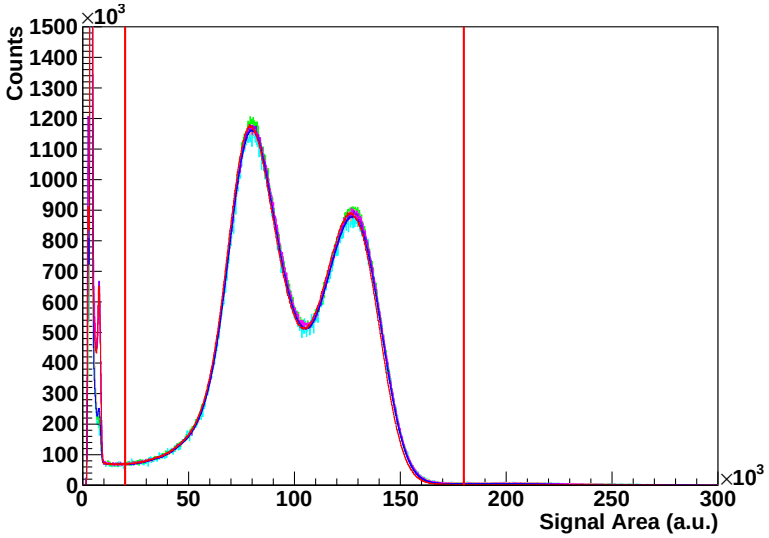

Figure 2.16: Energy deposition spectra for seven neutron energy intervals corresponding to halves of decade in TOF, from $3.16{\cdot}10^3$ to 10^7 ns. The two-bump structure of the bell-shaped curves proves that these are fission events. The curves have been renormalized to the same integral between 20000 and 180000 (thresholds) to prove that the fraction of fission fragments lost below the threshold is independent of the neutron energy.

Dead Time Correction

Dead-time corrections were computed following the non-paralyzable response model [97] assuming a fixed dead time for each detector. The real count rate, C_R, can be computed by means of a correction factor, f_{DT}, to the measured count rate, C_m, as:

$$C_R = C_m \cdot f_{DT}, \quad f_{DT} = \frac{1}{1 - \Delta t_{DT} \cdot C_m}. \tag{2.10}$$

Δt_{DT} is the fixed dead time of each detector, corresponding to the time in which the detection system is not recording any event. This can be estimated via several methods. In this case, an agreement between the different methods was used in order to ensure an adequate estimate for each detector:

- The dead time depends on the time duration of the signals. Therefore, a first estimate of Δt_{DT} is the average FWHM of the signals of interest.
- A second estimate can be obtained by elaborating on the previous one. Using a large data-set of pulses allows to compute statistics on the time interval between consecutive pulses. The distribution of time intervals shall be somewhat flat given the random occurrence of nuclear reactions. However, there shall be a minimum time interval, different from zero, where two consecutive pulses are recognized as a single pulse (and this would then be an event of pile-up). This is observed as a rather sharp cut-off. The location of this cut-off can be used as an estimate of Δt_{DT}.
- The third estimate is more related to the fact that the dead time correction is dependent on the actual count rate. Since at n_TOF there are two types of pulses with different intensities, then the count rate and thus the dead time correction would be different for these two types of pulses. The actual ratio between the yield from high and low intensity pulses shall be 1. By calculating the ratio between the (non-corrected) yield from high and low intensity pulses, one can infer the value Δt_{DT} that restores the ratio to unity. Alternatively, this method can be used as a check for the value obtained with the first two methods.

In the case of the adenine samples, the count rate was low enough that the dead time corrections were negligible in most of the energy range, with a maximum below 0.1 % at the thermal peak. However, for ^{10}B this correction accounted up to 5.5 % and 2.2 % near the thermal peak for dedicated and parasitic pulses, respectively. For ^{235}U the correction peaked around 1.4 % at thermal and some 3-7 % at some resonance peaks. It also went up at low TOF where time separation between events is reduced. Figure 2.17 shows the dead time corrections for the case of ^{235}U and ^{10}B, both for high and low intensity pulses.

Energy Calibration

The TOF-to-energy calibration was performed according to methods described in Ref. [88]. The experimental TOF yield was compared to the simulations from the n_TOF Transport Code, which includes the effect of the n_TOF-EAR2 resolution function. The flight path length, L, was varied as a parameter and the data was fitted to the simulations until a good agreement was found. In order to have an adequate determination of the flight path length, a material with a large number of well known resonances in a broad energy range is needed. This was one of the main reasons to include an ^{235}U sample in the first position in the stack of samples. The agreement between the simulation and the data is shown for a broad set of resonances of ^{235}U in Figure 2.18.

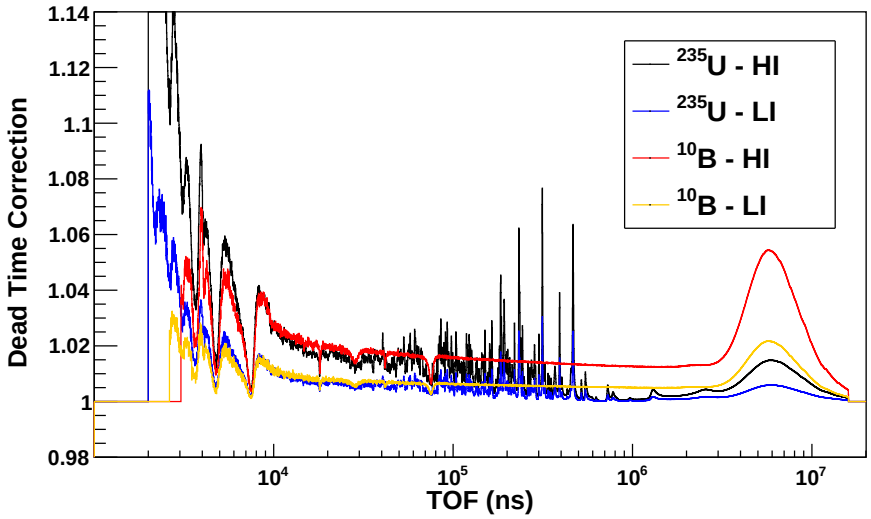

Figure 2.17: Dead time correction, f_{DT}, for ^{235}U and ^{10}B, separated in dedicated (High Intensity, HI) and parasitic (Low Intensity, LI) pulses.

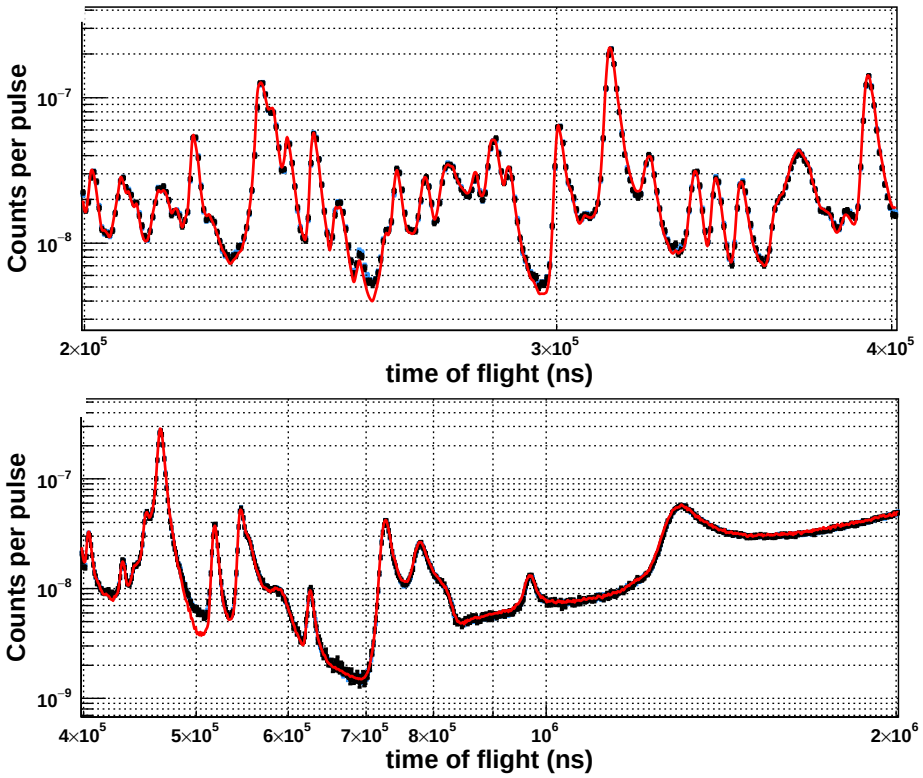

Figure 2.18: Measured ^{235}U TOF spectra in the low energy and resonance region (blue points for low intensity pulses, black points for high intensity pulses), compared to the ENDF/B-VIII.0 evaluation (red line) convoluted with the resolution function by means of the n_TOF Transport Code.

The extracted effective flight path was 19.39 m for the position of the ^{235}U sample in the MicroMegas Chamber. This corresponds to the geometrical distance of the experimental apparatus from the surface of the Pb spallation target. This flight path was adjusted for the subsequent samples according to their position inside the Micromegas chamber.

Neutron Flux and Normalization

The cross-section of the ^{14}N(n,p) reaction was computed relative to the ^{10}B(n,α) reaction, which is a standard reaction in the whole energy range of interest for this measurement. However, the uncertainty in the mass of the boron sample was much larger than that of radioactive samples such as an ^{235}U sample. For this reason, and given that the ^{235}U(n,f) cross-section is a standard for thermal neutrons, the boron sample was normalized to the uranium. This results in a lower uncertainty, as the mass of the uranium sample was determined with an accuracy of 0.425 %.

In addition, the ^{235}U/^{10}B yield ratio was calculated for the whole energy range (not only thermal neutrons) to check the adequacy of the measurement and for validation purposes. A good agreement between the two samples was found, as shown in Figure 2.19, comparing the ratio of the TOF spectra compared to the simulations, where the different detection efficiencies and the neutron beam resolution function are considered, following Ref. [88]. The effect of neutron attenuation due to the relative position of the uranium and boron samples was also considered.

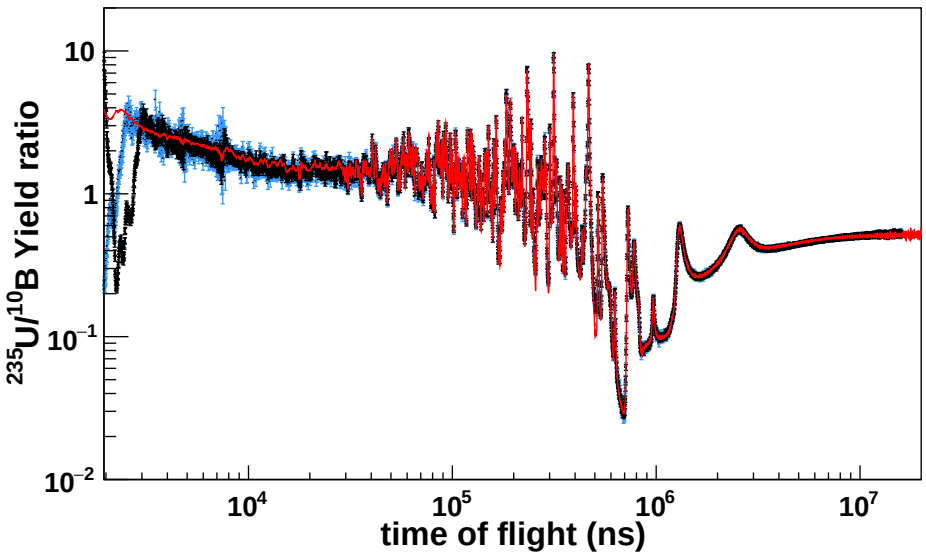

Figure 2.19: Measured ^{235}U/^{10}B TOF ratio with high intensity pulses (black points) and low intensity pulses (blue points), compared to the ENDF/B-VIII.0 evaluation (red line) convoluted with the resolution function by means of the n_TOF Transport Code. The reduced effect of the gamma flash in the low intensity pulses allows to extend the energy range (low TOF).

Simulations on the efficiency

The efficiency corrections for the MicroMegas detectors were determined by detailed Monte Carlo simulations of the reaction products' energy loss in the samples and the gas. In these simulations, the thickness profile distributions of the samples have been considered. Energy and angular distributions were adopted from [98] for the boron sample, and was assumed as isotropic at the center of mass for U and N samples. The reaction events were assumed to occur uniformly along the beam direction inside the sample, and the beam profile from the n_TOF Transport Code was used. The simulations were performed with the MCNP6.2 code [54].

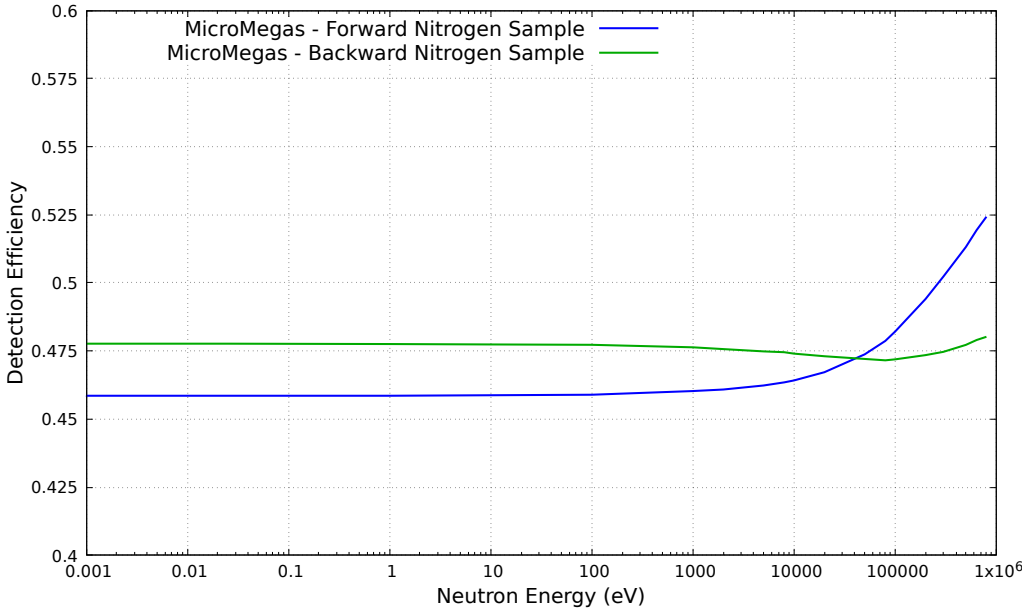

Figure 2.20: Simulated detection efficiency at the MicroMegas detector. Forward (*blue* and backward (*green*) adenine samples are show.

Figure 2.20 shows the total efficiency for the forward and backward nitrogen samples. The efficiency at low neutron energies corresponds to that of proton emission from thermal neutrons, which then changes once the incident neutron energy becomes comparable to the reaction Q-value. The efficiency at low neutron energy is different for forward and backward samples due to the different thickness of the samples (larger for the forward sample), which becomes relevant for proton emission near grazing angles, though this effect becomes less relevant at higher neutron energies. Furthermore, at higher energy the angular distribution in the laboratory system contributes to a larger emission in the forward direction.

2.5.2 DSSSD Analysis

Signal Identification

The identification of the signals from protons due to the ^{14}N(n,p) reaction in the adenine sample or the α and ^{7}Li from the ^{10}B(n,α) reaction in the boron carbide sample was straightforward as in the MicroMegas case. However, the signals related to the γ-flash, which were supposed to serve as the time reference, proved not to be as clear. In most of the cases, the γ-flash signal was intense and very sharply defined, which allowed a clear identification and precise determination of t_γ. However, a non-negligible amount of γ-flash signals (around 20 %) showed a weird-like behavior. In some cases, the shape of the signal was not as sharp or showed multiple minima instead of a first deep peak and a smooth recovery. In these cases, the timestamp of the γ-flash was shifted and therefore it was not reliable. Many other cases had a dim γ-flash signal, which usually could not fall below the selection threshold and hence the signal could not be identified as a γ-flash signal. In these cases, the start of the movie was taken as the time reference, and the TOF determination yielded wrong results. Some more cases did not even show a γ-flash signal, which at the end consisted in the extreme case of the previous behavior.

Some examples of such improper γ-flash identification can be seen in Figure 2.21. Each of the movies correspond to a well defined γ-flash (top movie), a weird-like signal (second

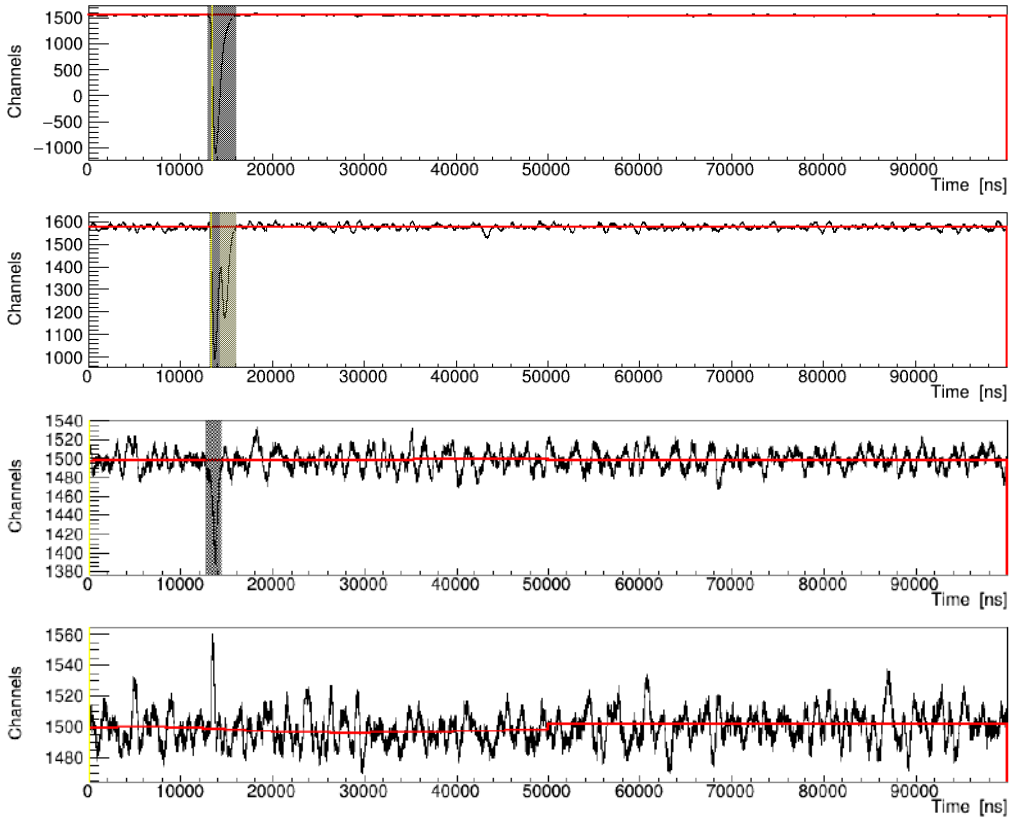

Figure 2.21: Some examples of the movies from several strips in the DSSSD. The movies capture the first 100 μs since the trigger, thus comprising the γ-flash. The baseline is indicated with the red line, and the identified signals are shaded in grey. The γ-flash timestamp is indicated with the vertical yellow line. It can be clearly noted that the γ-flash signal is not present in the 4^{th} movie, it is very dim in the 3^{rd} and deformed in the 2^{nd} movie.

movie), a dim γ-flash (third movie) and no γ-flash signal at all (bottom movie). This behavior was not characteristic of a particular strip or group of strips, but was rather found thorough the whole set of front and rear strips. Moreover, this phenomena was observed in both dedicated and parasitic pulses. It was also checked that these *wrong* γ-flashes were not a feature of a particular bunch, since in most cases these appeared in a single strip while at the same time, adjacent strips presented a well defined signal.

In order to overcome this situation, and given that using the t_γ as time reference would lead to discarding 20 % of the data[1], a different strategy was followed. The grounds of this procedure were described in the previous section, where the TOF technique was presented. The PKUP signal from the proton beam just before impinging onto the n_TOF target was used as time reference, with a time offset, t_{offset}, yet to be determined by calibration. This calibration will be discussed in the next sections.

Time coincidence analysis between front and rear strips in the detector was performed in order to reduce part of the low energy background, which was followed by a pulse-area coincidence signal rejection which allowed a significant signal cleaning. Figure 2.22 shows a scatter plot of the area of the signal versus their TOF for the DSSSD facing the nitrogen

[1]Even more given that a posterior step in the analysis procedure was the time coincidence analysis between front and rear strips, and a significant fraction of signals with a proper t_γ defined would not find a coincidental one, since the other did not have a reliable time reference.

sample. The event data before the coincidence signal cleaning is shown in black, and the cleaned data is superimposed in color. The signal cleaning near the gamma flash allows to separate and identify the signals corresponding to the first two resonances of the reaction. The signals corresponding to the first two resonances can be clearly identified around 2000 ns. The behavior at low TOF is related to the effect of the γ-flash. This is clearly noticed in the *lower panel* of Figure 2.22, zooming in the resonance region. However, even after this signal cleaning, a small amount of unidentified background could not be removed, which is specially relevant in the 10-300 keV range where the cross-section is smaller. That additional background would be subtracted later during the SAMMY fitting in order to extract the final unbroadened cross-section data. Pile-up events are negligible, but a small amount of boron contamination is observed, which does not affect the analysis as it appears at higher signal area (*i.e.* deposited energy). An energy dependent area threshold has been applied to select the protons from the ^{14}N(n,p) reaction, whose contours are delimited with red lines. This procedure led to success using the low intensity pulses, which generate a shorter detector blindness after the gamma flash, but could not be reproduced with high intensity pulses. As the detector recovery from the γ-flash had a duration in the range of 1400-2000 ns (for parasitic and dedicated pulses, respectively), the maximum neutron energy for which reaction products could be observed as separate from the γ-flash was in the range of 0.5-1.0 MeV. This was therefore the maximum energy achievable with this setup. A conservative margin was also applied to avoid any possible count loss in the edge of pulse discrimination. This led to defining the upper limit at 300 keV for dedicated pulses and 800 keV for parasitics. That resulted in a lower collection of statistics above 300 keV, including the resonance region, as there was count collection for parasitic pulses. Below that energy, the full statistics from both dedicated and parasitic pulses was collected and used in the further analysis.

Energy Calibration

In the absence of a sample with a large number of resonances in the DSSSD setup, a different strategy was followed in this case. First, the geometrical distance between the two setups was measured using a ruler. Second, the same procedure as in the MicroMegas setup was followed (*i.e.* fitting the simulated count rate to the experimental data with the flight path length as a parameter). The simulated count rate was computed using the Transport Code as in the MicroMegas case. In this case, the smooth cross-section of the ^{10}B(n,α) reaction was used, in the aim of profiting from the features in the neutron spectrum (*e.g.* the large thermal peak and the many dips in the flux related to Al absorption. In addition to the flight path length, in the case of DSSSD, a second parameter had to be fixed during the calibration. This was the case of the t_{offset} that had to be included due to usage of the PKUP signal instead of the γ-flash as a time reference. The presence of many dips in the flux in a broad energy range together with the thermal peak allowed the determination of both parameters at once, being the t_{offset} more sensitive to the high energy dips (lower TOF), and L had a larger sensitivity at the thermal peak. The results from the fitting for the DSSSD chamber showed that the extracted effective flight path was 19.75 m, in accordance with the geometrical distance between the two detection systems. Figure 2.23 shows the fitting of the simulated yield from the Transport Code with the experimental data from the ^{10}B sample in the DSSSD chamber.

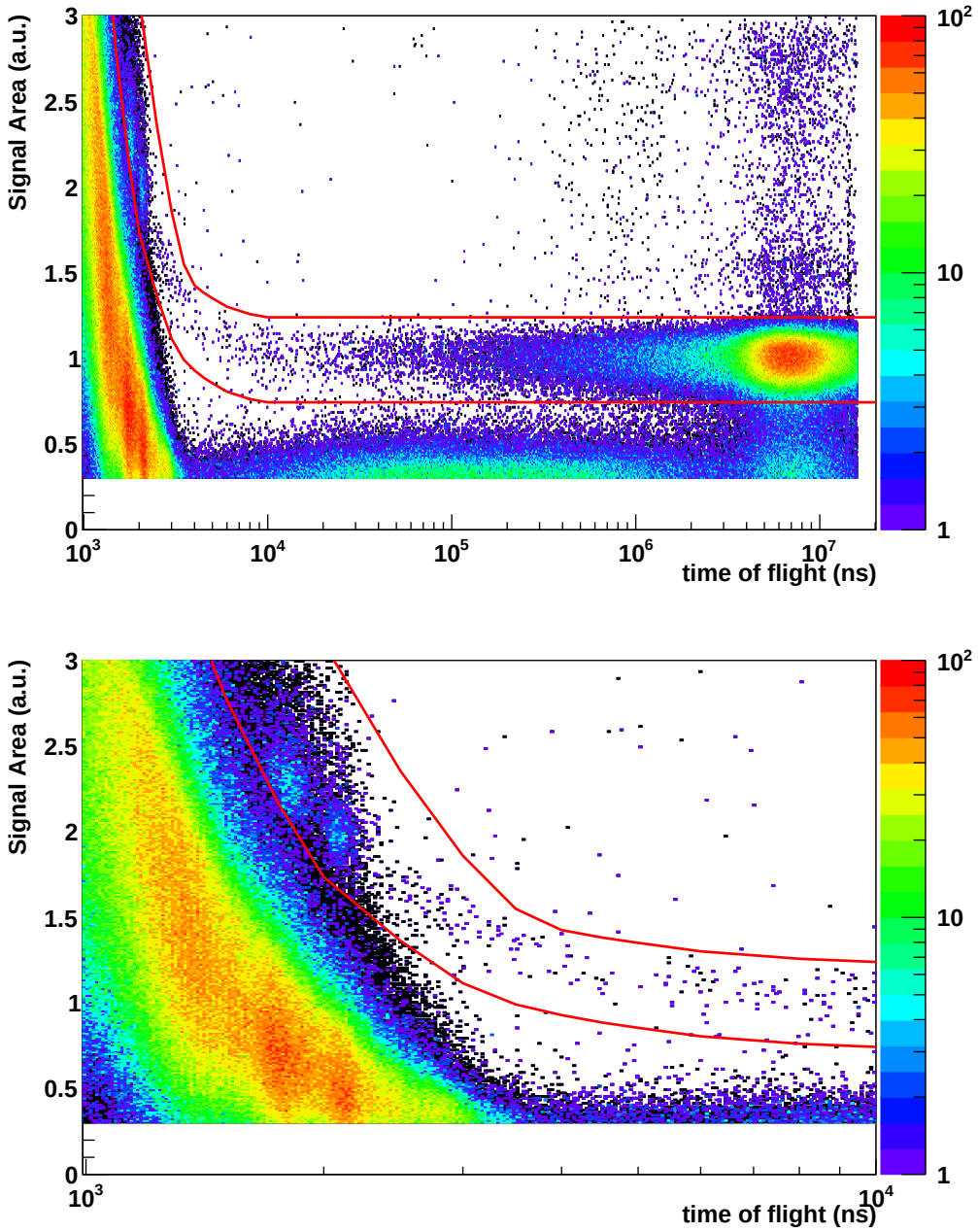

Figure 2.22: Scatter plot of deposited energy (signal area) vs. time of flight for the signals in the DSSSD facing the adenine sample. The the black counts correspond to all the recognized signals before the coincidence analysis, while the coloured counts correspond to the signals after the coincidence analysis. The red lines are the energy-dependent threshold applied to select the protons from the ^{14}N(n,p) reaction. Signals below 0.3 in area were discarded as completely covered by low energy noise.

Simulations on the efficiency

For the case of the DSSSD, in addition to the abovementioned details for the MicroMegas setup regarding kinematics and the description of the adenine sample, the specific geometry of the detector was implemented in the simulations, including the silicon layer thickness and the double strip features, specially regarding the inter-strip spacing. Figure 2.24 shows the simulation of the protons produced in the ^{14}N(n,p) with thermal neutrons,

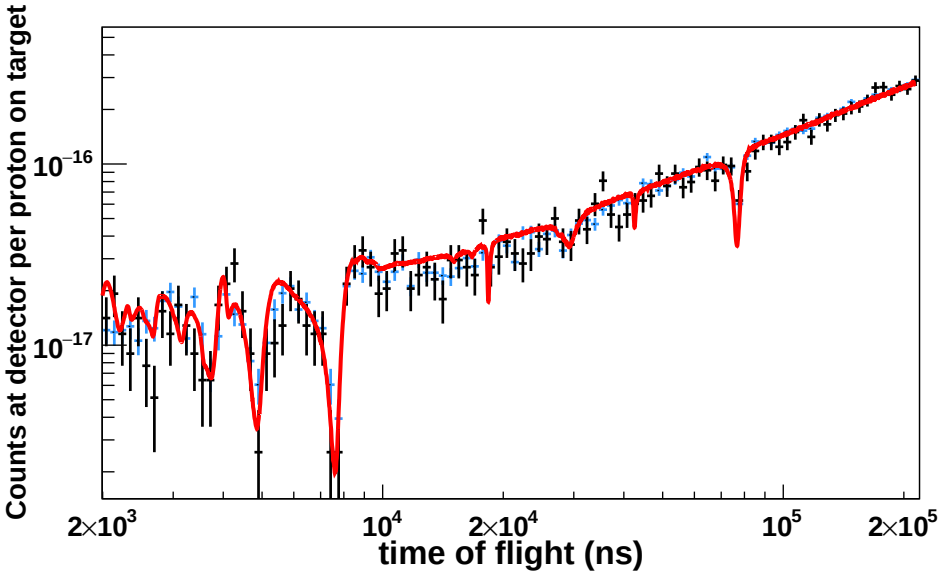

Figure 2.23: Fitting of the simulated counts at the DSSSD (red) to the experimental data with the boron sample (blue for dedicated, black for parasitic pulses).

together with the of the simulated count efficiency, from thermal neutrons and also from 500 neutrons for comparison.

The positioning and orientation of the detector with respect to the sample and the beam were checked with the observed count distribution at the detector, by using an ^{241}Am source and also the counts from the thermal region with the ^{10}B sample, assuming isotropic α particle emission. Furthermore, some of the strips from the DSSSD were broken or noisy, whose geometrical contribution to the detection efficiency was removed from the computations. The detection efficiency for the nitrogen sample is shown in Figure 2.25. The efficiency increases with the impinging neutron energy due to two contributing factors. The first one is the fact that increasing the neutron energy does the same for the outgoing proton by energy conservation. This in turn reduces the likelihood that a proton be kept inside the adenine sample when emitted in a direction far from normal to the sample orientation. The second effect, which is dominating, is the fact that increasing the neutron energy makes the angular distribution peak towards the incident neutron beam direction, also by kinematics. Since the DSSSD is located at an angle closer to the forward direction, the efficiency increases. This effect is also seen in the count distribution within the strips, which shifts towards the forward direction, as it can be seen in Figure 2.24 (*bottom*) when comparing the count distribution within the horizontal strips due to protons from thermal- or 500 keV-neutron-incident reactions.

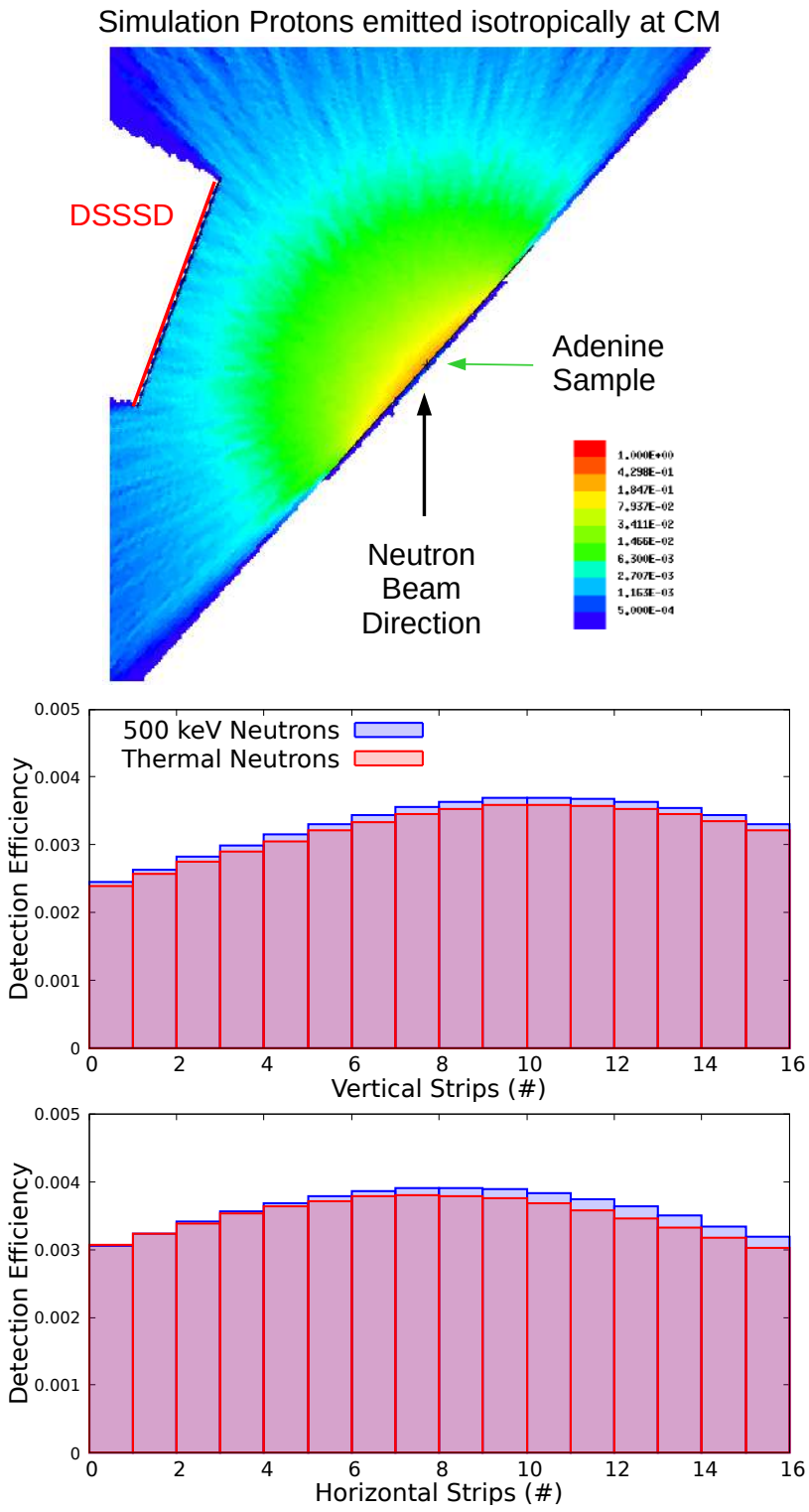

Figure 2.24: *Top:* Plot of the geometry of the MCNP simulation to determine the geometrical efficiency of the DSSSD detector. The position of the adenine sample and the DSSSD are indicated, as well as the incoming neutron beam which serves as the reference direction. *Bottom:* Plots of the proton distribution within the vertical (*top*) and horizontal (*bottom*) strips. Protons generated from thermal neutrons (red) and from 500 keV neutrons (blue) are shown.

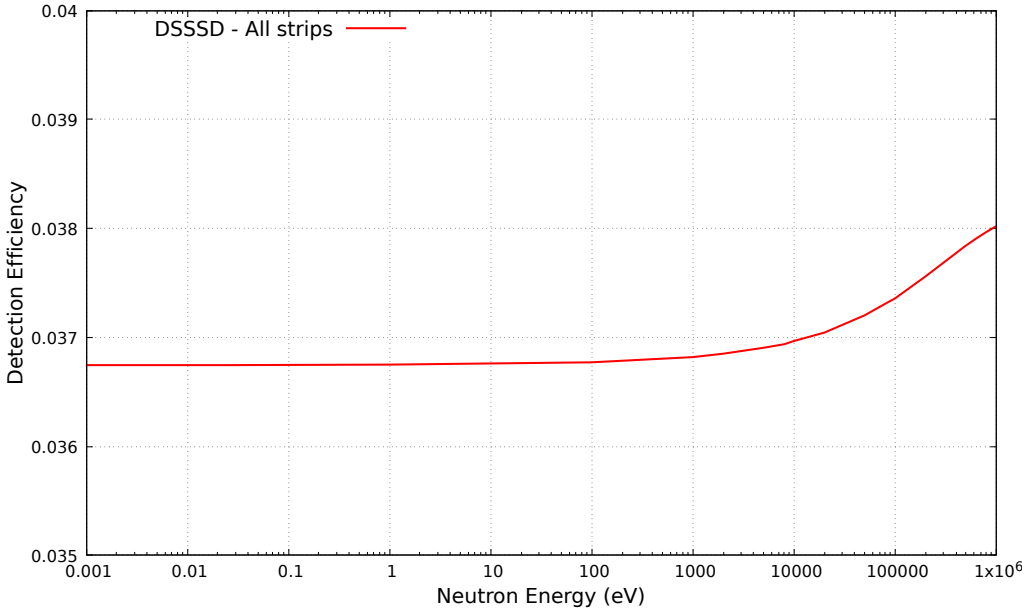

Figure 2.25: Simulated detection efficiency at the DSSSD. The total efficiency (all strips added, discarding the broken ones) is shown.

Neutron Flux and Normalization

As in the case of MicroMegas, a ^{10}B sample was used to estimate the neutron flux at the position of the measurement of the ^{14}N(n,p) reaction. However, in the case of DSSSD, both reactions could not be measured at the same time. Therefore, the adenine sample was substituted by a $^{10}B_4C$ sample at the beginning and at the end of the measurement. The duration of each period was defined so that the amount of statistics was enough and comparable for both measurements, given the limitation in statistics for the DSSSD setup due to the smaller solid angle between sample and detector. Moreover, in the case of the DSSSD setup, the adenine sample was smaller both in size (2.5 cm radius) and in terms of mass (almost 7 times smaller), reducing even further the counting statistics. A larger uncertainty in the sample-detector positioning compared to MicroMegas was also a concern, even after careful measurements and checks of the position distribution of the detections within the DSSSD, which reduced this uncertainty to a lower level.

These reasons led to deciding that the DSSSD cross-section data be normalized to the MicroMegas data, in the range where both reactions were measured at once (the full range of MicroMegas, from 8 meV to 80 keV). This reduced reasonably the systematic uncertainty of this measurement.

2.6 Experimental data from the MicroMegas and DSSSD Measurement

The main goal for this measurement was to obtain a consistent data set spanning from thermal to the resonance region, including a new measurement of the thermal value and covering also the astrophysical range of interest where data was scarce and also discrepancies were found. Furthermore, to provide a new measurement of the first two resonances after previous experiments suggested a possible deviation of a 3.3 factor.

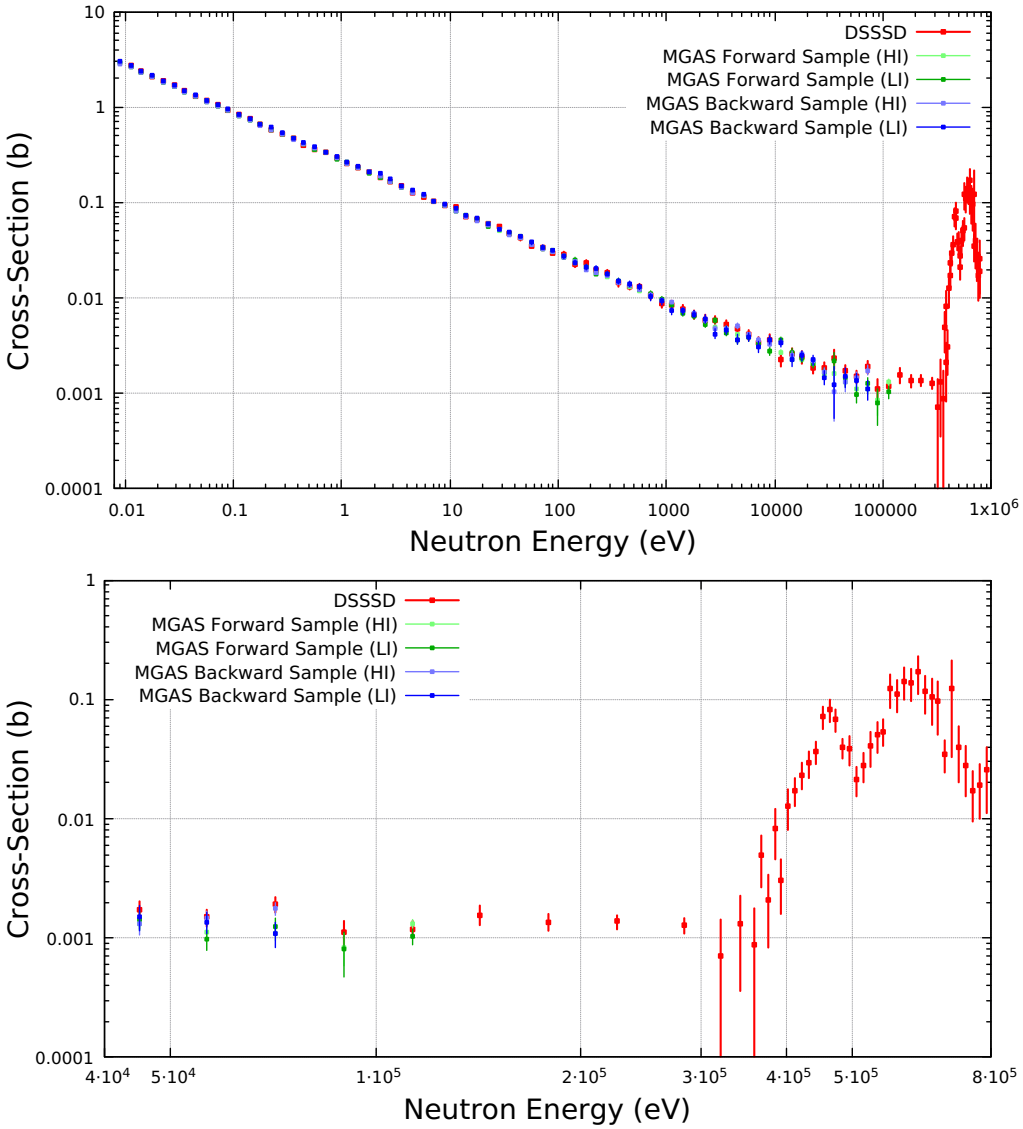

Figure 2.26: Nuclear data from the measurement. Experimental data is still affected by residual background and resolution broadening. Results are shown at 10 bins per decade below 300 keV and 100 bins per decade above 300 keV (resonance region). MicroMegas results are separated in Forward (green) and Backward (blue) samples, and also in High Intensity (HI) and Low Intensity (LI) pulses. DSSSD data is shown in red, corresponding to the merge of HI and LI below 300 keV, and only LI above 300 keV.

The measurement with MicroMegas detectors has covered the range from 8 meV to 80 keV with the backward sample, and up to 130 keV with the forward sample. The results from both samples agree with each other within uncertainties. The measurement covers

the complete 1/v range, including the thermal point, thus reproducing and extending the data by Koehler [69]. It also covers part of the astrophysical range of interest. The measurement with MicroMegas detectors offers reliable results profiting from thick samples and a larger detection efficiency (close to 50 %), from which the thermal cross-section can be obtained and the 1/v behavior confirmed. The measurement with DSSSD detectors extends the range up to 800 keV. This allows to fully cover the astrophysical range of interest, and allows to analyze the first two resonances. The data from DSSSD has a lower counting statistics due to a thinner sample and specially a much more reduced geometrical efficiency. Also increased systematic uncertainties due to the simulation of the geometrical arrangement of the sample and the detector. For this reason, the data from DSSSD have been normalized to that of MicroMegas detectors in the 1/v range, where there are data from both detection systems. Overall, this measurement spans eight orders of magnitude providing for the first time a common consistent data for the thermal and 1/v range, the astrophysical range and the resonance region. Figure 2.26 shows the experimental data from MicroMegas detectors (including forward and backward samples, and also separated by HI and LI pulses) and DSSSD.

These data are still affected by the resolution broadening of the n_TOF-EAR2. This effect is not negligible, and can be noted particularly near the thermal region and more evidently by the broadened resonances. The unbroadened cross-section will be shown after the deconvolution of the data, in order to remove the effect of the n_TOF Resolution Function, specifically computed for the EAR2 at 19.75 m of flight path, by means of a fitting of the data with the SAMMY code [99].

2.6.1 Angular distribution of protons at the 493 keV resonance

Previous measurements of this reaction did not carry out an angular distribution analysis at the resonances. Any deviation from isotropy would be an indication that the spin of the resonance is larger than $\frac{1}{2}$. The available information on the spin and parity for the corresponding ^{15}N state was assigned as $\frac{1}{2}^-$ from a measurement of the $^{14}C(p,\gamma)$ reaction [79]. This would indicate an isotropic proton distribution. Previous measurements of the reverse reaction $^{14}C(p,n)^{14}C$ measured the anisotropy of neutron emission, with Sanders [80] observing a possible anisotropy but attributing it to target non-uniformity, and later Gibbons *et al.* not observing such anisotropy at the center of mass [81].

The angular distribution of the protons emitted at the 493 keV resonance was analyzed by means of the counts at individual strips in the DSSSD. Dedicated MCNP simulations were run using an isotropic proton distribution in the Center of Mass reference system. The reaction kinematics was included in the simulations. Protons were generated along the adenine sample with a spatial distribution given by the neutron beam profile at a distance of 19.75 m from the n_TOF target and 493 keV. Figure 2.27 shows the count distribution in the strips of the detector in the vertical direction that is sensitive to the angular distribution (the strips in the horizontal direction lie perpendicular to the beam and the possible differences between angular distributions is minimal). The experimental data is in agreement with a distribution arising from protons emitted isotropically. However, a small deviation from the isotropic distribution below the uncertainty levels can not be discarded, given the sensitivity limited by statistics. The observed result, compatible with isotropy, is in line with the spin assigned by the compilations ($\frac{1}{2}$) for the first resonance, for which only isotropical angular distributions can be observed.

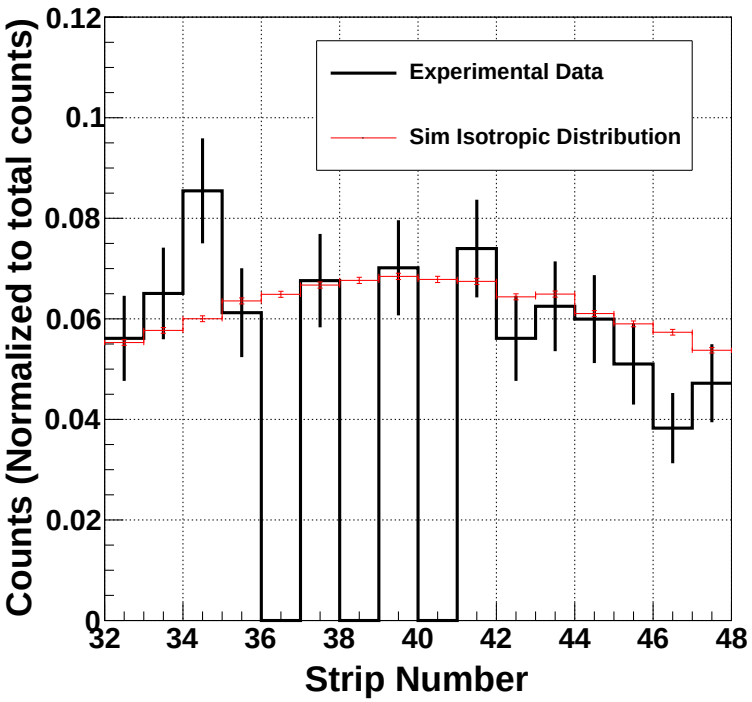

Figure 2.27: Experimental counts at the horizontal strips of the DSSSD (black), compared with the simulated distribution of counts for protons emitted isotropically (red).

2.6.2 R-Matrix Analysis - sammy - RF Deconvolution

The analysis the determination of J^π of each resonance from Ref [70] was assumed in the present analysis. The Γ_γ values were considered from the Atlas of Neutron Resonances by Mughabghab [83], and the rest of parameters were taken as initial guess for the R-Matrix fitting. The channel radii were also taken as 5.5 fm from Ref [83].

The Bayesian code SAMMY [99] in the Reich-Moore approximation of the R-matrix theory was used for the analysis. A fit of the data from DSSSD has been performed. The DSSSD data are shown with black points in Figure 2.28, together with MGAS data in greenish colors, where the fit of the experimental data is displayed, in red. Only statistical uncertainty has been included in the fitting procedure. A small constant background of 0.42 mb was also included, to compensate the small background left after coincidence analysis. The experimental data are affected by Doppler broadening and Resolution broadening, which is ultimately handled with the n_TOF-EAR2 Resolution Function. These effects were included in the SAMMY fit. Multiple scattering and self-shielding effects were negligible given the small thickness of the adenine samples.

The experimental data was consistently described in the range from 8 meV to 800 keV after the SAMMY fit. The resonance parameters and p strengths extracted from the fitting are shown in Table 2.2. The p strength is defined as $g\Gamma_n\Gamma_p/\Gamma$, where $\Gamma = \Gamma_n + \Gamma_p + \Gamma_\alpha + \Gamma_\gamma$ is the total width. Γ_α is only non-zero above the (n,α) threshold, and in this case only for the resonance at 644 keV. The statistical factor is defined as $g = (2J+1)/[(2I+1)(2i+1)]$, and J, I and i are the spins of the resonant state, the target (1^+) and the projectile ($\frac{1}{2}^+$), respectively.

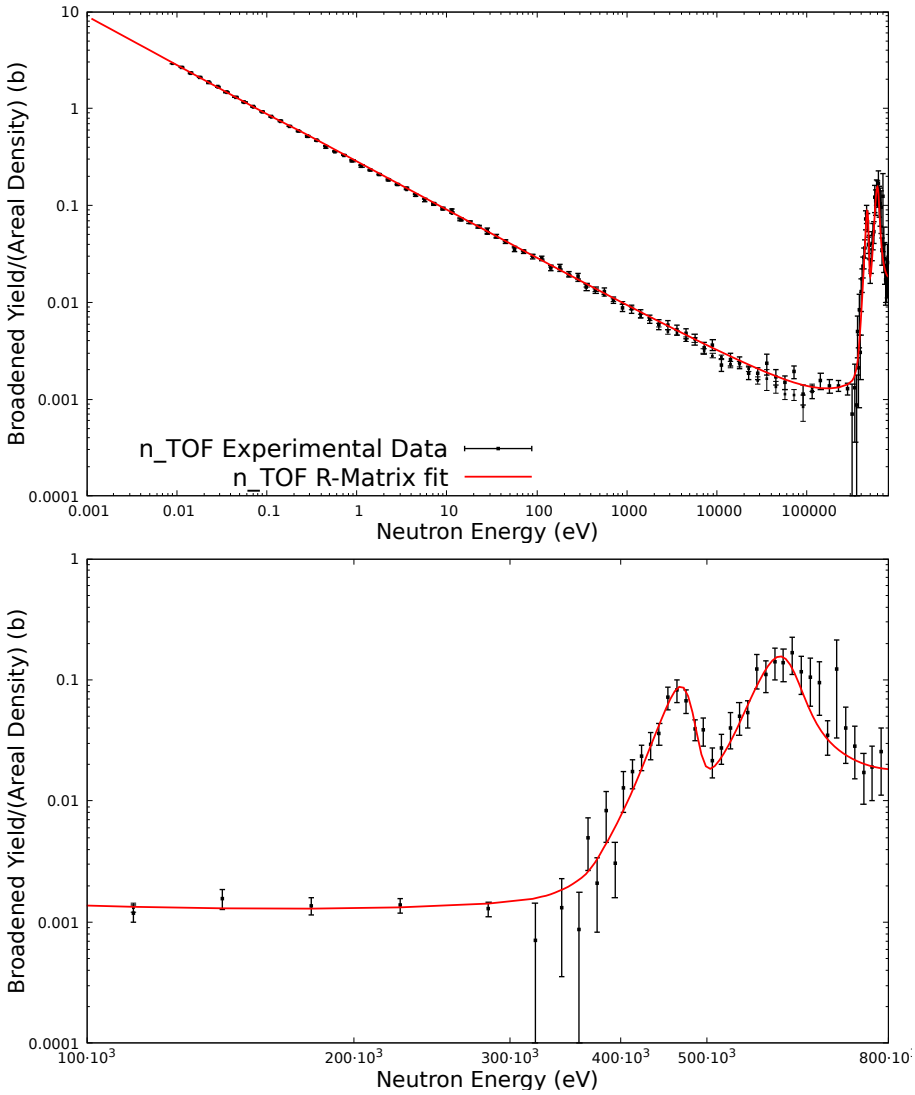

Figure 2.28: SAMMY fit (red) of the experimental data (black). The *upper panel* shows a depiction of the full range covered by this measurement, from 8 meV to 800 keV, and the *lower panel* shows a detail of the resonance region.

The fit of the experimental data (in red) includes the effect of the Resolution Function, which is specially relevant in the resonance region, as it can be clearly observed in the *lower panel* of Figure 2.28. The Resolution Function broadens the resonances but also shifts them towards lower energy in an evident manner. However, this effect can be taken into account to recover the cross-section data due to the good quality of the simulations used to obtain the Resolution Function data of the n_TOF-EAR2, described in Ref [88]. Another remarkable effect of the Resolution Function is the dampening of the experimental data, which appears as lower than the 1/v behavior near the thermal range, due to the presence of a relevant neutron thermalization (which also causes the thermal peak in the n_TOF-EAR2 spectrum), which in an effective manner increases the flight path length.

$E_n(keV)$	J^π	Γ_γ (eV)	$\Gamma_n(keV)$	Γ_α (keV)	Γ_p (keV)	$g\Gamma_n\Gamma_p/\Gamma$ (keV)
492.7	$\frac{1}{2}^-$	0.29	1.90 ± 0.15	–	6.2 ± 0.8	0.48 ± 0.04
644	$\frac{1}{2}^+$	4.2 ± 0.7	35 ± 5	< 0.3	9.2 ± 0.7	2.41 ± 0.22

Table 2.2: Resonance parameters and (n,p) resonance strength of the ^{14}N(n,p)^{14}C resonances obtained in the present work. J^π are taken from Ref [70]. Gamma and α widths as in the Atlas of Neutron Resonances by Mughabghab. Neutron and proton widths obtained from the SAMMY fit of the n_TOF data. Proton strengths derived from all other parameters.

2.7 Results: The ^{14}N(n,p) reaction cross-section

Figure 2.29 shows a comparison of the obtained cross-section from the SAMMY fit, compared to the ENDF/B-VIII.0 evaluation.

The reconstructed cross-section describes well the 1/v behavior below 10 keV. The resonance region is found close to the previous evaluations, lower than ENDF/B-VIII.0 but within uncertainties. However, the low energy tail of the first resonance at 492.7 keV is found to have a different, finer shape than previous evaluations. This contributes to a lower cross-section in the 10-300 keV range, which is compatible with previous experiments such as the resonance measurement by Johnson *et al.*, in an energy range that did not match well with the evaluations. In particular, the reconstructed cross-section also matches well the experimental data by Wallner *et al.* at 127 and 178 keV, and given the reliable data obtained in that measurement, this provides a good confirmation of the goodness of the results.

The fact that the cross-section exhibits this shape due to the presence of the resonance at 492.7 keV but also the tail of the wider one at 644 keV confirms, in particular, the strength of the first resonance, which was questioned with the extrapolation of the integral measurements by Wallner *et al.*, in which they assumed the shape of the resonance as the same in the evaluation. Now, given the change in the low energy tail of the 492.7 keV resonance, the experimental data by Wallner *et al.* fully agree with the results given in this work.

2.7.1 Thermal Cross-Section

The thermal cross-section for the ^{14}N(n,p)^{14}C reaction has been extracted from the results of the fit of the experimental data, from where the effects of the resolution broadening described by the n_TOF-EAR2 Resolution Function could be removed. The thermal cross-section is found to be 1.809±0.045 b, with a systematic uncertainty of 2.5 %. Figure 2.30 shows a comparison of this result with previous measurement of this quantity and also the reference evaluations.

Our result is in agreement with the most recent ENDF/B-VIII.0 and JEFF-3.3 evaluations, and previous measurements. The result is lower than the JENDL-5 evaluation, which used the data by Wagemans *et al.* for its thermal value. It is also lower but within 1.2 standard deviations with the measurements by Wagemans *et al.* (1999) and 1.3 standard deviations with the most recent findings by Kitahara *et al.* (2019). The data by Wagemans *et al.* has been renormalized due to a change in the ^{235}U(n$_{th}$,f) cross-section, from which they measured relative to. The thermal cross-section extrapolated from the data by Koehler *et*

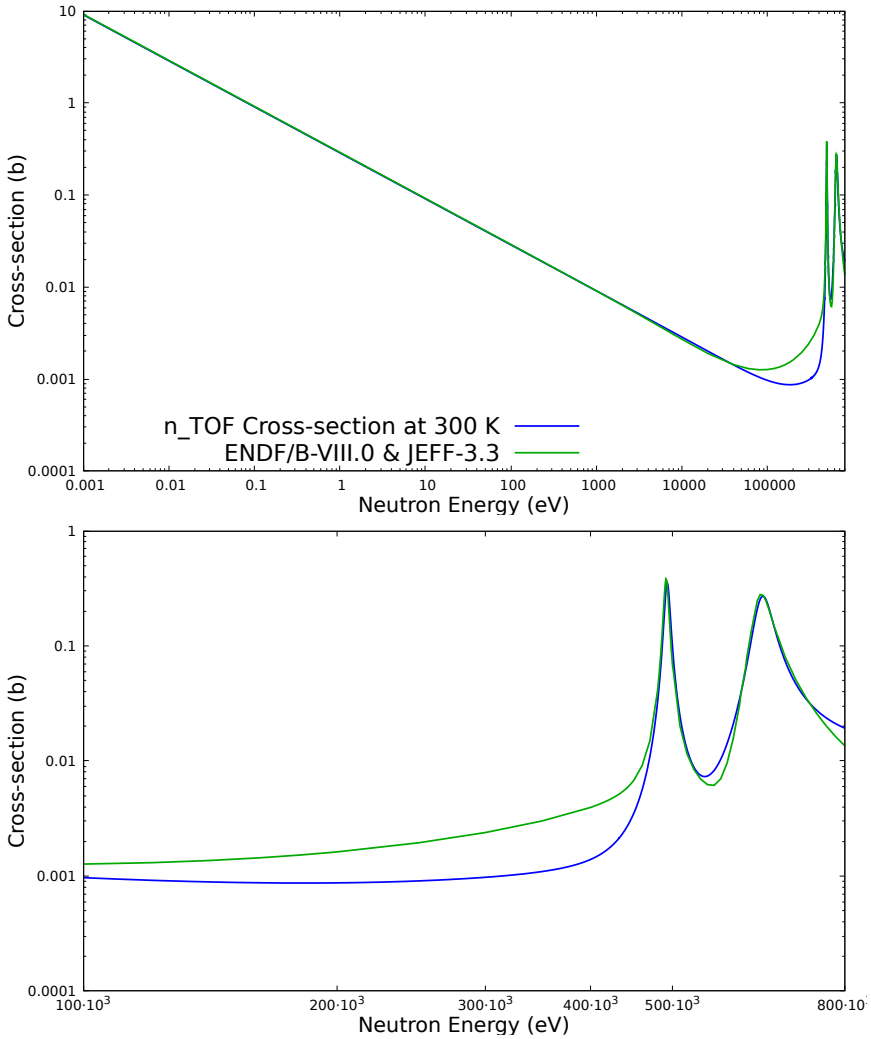

Figure 2.29: Reconstructed cross-section at 300 keV obtained from the SAMMY fit (blue) and the ENDF/B-VIII.0 (same as JEFF-3.3) evaluation is included (green). The *upper panel* shows a depiction of the full range covered by this measurement, from 8 meV to 800 keV, and the *lower panel* shows a detail of the resonance region.

al. (1989), which was normalized to the Nuclear Data Compilation by Ajzenberg-Selove, at 1.83±0.03 b, is in good agreement with the outcome of this work, as well as previous measurements as Gledenov *et al.*. This result is also compatible within uncertainties with the Compilation of the Atlas of Neutron Resonances by Mughabghab.

2.7.2 Maxwellian-Averaged Cross-Section

Maxwellian Averaged Cross-Sections (MACS) have been calculated for thermal energies in the range 5-100 keV, using the reconstructed cross-section obtained from the SAMMY fit. The results are listed in Table 2.3, together with the comparison of the previous estimates by Wallner *et al.* and the ones derived from the ENDF/B-VIII.0 evaluation.

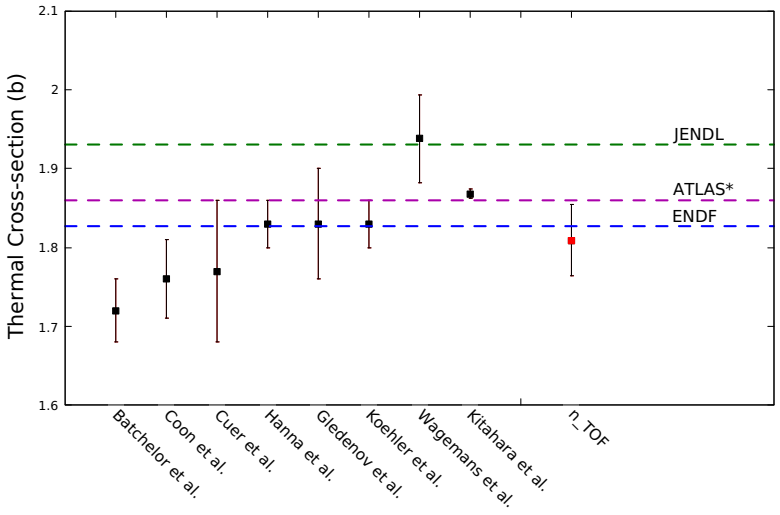

Figure 2.30: Experimental results of the measurement of the thermal Cross-section of the ^{14}N(n,p)^{14}C reaction. The values for the most recent evaluations of ENDF/B-VIII.0 and JEFF-3.3 (*blue*, labelled ENDF) and JENDL-5 (*green*, labelled JENDL) are indicated with the dashed lines. Also the tabulated value in the Atlas of Neutron Resonances of Mughabghab [83] is shown (purple, labelled ATLAS*). The results from previous measurements are marked with black squares, and this measurement, in the right-most position, is shown in red. Data from Wagemans *et al.* has been re-normalized due to changes in the standard they measured relative to. Koehler *et al.* normalized their data to the reference values of Ref [70].

kT (keV)	Wallner *et al.*	ENDF/B-VIII.0	This Work
5	3.78 ± 0.06	3.807	3.91 ± 0.10
8	3.12 ± 0.05	3.007	3.09 ± 0.08
10	2.89 ± 0.05	2.702	2.76 ± 0.07
15	2.47 ± 0.04	2.256	2.26 ± 0.06
20	2.21 ± 0.04	2.018	1.97 ± 0.05
23	2.09 ± 0.04	1.926	1.84 ± 0.04
25	2.03 ± 0.04	1.879	1.77 ± 0.04
30	1.93 ± 0.04	1.796	1.63 ± 0.04
40	1.85 ± 0.05	1.746	1.47 ± 0.03
50	1.83 ± 0.06	1.861	1.46 ± 0.03
60	1.84 ± 0.07	2.225	1.69 ± 0.04
80	1.84 ± 0.08	3.961	3.14 ± 0.10
100	1.83 ± 0.08	6.917	5.83 ± 0.20

Table 2.3: Maxwellian Averaged Cross-Sections derived from the reconstructed cross-section, compared with the previous calculation by Wallner *et al.* and from the ENDF/B-VIII.0 evaluation.

Chapter 3

Evaluation of the impact of the measurement in dose calculations for BNCT

The objective of measuring the ^{14}N(n,p) reaction cross-section towards BNCT was to improve the accuracy of the data and solve the discrepancies in the low-energy cross-section that could lead to significant under- or over-dosification in the patients under neutron irradiation. This is due to the fact that the ^{14}N(n,p) reaction produces the largest contribution to the neutron dose in normal human tissues due to low energy neutrons, and generates around 30-35 % of the total dose in normal tissues under a neutron field, in absence of boron administration. For a typical boron uptake (10-25 ppm in blood and normal tissues), the nitrogen dose contribution can count up to 16-20 % of the total dose in the normal tissues. Once the measurement has been performed and the data has been analyzed, the implications of the results will be discussed and compared to the reference value for the ^{14}N(n,p) reaction cross-section that has been used for BNCT treatment plannings in Europe and US, based in the ENDF/B-VIII.0 evaluation. To do so, the new reconstructed cross-section has been formatted so that it could be interpreted by the MCNP code and then a series of simulations were run to analyze the effects of the new values of the cross-section in both the neutron transport and neutron dose.

3.1 New ^{14}N(n,p)^{14}C cross-section Data in MCNP

In order to include the new reconstructed data for the $^{14}N(n,p)$ cross-section in MCNP simulations, one has to consider two effects of the change in the cross-section:

- The first one is the effect in neutron transport. This effect can be handled once the new cross-section is included in the MCNP data libraries, which are written in the ACE format. The NJOY program [100] is capable of creating ACE files given the cross-section in ENDF-6 format. To do so, SAMMY is able to generate an output file in ENDF-6 format.

- The second effect is the change in the dose functions, depending on tissue composition. This can be overcome with the use of kerma factors which can be calculated for any material given its composition and included in the MCNP computations.

3.1.1 Preparation of ACE files for MCNP Simulations

The standard output from the SAMMY code does not generate files in the ENDF-6 format. Such file can be produced by means of the ENDF connection of the SAMMY code. This feature allows to produce the ENDF sections corresponding to the resonance parameters and also the point-wise cross-section. The point-wise cross-section data is generated through `File 3` from SAMMY. This ENDF-6-formatted data can be inserted in the corresponding section of the full ENDF file for the material of interest. In our case, the material is ^{14}N, which is labeled MAT=725 in ENDF-6. For this material file, the section of reaction MT=600, corresponding to the (n,p) reaction leading to the ground state of ^{14}C, has to be replaced with the new data from `File 3` from SAMMY. `File 3` generated by SAMMY is also included in Appendix A, together with experimental and the point-wise reconstructed cross-section.

The corrected ENDF-6 file can then be used as input file for NJOY in order to create the ACE file. The `moder`, `reconr`, `broadr`, `heatr` and `gaspr` modules of NJOY are used in order to interpret the ENDF-6 file and produce the relevant data that is subsequently brought together into the ACE file via the `acer` module. The `viewr` module is also used to generate a set of plots with the total and partial cross-section and other features as heating, damage or angular distribution of secondary particle emission. These plots are collected in a pdf file where the cross-section data can be checked. Figure 3.1 shows the first plot from the NJOY output, including the total, elastic, gamma production and absorption cross-sections. The absorption cross-section already includes the changes found in the previous Chapter.

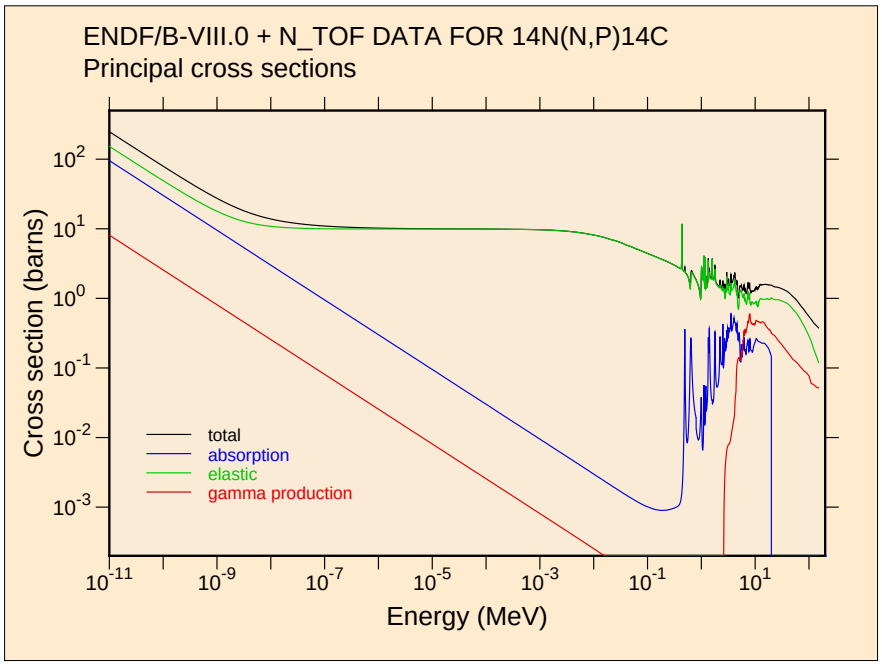

Figure 3.1: Plot from the output file of the `viewr` module of NJOY. The plot corresponds to the first page of the file, showing the total, absorption, elastic and gamma production cross-sections. The absorption cross-section is altered to include the changes in the ^{14}N(n,p) cross-section below 800 keV.

3.1.2 Recalculated Kerma Factors

Neutron kerma factors can be computed as a sum of partial kerma factors, each corresponding to a neutron-induced nuclear reaction that can be produced in the material of interest. The two main sources of charged secondary particles from neutron interaction are elastic scattering, as the recoiling nucleus carries part of the initial neutron energy before the collision, and nuclear reactions such as (n,p) or (n,α), where both the energy of the recoiling nucleus and the outgoing particle (typically p or α) have to be accounted for the calculation. The total kerma factor for a neutron of energy E_n is then:

$$k_{f,T} = \sum \chi_i k_{f,i} \tag{3.1}$$

where χ_i is the isotopic fraction of the i-th isotope in the material. The partial kerma factor due to an elastic scattering is:

$$k_{f,el} = N_A \sigma_{el} \frac{2E_n}{(M_M+1)^2} \cdot \left(\left(1 + \frac{E_{th}}{2M_M E_n}\right) \operatorname{erf}\left(\sqrt{M_M \frac{E_n}{E_{th}}}\right) + \frac{e^{-M_M \frac{E_n}{E_{th}}}}{\sqrt{M \frac{E_n}{E_{th}}}} \right) \tag{3.2}$$

where N_A is the Avogadro Number and σ_{el} is the elastic scattering cross-section at neutron energy E_n. The second factor in the equation accounts for the recoiling nucleus' initial energy, in thermal equilibrium with the medium.

Similarly, the partial kerma factor due to a nuclear reaction is:

$$k_{f,r} = N_A \sigma_R \frac{Q + E_n}{M_M} \tag{3.3}$$

where Q is the reaction q-value and σ_R the reaction cross-section at neutron energy E_n.

In our case, all kerma factors corresponding to tissues in human body that contain nitrogen have to be corrected with the new cross-section data. As almost all human tissues contain nitrogen, here the computation of corrected kerma factors is shown for a selection of relevant tissues. These tissues are muscle tissue, adipose tissue, bone tissue, brain tissue, skin and the lens of the eye. These last two tissues are specially relevant here due to their comparatively higher nitrogen content. In addition, the neutron kerma factor has been computed for the ICRU 4-component reference tissue (ICRU-33). Material compositions were obtained from the NIST Standard Reference Database 124 [52].

Figure 3.2 shows the kerma factors using the previous ENDF/B-VIII.0 evaluation and the results of the measurement from this thesis. The changes are small given that the difference found in the cross-section is of 1.0 % at the thermal energy, where the nitrogen dose is the most dominant contribution. Also small differences are found near the two resonances around 493 and 644 keV, but these changes are much less relevant. Given that the kerma factors range from 10^{-15} and 10^{-10} Gy cm^2 depending on the neutron energy, the effect is not clearly noticeable when the full range is shown. The bottom panel in Figure 3.2 shows the detail at thermal energy. The Kerma Factor for ICRU-33 is given in a Table in the Appendix A.

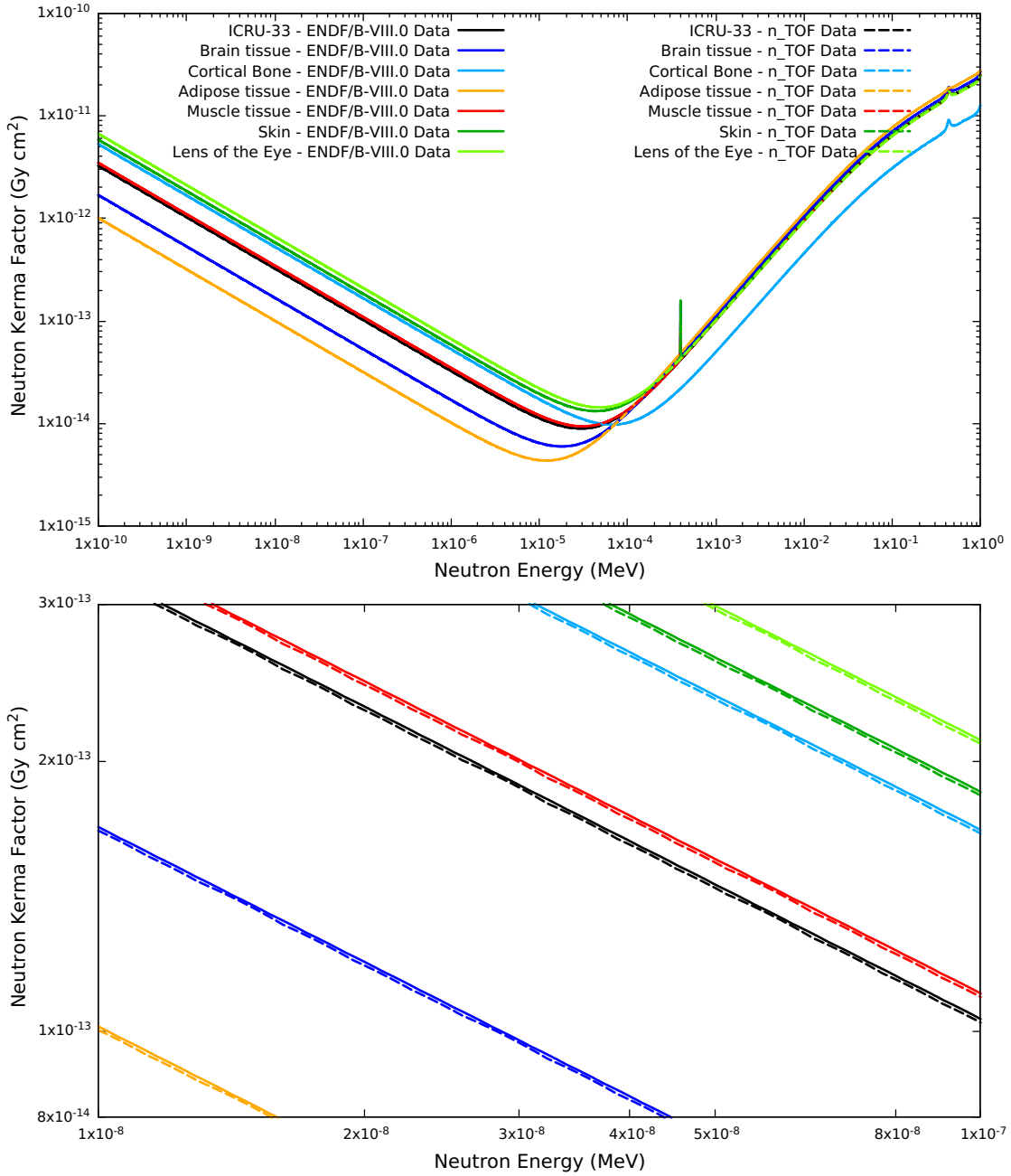

Figure 3.2: Neutron Kerma factors for some relevant tissues, including brain tissue (dark blue), cortical bone (light blue), adipose tissue (orange), muscle tissue (red), skin (dark green) and the lens of the eye (light green). The kerma factors computed using the last ENDF evaluation are shown in solid lines, while the new kerma factors computed with the new data from the ^{14}N(n,p) reaction measurement are shown in dashed lines. The differences are small and not noticeable in the *top panel*. The *bottom panel* shows the detail in the 10 meV to 100 meV range (including the thermal energy), where the small reduction of a 1 % in the kerma factors can be observed.

3.2 Evaluation of the dose in a standard phantom with MCNP

In order to study the dosimetric effect of this measurement, a couple of simulations in standard phantoms are made, in order to test the effect in the neutron flux (accountable from the change in the cross-section that affects neutron transport) and the neutron dose (that includes both the change in the flux and the differences in the kerma factors. The study will be shown for a cylindrical phantom filled with ICRU-33 tissue.

3.2.1 Evaluation in a ICRU-33 cylindrical phantom

A set of simulations in order to check the effect in neutron transport and in neutron dose were made. The simulations were made using MCNP6.2 with the standard built-in databases (ENDF/B-VII.1) and with the new data as described in the previous section. Monodirectional neutron beams of 5 cm radius were sent towards a cylindrical phantom of 20 cm depth and 10 cm radius, filled with ICRU-33 standard tissue. Three monoenergetic neutron beams were used to analyze the changes in flux and dose, namely thermal (25.3 meV), 10 keV and 1 MeV neutrons. The flux and the dose are computed by means of tally type 4 (weighted with the kerma factors in the case of dose), in dedicated cells of 1 cm radius along the beam axis.

Effect in the neutron flux

The neutron flux inside the cylindrical phantom is shown in Figure 3.3 for the three beams of different initial neutron energy. The results from the simulations appear to be the same, independently of the nuclear data used for the simulations. The effect of the ^{14}N as a neutron poison is not as determinant in the flux as to create an increase in the neutron flux due to a lower absorption cross-section. The *bottom panel* of Figure 3.3 shows the relative difference of the flux, between the ENDF/B-VII.1-based and the n_TOF Data-based simulations. The differences are negligible, even when observing in detail. In all cases, the effect in the neutron flux is lower than 0.1 %, and all deviations from a zero-difference are contained within 1σ of standard deviation. Thus the change in the cross-section from the new measurement does not generate a relevant effect in the neutron transport of human-like tissues.

Effect in the total dose

In this case, the neutron kerma factors determine the influence in the dose, given than the neutron flux stays unchanged, as previously discussed. As is was indicated before, the reduction in the cross-section produces a lower kerma factor by around -1 % in the low energy range, where the ^{14}N(n,p) reaction is the dominant component of the kerma. At higher energies, the effects are reduced and only become more noticeable as the beam moderates inside the materials. At sufficiently high energy, most of the dose is delivered by elastic scattering off hydrogen, which strongly preponderates over the nitrogen dose. This can be clearly observed in Figure 3.4, where the neutron dose is shown for three beams of thermal, 10 keV and 1 MeV neutrons. The differences in all cases are small and within 1 % given that the correction to the kerma factors was of this size. The *bottom panel* shows the relative difference between the dose computed via the kerma factors using the ENDF/B-VIII.0 cross-section data and the new kerma factors using the last measurement from n_TOF. The difference in dose for the thermal beam corresponds to the described above, with a reduction close to 1 % in the neutron dose. In the case of 10 keV neutrons, the first 2-3 cm inside the phantom show a lower reduction of the dose, given that the

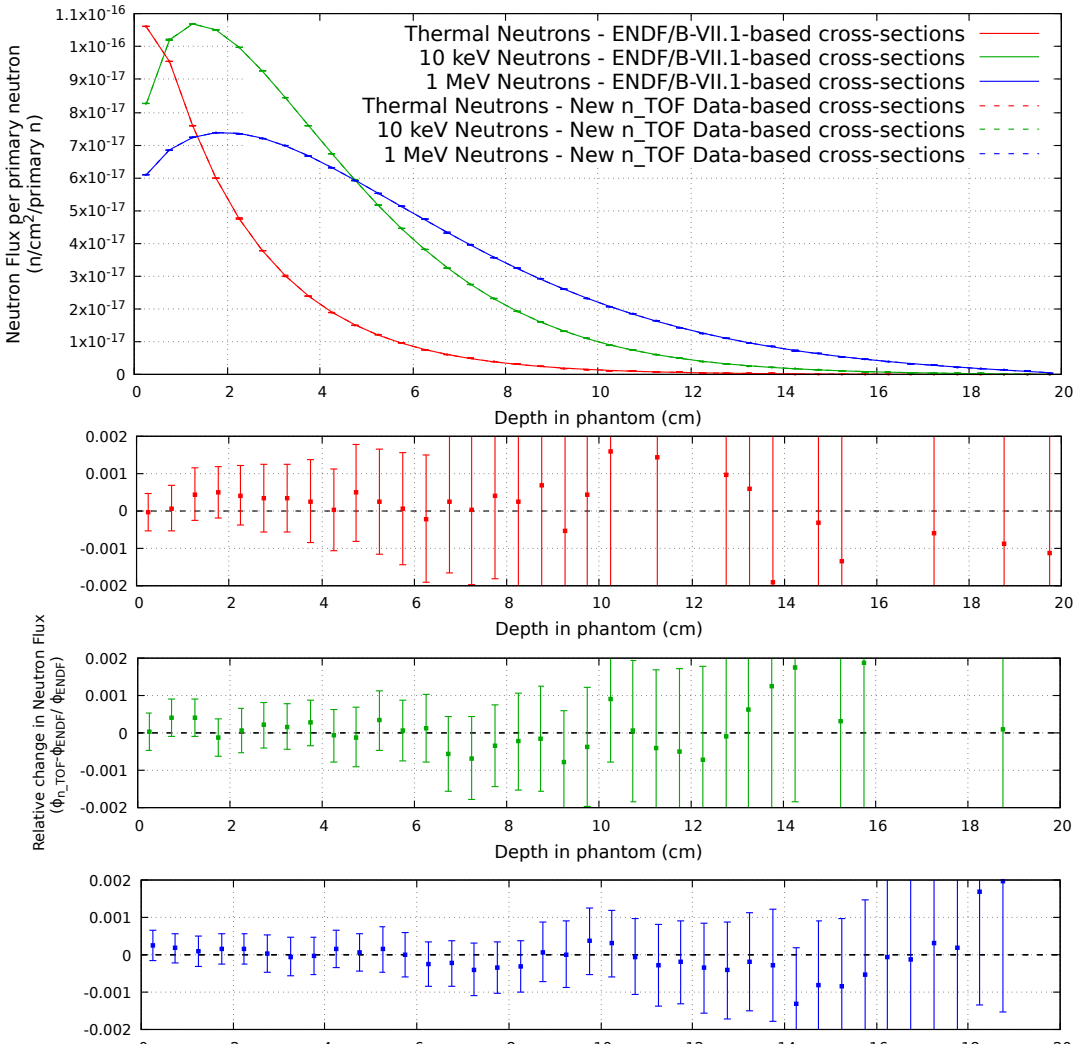

Figure 3.3: Neutron flux in the beam axis of the ICRU-33 phantom for three beams of thermal (red), 10 keV (green) and 1 MeV neutrons (blue). Solid lines correspond to the simulation of neutron transport using ENDF/B-VII.1-based cross-sections, and dashed lines correspond to the same except the ^{14}N(n,p) reaction, where the new n_TOF Data is used. The difference cannot be observed in the main (*top*) plot. The *bottom panel* shows the relative change in the neutron flux, which also shows not to deviate from zero.

neutrons have to moderate first, and in doing so they release their kinetic energy, thus reducing the effect of the change in the ^{14}N(n,p) cross-section. After 3-4 cm, the neutron moderation generates a neutron population that is thermalized and hence the reduction in the dose matches with the thermal beam. In the case of the 1 MeV beam, the kinetic energy released during moderation dominates overwhelmingly over the other components of the dose, and hence the reduction in dose caused when thermal neutrons interact with nitrogen is negligible.

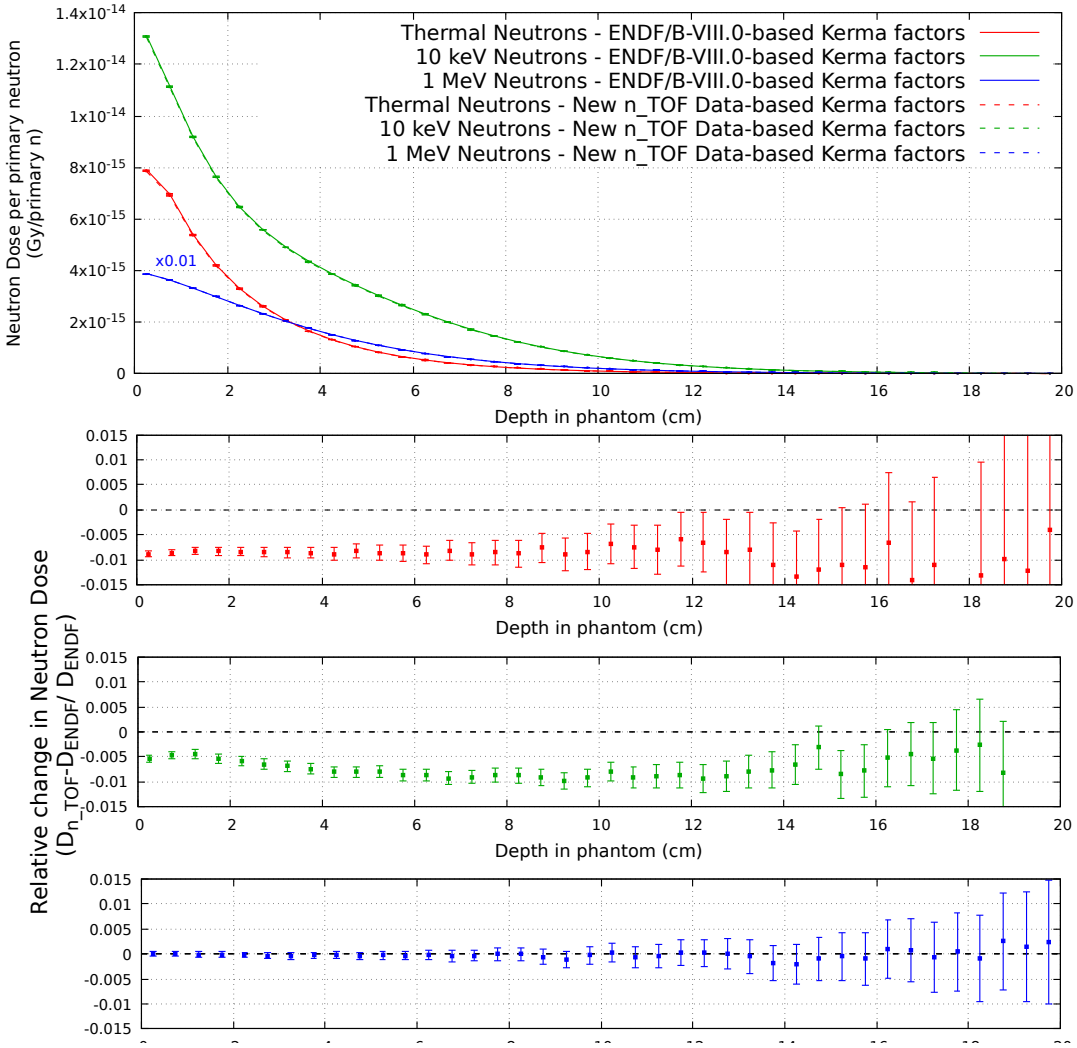

Figure 3.4: Neutron Dose in the beam axis of the ICRU-33 phantom for three beams of thermal (red), 10 keV (green) and 1 MeV neutrons (blue). Solid lines correspond to the simulation using ENDF/B-VII.1-based kerma factors, and dashed lines correspond to the same except the ^{14}N(n,p) reaction, where the new n_TOF Data is used. The neutron dose corresponding to the 1 MeV beam has been reduced by a factor of 100 in order to fit in the range, for easier comparison. The difference cannot be clearly observed in the main (*top*) plot. The *bottom panel* shows the relative change in the neutron dose comparing the cross-section data, which shows a clear reduction around 1 % for thermal neutrons, being lower for 10 keV and negligible for the 1 MeV beam.

3.3 Implications of the new measurement

As it has been described through the analysis of the simulations, the effect on the change in the cross-section data is not large. In radiotherapy, the ICRU recommendations state that all steps in the determination or computation of the dose should have a maximum of 5 % of deviation from the real values, in order to minimize the dose uncertainties. The effect in the neutron transport, which could also affect other dose components as the neutron flux changed is negligible at least to the needs for radiotherapy. The effect in dose, however, is small but noticeable, specially in low energy neutron fields. In BNCT, 30-35 % of the total dose in absence of boron is due to the ^{14}N(n,p) reaction. Therefore, a variation of -1 % in the dose estimates leads to a change around 0.30-0.35 % below the estimates

using previous data. In the presence of typical boron uptakes for BNCT treatments, the nitrogen-related dose contribution reduces to 16-20 %, and thus, the change due to the new data falls below 0.16-0.20 % maximum. The results from this new data confirm that the previous data was reliable and the dose estimates were not affected by a large error due to the uncertainty in the cross-section of the ^{14}N(n,p) reaction.

In turn, there is another aspect of relevance that should not be disregarded. In BNCT, there are large uncertainties present in the dose estimates. This makes the clinicians and medical physicists that are responsible of the patient treatment to enlarge the safe margins. This reduces the chances for a positive outcome in the treatment, given the possible infradosing of the tumor. The outcome of the measurement allows to reduce the uncertainty in the neutron dose, given that the uncertainty in nitrogen-related dose is attained to 2.5 % (the uncertainty in the thermal cross-section), which is sufficiently within the ICRU recommendations.

Chapter 4

Design of a Beam Shaping Assembly for deep-seated tumor treatment with BNCT

In BNCT, the design of neutron beams adequate for treatments is one of the main technical aspects of the research. High-intensity neutron sources as the nuclear reactors, outside hospitals, are not a best-suited solution for BNCT, although they have been used in all clinical trials until recently, since they were the only technology available. In the recent years, the research and development of new accelerator-based neutron sources has prompted a thorough investigation in order to define and conform neutron beams for BNCT using accelerators. To such aim, a tight list of nuclear reactions has been explored, from which a large neutron yield is expected, and also their energy and other features centered near the optimum for BNCT treatments. Some of these reactions include (p,n) and (d,n) reactions onto lithium or beryllium targets. These reactions can produce a neutron yield large enough, but their spectrum is not suitable for BNCT. Therefore, there is a need for moderation and conformation of the neutron field from the target to a beam aperture, where the beam is delivered to the patient. These steps are performed by a device that is called Beam Shaping Assembly (BSA) in the BNCT research community.

In this chapter, we will explore a few aspects that determine the optimal characteristics of the neutron beams (including the upper limit of the epithermal neutrons suitable for BNCT, among others) taking into account also the recommendations from the IAEA. Once these aspects of the beams are caught, the focus will turn to the design of a BSA. These will include the choice of the target and charged particle current and energy and the set of materials used for moderation and conformation of the beam, and also the correct geometrical assemblage of these materials to match the IAEA recommendations.

4.1 Studies seeking the optimal energy range for neutrons in BNCT

Regarding the guidelines for the design of adequate neutron beams for BNCT treatments, a pair of studies were made and considered together with the general specifications in the IAEA technical document [11]. These studies focused in the extent of the epithermal range and the usefulness of neutrons near the upper epithermal limit.

The first study [101] concentrated in the search and benchmarking of Figures of Merit using a cylindrical phantom filled with ICRU33 tissue (4 Component Standard Tissue). The upper limit for the energy of neutrons was scanned in the range 1-40 keV. The FOMs showed that neutrons slightly above the 10 keV limit were usable. This was complemented with the presentation of examples of neutron spectra mostly shifted above the current limit of 10 keV that kept being applicable for treatments.

The second study [102] extended the search to multiple body regions (namely brain, neck and abdomen). These illustrate some of the main applications of BNCT for deep-seated tumors. The study also centered not only in the upper limit but also in the optimal energy for a neutron beam to be applied to deep tumors. This study comprised a more general view of the application in BNCT, considering, together with the different body regions, the variation of boron uptake and the ratio of this uptake between tumor and normal tissue. Also other features of the neutron beam were assessed in the investigation of the upper energy limit, as beam divergence and beam aperture. This general research confirmed that neutrons above 10 keV are still suitable for BNCT, specially below the limits of 40 and even more below 20 keV. In addition, the study showed that the maximum Advantage Depth (AD) is typically found around 10 keV, while the maximum Therapeutic ratio (maximum dose in tumor relative to the maximum dose in normal tissue) is found around 2-3 keV.

4.1.1 Some considerations on the beam quality

Here we will show some of the most relevant findings on the beam characteristics that define a neutron beam suitable for BNCT treatments, as discussed in the above mentioned papers.

When defining a most adequate energy for a neutron beam, we have to consider the energy dependence of the dose deposition, taking other parameters as the boron concentration or the body region. Other characteristics as the beam divergence also play a role in the beam quality.

To this aim, a series of MCNP6 simulations to determine the total dose in normal tissue and tumor tissue was computed along the beam axis, for three different body regions, namely neck, brain and abdomen. The MIRD-ORNL male model was used for both neck and abdomen, and the Snyder model was used for skull and brain [103]. Monoenergetic neutron beams with a fixed diameter were used at each simulation. The results of the simulations were then analyzed and the tumor dose profiles were normalized to the maximum dose in normal tissue. Then, these results can be presented in plots as in Figure 4.1.

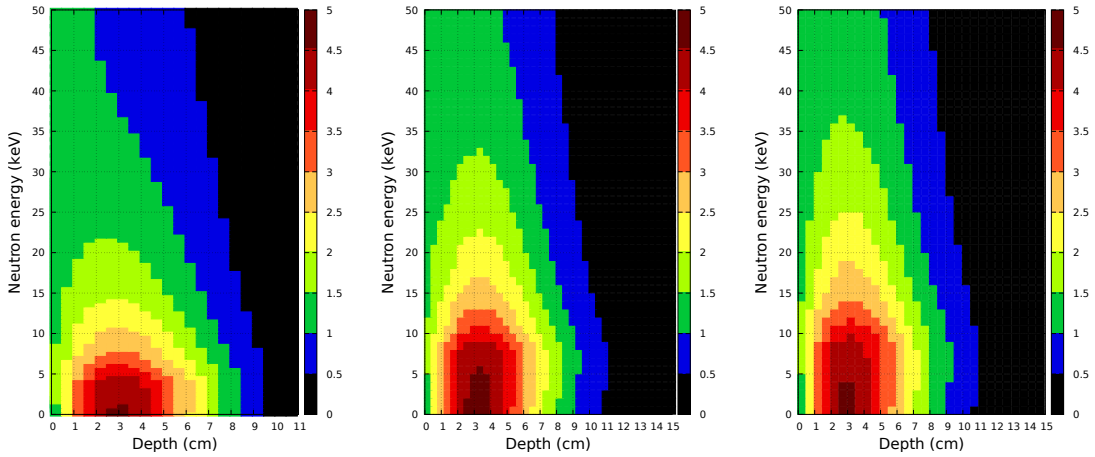

Figure 4.1: Dose profile plots for neutron energies in the range 1-50 keV for neck (*left*), brain (*middle*) and abdomen(*right*). Color represents tumor dose relative to the maximum dose at normal tissue, for each neutron energy and tissue.

There, for the three body regions analyzed, the tumor dose along the beam axis (horizontal axis) is shown as a function of the neutron energy (vertical axis). These plots can be prepared for the different beam sizes and boron concentrations to be discussed, though here we only show those of 10 cm diameter beam size, with 10 ppm of boron in normal tissue and 3.5 tumor-to-normal tissue concentration ratio. In these plots, color represents the dose in tumor, relative to maximum dose in normal tissue. Thus, a ratio of 1 (edge between blue and green regions) corresponds to the position of the Advantage Depth (AD) at each neutron energy, and similarly, yellow-to-green and orange-to-red delimits where dose in tumor is twice (DDD) and trice (TDD) as in normal tissue. The relevant parameters from these and other configurations varying the diameter beam size and boron concentrations can be found in Table 4.1.

Upon these results, some analysis about neutron energy can be extracted. The most adequate neutron energy, defined as that where AD is maximum, reaches its maximum in the 2-9 keV, depending on the body region and boron concentration. Moreover, AD reduces progressively, with no sharp end as neutron energy increases. On the contrary, TDD (twice as normal tissue) ceases to exist at different energies from 15 to 40 keV, where the lowest corresponds to neck and highest to abdomen, where a larger surrounding volume allows some extra thermalization.

Along with this, the maximum dose at tumor relative to maximum dose at normal tissue or Therapeutic Ratio (TR) can be computed for each tissue. This figure evolves as neutron energy rises. First, below some certain threshold this figure is mostly flat, peaking around 2 keV, and after this threshold, TR shows a progressive decline until it approaches TR = 1 near 40 keV, where the maximum dose in tumor is no longer higher than that of normal tissue. This depends on the body region, being the threshold at a higher energy for abdomen and at lower energy for neck. This is also specially influenced by the beam size or aperture diameter. A larger aperture allows to increase the range of applicability of neutrons. A change in aperture from 10 to 25 cm in diameter pushes the threshold 5 to 10 keV upwards, at the cost of slightly reducing the maximum value of TR. In Figure 4.2 can be seen the variation of TR with neutron energy in neck, brain and abdomen.

Boron Uptake (ppm)	T/N Ratio	Aperture Diameter (cm)	AD_{Max} (cm)	$E(AD_{Max})$ Range (keV)	DDD_{Max} (cm)	E_{Max}(DDD) (keV)	TDD_{Max} (cm)	E_{Max}(TDD) (keV)	MTR_{Max}
			Neck						
10	2.5	10	7.75	1-6	5.75	10	4.25	5	3.45
		25	7.75	1-10	5.75	15	3.75	6	3.2
	3	10	8.25	2-5	6.25	13	4.75	7	3.95
		25	8.25	1-9	6.25	19	4.75	9	3.7
	3.5	10	8.25	1-6	6.75	15	5.25	8	4.55
		25	8.75	4-7	6.75	23	5.25	12	4.2
	4	10	8.75	2-5	7.25	17	5.75	10	5.15
		25	8.75	1-9	7.25	27	5.75	14	4.75
25	2.5	10	8.25	1-12	6.75	26	5.75	15	4.8
		25	8.75	2-14	7.25	43	5.75	22	4.6
	3	10	8.75	1-11	7.25	33	6.25	19	5.75
		25	9.25	9-10	7.75	>50	6.25	29	5.45
	3.5	10	8.75	1-13	7.75	39	6.75	23	6.65
		25	9.25	2-15	7.75	>50	6.75	36	6.3
	4	10	9.25	2-10	7.75	47	6.75	27	7.55
		25	9.25	2-18	8.25	>50	7.25	43	7.15
			Brain						
10	2.5	10	8.6	2-10	7	16	4.6	9	3.5
		25	10.2	8-14	7.4	24	5	14	3.3
	3	10	9	4-9	7	19	5.4	11	4
		25	10.6	6-14	8.2	29	6.2	17	3.9
	3.5	10	9.4	6-8	7.4	23	5.8	13	4.65
		25	11	7-13	8.6	34	7	20	4.45
	4	10	9.4	2-10	7.8	26	6.2	16	5.25
		25	11.4	11-13	9	40	7.4	23	4.95
25	2.5	10	9.4	4-16	7.4	41	6.2	24	4.9
		25	11.4	20-21	9	>50	7.4	37	4.75
	3	10	9.8	4-16	8.2	>50	7	30	5.8
		25	11.8	16-21	9.4	>50	8	47	5.65
	3.5	10	10.2	6-16	8.6	>50	7.4	35	6.75
		25	12.2	19-20	9.8	>50	8.6	>50	6.45
	4	10	10.6	7-15	9	>50	7.8	42	7.65
		25	12.2	6-26	10.2	>50	9	>50	7.4
			Abdomen						
10	2.5	10	8.25	1-11	6.25	18	4.25	10	3.45
		25	9.75	11-15	6.75	30	4.25	9	3.15
	3	10	8.75	2-10	6.75	21	5.25	12	4
		25	10.25	12-15	7.25	36	5.25	19	3.6
	3.5	10	9.25	5-9	7.25	25	5.75	14	4.55
		25	10.25	5-19	7.75	43	5.75	24	4.1
	4	10	9.25	2-11	7.25	29	6.25	17	5.15
		25	10.75	9-18	8.25	>50	6.75	29	4.6
25	2.5	10	9.25	4-18	7.25	46	5.75	26	4.8
		25	10.75	11-28	8.25	>50	6.75	45	4.55
	3	10	9.75	5-18	7.75	>50	6.75	33	5.75
		25	11.25	11-30	8.75	>50	7.25	>50	5.3
	3.5	10	10.25	8-16	8.25	>50	6.75	39	6.65
		25	11.75	17-30	9.25	>50	7.75	>50	6.2
	4	10	10.25	3-19	9.75	>50	7.25	47	7.55
		25	11.75	5-36	9.75	>50	8.25	>50	6.95

Table 4.1: Relevant FOMs extracted from the simulations are given. Data for neck, brain and abdomen is given, considering boron concentrations in normal tissue of 10 and 25 ppm, and T/N ratios from 2.5 to 4.0. Two beam apertures (10 and 25 cm diameter) for the monodirectional beam are included. These results are shown in Ref [102]. MTR stands for Maximum TR.

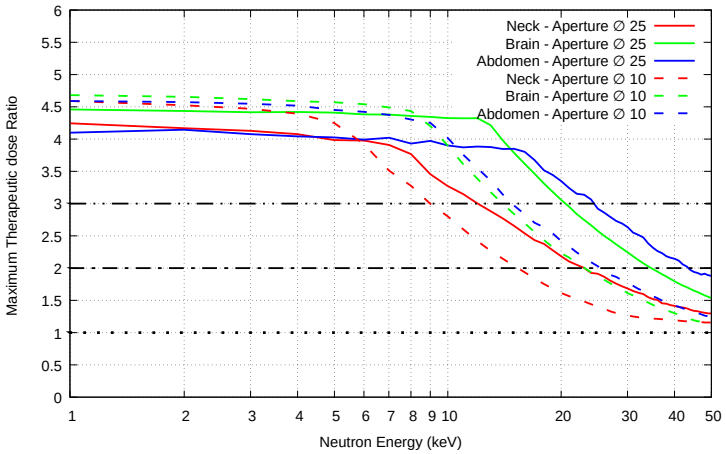

Figure 4.2: Maximum Therapeutic dose Ratio (TR) as a function of neutron energy in monoenergetic beams of 10 and 25 cm in diameter, impinging into the neck, brain and abdomen.

Aside from this, some simulations were made to corroborate the importance of a well-defined and low in divergence beam. Of special interest is a result that links its importance to the overall boron uptake. This shows that there is a much larger effect of a poorer beam definition for low boron uptake patients than for higher uptakes, in that for a patient with normal to high boron uptake (25 ppm), the use of a divergent beam ($J/\phi = 0.7$) does not affect TR, and AD slightly decreases less than 1 cm, while for a low uptake (10 ppm), TR is reduced by more than a 40 % and AD shrinks by 2 cm. This is shown in Figure 4.3.

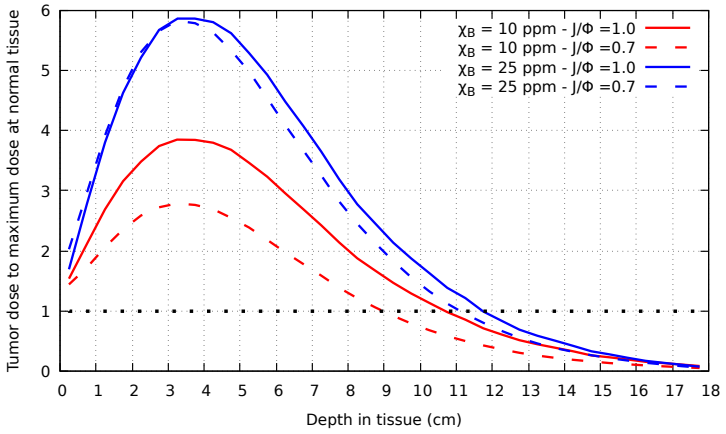

Figure 4.3: Dose profile at tumor, relative to maximum in normal tissue, for a low loaded tissue (10 ppm ^{10}B, *red*) and high loaded tissue (25 ppm ^{10}B, *blue*), in comparison for two different beams with no divergence ($J/\phi = 1.0$, *solid line*) and with the maximum accepted divergence for BNCT ($J/\phi = 0.7$, *dashed line*).

Finally, and in order to emphasize the importance of limiting the use of high energy neutrons, the dose calculation for an incident monoenergetic neutron beam of 15 keV into brain is shown in Figure 4.4. This highlights that neutrons above 10 keV are still useful for BNCT treatments, and in accordance they are not a real issue

when part of a full spectrum, but higher energy neutrons degrade the beam quality to a larger extent and thus shall be avoided.

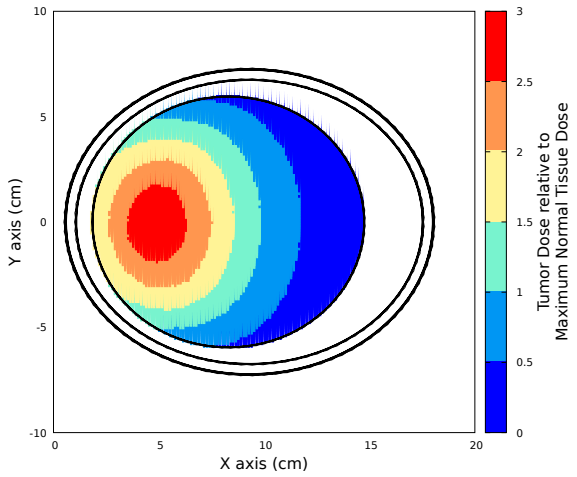

Figure 4.4: Tumor dose distribution relative to the maximum dose in normal tissue inside the brain on the Snyder Model, for a monoenergetic neutron beam of 15 keV.

Considering all this, some conclusions regarding the neutron beam design can be derived.

- The 10 keV upper limit for epithermal neutrons used in the IAEA technical document is not a sharp and physically defined threshold. It is better defined as a reference. This is specially true considering that the most adequate neutron energies for BNCT treatments move in the range 2-9 keV, as previously shown. Neutrons above and not far from this limit are also beneficial and including neutrons up to 20 keV in the epithermal range does not degrade the beam quality.
- Neutrons far from the 10 keV epithermal limit, above 40-50 keV are not as adequate for BNCT treatments and hence they shall be suppressed from the beam to the greater extent possible.
- The neutron beam should be of large diameter in order to cover the full treatment area and also because this extends the suitability of higher energy neutrons. This should not be rigidly considered as a larger beam tends to produce more irradiation to body regions farther from the target volume. In addition, technical issues arise around this, since a larger beam size needs a higher neutron yield from the production reaction, hence a more powerful accelerator.
- A neutron beam of low divergence is specially key in case of low boron uptake patients.

4.2 General structure of the design

A BSA consists of a device designed to conform a neutron beam to be used for BNCT treatments. This device has to contain or be attached to a neutron source. The main components of the BSA are the neutron moderator, which serves to set a

neutron spectrum centered in the adequate energies; and a neutron shaper, to direct and focus the neutron beam to an aperture towards the target volume in the patient. Additional components complement this general design to improve its performance, including a set of filters to avoid neutrons of inadequate energies (fast or thermal) or other particles (e.g. gamma radiation). Also a neutron reflector has to be considered to avoid large neutron loses in the process of moderation. In addition, shielding is specially important in the front side of the moderator, in what neutrons or other radiation shall not escape from the BSA out of the aperture, to the extent possible. Moreover, in the case of an accelerator-based source, a refrigeration system has to be included to prevent the damage to the target.

4.3 Broad requisites and limitations

The use of a low energy accelerator limits the choice of source reactions to ^{7}Li(p,n)^{7}Be. On the determination of the neutron production from the ^{7}Li(p,n)^{7}Be reaction, which serves as an input for the Monte Carlo simulations, reliable nuclear data for this reaction is considered, following [104, 105]. In this part, the presence of an excited state of ^{7}Be at 431 keV above the threshold generates uncertainty in the neutron yield and angular distribution. Therefore, in order not to populate this first state, our choice for the maximum proton energy for this type of design will move below 2.37 MeV. In addition, other sources of uncertainty related to nuclear data as the reaction cross section of neutrons off the materials have to be taken into account. For instance, fluorine and magnesium are found among the main elements used for BSA designs. There is a discrepancy in inelastic scattering of fluorine between evaluations used as input for simulations and experimental data in the neutron energy range from 400 keV to 1 MeV. By working at low enough energies, this neutron energy range can be excluded and hence uncertainties minimized. Along with that, the first excited state of the Mg natural isotopes is found at 585 keV from the neutron separation energy, so the population of these states can be also avoided. Besides, the RBE of neutrons has an energy dependence and some authors have suggested that neutrons in the range from tens of keV to few MeV have a higher RBE than thermal neutrons [106], which is the standard RBE value used in the literature and assumed in calculations. This extra source of uncertainty may lead to a larger dose than expected due to high energy neutrons, mainly due to neutrons in this energy range but also neutrons of higher energy ending up into this range due to moderation. Therefore, avoiding high energy neutrons removes any possibility of such RBE-related uncertainty in the dose.

On the other hand, the high intensity of the existing accelerators, capable of reaching 30 mA, outweights the lower neutron yield of the ^{7}Li(p,n)^{7}Be reaction at near-threshold energies.

The beam aperture of the BSA will be fixed at 14 cm in diameter, as shown in the IAEA recommendations. Though it was seen from the previous discussion that a larger diameter improves the performance of higher energy neutrons, in this case the lower neutron yield from the ^{7}Li(p,n) reaction near threshold imposes a further limitation so that the flux at aperture be around 10^{9} n/cm^{2}s. Hence, neutrons at energies higher than 20 keV are not as suitable as they could be with other designs with higher apertures.

Moreover, the BSA design is expected to fulfill the IAEA recommendations in its original definition [11]. The spectrum of the designed neutron beam will be studied considering the extent of the epithermal energy range from 0.5 eV to 10 keV. In addition, an extended range to 20 keV will also be included to remark the adequacy of the beam considering neutrons in this range, as stated in 4.1.

4.3.1 Computing the IAEA recommendations from MCNP simulations

MCNP simulations were used to test the performance of the BSA designs in terms of the IAEA criteria. These criteria can be listed, together with the assessment followed to compute them via MCNP simulations [1]. The MCNP simulations consisted of transport of primary neutrons or photons directly generated due to the ^{7}Li(p,n)^{7}Be reaction at the target and all secondary particles generated thereafter.

- Epithermal neutron flux, ϕ_{epi}, measured in n/cm^{2}s. This figure is computed by means of the product of the total neutron yield per incident proton from the ^{7}Li(p,n)^{7}Be reaction, times the proton current provided by the accelerator, and times the neutron flux per initial neutron in the simulation at the aperture. This was computed using the standard F4 tally, restricted to the epithermal range, from 0.5 eV to 10 keV.

- Thermal to epithermal neutron flux ratio, ϕ_{th}/ϕ_{epi}. This is computed as the ratio of thermal flux and epithermal flux per initial neutron in the simulation at the aperture, in the same way as the previous one.

- Current to epithermal neutron flux ratio, J_n/ϕ_{epi}. This is calculated as the ratio of the total neutron current to the epithermal flux, where the neutron current is computed using the standard F1 tally divided by the aperture's surface area.

- Fast dose per epithermal neutron, $\dot{D}_f/\phi_{epi}$, measured in Gy· cm^2. In this case, the dose is computed by means of the corresponding kerma factor in standard tissue as a dose function weighting the F4 tally, further dividing by the epithermal flux F4 tally as in the previous cases to determine the figure.

- Gamma dose per epithermal neutron, $\dot{D}_\gamma/\phi_{epi}$, measured in Gy· cm^2. This is computed as in the fast dose figure, but replacing the kerma factor with that of photons. Moreover, two separate MCNP6 simulations are needed in order to compute this figure. On the one hand, the general primary neutron-transport simulation, used to compute the previous figures, in order to get the gamma dose due to indirect photon production via neutron induced reactions. On the other hand, the primary photon-transport simulation, comprising the protons generated due to direct interaction between the accelerated protons and the Li target. The two components of dose are then weighted and summed up.

[1] All the criteria were computed at the BSA aperture, comprising an specific cell covering the whole aperture with a small thickness to define the volume or just the surface, depending on the type of tally needed in each case.

4.4 The lithium source

The neutron source used for this design is the ^{7}Li(p,n) reaction. This reaction has a threshold energy of 1.88 MeV. At the threshold energy, neutrons of 27 keV are produced in the forward direction. However, neutron production is too low to create a feasible neutron beam for BNCT. In order to increase the neutron yield, a higher proton energy is needed. By increasing the proton energy, a wide range of neutron energies generated in all directions is produced. In order to compute the neutron yield angular and energetic distribution, the data from Liskien and Paulsen, [105] and the study by Lee and Zhou [104] has been followed.

The aim is to use the lowest energy possible for protons while at the same time keeping it sufficiently high in order to obtain a high enough neutron yield. This constraints the maximum neutron energy, which is produced in the forward direction, reducing the needs for moderation. The strong resonance in the production cross-section at 2.25 MeV is of key relevance. On the one side, by using protons of that energy or higher, a large amount of neutrons can be produced. On the other side, the energy of the neutrons produced through the resonance is around 500-600 keV. Furthermore, due to the strength of the resonance, the largest part of the neutron population would have a high energy. This would significantly increase the needs for moderation. By choosing a proton energy below the resonance, the neutron production is lower but also, since the moderation is not as prominent (highest energy neutrons have 350 keV if produced by protons at 2.1 MeV), neutron absorption and leakages from the moderating parts would not be as high, and the aim of this design is to find a compromise between these two counterparts. In addition, by operating an accelerator at a proton energy below the resonance, where the cross-section is mostly flat, the slight instabilities of the proton beam from the accelerator would not give rise to a large effect neither in neutron flux nor in the neutron spectrum [107].

4.5 Selection of adequate material candidates for a BSA design

The choice of the materials to be used in the design deserved a careful study. Before looking upon the actual isotopes and their characteristics, a few general considerations need to be addressed. These concern the mass and cross-section for the isotopes to be used as neutron moderator.

The isotopic mass is a relevant aspect, specially with respect to its influence in collision kinematics. Using the non-relativistic approximation, the energy loss after an elastic collision is:

$$E_n - E_n^0 = \frac{2m_n m_A}{(m_n + m_A)^2}(1 - \cos(\theta))E_n^0 \tag{4.1}$$

where E_n and E_n^0 are the neutron energy prior and after the collision, m_n and m_A the masses of the neutron and the colliding isotope, and θ is the scattering angle in the center-of-mass reference system.

The final direction of the neutron after the collision in the laboratory frame (ϕ), is:

$$\phi = \arctan\left(\frac{\sin(\theta)}{\cos(\theta) + \frac{m_n}{m_A}}\right) \tag{4.2}$$

In collisions with light elements, neutrons lose a larger fraction of their initial kinetic energy. Collisions with heavy isotopes tend to reduce less the neutron energy.

In addition, and neglecting the actual angular distribution for the neutron after the collision, in the case of light isotopes, the final direction is deformed towards the initial direction, while in heavy isotopes this effect is much less relevant.

Hence, in the aim of reducing the neutron energy and keeping its original forward direction, light isotopes will be preferred. On the other hand, heavy isotopes will be more useful as neutron reflectors, as neutrons are more back-scattered from them, comparatively. Considering that no additional moderation is pursued when neutrons enter the reflector parts of the BSA, the fact that neutron energy loss per collision is in fact smaller also contributes to choose them as the most appropriate reflectors. This is shown in Figure 4.5, where isotopes suitable for both moderation and reflection are displayed together with the average and maximum neutron energy loss per collision.

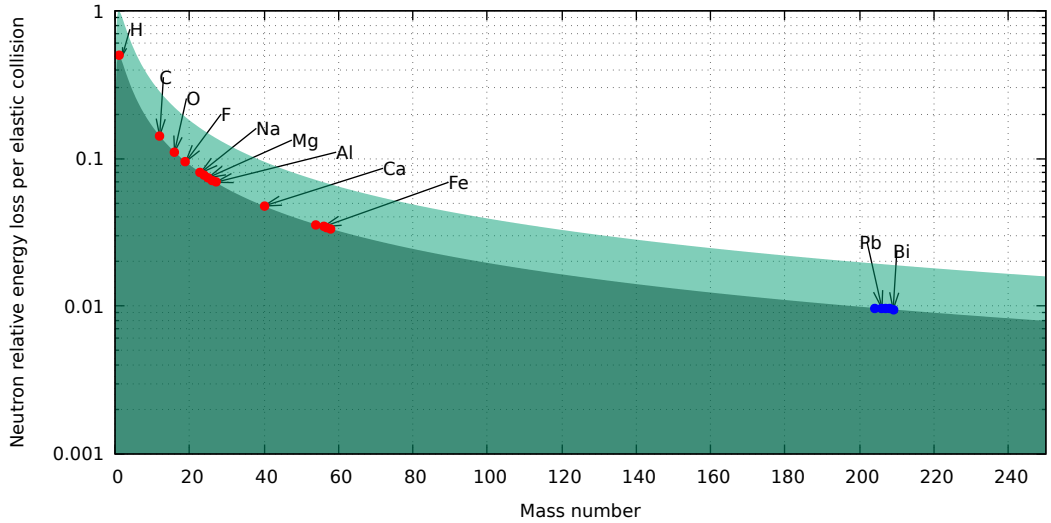

Figure 4.5: Neutron relative energy loss per elastic collision, as a function of the mass number of the collided isotope. Energy loss ranges from 0 to a maximum depending on the scattering angle. The maximum is shown in light green, and the mean is shown in dark green. Isotopes whose behavior serves well for moderation are shown in red, and those better suited for reflection without moderation are shown in blue.

Regarding the cross-section of the isotopes to be used, a high elastic cross section above the epithermal range will be pursued, so that the process of moderation can be more efficiently achieved. In the same way, low absorption cross-section will be desired, in order not to lose neutrons that could be profitable if moderated. It has to be stated that the complete neutron moderation to the thermal energies is not desired, but the partial moderation to the epithermal range. In this aim, the

aspiration is to moderate the neutrons to energies below 10 keV, with a spectrum centered around 2-3 keV.

The presence of resonances above the epithermal range in the elastic cross-section speeds up the moderation, reducing the number of neutrons at the resonance's energy, and provoking an increase of it at an energy related to the energy loss following Eq. 4.1. Thus the concatenation of a sequence of resonances towards the epithermal range would lead to a more effective moderation. Accordingly, a high elastic cross section or the presence of resonances below the epithermal range would degenerate in over-moderation. Hence, the choice of isotopes with intense or multiple resonances in the epithermal range shall be discarded.

To better describe the characteristics of different isotopes in what regards the neutron moderation process, the use of the macroscopic cross-section as an indicator is essential.

The Macroscopic Cross-Section The macroscopic cross-section (Σ) is the product of the cross-section times the atomic density of the material. It is defined as:

$$\Sigma = \sum_i n_i \sigma_i \tag{4.3}$$

where n_i are the isotopic/atomic densities. The macroscopic cross-section has units of inverse of length, and it can be shown that the total macroscopic cross-section is the inverse of the mean free path of neutrons inside the material ($\lambda = 1/\Sigma_t$).

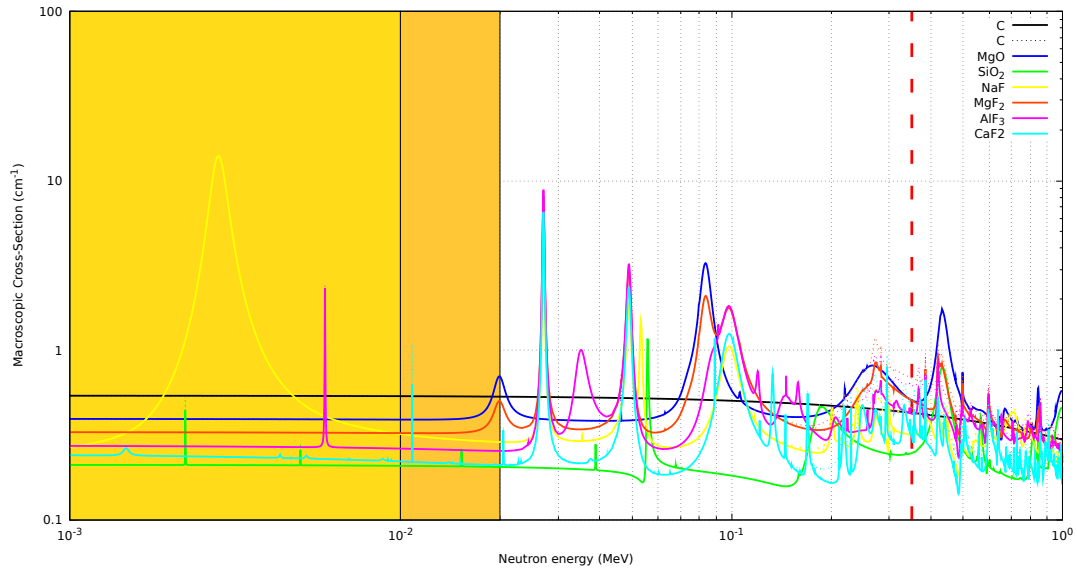

Figure 4.6: Macroscopic cross-Section of candidate compounds as main moderator. Carbon, Magnesium Oxide, Silica, Sodium Fluoride, Magnesium Fluoride, Aluminum Fluoride and Calcium Fluoride are included. Maximum neutron energy with the ^{7}Li(p,n) source at 2.1 MeV is marked with the vertical dashed line, at 350.4 keV. Target neutron energy range (below 10 keV) is shown with the filled area in gold, and the acceptable neutron range between 10 and 20 keV is shown in orange.

Taking all previous considerations into account, an appropriate choice for the moderating material points to a salt of light elements, i.e. oxides and fluorides of light atomic weight metals as sodium, magnesium and aluminum, or heavier calcium or iron salts. Other options are the use of carbon in the form of graphite, or silica. Carbon has a flat high cross-section with no resonances in the range of interest, and hence not being the most indicated for this, also given that its elastic cross-section remains high below 10 keV, thus leading to over-moderation. Silica has one of the lowest elastic cross-sections with small resonances, being easily outperformed by other materials in most of the range of interest.

Concerning oxides, oxygen has no resonances below 400 keV and also has a low elastic cross-section, being almost invisible and thus not enhancing the moderating features of the material. However, it shall be stated that it is a very interesting option to try when primary neutrons come around 400-500 keV, given its strong resonance at these energies. In these circumstances, a thick block of an oxide, e.g. magnesium oxide could be used right after the neutron source.

Fluorine offers a wide-spread amount of resonances starting right above 10 keV. This makes fluorine a good option for the resonance crossing technique of moderation when combining with metals.

Concerning the light metals, sodium shows a strong resonance below 10 keV, hence making it inadequate as a neutron moderator for BNCT, as it would make 2-3 keV neutrons disappear and migrate to lower (less suitable) energies. Magnesium and aluminum show many resonances in the 10-350 keV range, then being both good candidates for the core of the moderating material. Magnesium fluoride shows specially good characteristics compared to aluminum fluoride, given the alternate series of resonances along the 10-350 keV range, thus complementing the resonance crossing for neutrons. Special emphasis comes near 100 keV, around the mean energy of neutrons produced at the ^{7}Li source at 2.1 MeV. There, a pair of resonances partially overlap giving a broad range for continuous neutron energy reduction. Also the elastic cross-section at the highest energy of the primary neutron spectrum is higher for magnesium fluoride than for aluminum fluoride. Aluminum presents a strong resonance at 30-40 keV, thus making it a good element for the final stages of moderation.

In this direction, magnesium fluoride will be used as the core material for the neutron moderation. A final layer of aluminum (metal) will be placed after the moderating core to complete the moderation, partially behaving like a fast neutron filter.

To keep the core where neutrons moderate and to avoid large loses of neutrons from scattering off the BSA, specially considering the relatively low neutron production from the low energy incident protons onto ^{7}Li, some reflecting materials need to be attached closely surrounding the moderating core. This also serves to enhance the moderation, effectively bringing high energy neutrons back to moderation, remarkably for backward-produced neutrons at the source. For this purpose, a heavy isotope as Pb or Bi is key as it was already mentioned. Among them, Pb is slightly denser and its elastic cross-section is around twice as high on average. On top of that, it is easier to cast, it is less brittle and is cheaper. Therefore Pb is considered as the main reflector.

In turn, Bi is contrarily best suited as a gamma radiation end-filter due to these very same reasons, since its lower elastic cross-section alters less the final spectrum, while the high Z maintains the gamma absorption properties.

Besides, a thermal neutron filter is needed, and high thermal absorption cross-section isotopes as ^{6}Li, ^{10}B or ^{113}Cd are best suited. Specially, ^{6}Li is preferred among others since it does not generate secondary gamma radiation after thermal neutron absorption. This compensates its lower absorption cross-section, remarkably considering that this filter is placed after all moderation has taken place, and therefore the gammas would only be absorbed by the Bi filter. The use of ^{6}Li, compared with ^{10}B and ^{113}Cd, reduces the Bi thickness and hence the beam degradation.

Finally, in order to limit the neutron and gamma spread out of the beam aperture, a set of materials are chosen in order to fully thermalize and then absorb neutrons and gammas generated in this process. For this, lithiated polyethylene blocks are used, together with layers of ^{6}Li in the form of LiF and Pb are used to cover the front side of the BSA.

4.6 Design and optimization of the BSA to meet the IAEA recommendations

The general design is then constrained by the previous considerations. An axially symmetric geometry is considered with solid or hollow cylindrical shapes. In addition, in order to conform the beam towards the aperture, and to keep the beam divergence low enough, a final step of tapered reflecting geometry is used. A beam insertion is also included, together with the lithium target and simple model of a Cu refrigeration system cooled with water. The aperture diameter was fixed to 14 cm following the IAEA technical document. A general design of this is shown in Figure 4.7.

This design was built into a MCNP6 input and simulations were run to test the design performance.

The simulations were run with variations in the most relevant dimensions (MgF_2 moderator thickness and radius) in order to optimize the IAEA recommendations. These were not enough to fulfill all five criteria, and hence an iterative process varying all relevant dimensions followed. Special care had to be taken with epithermal flux, due to the low neutron production from the proton-lithium reaction, thus most of the efforts aimed at limiting the neutron leakages, reduce over-moderation and recover useful neutrons via reflection.

A few relevant considerations and findings that raised from the process of optimizing the design will be mentioned here.

- Size of the moderator in the backward direction. Although the ^{7}Li(p,n)^{7}Be reaction is forward-peaked and the most energetic neutrons are emitted in the forward direction, there is a significant amount of neutrons generated in the backward direction. These neutrons are key in this design due to the overall low yield for the reaction at $E_p = 2.1$ MeV. Being able to recover at least part of them is paramount, hence some part of the moderator is

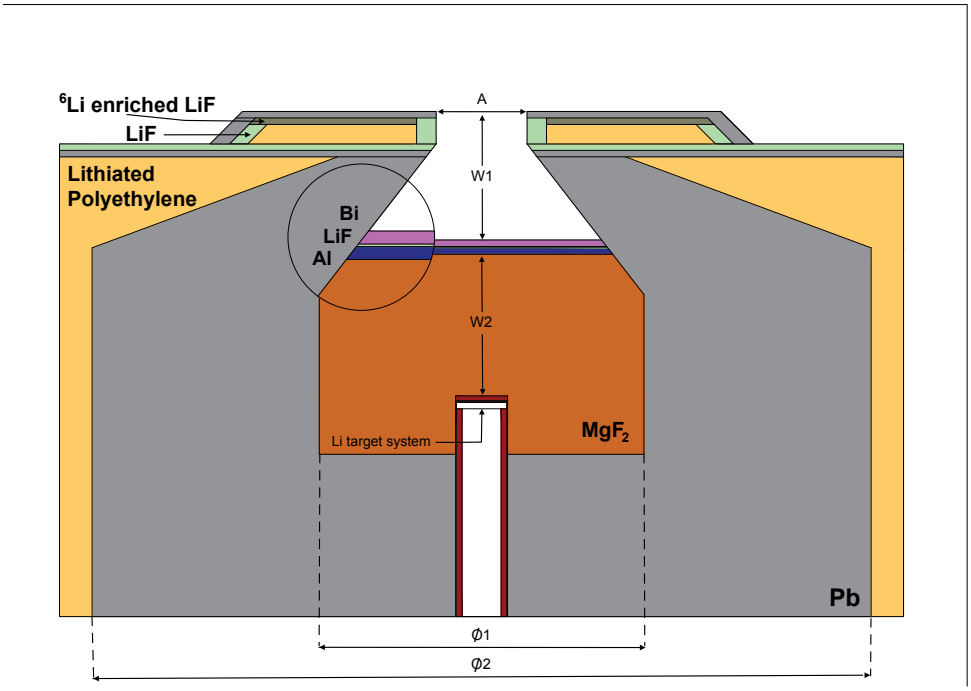

Figure 4.7: Lateral view of the general design of the BSA. Each material block is shown in different colors, with detail at the final step of moderation and neutron filtering with three successive layers of Al, LiF and Bi.

extended in the backward direction, with additional Pb reflector afterwards in this aim. This enlargement of the BSA in the backward direction has some effects in the spectrum and thus in the dose. Since lower energy neutrons are produced in backward directions and also neutrons that arrive to the aperture had made a longer tour, this increases the overall epithermal and thermal fluxes, shifting the spectral peak towards lower energies. Nevertheless, the epithermal flux enhancement compensates the side effects, as thermal can be more easily subtracted via thermal filters. Additionally, this reduces slightly the fast dose ratio.

- Thickness of Pb reflector. In general, the addition of extra Pb reflector thickness increases the neutron flux in the core. This leads to the increase of neutron flux at the aperture, at the expense of over-moderation and a general shift of the spectrum towards lower energies. Indirectly, the use of Pb reduces the gamma radiation and hence the gamma dose. This pattern is consistent and saturates after the thickness is large enough.

- Ratio of Al layer and last MgF_2 layer thicknesses. Both components are mainly used as moderators, but the elastic cross-section is bigger for MgF_2 on average. In this sense, a larger amount of Al can be compensated by not removing all the same thickness of MgF_2 in exchange. Under this design, as previously described, Al is used for the last stage of moderation, mainly for the 33 keV resonance crossing, with no much more extra moderation needed. This way, a thickness around 1 cm is enough, specially considering that the macroscopic cross-section for Al at the resonance peak is 2 cm^{-1}, hence this thickness is enough for two-times the mean free path.

- LiF blocks at the aperture to limit neutron divergence. Beam divergence is in general hard to control, thus having a feature in the BSA design that plays a determinant role on this is not possible. Instead, many different aspects modify the beam divergence and usually improving other criteria comes at the expense of increasing the beam divergence. To solve this, a different approach based on rejecting large-angle outgoing neutrons is followed. This is specially effective for lower energy neutrons, since these neutrons come out of the BSA with more isotropic directions, while faster neutrons had to be previously (partially) directed towards the aperture by means of the main tapered Pb reflector. To do this, an annular set of neutron absorbers made of LiF is placed as a collimator right before the beam aperture. This feature also avoids thermalized neutrons from the out-of-field shielding that is placed beside, as it will be commented next.

After all these considerations were properly addressed, a final configuration fulfilled all criteria at once. Then, a set of extra changes and optimizations were inserted in the aim of reducing neutron leakages out of the aperture, in order to reduce the patients over-irradiation in body-parts far from the treatment volume. Special care was taken not to disrupt the previously attained beam properties. These additions consisted of layers of lithiated polyethylene blocks subsequently covered with LiF and Pb layers to fully moderate epithermal neutrons and absorb thermal neutrons and gamma radiation, specially in this case due to the gamma emission after neutron capture by hydrogen. These aspects of the design can be observed in the Figure 4.8, that shows neutron and photon flux within and around the BSA design.

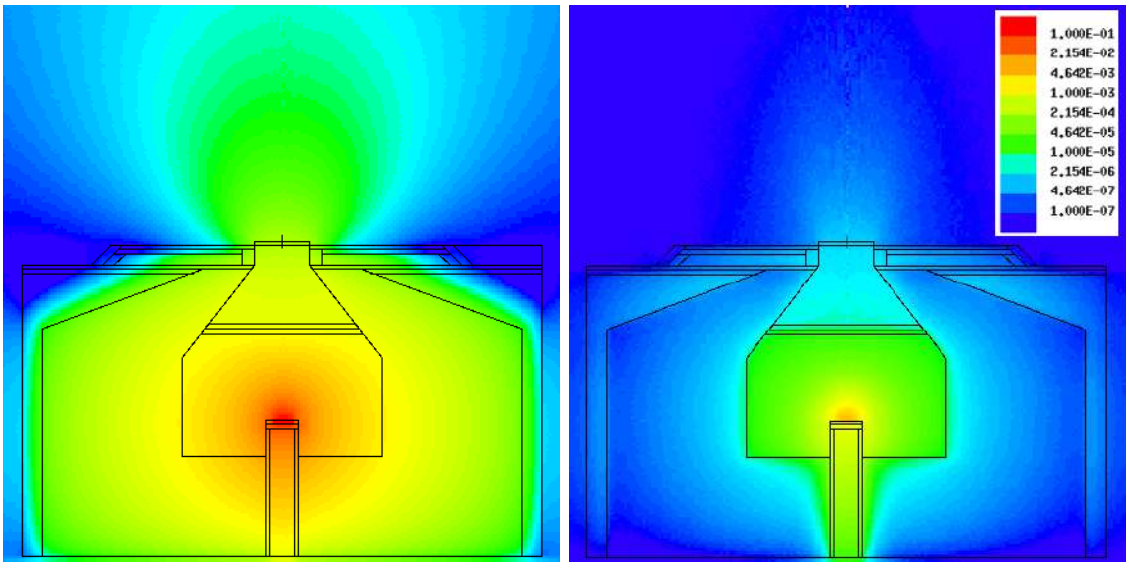

Figure 4.8: Neutron (*left*) and Photon (*right*) fluxes inside and around the BSA. The scale refers to particles per initial (simulated) neutron. These plots display the effect of the main features of the BSA, including those discussed in the text, as the role of the annular LiF collimator on controlling the beam divergence or the Pb reflector in recovering neutrons from loses and gamma absorption.

In order to demonstrate the optimization of the BSA design, some examples are given for the epithermal flux and fast dose figures in design configurations around the definitive one, with slightly larger or shorter moderator thickness (Figure 4.9) and

moderator radius (Figure 4.10), which prove to be the most significant parameters in the design.

The moderator thickness, namely the MgF_2 width in the forward direction, is the most relevant parameter in the optimization, and its variation produces effects in the total epithermal flux, thermal flux ratio and fast dose, with minor variation of the other two criteria. Since thermal flux is easier to control, we will concentrate in total epithermal flux and fast dose. The increase or decrease in the moderator thickness produces an opposite effect in the goal of achieving the IAEA figures. By increasing the thickness, more moderation occurs, hence the neutron flux is reduced due to loses at the walls and absorption, while its mean energy shifts down. This makes the fast neutron dose decrease. A compromise between the two has to be attained under these circumstances. This can be graphically seen as the intersection between two lines, each corresponding to epithermal flux and fast dose, against moderator thickness, in Figure 4.9. However, this crossing point can happen above or below the horizontal line that defines the fulfillment of both criteria. It is only when all previous considerations have been taken into account that the epithermal flux is above the figure and the fast dose is below it, for the same thickness.

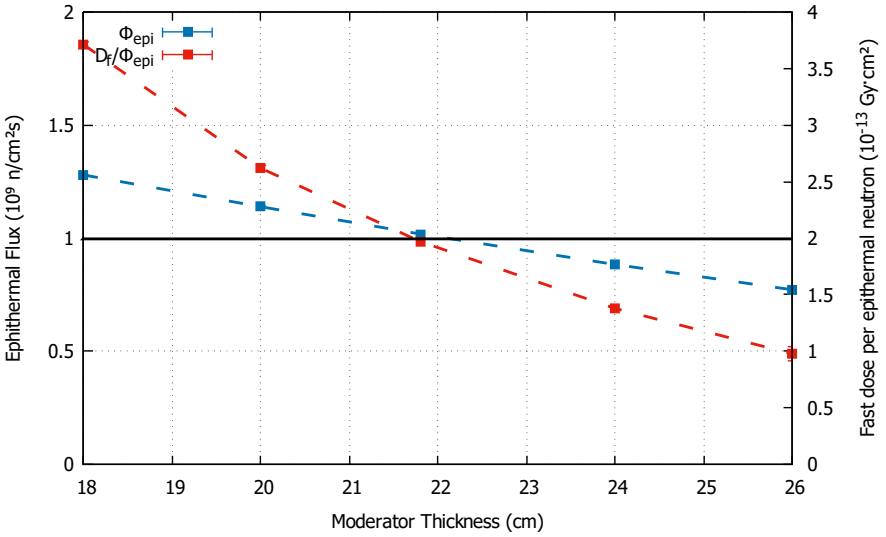

Figure 4.9: Epithermal flux (*blue, left-side scale*) and Fast dose (*red, right-side scale*) figures as a function of moderator thickness. Both scales are adjusted so that the reference figure coincides at the horizontal black line. Above this line, epithermal flux is fulfilled, while fast dose has to be below the line for the criterion to be attained.

The same occurs for the moderator radius, that its to say its lateral width. An increase in moderator radius increases the volume where neutrons thermalize, thus lowering their energy and reducing the fast dose. This can be seen in the left part of the Figure. At the same time, moderation reduces the flux due to loses, which explain the constant reduction of flux as moderator radius enlarges. At some point, extra moderator radius does not further reduce the fast neutron component[2], so the fast dose flattens. However, in this case another consideration has to be addressed.

[2]A large moderator radius provides the possibility of recovering partially thermalized neutrons that take a detour, which increases the epithermal flux. However, the fast neutron component that reaches the aperture via a more direct path is not affected by the change in the moderator radius.

The fast dose per epithermal neutron criterion is in fact a ratio between fast dose and epithermal flux. Thus, if the fast dose remains flat while the epithermal flux diminishes, the figure will increase. This is in fact what is observed in Figure 4.10), thus effectively defining a minimum around 25 cm of moderator radius. In the same way as above, this distinctive point fulfills the criteria after considering all previous concerns.

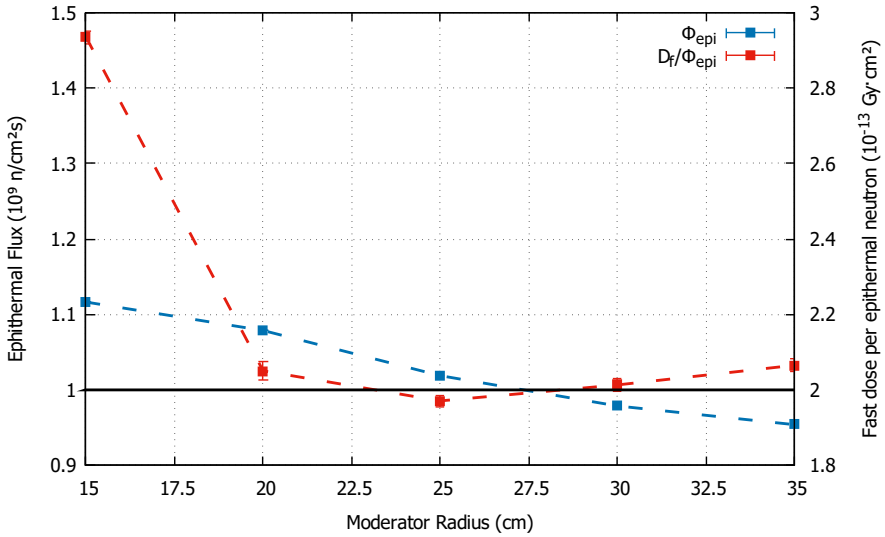

Figure 4.10: Epithermal flux (*blue, left-side scale*) and Fast dose (*red, right-side scale*) figures as a function of moderator radius. Both scales are adjusted so that the reference figure coincides at the horizontal black line. Above this line, epithermal flux is fulfilled, while fast dose has to be below the line for the criterion to be attained.

A final comment has to be included before fully analyzing the performance of the optimized design of the BSA. This comes in regard to the proton energy utilized for neutron generation. This BSA has followed a process of optimization for a fixed proton energy of $E_p = 2.1$ MeV. However, it is relevant to study its performance in case of variation of this energy. Therefore, a comparative analysis of the IAEA figures is adopted here and is displayed in Figure 4.11.

As the impinging proton energy increases, a greater extent of the cross-section is in play, as protons slow down inside the ^{7}Li target. That is, a larger amount of neutrons is generated on top of those created at lower energies. Those newly generated neutrons have a greater energy, thus are moderated to a lesser extent and contribute more dominantly to the fast dose. This effect is not really noticeable until the proton energy enters the region of the 2.25 MeV resonance of the ^{7}Li(p,n) reaction. At that point, the progressive increase in epithermal flux and fast dose steps up. This can be clearly observed in Figure 4.11, where one can find a slow increase (nearly a plateau) in the fast dose to epithermal flux ratio until it bends upwards as it approaches the 2.25 MeV resonance. This is specially relevant in case of slight variations of the energy of the protons delivered by the accelerator, as these variations would not produce a large change in the main characteristics and figures of the beam.

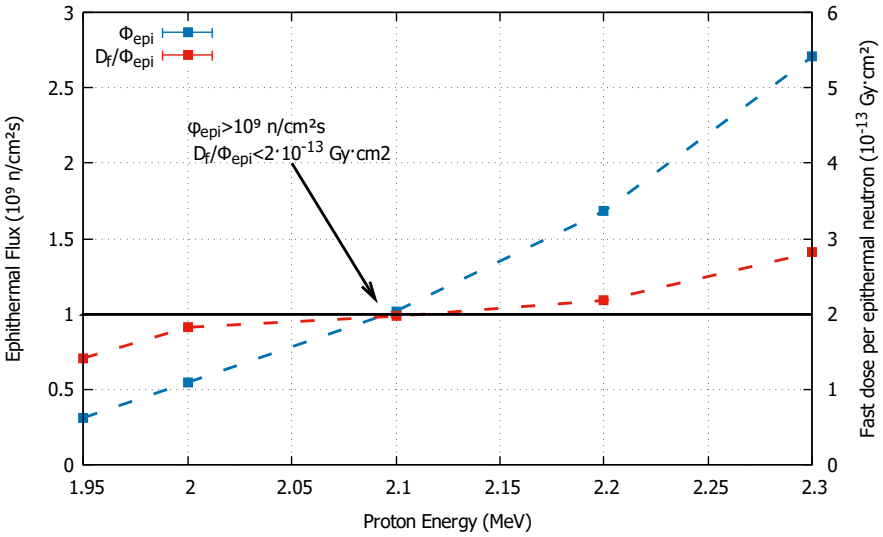

Figure 4.11: Epithermal flux (*blue, left-side scale*) and Fast dose (*red, right-side scale*) figures as a function of incident proton energy to the Li target. Both scales are adjusted so that the reference figure coincides at the horizontal black line. Above this line, epithermal flux is fulfilled, while fast dose has to be below the line for the criterion to be attained.

4.7 Results: The final design of the BSA

The design and optimization of the BSA brought in a specific set of materials and dimensions, in line with the already discussed and following the scheme in Figure 4.7.

The core moderator is made of MgF_2, with 21.8 cm in thickness in the forward direction from the target, and 25 cm in radius. The the backward-extended part is of 9 cm thick. The Al layer, completing the moderation, is 1 cm thick. Next in the forward direction is the thermal neutron filter, made of LiF and 0.2 cm thick. The last layer, serving as gamma filter and made of Bi, is 1 cm thick. The surrounding Pb reflector, shaped as a cylindrical corona, is of 60 cm outer radius, and it is 25 cm thick in the backward direction.

To illustrate the contribution of each consecutive layer, Figure 4.12 shows the spectral flux from the target to the aperture, computed at the interfaces between different layers. This shows the unmoderated spectrum near the target, a partially moderated spectrum at an intermediate position. At the end of the MgF_2 block, the spectrum is mostly moderated and already centered around 2 keV, and the last 1 cm Al layer helps in reducing the fast flux around the corresponding resonances. Then the effect of the LiF layer in the thermal region is showed, together with the little effect of the Bi layer, specifically designed to degrade the spectrum the least possible. Thus, only few narrow elastic-scattering resonances disturb this spectrum, in the form of few spikes in the 1-20 keV range. Then the flux at the aperture is reduced due to the collimation.

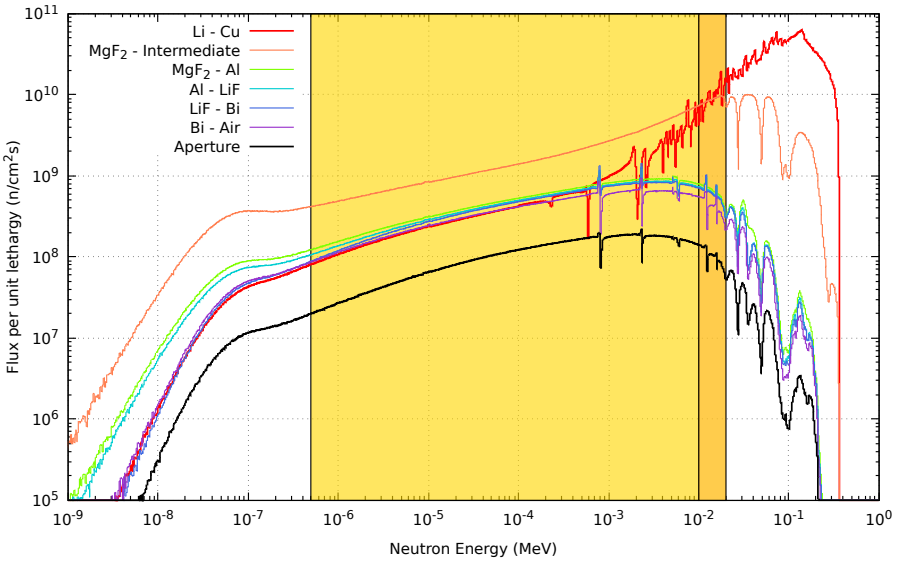

Figure 4.12: Neutron spectra at different positions in the BSA, from the target to the aperture, including intermediate locations inside the moderator block, and in the interfaces of the various filtering layers. The epithermal range (0.5 eV - 10 keV) and its extension (10-20 keV) are highlighted in yellow and orange, respectively.

The performance of this design has been published [108]. This design, whose intellectual property is wholly owned by the University of Granada, is patent pending (PCT/ES2021/070607).

In the following, a specification of the beam characteristics in terms of spectrum and profile, compliance with the IAEA recommendations and in-phantom performance is described.

4.7.1 Beam characteristics: spectrum and profile

The neutron beam spectrum (wherein all neutrons exiting the BSA through the aperture are considered), was designed to be centered in the epithermal region (0.5 eV - 10 keV), with lower and higher energy components minimized to the extent possible. In addition, as it was previously discussed in the 4.1.1 section, the best energy range in terms of AD lies around 2-9 keV, while the maximum TR is found near 2-3 keV.

The final beam satisfactorily complies with these requirements, peaking at 2 keV, and with a larger part of the spectrum lying within the epithermal range (88.0 %), while only 3.3 % accounts for thermal neutrons and 8.7 % for fast neutrons. Moreover, when analyzing the high energy tail (neutron flux above 10 keV), 49 % of the fast flux is contained within the 10-20 keV range, and only 32 % of the fast neutron flux comes from neutrons above 40 keV. This highlights the specially well conformed neutron spectrum, specially noting that 10-20 keV neutrons are mostly adequate for BNCT treatments. Therefore, 92.3 % of the neutrons lie within the useful range for BNCT. Since neutrons from 20-40 keV can be accepted under some circumstances, more than 95 % of neutrons can be considered as adequate under this limit extension.

This spectrum is shown in Figure 4.13 in both linear and logarithmic scales, in comparison to two previous archetypal designs, the FiR-1, a Reactor-based design, and the C-BENS, an Accelerator-based neutron beam for BNCT. The epithermal range is explicitly highlighted in yellow, with the additional range from 10 to 20 keV in orange. This figure displays the well conformed spectrum with a sharply cut and short high energy tail, preventing a large fast dose in tissues, as compared with other designs whose spectrum extends to the tens of MeV, or even further.

Different strategies can be used to determine the actual spectrum experimentally when this design is built. One technique of relevance is multi-foil activation technique. This technique has been applied in order to extract the neutron beam spectrum of the newly available NEAR station of the n_TOF Collaboration at CERN. The details of this characterization can be found in Appendix C.

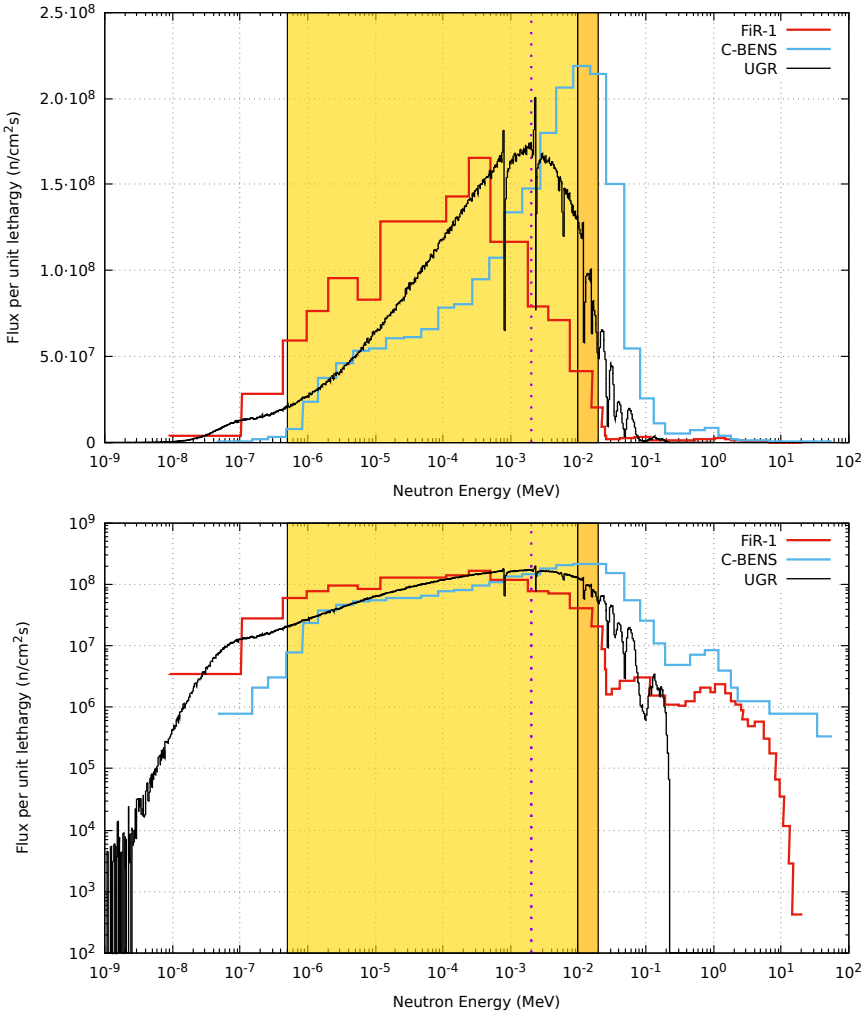

Figure 4.13: Neutron spectrum of the BSA at the aperture, compared to previous designs of reactor and accelerator-based BNCT. The epithermal range is marked in yellow, with the extension to 20 keV in orange. Additionally, a dotted vertical line denotes the 2 keV, corresponding to the position of the maximum of the spectrum.

Aside from the spectrum, other relevant characteristic is the beam profile. The beam profile has to be as sharply defined as possible, in order not to generate

over-irradiation of the patient in body parts far from the target volume. This is the main purpose in the design of the outer layers and collimation system of the BSA. The total flux averages 10^9 n/cm^{2}s inside the aperture region, and rapidly decreases by two orders of magnitude within the first 15 cm from the aperture. The epithermal neutron flux further reduces to three orders of magnitude from the center at 27 cm from the aperture. The collimation is tighter for the fast neutron component, and even more for thermal neutrons, where a sharp decrease of two orders of magnitude occurs within 5 cm from the aperture. The gamma radiation contamination is reduced to a lesser extent as we move apart from the aperture, though it was previously well attained within its safe margins at the aperture. Figure 4.14 displays the lateral flux at and to the sides of the aperture of the BSA.

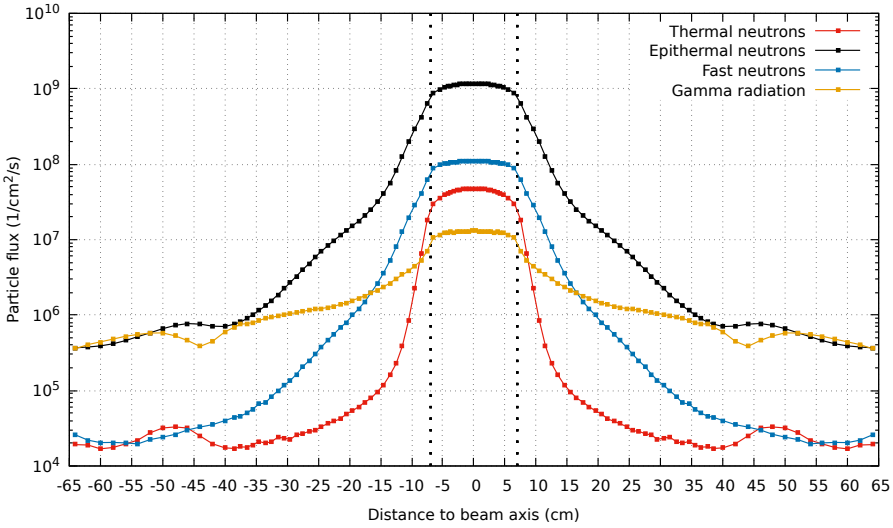

Figure 4.14: Lateral flux at the aperture and the out-of-field flux to the sides of the aperture. The neutron flux is evaluated separately in thermal, epithermal and fast components, and also gamma contamination flux is included in the Figure.

4.7.2 The in-air parameters: IAEA recommendations

The parameters of the IAEA recommendations constitute the main Figures-Of-Merit to assess the adequacy of the neutron beam in in-air conditions. The current design achieves the goal of fulfilling all IAEA recommendations at once, with an accelerator proton energy of 2.1 MeV and a current of 30 mA. It does so even with the restricted epithermal neutron limits in the range 0.5 eV - 10 keV and the strong figure aiming above 10^9 n/cm^{2}s in the epithermal flux. Table 4.2 presents the values of the Figures of Merit for that configuration (in bold), and also with the extended epithermal limits from 10 to 20 keV. The epithermal flux reaches just above 10^9 n/cm^{2}s in both cases, with a slightly higher value in the extended limits' case for obvious reasons. Likewise, the fast neutron dose is attained below the threshold, with all other Figures far within the limits. For further comparison, the Figures for a 2.0 MeV proton beam are included. This closely corresponds to the minimum energy at which this BSA can be used for BNCT treatments, given that the epithermal flux is just above the soft recommendation for the epithermal flux at $5{\cdot}10^8$ n/cm^{2}s. All other figures are also fulfilled in this case, with the additional note that the fast dose is around 8 % lower due to the lower energy neutrons produced in the source.

	IAEA recommendation	Epith. limits 0.5 eV - 10 keV	Epith. limits 0.5 eV - 20 keV
		(E_p=2.0 MeV)	
ϕ_{epi} (n/cm^2 · s)	$> 5 \cdot 10^8$	$5.459 \cdot 10^8$	$5.783 \cdot 10^8$
$\phi_{\text{th}}/\phi_{\text{epi}}$	< 0.05	0.0378	0.0357
J_n/ϕ_n	> 0.7	0.7128	0.7130
$\dot{D}_{\text{fast}}/\phi_{\text{epi}}$ (Gy · cm^2)	$< 2 \cdot 10^{-13}$	$1.82 \cdot 10^{-13}$	$0.94 \cdot 10^{-13}$
$\dot{D}_{\gamma}/\phi_{\text{epi}}$ (Gy · cm^2)	$< 2 \cdot 10^{-13}$	$1.01 \cdot 10^{-13}$	$0.92 \cdot 10^{-13}$
		(E_p=2.1 MeV)	
ϕ_{epi} (n/cm^2 · s)	$> 5 \cdot 10^8$	$\mathbf{1.019 \cdot 10^9}$	$1.081 \cdot 10^9$
$\phi_{\text{th}}/\phi_{\text{epi}}$	< 0.05	**0.0372**	0.0351
J_n/ϕ_n	> 0.7	**0.7120**	0.7119
$\dot{D}_{\text{fast}}/\phi_{\text{epi}}$ (Gy · cm^2)	$< 2 \cdot 10^{-13}$	$\mathbf{1.97 \cdot 10^{-13}}$	$1.09 \cdot 10^{-13}$
$\dot{D}_{\gamma}/\phi_{\text{epi}}$ (Gy · cm^2)	$< 2 \cdot 10^{-13}$	$\mathbf{0.99 \cdot 10^{-13}}$	$0.97 \cdot 10^{-13}$

Table 4.2: In-air beam parameters compared to the IAEA recommendations, for proton accelerator energies of 2.0 and 2.1 MeV. The results considering the epithermal upper limit at 10 and 20 keV are included. The final results with the standard epithermal limits and the operating proton energy of 2.1 MeV are highlighted in bold.

It is paramount to compare the in-air parameters of the beam from this BSA with previous of reactor-based and accelerator-based designs. Concerning reactor-based facilities, KURRI (Japan) in epithermal mode and THOR (Taiwan) share an adequate beam intensity ($9.1{\cdot}10^8$ and $1.7{\cdot}10^9$ n/cm^{2}s at KURRI [26] and THOR [29], respectively) and THOR has very low divergence ($J_n/\phi_n = 0.81$), but both of them suffer from a high fast neutron contamination above the recommendations (6.1 and 2.8, in units of 10^{13} Gy·cm^2 per epithermal neutron). Also THOR has a large thermal neutron ratio (0.12), more than doubling the recommendations. The FiR-1 Reactor in Finland [22, 109], where some of the most successful clinical trials have been performed so far, has a set of parameters really close to the ones that we report here, with a fast neutron contamination matching the limit of the recommendations, an epithermal flux of $1.1{\cdot}10^9$ n/cm^{2}s and a thermal ratio of 0.034. Their fast neutron flux accounts for 6.7 % of the total flux, which is slightly lower than the one from our design (8.7 %), but it is mostly composed of harmful high energy neutrons extending up to the tens of MeV, unlike this design, were the maximum neutron energy is around 200 keV [23]. Extending the discussion to accelerator-based facilities, the C-BENS [45], the first one of its kind in operation, has a high intensity ($1.2109{\cdot}10^9$ n/cm^{2}s) and low thermal neutron flux (thermal ratio of 0.04), but their fast neutron dose figure exceeds the maximum ($5.8{\cdot}10^{13}$ Gy·cm^2) even if they consider the upper epithermal limit at 40 keV instead of 10 keV. There are several other projects, which typically achieve enough beam intensities and have low thermal flux, though the fast dose figure is not low enough to fit with the recommendations [110, 111, 112]. Others do meet both the epithermal flux and low fast neutron dose figures, but fail on the side of collimation and provide a strong beam divergence [113, 114]. An Italian design reaches a good enough epithermal flux, but fast neutron and gamma doses lay above the limits [41].

4.7.3 The in-phantom performance: ICRU-33 and brain

In addition to the in-air parameters, it is compelling to analyze the performance of the beam in phantoms. In this case, the in-phantom performance was determined using the Snyder model of the head and brain, and a cylinder filled with ICRU-33 tissue. MCNP6.2 simulations were run were the out-going neutron field (and gamma contamination) from the BSA's aperture was directed onto the corresponding phantom. In both cases, the standard RBE used in the literature were used, namely $w_{th} = w_f = 3.2$, $w_\gamma = 1.0$, and $w_B = 1.3$ for the tumor and $w_B = 3.8$ for the normal tissues [17]. In the case of the ICRU-33 tissue, standard boron concentrations of 10 ppm for the normal tissue and 35 ppm for the tumor were used. These boron concentrations serve as minimum requirements for the treatments, as many studies have found higher boron concentrations both in tumor and normal tissues. For this reason, in the Snyder model of the brain, 18 ppm was used for normal tissues and 65 ppm for the tumor, as in Refs [16, 115, 116]. The dose rate components for both cases are shown in Figure 4.15. The dose rates are decomposed into thermal, fast neutron doses, the boron dose (at normal tissues), and the gamma dose is displayed as primary (due to the gamma contamination from the beam) ans total gamma dose (including both the neutron contamination from the beam and the secondary photons created within the phantom).

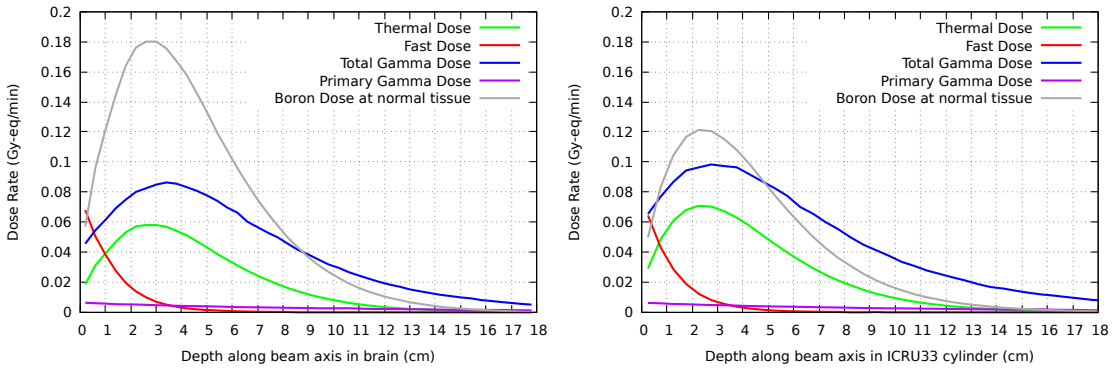

Figure 4.15: Dose components along the beam axis for the Snyder model of the brain (*left*) and for the ICRU-33 cylinder (*right*). The gamma dose is shown as total gamma dose (blue) and also the primary gamma dose (magenta), corresponding to the gamma contamination of the beam. The neutron component is separated in thermal dose (green) and fast dose (red). The boron dose is indicated for the normal tissues (grey).

The total dose received at each position along the beam axis and also the lateral dose profiles at several depths are shown in Figure 4.16. Total dose is computed as a weighted sum of the dose components, with each component multiplied by its corresponding RBE factor. In order to analyze the results from the simulations, a set of FOM was extracted, including the previously defined Advantage Depth (AD) and maximum Treatment dose Ratio (TR), but also the Advantage Depth Dose Rate (ADDR), which is the maximum dose rate delivered to normal tissues; Treatable Depth (TD), corresponding to the depth where the tumor dose rate equals twice the ADDR; and the Average treatment dose Ratio (AR), which is the ratio between the total tumor and normal tissue dose rates, each one averaged in the range from the tissue surface or skin to the AD. The values of these FOM are also included in the

boxes of the *top* panels in Figure 4.16. For the Snyder head phantom, AD reaches 9.74 cm with ADDR of 0.331 Gy-Eq/min; TD is 7.85 cm; the TR and AR ratios have values of 6.19 and 5.78, respectively. For the ICRU33 cylinder, AD equals 8.95 cm, with an ADDR of 0.301 Gy-Eq/min; TD is 6.80 cm; the TR and AR are 4.72 and 4.43, respectively.

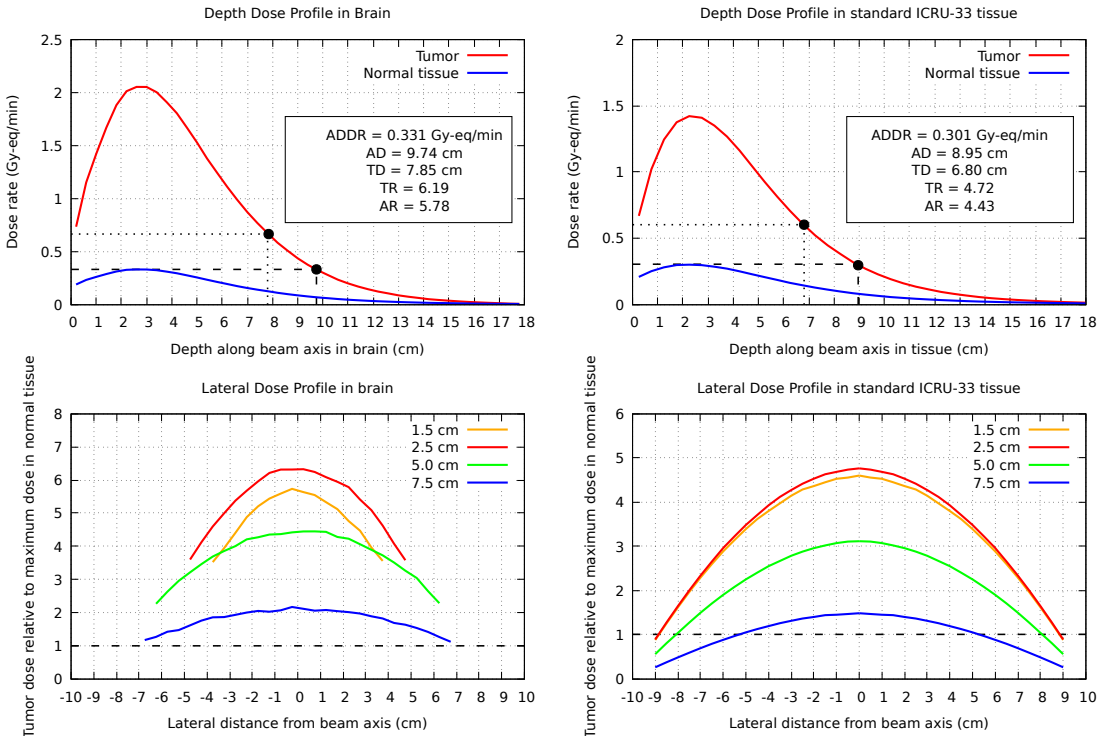

Figure 4.16: Total dose rates in tumor and normal tissue for the Snyder model (*left*) and the ICRU-33 cylinder (*right*). The dose rates along the beam axis are shown in the *top* panels, and the dose profiles at different depths are shown in the *bottom* panels. Additional information is shown in the white boxes in the *top* panels, concerning the main Figures of Merit, including the ADDR, AD, TD, TR and AR. Also in the *top* panels, the black dots indicate the depths and tumor doses that equals and does twice the maximum in normal tissues, hence showing visually the ADDR, AD and TD.

These results can be compared and discussed with the evidence of the literature. We can find examples of previous reactor-based BNCT facilities and of some of the newest accelerator-based ones. Also there are several other projects that have been under development and have published at least some of the FOMs that rely on simulations as in our case. Note that in the next comparisons, not in all cases the reported figures correspond to the same kind of simulation or dose measurement strategy, since the techniques to do so are not standardized. That is the reason for providing two different cases with a head model (65 and 18 ppm of ^{10}B in tumor/normal tissues) and an ICRU33 cylinder (35 and 10 ppm). For instance, the calculations from the R2-0 at Studsvik use 25 ppm of boron in their brain phantoms [28]. In other cases, the phantoms are located at a different position from the beam aperture, such as the case of THOR, where the phantom was placed at 10 cm from the aperture. Both of them (THOR and R2-0) together with FiR-1 provide the TD but none of them exceeds 7 cm, while our design almost reaches 8 cm. If we compare

AD, we perform slightly better than R2-0 (9.74 cm vs. 9.7 cm) even with a lower boron concentration. KURRI and C-BENS only reach an AD of 10 cm if the raise the boron concentration to 50 ppm and a tumor/normal tissue concentration ratio of 4.5:1 [46, 45]. Regarding ADDR, THOR peaks at 0.5 Gy/min and FiR-1 also reaches 0.45 Gy/min, in accordance with their higher beam intensity compared to our design, that attains 0.331 Gy/min. Regarding accelerator-based projects that have been under development in California (USA) [117], Obninsk (Russia) [113], Korea [118] or Argentina [119], none of them achieve AD higher than 9.5. A recent work in Osaka (Japan) stays behind at 9.1 cm [110]. A proposal in Novosibirsk (Russia) claims a similar AD (9.7 cm), but the other figures (TD = 7.52 cm and TR = 5.38 cm) are lower than ours [114].

Finally, in order to show an example of the dose distribution using the Snyder model of the brain, a couple of simulations were run, using an one- and two-field irradiation. The dose map corresponding to a slice of the model is shown in Figure 4.17. Dose is shown relative to the Maximum dose in normal tissue, in order to easily identify the regions where a BNCT treatment could produce a desirable result. In the Figures, a dose ratio over two is shown with turquoise color, and a dose ratio over three is shown in yellow. Any value over these (orange, red) correspond to larger dose ratios and hence more likelihood of a good response to treatment. We can see that when using a single field, there is a small region close to the beam aperture where the dose ratio is high, but then most of the brain is left with low doses. That would be appropriate for small tumors located close to the scull. In the event of large tumors, or tumors located far from the scull in the inner part of the brain, a set of two fields could be used. The *bottom* panel shows such example, where more than half of the brain region can be accessed and deliver a large dose to a tumor located there, compared to the dose received in normal tissues located nearby the tumor, which would be left with doses in some cases lower by a factor of 6.

A realistic example of a cancer patient with a large tumor in the brain will be shown in the next Chapter, where the BSA designed and discussed here will be used, together with the previously obtained nuclear data.

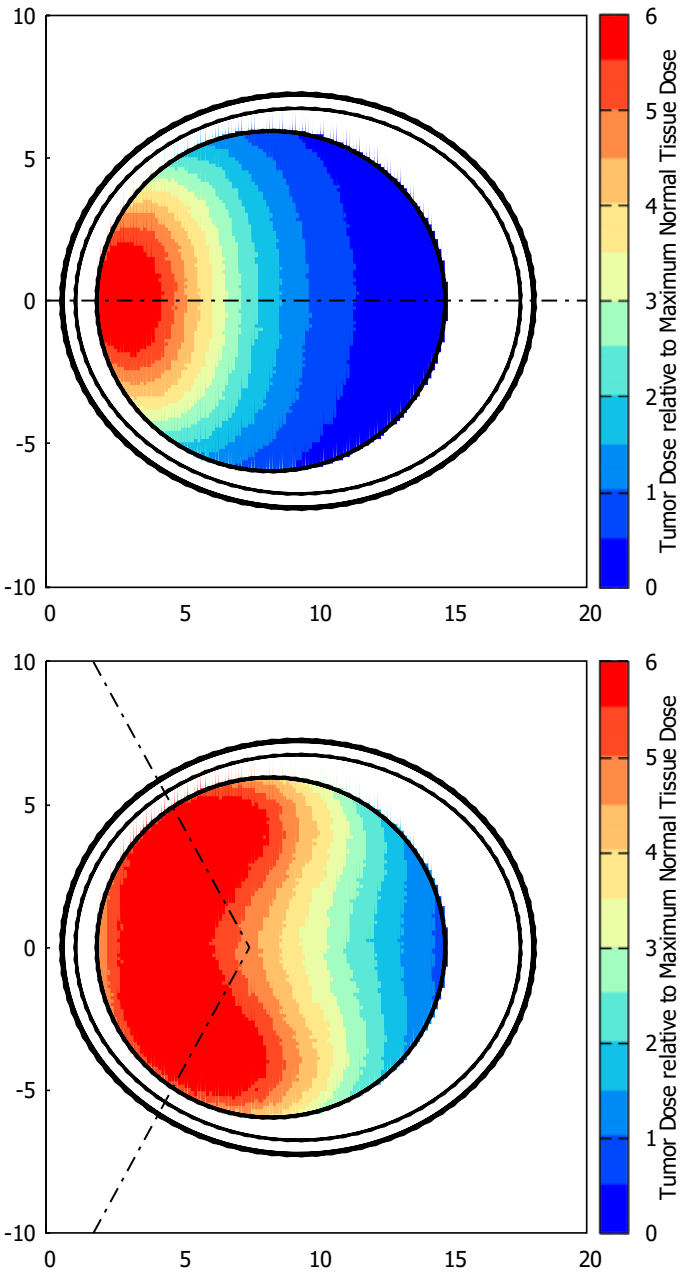

Figure 4.17: Examples of a one-field (*top* panel) and two-field (*bottom* panel) dose maps in the brain using the Snyder Model. The dose in the brain is shown relative to the maximum dose in normal tissue. The beam axis or axes are indicated with the dashed-dotted lines. The beam aperture is located 1 cm away from the skin surface of the model.

Chapter 5

Development of a BNCT Treatment Planning for a patient with Glioblastoma

Once the new nuclear data from the ^{14}N(n,p) reaction has been obtained and its relevance in BNCT dosimetry has been discussed, and also a new neutron beam has been designed, it is paramount to test it with realistic cases. To this aim, a Treatment Planning System (TPS) has been developed in order to simulate the BNCT treatment of a patient with Glioblastoma Multiforme.

The most important source of information for the treatment planning is the imaging data from the patient, where the images from the CT scan (and other data such as Magnetic Resonance Imaging, MRI) are stored. Moreover, valuable data such as the contours of all the Regions Of Interest (ROI) such as the Clinical Tumor Volume (CTV) and Planning Tumor Volume (PTV), and the Organs-At-Risk (OAR) are included in complementary files as the RT-Struct file.

From this data, a model of the patient has to be implemented into the neutron transport code, MCNP. A simulation of the dose deposited in each voxel region has to be run, considering the different tissues and their corresponding compositions and kerma factors. The new data from the $^{14}N(n,p)$ reaction obtained in Chapter 2 will be used for both the neutron transport in MCNP and the dose estimation via kerma factors, as described in Chapter 3. The beam obtained from the BSA designed in the previous Chapter 4 will be used. The beam orientation for the one or two neutron fields applied has to be determined and optimized for the particular patient and tumor position and extension.

In order to estimate the dose for the simulated treatment, a few assumptions had to be made, including the use of RBE data from the literature [17]. In addition, boron concentration data from a study of the boron uptake for the patient was not available, since a BNCT treatment was not performed. Thus the boron concentration was set as 18.5 ppm in normal tissues (other than tumor or skin), with a ratio of 3.5 for tumor and 1.5 for skin.

After this, the data from the simulations has to be analyzed in order to check the adequacy of the planned treatment. This can be assessed with the calculation of

Dose-Volume Histograms (DVH), average and maximum dose levels in OAR and with the help of plots of isodose contours or dose maps over medical images.

Figure 5.1 shows a scheme of the procedure used to design the treatment planning, including the main inputs (medical images of the patient and the neutron source) and additional input data as kerma factors, RBE and boron uptakes), the main results from the simulation and the loop for optimizing the beam orientations in order to achieve a final treatment planning.

The case of the patient used to present the treatment planning routines and the adequacy of the neutron beam off the BSA is a patient with GBM, with a large tumor in the frontal-right lobe of the brain. This tumor poses a challenge in treatment planning due to the closeness to key brain structures, as it partially surrounds the chiasma and is close to the optic nerves. The chiasma is the part of the brain where the optic nerves cross each other, and hence it is specially relevant for the vision. A harm to the chiasma can lead to blindness. With the use of Conventional Radiotherapy, it is difficult to design a treatment planning for this case that achieves a tumor control and at the same time leaves the chiasma undamaged, or at least to a dose that does not increase the risk of blindness. We would like to test if a BNCT treatment planning could improve this kind of situations.

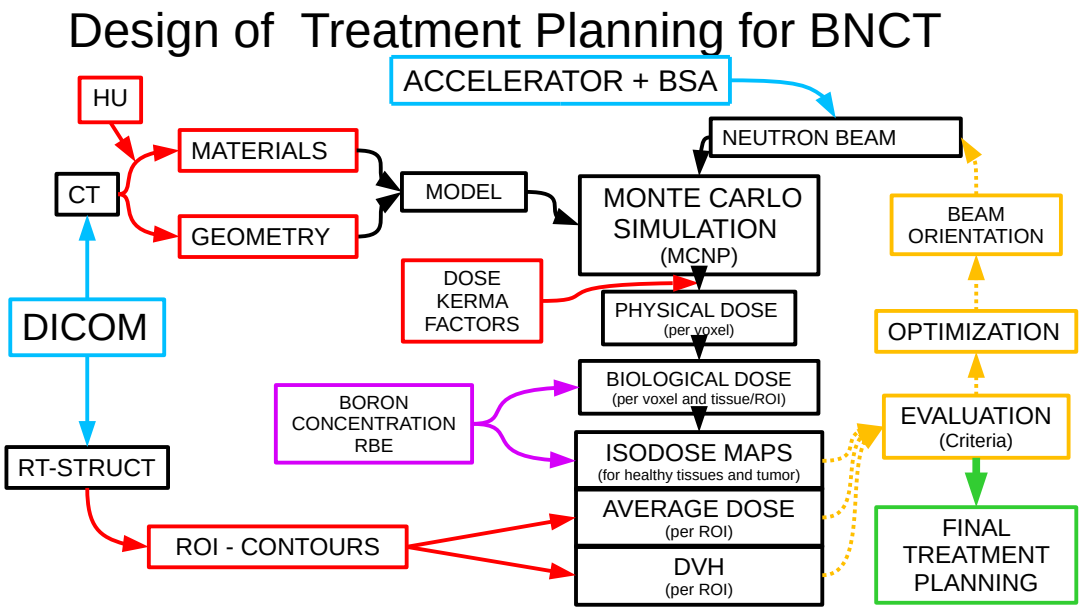

Figure 5.1: Scheme of the treatment planning used to simulate the BNCT treatment for a patient with GBM. The main input data, the simulation procedure and outputs from analysis are integrated, followed by a loop in order to optimize the beam orientation and define a final treatment planning.

5.1 Medical data: DICOM Files

DICOM (Data Imaging and Communications in Medicine) is the standard for the communication and management of medical imaging data, including CT scans, MRI and others. For our purposes, CT data contains information needed for the modelization of the patient. CT data is presented in a series of slices of pictures, where

all pictures have a defined pixel sizes. The pixel size and distance between slices define the voxel sizes and the spatial resolution of the data.

5.1.1 RT-Struct Files

In addition to images, some other auxiliary files are used in treatment plannings, including conventional RT-plan files which contain data on the parameters of the machines used to perform the treatment, RT-dose files, which contain the expected results of the treatment in terms of dose maps and DVH, and RT-struct files. These last files are specially useful for the BNCT treatment planning, since they include the contours of the tumor (CTV, PTV) and the OAR, as determined by the physicians. These data can be used, once integrated with the CT data, to check and separate different tissues that otherwise could be hard to separate from the actual information given in the CT. Figure 5.2 shows two slices of the CT scan with superimposed contours of the tumor (CTV in black and PTV in red) and OAR (for example, the chiasma in blue, the full brain in magenta and the eyes in green).

5.2 Patient Modelling

5.2.1 Material and Tissue Identification

CT data is given in the so-called Hounsfield Units (HU), which correspond to linear attenuation coefficients and can be related to electron densities of the tissues. HU are defined so that in the scale, 0 corresponds to the linear attenuation coefficient of water and -1000 corresponds to that of air. In order to perform a simulation of a BNCT treatment, where neutron transport is paramount, electron densities are not enough to achieve reliable results. To do so, the HU have to be matched with a corresponding tissue, thanks to scales that relate some HU ranges to different tissues. There are reference ranges for different tissues. For instance, bone tissues typically range above 300 HU and up to 1900 HU. Higher values are only found in CT scans in case of foreign bodies such as implants. Soft tissues have values around 0, with fat and adipose tissues ranging around -120 to -90 HU, and most other tissues presenting overlaps. For instance, brain tissues appear from +20 to +45 HU, and muscle tissue usually has +35 to +55 HU. That makes tissue assignment only based on HU unreliable. Figure 5.3, *left panel*, shows a slice of the CT where the material identification is based solely on HU values. Each color is related to a HU range as shown in the scale and all voxels with a value within a range is attributed the corresponding tissue. Some clearly distinguishable features are well separated as bone is told apart from others. Also the brain is well recognized as brain tissue and most of the muscles are also identified as muscle tissue. However, part of the muscular and other tissues are taken as brain, and more noticeably the eyeballs are identified also as brain. Another structures as the bed and the radiotherapy mask for patient immobilization, made of plastic materials, are assumed to be fat together with the mucosa tissues. This comports relevant distortions both in transport and in dose estimation. For this reason, the use of the RT-struct data allows to define the contours of some organs, specially those of most interest. In BNCT, tissues with a higher proportion of nitrogen or chlorine are suspect to receive larger doses and have to be analyzed in detail. For instance, the lens of the eye has a substantially higher

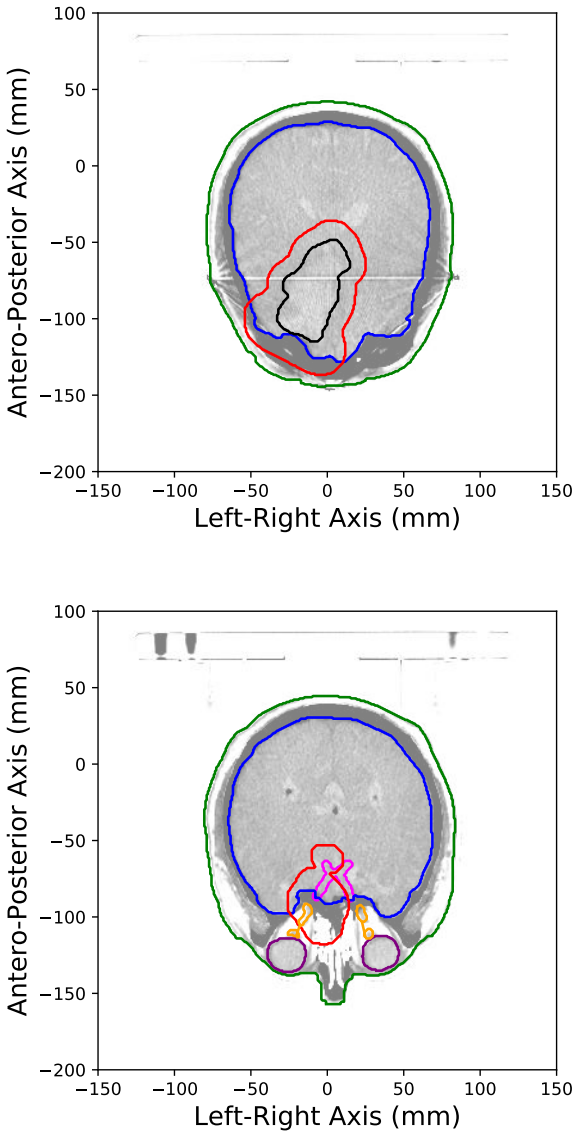

Figure 5.2: Two slices of the CT scan, with the contours of the CTV (black), PTV (red) and OARs are superimposed. These include the full brain (blue), the skin (green), the eyes (purple), the chiasma (magenta), and the optic nerves (orange). Other OARs are not shown as the the brainstem or the spinal cord as they appear at different positions in the vertical axis. The slices have been chosen to note the main location of the tumor (*left image*) and the fact that part of the PTV intersects the chiasma (*right image*). The horizontal and vertical axis and units are in mm, and correspond to the CT reference system.

nitrogen content, as does so the skin. The inclusion of those tissues as separate is key to a reliable treatment planning. Figure 5.3, *right panel*, shows a slice in the CT where the final material identification includes the contour data from the RT-struct files. Once all tissues of relevance in the medical images are determined, their corresponding kerma factors have to be computed.

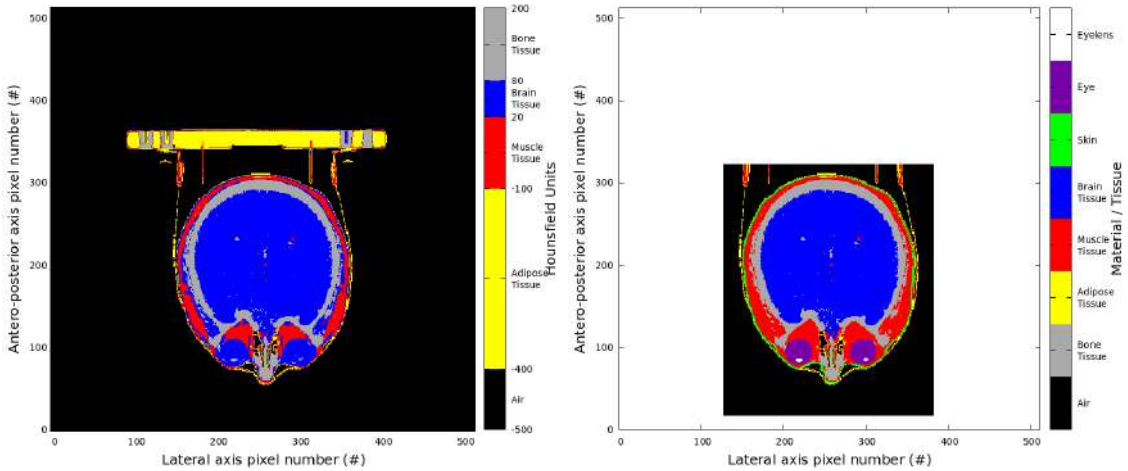

Figure 5.3: The *left* image shows a slice of the CT scan with tissue identification based only on HU. The tissues correspond to bone tissue (grey), adipose tissue (yellow), brain tissue (blue), muscle tissue (red), skin (green), the eyes (purple) and the eyelenses (white). Lower HU are considered as air (shown in black). The *right* image shows the final material identification with seven tissues. Non-tissue materials as the plastic mask for immobilization and the bed are identified as adipose tissues (discarded afterwards). The *right* image shows the tissue identification after contour data from the RT-struct DICOM file is included. Color code is the same. Also the geometry model has been cropped to the edges to reduce the amount of data.

One relevant aspect in the feasibility of the treatment planning is the simulation needs in terms of disk space, RAM and computing time. Since the patient data is voxelized, a large amount of information is entered to the simulation code (MCNP), and then a dose has to be computed for each of those voxels. In order to reduce the amount of data needed to construct the model and run the simulations, the CT geometry is cropped in the three axis in order to remove all excess of only-air-filled voxels, which do not add any extra information but strongly increase the voxel-data to be stored. Figure 5.3 shows the transition from the un-cropped CT-based data in the *left* image and the cropped data in the *right* image. This cropping procedure has to be done carefully in order to avoid leaving any relevant part of the geometry (e.g. part of the nose or ears that protrude from the main bulk of the head). In addition to this, in order to compute doses in BNCT treatments, four different dose components (thermal and fast neutron, gamma and boron doses) and hence tallies have to be computed and saved. This makes the simulation run slow and generates a vast amount of temporary data which can easily overload the memory of the computer. In order to avoid such problems, dedicated simulations have to be run for each tissue, where only the tallies corresponding to that tissue are calculated at each time (the full model of the head of the patient was simulated in all cases, but only one tissue was tallied at once). The downside of this strategy is that the same neutron transport simulation has to be run several times in order to retrieve the relevant data from each tissue. This limits the amount of possible tissues that can be simulated within a reasonable computing time. In this case, for a patient with GBM with a tumor inside the brain, the full head was simulated, and the

tissues used were in the following list: bone tissue, muscle tissue, fat, brain tissue, skin, eye and the lens of the eye. All other tissues were redirected to the closest tissue by composition. For example, the complete encephallus, including the brain, brainstem, cerebellum and other structures including, for instance, the chiasma and the optic nerves, were considered as brain tissue. Another case is that all bones in the skull, cartilages and teeth were considered as bone tissue.

5.2.2 MCNP Input

In order to construct the model of the patient in MCNP, including the voxelized data from the DICOM files, the special features of `universes` and `lattices` have to be applied. A large lattice of parallelepipeds is arranged and filled with several different `universes`, each of them containing a specific material composition, thus defining regions in space. Furthermore, the tallies, weighted with the corresponding kerma factors, are defined to compute dose in their corresponding cell (filled with the universe of its kind, where that means that a single cell contains all the voxels in the lattice filled with its universe). The neutron beam (including out-of-field leakages and gamma contamination) is included in the simulation via the `SSW/SSR` special type of source (surface source write/read) from MCNP, and oriented and located accordingly to the case by means of transformations (`TR`). Figure 5.4 shows the implementation of the model as seen from the MCNP plotter, where each material (and cell and universe) correspond to a different color. An example of such input files (corresponding to the one that tallies the brain tissues) is shown in the Appendix B.

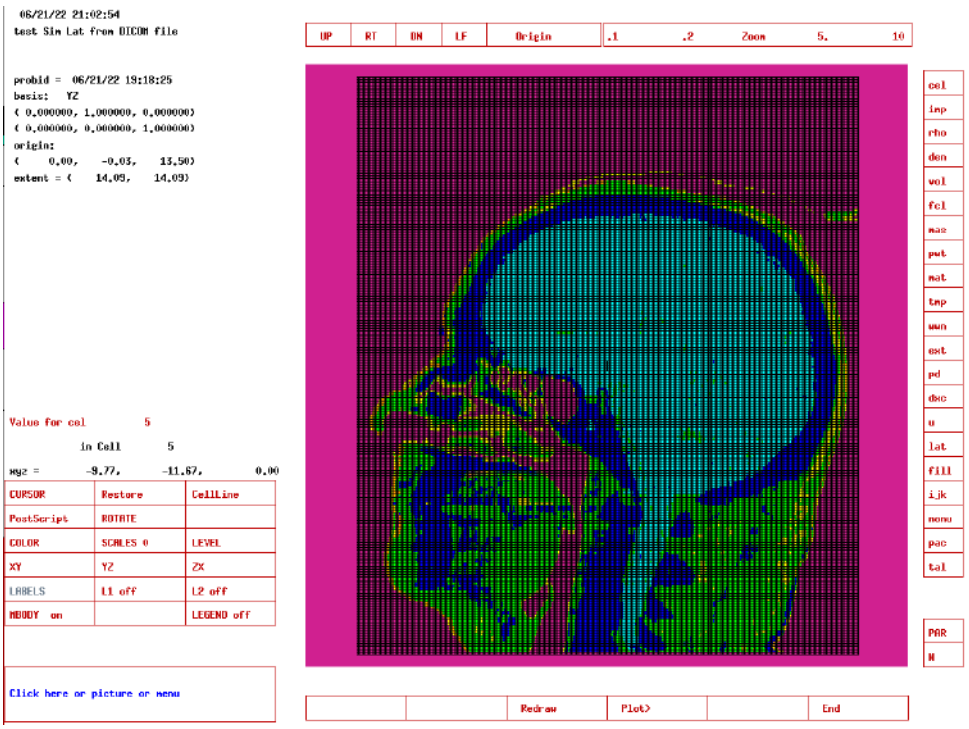

Figure 5.4: Plot from the MCNP viewer that shows the model of the patient as reconstructed with using the MCNP `lattice` (black lines that conform the grid). The plot uses the MCNP palette relating colors to materials: air (magenta), muscle tissue (green), adipose tissue (yellow), skin (orange), brain tissue (cyan) and bone tissue (dark blue).

5.2.3 Beam Definition and orientation

As it was already mentioned in the previous section, the neutron beam was introduced to the MCNP code via the `SSW/SSR` cards. Furthermore, the beam positioning and orientation were defined in a separate script that took into account the position of the tumor iso-center. The iso-center is defined as the point towards the beams converge, and it is usually located around the center of the tumor. In this case the tumor was spread in a large region of the craneal cavity, from near the skull to the center of the brain. For this reason, and in order to enhance the effect of using two neutron fields (two consecutive irradiations with a different patient positioning), the iso-center was moved towards the center of the brain in the aim of increasing the overall dose homogeneity due to the limited penetrability of neutrons. In order to define the beam positioning, the beam axis vector and the distance of the beam aperture to the iso-center were used as input. Manual checks were performed to verify that the position of the beams was correct and to avoid the BSA aperture plane to move away or to enter inside the patient model. The distance to the iso-center was fixed so that the BSA aperture plane was tangent to the skin of the patient. The beam axis pointed in all cases towards the iso-center.

A few tests with one-field and two-field irradiations were simulated following the described procedure. No clinical expertise was followed in the beam configuration, but two general guidelines were followed in order to choose from the results, namely to minimize the dose spread in the CTV (to avoid infra- and over-dosification of the tumor), and to minimize the dose in the OAR with respect to the tumor, by avoiding beam directions that passed through OAR in order to reach the tumor (e.g. the eyes). However, a dedicated optimization in order to find the best possible orientation and positioning of the neutron beam/s has not been made. In order to do so, a careful determination of the dependencies of the dose spread and dose limitations for the OAR shall be defined and input to a multi-criteria beam optimization procedure would have to be followed [120].

Figure 5.5 shows the final choice for the two-field configuration. Both fields contribute equally to the treatment, in that the irradiation time from both of the is half of the irradiation time. Both beam axes are tilted 30° with respect to the horizontal plane, from top to bottom. The first beam axis (violet in the Figure) points 15° to the front with respect to the left-right direction, reaching the patient around the right temporal bone, above and below the right ear. The second beam axis (purple in the figure) points 30° left with respect to the antero-posterior direction, reaching the patient at the forehead above the right eye. This beam configuration has been used for all results and discussions hereafter.

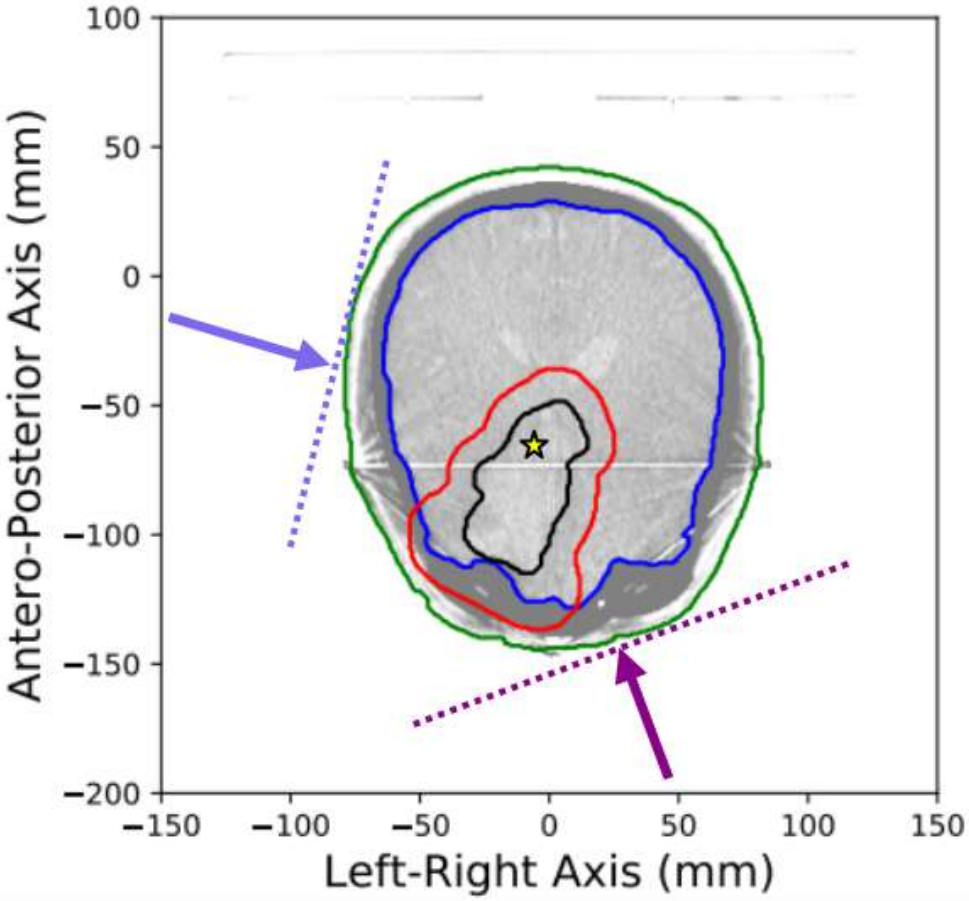

Figure 5.5: Slice of the CT with the contours of skin (green), brain (blue), CTV (black) and PTV (red), where the orientation and positioning of the two beams is indicated. Both beams contribute equally in terms of irradiation time. The location of the iso-center, where the beams point to, is indicated with the yellow star. The two beam axes correspond to the violet and purple arrows. The location of the plane containing the beam aperture is shown with the dotted-lines.

5.3 Data Analysis

Once the neutron transport simulations with the physical dose computations are performed, the data has to be processed and integrated onto a final dose estimation at each position. Total dose in each voxel is computed as:

$$D_T = w_{th} D_{th} + w_f D_f + w_B \chi_B D_B + D_\gamma \tag{5.1}$$

where w_i are the corresponding RBE factors to convert from physical dose to biologically equivalent dose. The values for the coefficients are taken from the common use in the literature [17]. Boron concentration varies from one tissue to another, and has been assumed as 18 ppm in normal tissues (all except tumor and skin), with a tumor to normal tissue boron concentration ratio of 3.5 and skin to normal tissue boron concentration ratio of 1.5.

From the 3D dose distribution, the dose maps corresponding to tumor and all other tissues can be obtained and superimposed to the CT scan data, showcasing color maps or isodose curves. Moreover, by means of analysis techiques, the dose data in the voxels included in the contours of the tumor or the OARs can be used to compute DVH and analyze the adecuacy of the beam.

The DVH are representations of the dose distribution within the volume of a ROI, and normalized to the total volume of the ROI. The DVH show the cumulative dose distribution, in a way that, for each dose value in the horizontal axis, the total volume that has received at least that amount of dose is marked. For a fully homogeneous dose distribution within the ROI of interest, the DVH would look as a step function, *i.e.* at 100 % volume below the prescribed dose, and a sharp cut-off at the prescribed dose. The DVH provide relevant information on the dose distribution, namely minimum, median and maximum doses within each ROI (the 0^{th}, 50^{th} and 100^{th} percentiles), but also many criteria on the dose restrictions for the OARs are defined in a way that DVH provide the information on whether the limits are exceeded or not. These criteria are not thoroughly studied and standardized for BNCT, and usually they have to be extrapolated from other kinds of radiotherapy, according to similarities considering mainly the duration of the treatment and the number of fractions. In this case, single-session Stereotactical Radio Surgery (SRS) provides a close-enough reference from which to define tentative dose limits for the OARs. From there we can reproduce the recommendations by the Quantitative Analyses of Normal Tissue Effects in the Clinic (QUANTEC) [121] for the brain and the specific case of the chiasma. For the chiasma, the recommendations define that the maximum dose should not exceed 10-12 Gy in any part of the OAR [122]. For the full brain, the QUANTEC criterion is that no more than 5-10 cm^3 of the volume of the healthy brain should be exposed to more than 12 Gy [123]. Considering a full brain volume of 1145 cm^3, less than 0.87 % of the volume of the brain should receive more than 12 Gy. In order to define treatment times, each clinical trial has proposed various criteria. For example, the last clinical trials from the first Accelerator-based BNCT facilities in Japan have defined two criteria, one for head and neck cancer and other for glioblastoma. For head and neck cancer, the irradiation time was set so that the maximum dose received by the mucosa is 12 Gy-eq [47]. For GBM, the maximum dose at the scalp was 8.5 Gy-eq [48]. The successful Clinical Trials from the FiR-1 Reactor in Finland, to which we will compare, defined a double criterion: the maximum dose for a 1 cm^3 volume in the brain should be 8 Gy-eq, and also the average dose of the full brain shall not exceed 6 Gy-eq [53]. Since we will make a comparison with FiR-1, we will use this criterion in order to define the dose and irradiation time for the BNCT treatment.

5.3.1 Simulation Run Time

In order to run reliable simulations, statistical sources of uncertainty have to be reduced at least to a point where they do not contribute substantially to the widening of the dose distribution. To do so, the `SSR/SSW` source file has to include as many primaries as possible. Two problems arise when increasing the number of primaries and hence the size of this source file. First, the production of the `SSW` file from the simulation of the neutron transport through the BSA is time consuming and the `SSW` file that is generated has at least 1 GB in order to fit minimum requirements of

sampling of the phase space. Fortunately, the production of this file has to be made only once and then it can be used for whichever purpose related to the BSA beam. The second problem is more challenging. When the size of the `SSW->SSR` file grows, the duration of the simulations that use it increases accordingly. This manifests as a major problem given that each transport simulation has to be run several times to account for all tissues of interest (as described before), but also since this procedure needs to be repeated with different beam configurations in order to optimize the beam (or beams) orientation and positioning respect to the patient.

For this reason, and in order to check the minimum amount of primaries needed to run the treatment planning simulation without artificially increasing the widths of the dose distributions of the tumor and OARs, a detailed analysis was carried out. To do so, the dose distribution for the case of the CTV of the analyzed patient with GBM was estimated using the 15.87^{th} and 84.13^{th} volume percentiles in the DVH, which correspond to $\pm\sigma$ in a fitting Gaussian distribution. The CTV was used as the volume of interest for this calculation since it is the most relevant volume and the OARs that could receive a larger dose would typically be found close to the CTV. Under these circumstances, there is a "real" or intrinsic width of the distribution caused by the CTV size and the underlying dose variation at different locations related to the beam positioning and orientation, and also an increase of the width of the distribution due to statistical artifacts. This increase in the overall variance can be described following the equation:

$$\sigma_T^2 = \sigma_I^2 + \sigma_{stat}^2 \tag{5.2}$$

that is, the total variance of the dose distribution in the CTV, σ_T^2, can be attributed to the intrinsic variance of the dose distribution, σ_I^2, plus a term created by under-sampling of the neutron source, σ_{stat}^2. That second term depends on the number of histories run in the simulations ($\sigma_{stat} = \sigma_0/\sqrt{N}$), and hence can be reduced to a point where it is no longer relevant to the total variance. By running a set of simulations with different number of primaries, the σ_I and σ_0 parameters can be determined and so the number of primaries N needed for a reliable simulation can be fixed. This effect can clearly be observed in Figure 5.6, *left* image, where the DVH of the CTV is displayed for one configuration of the beam (two fields of equal duration positioned at relatively suitable beam orientation compromise, though not a deliberate optimization of the orientation has been carried out). A set of simulations with different number of primaries show that if the initial beam is under-sampled (*reddish* colors in the Figure), the DVH spreads artificially and provides a wrong picture of the planned treatment. As the number of primaries increase, the corresponding statistical variance due to the sampling is reduced and hence the DVH approaches the real treatment planning (*greenish* colors in the Figure).

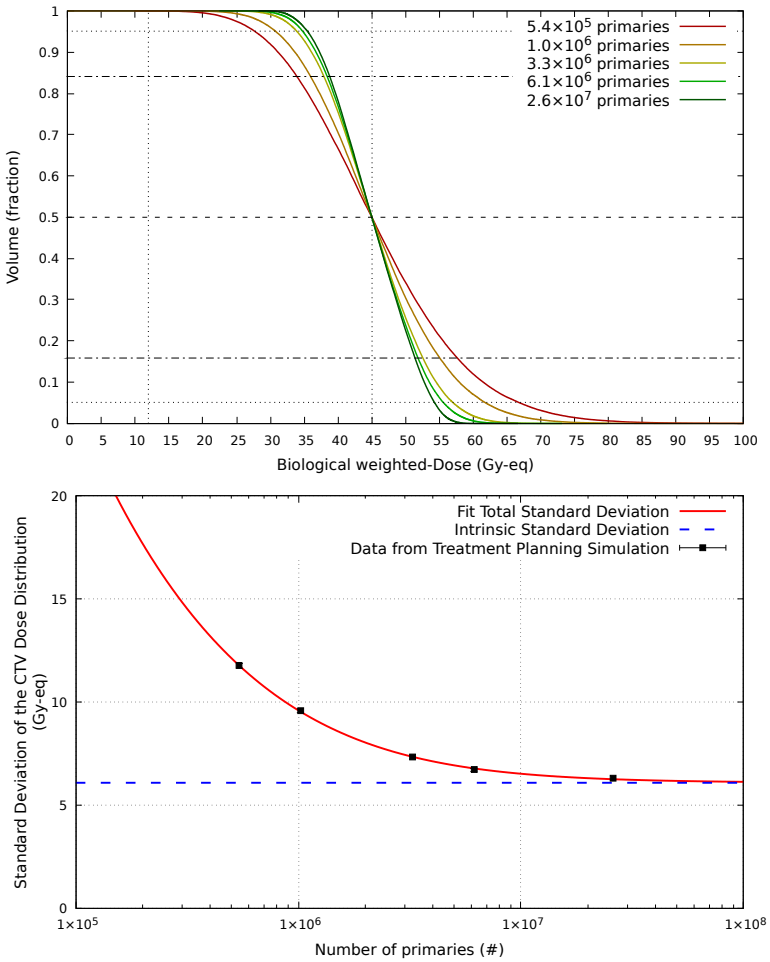

Figure 5.6: Example of the influence of the statistical uncertainty in the simulations. The *left* image shows the DVH of the CTV for five separate cases varying the number of primaries from $5.4{\cdot}10^5$ primaries (red) to $2.6{\cdot}10^7$ primaries (dark green). The horizontal lines indicate the 5^{th} and 95^{th} percentiles (dotted lines), the 15.87^{th} and 84.13^{th} percentiles ($\pm\sigma$, dash-dotted lines) and the median (dashed line). The vertical lines indicate 12 Gy-eq (typical value for maximum dose at OARs) and 45 Gy-eq (typical median dose at CTV). The duration of the treatment has been set so that the median dose at CTV is 45 Gy-eq. The *right* image shows the variation of the total standard deviation of the CTV dose distribution as a function of the number of primaries in the simulation. The red line correspond to the fit of the data points using equation 5.2, and the blue dashed line indicates the intrinsic standard deviation of the dose distribution.

Figure 5.6, *right* image, shows the results of this analysis. The standard deviation of the CTV dose distribution, estimated as half of the dose-distance between the $\pm\sigma$ percentiles, is shown as a function of the number of primaries, and fit to Equation 5.2. The intrinsic standard deviation can be obtained from the fit of data. The minimum number of primaries needed so that the statistical contribution is less than 5 % of the total standard deviation is of the order of $1.4{\cdot}10^7$ primaries recorded on the `SSW` source, which means around 26 h for creating the `SSW/SSR` file (1.34 GB) and 8.6 h to run the treatment planning simulations.[1]

[1]All simulations were performed in a computer with the following technical specifications: intel®Core™ i7-4770 CPU @ 3.4GHz x8 and 16 GB of RAM.

5.4 Results: The simulation of a GBM case

The development of a TPS allows to examine in more detail the real features of a beam designed for BNCT treatments, compared to Conventional Radiotherapy (CRT) and the BNCT beams that have produced promising clinical outcomes in the past, using reactors. We will present here the results of a Treatment Plan for the patient with GBM described along this chapter. The dose deposition distribution inside the patient will be shown using dose maps. The DVH will provide the quantitative results and will facilitate an easier identification of the improvement in the patient's treatment by using BNCT. We will compare to the Conventional RT Plan that the patient would receive at the hospital. We will also compare with the outcomes that would result from substituting the beam designed in this thesis by the neutron beam of the FiR-1 reactor in Finland.

5.4.1 Dose Map and DVH using BSA-UGR

The Dose distribution can be interpreted easily with the help of dose maps. These dose maps correspond to the actual dose prescribed for the treatment via simulations, and can be shown as slices corresponding to the CT scan, where also the contours of OAR and tumor can be displayed for a more straightforward interpretation. Figures 5.7 and 5.8 show four of such dose maps, corresponding to some slices that better represent the condition of the patient. Total dose in tumor is displayed inside the CTV, and total dose in normal tissues is displayed elsewhere, including the portion of the PTV outside the CTV. The *top-left* image corresponds to a slice through the eyes and the chiasma, which is penetrated by the PTV (though not the CTV). The rest of the images contain a portion of the tumor (CTV) where a large dose is delivered due to the high boron concentration assumed inside the tumor. The boundary between the tumor and the normal tissues is sharp in the absence of an estimate of boron distribution inside the patient. The dose in normal tissues is kept below a minimum of 10 Gy-eq through all the tissues, and a large fraction of the head receives less than 5 Gy-eq. Only the regions surrounding the tumor, where the neutron beams impinge onto and moderate until reaching the CTV, receive a larger dose, which is in any case kept below safe margins. The tumor dose is reasonably homogeneous, though the most deep regions of the tumor receive less dose, due to the limited penetration of neutrons to around 10 cm from the surface.

Together with dose maps, DVH provide the detailed view of the treatment plan under analysis, and allow to determine the constraints, pluses and limitations. The most important aspect is the determination of the duration of the treatment. Using the criteria from FiR-1, the average dose in brain shall not exceed 6 Gy-eq, and also at maximum 1 cm^3 of the brain shall receive 8 Gy-eq (asumming a male brain of 1260 cm^3 this accounts to 0.079 % of the brain volume).

In our case, the most limiting factor is the maximum dose for a 1 cm^3 of the brain, and this allows to scale properly the horizontal axis of the DVH, and also to calculate the duration of the treatment. The total duration of the treatment with the two-equal-time field irradiations with the BSA-UGR beam is 47.39 min (23.695 min each field). This duration for the treatment is adequate and within the recommendations, below one hour. Furthermore, both irradiations could be performed sequentially,

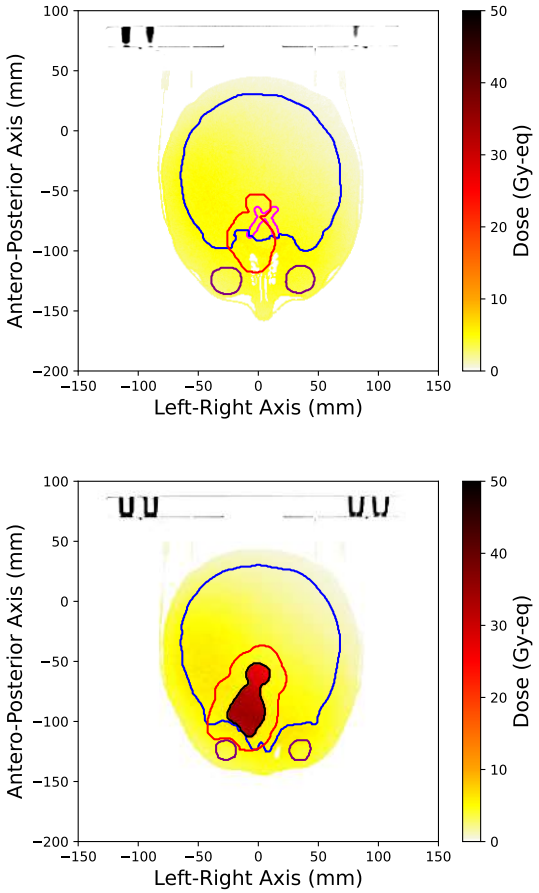

Figure 5.7: Two slices of the central part of the head showing the dose distribution obtained by the simulation of the Treatment Plan for the patient with GBM. The contour of the brain is shown in blue, eyes in purple, chiasma in magenta, PTV in red and CTV in black.

leaving some time in between for the patient re-orientation.

Using this information, we can now construct the normalized DVH, as shown in Figure 5.9. The *top panel* shows the full DVH for the CTV, PTV and OAR, while the *bottom panel* does for the detail the OAR, in the range below 10 Gy-eq. It can clearly be observed from these plots that the tumor receives a much larger dose than the normal tissues in the OAR, which are safely protected below the margins. All normal tissues fall below the overall tissue-independent limit of 12 Gy-eq, and all tissues receive less than 5 Gy-eq of median dose. Specially relevant is the dose in the chiasma (magenta) due to its relative closeness to the tumor. The skin (green) receives large differences of dose depending on its location, being higher near the position of the beam incidence and much lower in parts of the head far from these points. Other relevant tissues as the brainstem and the spine do not receive large doses due to their relative far location with respect to the tumor. Concerning the tumor, in BNCT it its considered that 30 Gy-eq in a single session is enough to completely destroy the tumor. This treatment achieves a 30 Gy-eq dose for more than 90 % of the CTV, and the rest receives at least 25 Gy-eq. The dose at PTV is computed here as if it was filled with tumor content, though the medical images do

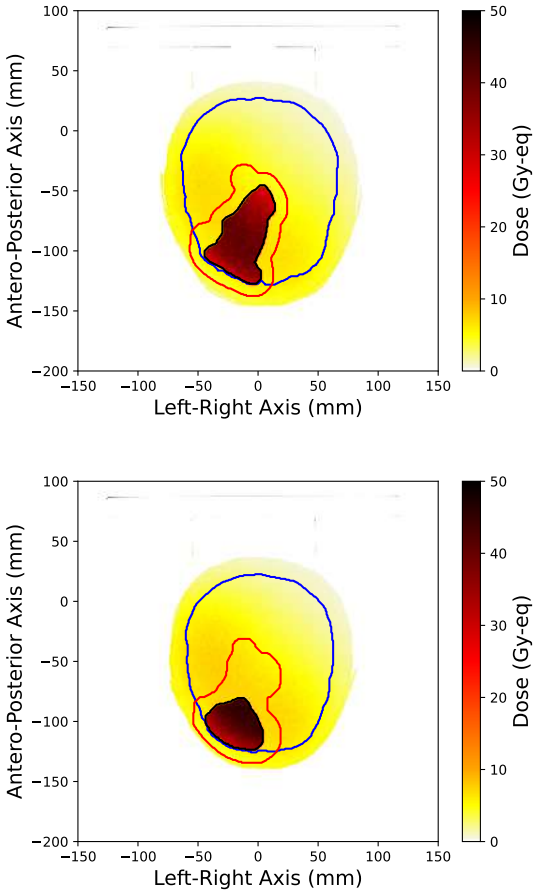

Figure 5.8: Two slices of the top part of the head showing the dose distribution obtained by the simulation of the Treatment Plan for the patient with GBM. The contour color code is the same as in the previous Figure.

not reveal that. This is done so that any possible non-visible extension or infiltration of the tumor outside the CTV can be analyzed as tumor-like.

One facet that can be analyzed using the DVH is the homogeneity of the dose deposition through the head. One of the main concerns is to try to minimize the spread in dose in the tissues, specially in the tumor, in order to avoid infra- and over-dosed regions. This spread depends mainly on two factors, the size of the ROI and the homogeneity of the neutron field determined by both the neutron difusion and the beam orientation. For small ROI, of the size or smaller than the typical mean-free-path of neutrons in the head, the dose is mostly homogeneous, and the DVH shows a moderately sharp cut-off, as in the chiasma, eyes or the optic nerves. In large ROI, such as the tumor, the full brain or the skin, the beam orientation plays a more determinant role. That was the main reason for using a two-field irradiation with two fields entering the head in lateral sides with respect to the tumor location, in the aim of enlarging the plateau region of large dose deposition around the tumor.

It is also noteworthy to remind that the treatment plan described here is not optimized *stricto sensu* in what regards the beam orientation and positioning, which means that this case could find a better outcome if this optimization was carried out. However, few general matters were considered in order to present a realistic

case not far from the optimal.

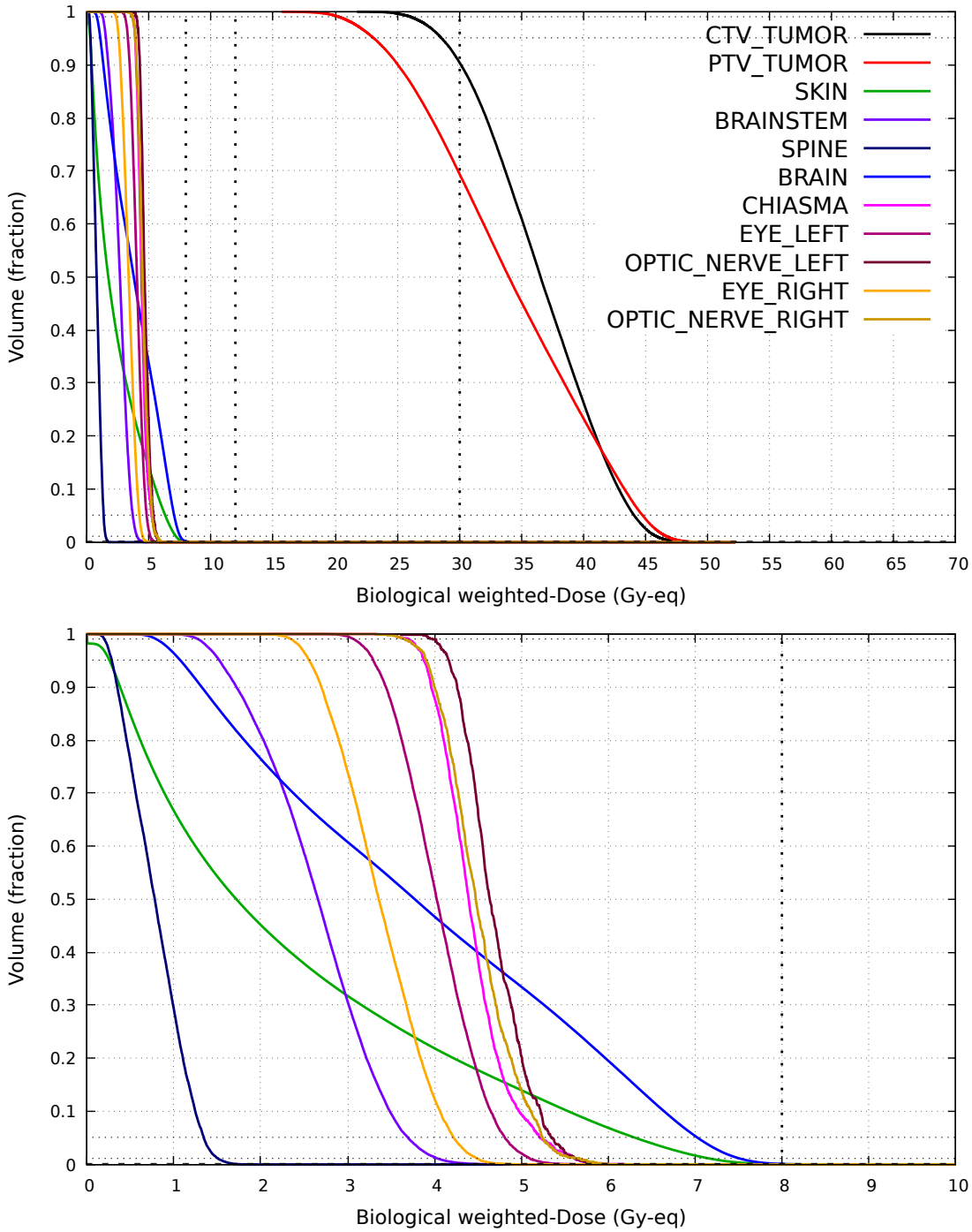

Figure 5.9: Dose-Volume Histograms of the OAR, PTV and CTV of the patient with GBM, for the BNCT Treatment Plan using the BSA-UGR neutron beam. The *top panel* corresponds to the complete DVH including CTV, PTV and all the OAR of interest, as indicated in the key. The *bottom panel* shows the detail in the range 0-10 Gy-eq to better showcase the dose in the OAR. The color code for the *top* and *bottom panels* is the same.

5.4.2 Comparison with Conventional Radiotherapy

A direct comparison between a BNCT treatment plan and the conventional RT plan is not straightforward.

First of all, conventional RT is a standard in medical treatments, and all parameters and inputs to the simulation of the treatment are much more precisely determined than the case of BNCT, which is an experimental form of radiotherapy for which clinical output is scarce in comparison. Moreover, several assumptions have to be considered in the BNCT plan, as the case patient did not actually receive a BNCT treatment and therefore some patient-specific data such as the boron uptake and boron distribution in- and around the tumor region are not known.

Secondly, the units in BNCT and conventional RT are not the same, as conventional RT uses Gy, while BNCT uses Gy-eq, that has been shown not to be directly comparable. There have been some studies developing an approach to the same unit system, including the photon iso-effective dose models for BNCT. However, in the BNCT research field, Gy-eq units are still used and all Clinical Trials reports its outcome that way.

Third, the conventional RT plan consists of several (around 30) short sessions spanning over few weeks, while BNCT performs the treatment in a single session. This leads to a fundamental difference, as in conventional RT, the tissues are able to recover from one fraction to the next. This is specially the case due to the use of low LET radiation as photons. In BNCT, the use of high LET radiation makes this effect less relevant. For this reason, a single session with high LET radiation to a dose of 30 Gy-eq can lead to similar results as a 60 Gy with low LET radiation.

Even with such relevant differences, still a semi-quantitative comparison can be assessed. Figure 5.10 shows both the DVH for the BNCT treatment plan (*top panel)* and the conventional RT treatment plan (*bottom panel*). Notably, the dose received in the OAR in a BNCT treatment is much lower with respect to the tumor dose, when compared to conventional RT, where most of the OAR receive large doses in a significant fraction of the volume. Consider for instance the skin and the brain, where over 10 % and 20 % of the volume receive more than 40 Gy and therefore the normal tissue death is likely guaranteed in these regions. The most palpable case of such plan is the dose in the chiasma (magenta in the Figure), where all of the volume receives at least 45 Gy. The medical physicists that realized and executed the conventional RT plan pointed out that this would increase the risk of damaging the chiasma, with the subsequent danger of leaving the patient blind. In the event of a BNCT treatment, that would not be an outcome, given the low dose received by the chiasma, in all cases below the safe margin criteria. In contrast, the use of several dose fractions allows a very precise conformation of the beams to deliver an homogeneous dose inside the CTV, where 95 % of it receives between 60 and 65 Gy, and 5 % receives 55 to 60 Gy. A one- or two-field BNCT treatment can not achieve such homogeneity inside the CTV. Even if the BNCT treatment were split in several sessions to conform many fields, the nature of neutron transport would lead to a expansive and softly varying neutron field where the dose does not find sharp variations within the patient. In contraposition with conventional RT (and other forms of particle therapy as proton therapy or heavy-ion therapy), the dose differences between tumor a normal tissues does not rely primarily on the beam

orientation, positioning and conformation, but rather on the selective boron uptake in the tumor compared to normal tissues.

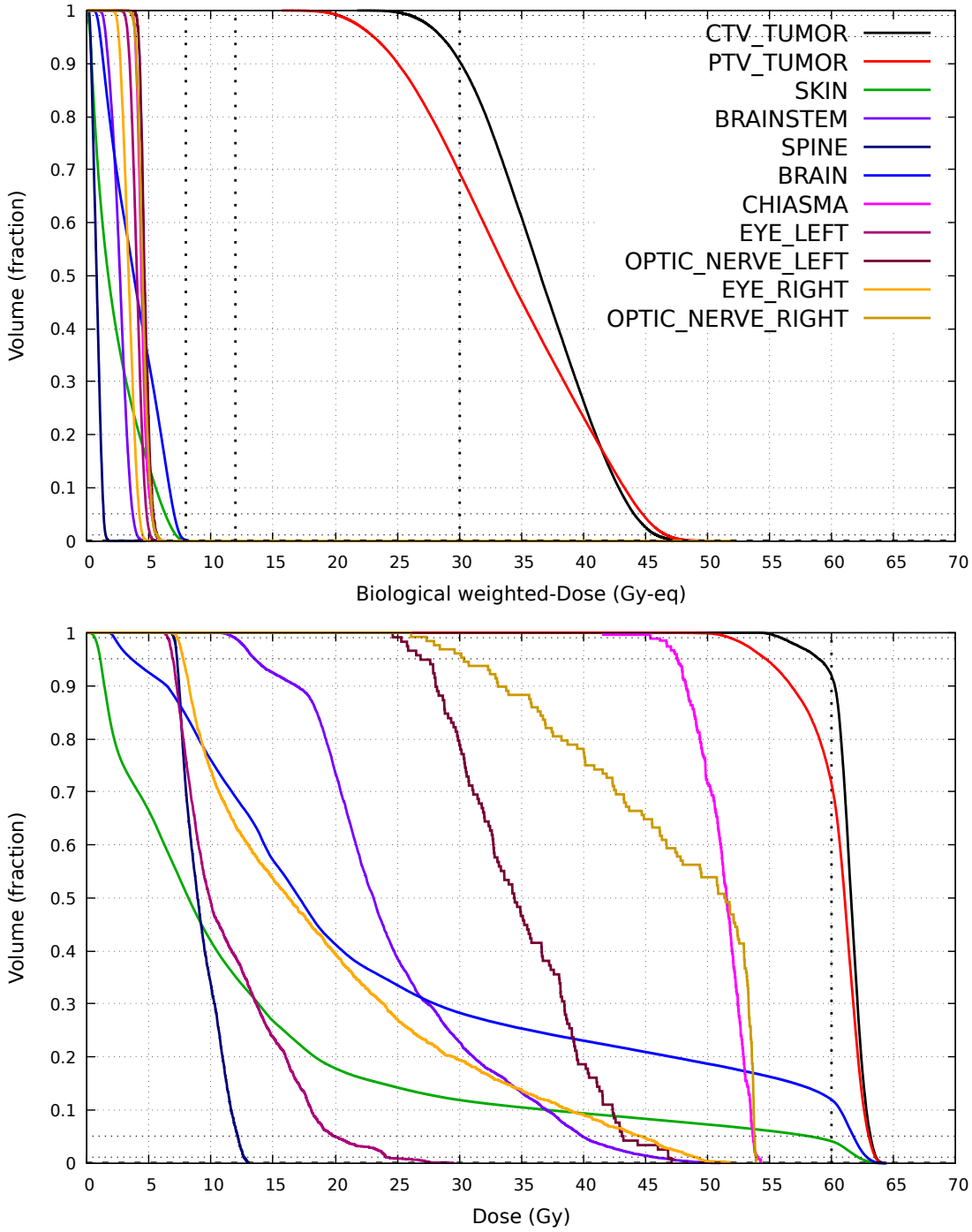

Figure 5.10: Dose-Volume Histograms of the OAR, PTV and CTV of the patient with GBM, for the BNCT Treatment Plan using the BSA-UGR neutron beam (*top panel*) and the actual Treatment Plan administered to the patient, using CRT (*bottom panel*). Note the different units in the horizontal axes, in Gy-eq for the BNCT treatment and Gy in the conventional RT treatment. The color code for the *top* and *bottom panels* is the same.

5.4.3 Comparison with the Neutron Beam from the FiR-1 Reactor

The comparison with the FiR-1 neutron beam is much more direct, since the characteristics of the therapy are the same, including the same units and RBE factors. Also the boron uptake and T/N ratio have been chosen to be the same values, as indicated in the clinical trials that used the FiR-1 reactor [53]. The simulations and data analysis of the treatment with each neutron beam have been identical, including the orientation and positioning of the beam. The only exception is the `SSW/SSR` source containing the specific sampling of each neutron beam, for obvious reasons.

The duration of the treatment is fixed in both cases following the criteria from FiR-1 on the maximum dose of 8 Gy-eq in 1 cm^3 in the brain, as the dose distribution is fairly similar in both cases. Due to the similar beam intensities, the duration of the treatment with FiR-1, estimated to be 44.20 min (22.10 min each field) is very similar to BSA-UGR (47.39 min total). The choice of this criterion determines the total dose deposition, which is key to the comparison that follows.

Figure 5.11 shows the comparison between the treatment of the patient with GBM using the BSA-UGR beam (solid lines) and the FiR-1 beam (dashed lines). The *top panel* shows the DVH for the CTV, PTV and OAR in full scale, with the *bottom panel* showing the detail of the DVH of the OAR. The dose distribution delivered by BSA-UGR is slightly more homogeneous than the one coming from FiR-1. This is mainly due to the lack of high energy neutrons in the beam from BSA-UGR compared to the large tail of the reactor beam from FiR-1, and also to the flatter neutron distribution of BSA-UGR. This leads to main aspects being slightly different in the Treatment Plan here shown by the DVH:

- The dose at PTV, and specially at CTV is more homogeneous in the BSA-UGR plan compared to FiR-1, as seen from the *top panel* of Figure 5.11. This can be noted in the higher shoulder of the dose in CTV by BSA-UGR. This is specially relevant considering that 30 Gy-eq is considered as the dose needed for tumor remission. The simulated plan for FiR-1 delivers 30 Gy-eq to 82 % of the CTV, while this number hovers over 92 % of the CTV in the BSA-UGR plan, leading to a possibly better tumor control. A second aspect of the homogeneity in dose deposition is that the maximum dose delivered to the tumor is similar or smaller in the BSA-UGR plan, which is aimed by physicians to avoid overkill and the negative effects of that in the surrounding normal tissues.

- The dose at OARs is similar in both cases and kept below the safe limits, which is one of the main objectives of the planning, together with tumor control and remission. As a side effect of the more homogeneous beam delivered by BSA-UGR, the dose distribution at OARs is slightly larger in some cases, specially in tissues farther from the target area, as the brainstem and the spine. Nevertheless, these tissues receive very low doses mostly below 3 Gy-eq and 1 Gy-eq respectively, and the dose differences between plans is always smaller than 0.5 Gy. Considering OAR close to the target area, the eyes, optic nerves and the chiasma receive a very similar dose, being slightly smaller in the left optic nerve for the BSA-UGR plan and the opposite in the rest.

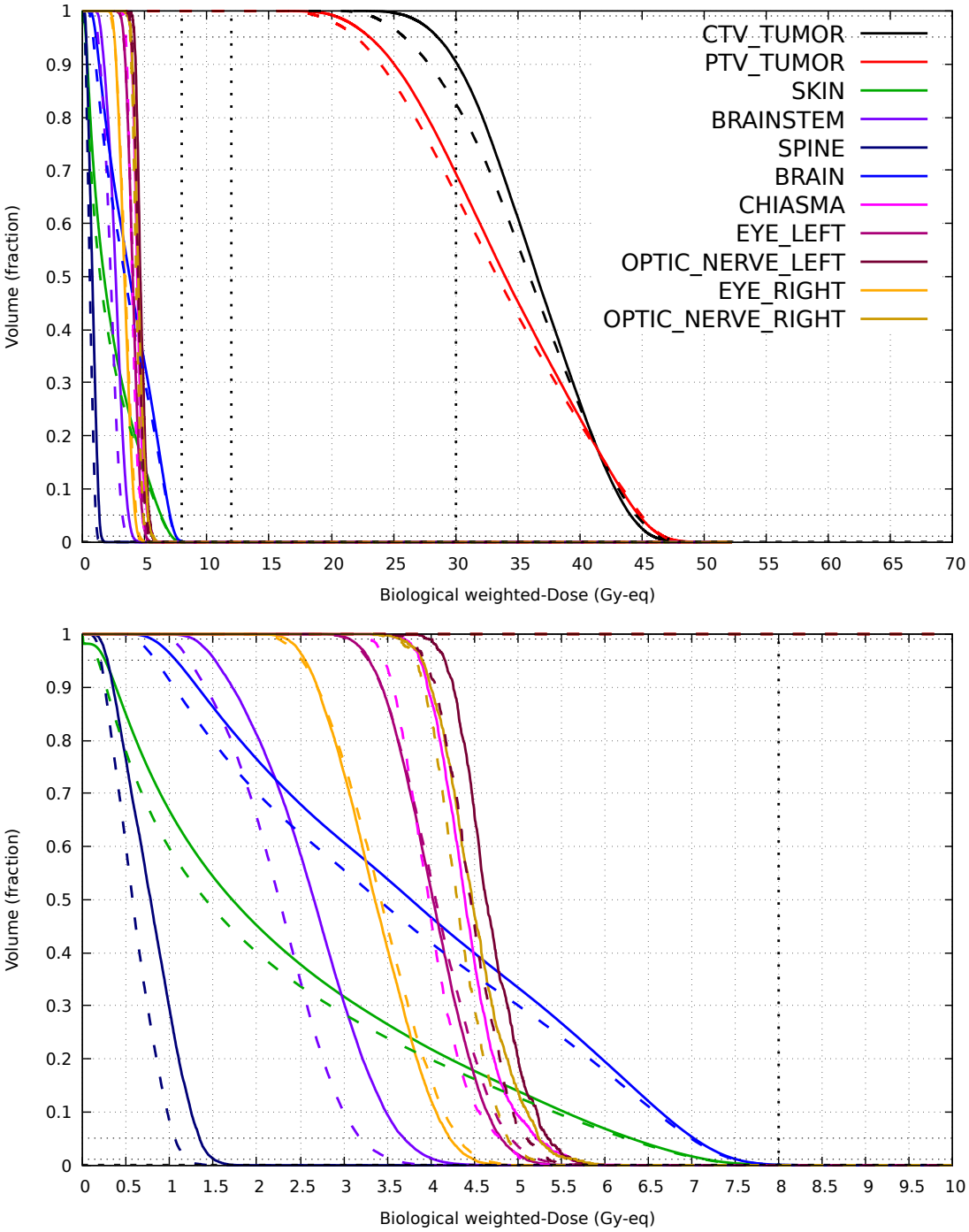

Figure 5.11: Dose-Volume Histograms of the OAR, PTV and CTV of the patient with GBM, for the BNCT Treatment Plan using the BSA-UGR neutron beam (solid lines) and the FiR-1 neutron beam (dashed lines). The *top panel* corresponds to the complete DVH including CTV, PTV and all the OAR of interest, as indicated in the key. The *bottom panel* shows the detail in the range 0-10 Gy-eq to better showcase the dose in the OAR. The color code for the *top* and *bottom panels* is the same.

It is also paramount to note that the beam from FiR-1 is considered as one of the cleanest beams for BNCT and that yielded to successful clinical trials in the past. The main aim of the design of new beams for BNCT using accelerators is to try to replicate or at least achieve a beam delivery close to the FiR-1 features. In this case, the BSA-UGR is able to replicate FiR-1 and furthermore, we find some improvements in a few aspects of relevance than can lead to a better outcome in cancer treatment.

This case of a patient with GBM is only an example of what could be achieved with BNCT using the newly designed BSA-UGR beam. This beam can also be used and tested for other tumor locations within and outside the brain, including other tumors historically targeted for BNCT as head-and-neck cancers, but also other tumor locations as the lungs or the liver. The treatment planning system developed to simulate this case is also extensible to such tumors, in the aim of understanding better and expand the possibilities of BNCT treatment for cancer patients for which this can be a real hope to hold onto.

Conclusions

- The ^{14}N(n,p)^{14}C reaction cross-section has been measured at the n_TOF Facility of CERN and for the first time, the measurement has completed a continuous measurement from the thermal to the resonance region, covering eight orders of magnitude from 8 meV to 800 keV. A new thermal value has been obtained (1.809±0.025 b) and a R-Matrix analysis including the first two resonances has been performed.
- The implications of the new data from the ^{14}N(n,p)^{14}C reaction cross-section have been discussed and analyzed for BNCT, considering both the effects in neutron transport by generating a new ACE file to be used by MCNP; and in dosimetry via the calculation of new Kerma factors. The effect in neutron transport is negligible for BNCT applications, and the variation in Kerma factors lies around 1 % below the previous reference, for thermal neutron beams, and under 1 % for higher energy beams.
- Some considerations on the beam design for BNCT have been assessed. These have been integrated in the design of a new beam optimized for BNCT, that makes use of a low energy proton accelerator (2.1 MeV, 30 mA) onto a Li target. The use of this reaction at low energy allows to kinematically avoid the presence of high energy neutrons. A BSA has been designed to moderate and conform the beam to the needs of BNCT treatment. This BSA achieves the goal of delivering a beam that shows good features in in-phantom figures of merit compared to previous designs and fulfills all IAEA recommendations for the first time.
- A Treatment Planning System for BNCT has been developed and tested for the case of a Glioblastoma patient, using the beam delivered by the BSA designed before. The test case has been compared with the actual treatment with conventional RT received by the patient, and with the simulation of a FiR-1 treatment with the same patient.

Outlook

This thesis has led to a series of results discussed before. Together with this, there are some research developments that can be continued from this thesis and other applications that can profit from the experience obtained with this work.

- Other neutron induced reactions of interest in medical physics can be measured at n_TOF and analyzed using these techniques. This is the case of the ^{35}Cl(n,p) reaction, which was measured in the same experimental campaign as the ^{14}N(n,p) reaction at n_TOF. This measurement will be analyzed soon after the defense of this thesis, and its implications will be studied in a similar manner as in the ^{14}N(n,p) case.
- Concerning the design of the BSA, a prototype including the main features is expected to be manufactured and tested in order to check consistency with the simulations. For such duty, techniques such as the time-of-flight and the multi-foil activation (described in Appendix C) can be used to characterize both the spectrum and beam profile. Other aspects such as the out-of-field dose, long-term activation of the BSA and other radioprotection considerations are also being analyzed.
- Regarding the TPS, several improvements in terms of runtime efficiency and analysis capabilities are being proposed and included. For instance, the generalization of the codes to be used with different types of malignancies and body locations, the use of machine learning techniques to better identify tissues and organs from CT scans. The use of imaging techniques such as SPECT and Compton Cameras is also needed to determine the location of the boron administered to the patients, in order to improve the accuracy of the dose estimations. The development of a multi-criteria optimization algorithm is also pursued in order to define best-suited treatment plans for any given case.

Appendices

Appendix A

Nuclear Data from the ^{14}N(n,p) reaction measurement at n_TOF

A.1 Experimental Nuclear Data

Table A.1: Experimental data from the ^{14}N(n,p) measurement at n_TOF EAR-2. The columns correspond to the four series of data from MicroMegas, two from the Backward Sample (MGAS BW) and two from the Forward Sample (MGAS FW), and the DSSSD data. MGAS series are separated in High Intensity (HI) and Low Intensity (LI).

Table A.1					
Energy (eV)	MGAS BW HI (b)	MGAS BW LI (b)	MGAS FW HI (b)	MGAS FW LI (b)	DSSSD (b)
$7.13{\cdot}10^{-3}$	2.882 ± 0.010	2.888 ± 0.017	2.866 ± 0.012	2.989 ± 0.021	-
$1.13{\cdot}10^{-2}$	2.640 ± 0.008	2.660 ± 0.013	2.631 ± 0.010	2.706 ± 0.016	2.684 ± 0.020
$1.42{\cdot}10^{-2}$	2.291 ± 0.006	2.293 ± 0.010	2.288 ± 0.007	2.349 ± 0.013	2.356 ± 0.015
$1.79{\cdot}10^{-2}$	2.079 ± 0.005	2.087 ± 0.008	2.083 ± 0.006	2.138 ± 0.010	2.114 ± 0.012
$2.25{\cdot}10^{-2}$	1.822 ± 0.004	1.813 ± 0.006	1.818 ± 0.004	1.866 ± 0.008	1.864 ± 0.009
$2.84{\cdot}10^{-2}$	1.649 ± 0.003	1.648 ± 0.005	1.647 ± 0.004	1.702 ± 0.006	1.693 ± 0.008
$3.57{\cdot}10^{-2}$	1.4555 ± 0.0025	1.448 ± 0.004	1.443 ± 0.003	1.491 ± 0.005	1.486 ± 0.006
$4.50{\cdot}10^{-2}$	1.3072 ± 0.0022	1.299 ± 0.004	1.297 ± 0.003	1.349 ± 0.005	1.314 ± 0.006
$5.66{\cdot}10^{-2}$	1.1550 ± 0.0020	1.150 ± 0.003	1.149 ± 0.002	1.184 ± 0.004	1.177 ± 0.005
$7.13{\cdot}10^{-2}$	1.0298 ± 0.0019	1.031 ± 0.003	1.028 ± 0.002	1.065 ± 0.004	1.054 ± 0.005
$8.97{\cdot}10^{-2}$	0.9265 ± 0.0019	0.922 ± 0.003	0.919 ± 0.002	0.955 ± 0.004	0.932 ± 0.005
0.113	0.8194 ± 0.0021	0.821 ± 0.004	0.815 ± 0.003	0.840 ± 0.004	0.825 ± 0.005
0.142	0.7350 ± 0.0024	0.727 ± 0.004	0.734 ± 0.003	0.760 ± 0.005	0.748 ± 0.006
0.179	0.6520 ± 0.0026	0.652 ± 0.004	0.647 ± 0.003	0.663 ± 0.006	0.660 ± 0.007
0.225	0.5859 ± 0.0027	0.580 ± 0.005	0.585 ± 0.003	0.610 ± 0.006	0.586 ± 0.007
0.284	0.5222 ± 0.0026	0.523 ± 0.005	0.521 ± 0.003	0.546 ± 0.006	0.517 ± 0.007
0.357	0.4649 ± 0.0025	0.465 ± 0.004	0.462 ± 0.003	0.472 ± 0.005	0.471 ± 0.007
0.450	0.4157 ± 0.0024	0.407 ± 0.004	0.411 ± 0.003	0.427 ± 0.005	0.399 ± 0.006
0.566	0.3638 ± 0.0023	0.366 ± 0.004	0.366 ± 0.003	0.384 ± 0.005	0.361 ± 0.006
0.713	0.3317 ± 0.0021	0.332 ± 0.004	0.333 ± 0.003	0.340 ± 0.005	0.331 ± 0.006
0.897	0.2944 ± 0.0020	0.287 ± 0.003	0.294 ± 0.003	0.303 ± 0.004	0.289 ± 0.005
1.13	0.2607 ± 0.0020	0.262 ± 0.003	0.2606 ± 0.0025	0.265 ± 0.004	0.255 ± 0.005
1.42	0.2332 ± 0.0018	0.233 ± 0.003	0.2322 ± 0.0023	0.240 ± 0.004	0.230 ± 0.005
1.79	0.2083 ± 0.0017	0.205 ± 0.003	0.2069 ± 0.0021	0.213 ± 0.004	0.210 ± 0.004

Continuation of Table A.1

Energy (eV)	MGAS BW HI (b)	MGAS BW LI (b)	MGAS FW HI (b)	MGAS FW LI (b)	DSSSD (b)
2.25	0.1857 ± 0.0016	0.186 ± 0.003	0.1866 ± 0.0020	0.200 ± 0.004	0.184 ± 0.004
2.84	0.1648 ± 0.0015	0.164 ± 0.003	0.1635 ± 0.0019	0.176 ± 0.003	0.164 ± 0.004
3.57	0.1458 ± 0.0015	0.1451 ± 0.0025	0.1468 ± 0.0018	0.149 ± 0.003	0.151 ± 0.004
4.50	0.1304 ± 0.0014	0.1297 ± 0.0023	0.1282 ± 0.0017	0.135 ± 0.003	0.128 ± 0.003
5.66	0.1169 ± 0.0013	0.1180 ± 0.0022	0.1170 ± 0.0016	0.121 ± 0.003	0.113 ± 0.003
7.13	0.1039 ± 0.0012	0.1041 ± 0.0021	0.1034 ± 0.0015	0.103 ± 0.003	0.104 ± 0.003
8.97	0.0931 ± 0.0011	0.0938 ± 0.0019	0.0922 ± 0.0014	0.0966 ± 0.0024	0.092 ± 0.003
11.3	0.0828 ± 0.0011	0.0823 ± 0.0018	0.0810 ± 0.0013	0.0873 ± 0.0023	0.089 ± 0.003
14.2	0.0724 ± 0.0010	0.0730 ± 0.0017	0.0713 ± 0.0012	0.0740 ± 0.0021	0.0714 ± 0.0025
17.9	0.0665 ± 0.0009	0.0672 ± 0.0016	0.0653 ± 0.0012	0.0677 ± 0.0020	0.0672 ± 0.0024
22.5	0.0595 ± 0.0009	0.0570 ± 0.0015	0.0577 ± 0.0011	0.0598 ± 0.0019	0.0604 ± 0.0023
28.4	0.0511 ± 0.0008	0.0532 ± 0.0014	0.0522 ± 0.0010	0.0528 ± 0.0017	0.0560 ± 0.0022
35.7	0.0468 ± 0.0007	0.0474 ± 0.0013	0.0453 ± 0.0009	0.0484 ± 0.0016	0.0479 ± 0.0020
45.0	0.0431 ± 0.0007	0.0440 ± 0.0012	0.0431 ± 0.0009	0.0446 ± 0.0015	0.0423 ± 0.0019
56.6	0.0370 ± 0.0007	0.0373 ± 0.0012	0.0366 ± 0.0009	0.0382 ± 0.0015	0.0351 ± 0.0017
71.3	0.0338 ± 0.0006	0.0332 ± 0.0011	0.0324 ± 0.0008	0.0344 ± 0.0014	0.0333 ± 0.0016
89.7	0.0307 ± 0.0006	0.0315 ± 0.0011	0.0306 ± 0.0008	0.0316 ± 0.0013	0.0298 ± 0.0015
$1.13{\cdot}10^2$	0.0278 ± 0.0006	0.0268 ± 0.0010	0.0268 ± 0.0007	0.0272 ± 0.0012	0.0286 ± 0.0015
$1.42{\cdot}10^2$	0.0234 ± 0.0005	0.0254 ± 0.0009	0.0238 ± 0.0006	0.0236 ± 0.0011	0.0227 ± 0.0013
$1.79{\cdot}10^2$	0.0211 ± 0.0005	0.0213 ± 0.0009	0.0199 ± 0.0007	0.0212 ± 0.0011	0.0234 ± 0.0013
$2.25{\cdot}10^2$	0.0191 ± 0.0005	0.0180 ± 0.0008	0.0183 ± 0.0006	0.0205 ± 0.0010	0.0195 ± 0.0012
$2.84{\cdot}10^2$	0.0168 ± 0.0004	0.0180 ± 0.0008	0.0172 ± 0.0005	0.0179 ± 0.0009	0.0187 ± 0.0012
$3.57{\cdot}10^2$	0.0150 ± 0.0005	0.0152 ± 0.0009	0.0147 ± 0.0007	0.0150 ± 0.0011	0.0144 ± 0.0012
$4.50{\cdot}10^2$	0.0133 ± 0.0004	0.0136 ± 0.0007	0.0135 ± 0.0005	0.0142 ± 0.0009	0.0134 ± 0.0010
$5.66{\cdot}10^2$	0.0119 ± 0.0003	0.0125 ± 0.0006	0.0122 ± 0.0004	0.0132 ± 0.0008	0.0130 ± 0.0010
$7.13{\cdot}10^2$	0.0106 ± 0.0003	0.0112 ± 0.0006	0.0109 ± 0.0004	0.0102 ± 0.0007	0.0106 ± 0.0009
$8.97{\cdot}10^2$	0.0098 ± 0.0003	0.0097 ± 0.0005	0.0095 ± 0.0004	0.0092 ± 0.0007	0.0088 ± 0.0008
$1.13{\cdot}10^3$	0.0087 ± 0.0003	0.0086 ± 0.0005	0.0091 ± 0.0004	0.0074 ± 0.0006	0.0085 ± 0.0008
$1.42{\cdot}10^3$	0.0072 ± 0.0003	0.0069 ± 0.0005	0.0074 ± 0.0004	0.0073 ± 0.0006	0.0077 ± 0.0007
$1.79{\cdot}10^3$	0.0067 ± 0.0003	0.0064 ± 0.0004	0.0069 ± 0.0003	0.0067 ± 0.0006	0.0068 ± 0.0007
$2.25{\cdot}10^3$	0.0058 ± 0.0003	0.0053 ± 0.0004	0.0059 ± 0.0004	0.0060 ± 0.0006	0.0059 ± 0.0007
$2.84{\cdot}10^3$	0.0050 ± 0.0003	0.0059 ± 0.0005	0.0048 ± 0.0003	0.0042 ± 0.0005	0.0058 ± 0.0006
$3.57{\cdot}10^3$	0.00483 ± 0.00024	0.0043 ± 0.0004	0.0047 ± 0.0003	0.0047 ± 0.0005	0.0052 ± 0.0006
$4.50{\cdot}10^3$	0.00415 ± 0.00022	0.0036 ± 0.0003	0.0051 ± 0.0003	0.0037 ± 0.0004	0.0048 ± 0.0006
$5.66{\cdot}10^3$	0.00409 ± 0.00020	0.0039 ± 0.0003	0.0041 ± 0.0003	0.0039 ± 0.0004	0.0042 ± 0.0005
$7.13{\cdot}10^3$	0.00316 ± 0.00019	0.0033 ± 0.0003	0.0037 ± 0.0003	0.0031 ± 0.0004	0.0034 ± 0.0005
$8.97{\cdot}10^3$	0.00282 ± 0.00017	0.0028 ± 0.0003	0.00328 ± 0.00022	0.0036 ± 0.0004	0.0036 ± 0.0005
$1.13{\cdot}10^4$	0.00272 ± 0.00015	0.0036 ± 0.0003	0.00337 ± 0.00021	0.0034 ± 0.0003	0.0023 ± 0.0004
$1.42{\cdot}10^4$	0.00228 ± 0.00017	0.0027 ± 0.0003	0.00255 ± 0.00023	0.0022 ± 0.0003	0.0026 ± 0.0004
$1.79{\cdot}10^4$	0.00231 ± 0.00014	0.00233 ± 0.00023	0.00256 ± 0.00019	0.0025 ± 0.0003	0.0024 ± 0.0003
$2.25{\cdot}10^4$	0.00207 ± 0.00012	0.00204 ± 0.00020	0.00218 ± 0.00017	0.0022 ± 0.0003	0.0019 ± 0.0003
$2.84{\cdot}10^4$	0.00157 ± 0.00014	0.00168 ± 0.00020	0.00166 ± 0.00019	0.0015 ± 0.0003	0.0019 ± 0.0003
$3.57{\cdot}10^4$	0.0016 ± 0.0004	0.0022 ± 0.0005	0.0011 ± 0.0005	0.0012 ± 0.0007	0.0023 ± 0.0006
$4.50{\cdot}10^4$	0.00134 ± 0.00018	0.00145 ± 0.00025	0.00131 ± 0.00025	0.0015 ± 0.0004	0.0017 ± 0.0003
$5.66{\cdot}10^4$	0.00112 ± 0.00014	0.00097 ± 0.00018	0.00146 ± 0.00020	0.0014 ± 0.0003	0.00149 ± 0.00023
$7.13{\cdot}10^4$	0.00110 ± 0.00014	0.00126 ± 0.00019	0.00176 ± 0.00021	0.0011 ± 0.0003	0.0019 ± 0.0003
$8.97{\cdot}10^4$	0.00084 ± 0.00025	0.0008 ± 0.0003			0.0011 ± 0.0003
$1.13{\cdot}10^5$	0.00131 ± 0.00011	0.00104 ± 0.00015			0.00120 ± 0.00019

Continuation of Table A.1

Energy (eV)	MGAS BW HI (b)	MGAS BW LI (b)	MGAS FW HI (b)	MGAS FW LI (b)	DSSSD (b)
$1.42 \cdot 10^5$					0.0016 ± 0.0003
$1.79 \cdot 10^5$					0.00137 ± 0.00022
$2.25 \cdot 10^5$					0.00138 ± 0.00018
$2.84 \cdot 10^5$					0.00129 ± 0.00018
$3.20 \cdot 10^5$					0.0007 ± 0.0007
$3.27 \cdot 10^5$					0.0
$3.35 \cdot 10^5$					0.0
$3.43 \cdot 10^5$					0.0013 ± 0.0010
$3.51 \cdot 10^5$					0.0
$3.59 \cdot 10^5$					0.0009 ± 0.0009
$3.67 \cdot 10^5$					0.0050 ± 0.0023
$3.76 \cdot 10^5$					0.0021 ± 0.0013
$3.85 \cdot 10^5$					0.008 ± 0.004
$3.94 \cdot 10^5$					0.0031 ± 0.0015
$4.03 \cdot 10^5$					0.013 ± 0.005
$4.12 \cdot 10^5$					0.017 ± 0.005
$4.22 \cdot 10^5$					0.023 ± 0.006
$4.32 \cdot 10^5$					0.029 ± 0.007
$4.42 \cdot 10^5$					0.036 ± 0.008
$4.52 \cdot 10^5$					0.072 ± 0.016
$4.62 \cdot 10^5$					0.083 ± 0.018
$4.73 \cdot 10^5$					0.068 ± 0.015
$4.84 \cdot 10^5$					0.039 ± 0.008
$4.95 \cdot 10^5$					0.038 ± 0.010
$5.07 \cdot 10^5$					0.021 ± 0.006
$5.19 \cdot 10^5$					0.028 ± 0.008
$5.31 \cdot 10^5$					0.040 ± 0.013
$5.43 \cdot 10^5$					0.050 ± 0.015
$5.56 \cdot 10^5$					0.054 ± 0.014
$5.69 \cdot 10^5$					0.12 ± 0.04
$5.82 \cdot 10^5$					0.11 ± 0.03
$5.96 \cdot 10^5$					0.14 ± 0.04
$6.10 \cdot 10^5$					0.14 ± 0.04
$6.24 \cdot 10^5$					0.17 ± 0.06
$6.38 \cdot 10^5$					0.12 ± 0.04
$6.53 \cdot 10^5$					0.11 ± 0.05
$6.68 \cdot 10^5$					0.10 ± 0.04
$6.84 \cdot 10^5$					0.035 ± 0.011
$7.00 \cdot 10^5$					0.12 ± 0.09
$7.16 \cdot 10^5$					0.040 ± 0.020
$7.33 \cdot 10^5$					0.028 ± 0.013
$7.50 \cdot 10^5$					0.017 ± 0.008
$7.67 \cdot 10^5$					0.019 ± 0.009
$7.85 \cdot 10^5$					0.026 ± 0.014

End of Table A.1

A.2 ENDF-6-formatted pointwise data

```
  7014.0   1.388278+1          0          0          0          0 725 3600    1
0.0000E+00 0.0000E+00          0          0          1        479 725 3600    2
         0          0                                              725 3600    3
8.971640-3 3.038159+0 1.129463-2 2.707761+0 1.421909-2 2.413295+0 725 3600    4
1.790078-2 2.150851+0 2.253574-2 1.916948+0 2.837082-2 1.708482+0 725 3600    5
3.571675-2 1.522686+0 4.496472-2 1.357095+0 5.660723-2 1.209513+0 725 3600    6
7.126428-2 1.077979+0 8.971641-2 9.607499-1 1.129463-1 8.562692-1 725 3600    7
1.421909-1 7.631507-1 1.790078-1 6.801587-1 2.253574-1 6.061921-1 725 3600    8
2.837082-1 5.402692-1 3.571675-1 4.815154-1 4.496472-1 4.291510-1 725 3600    9
5.660723-1 3.824812-1 7.126428-1 3.408866-1 8.971641-1 3.038155-1 725 3600   10
1.129463+0 2.707758-1 1.421909+0 2.413291-1 1.790078+0 2.150847-1 725 3600   11
2.253574+0 1.916943-1 2.837082+0 1.708477-1 3.571675+0 1.522680-1 725 3600   12
4.496472+0 1.357089-1 5.660723+0 1.209506-1 7.126428+0 1.077972-1 725 3600   13
8.971641+0 9.607416-2 1.129463+1 8.562601-2 1.421909+1 7.631407-2 725 3600   14
1.790078+1 6.801477-2 2.253574+1 6.061799-2 2.837082+1 5.402557-2 725 3600   15
3.571675+1 4.815004-2 4.496472+1 4.291344-2 5.660723+1 3.824627-2 725 3600   16
7.126428+1 3.408661-2 8.971641+1 3.037927-2 1.129500+2 2.707459-2 725 3600   17
1.421900+2 2.413016-2 1.790100+2 2.150518-2 2.253600+2 1.916581-2 725 3600   18
2.837100+2 1.708079-2 3.571700+2 1.522237-2 4.496500+2 1.356596-2 725 3600   19
5.660700+2 1.208963-2 7.126400+2 1.077366-2 8.971600+2 9.600658-3 725 3600   20
1.129460+3 8.555059-3 1.421910+3 7.623001-3 1.790080+3 6.792135-3 725 3600   21
2.253570+3 6.051449-3 2.837080+3 5.391104-3 3.571670+3 4.802379-3 725 3600   22
4.496470+3 4.277484-3 5.660720+3 3.809502-3 7.126430+3 3.392280-3 725 3600   23
8.971640+3 3.020371-3 1.129463+4 2.688954-3 1.421909+4 2.393797-3 725 3600   24
1.790078+4 2.131210-3 2.253574+4 1.898025-3 2.837082+4 1.691577-3 725 3600   25
3.571675+4 1.509717-3 4.496472+4 1.350829-3 5.660723+4 1.213865-3 725 3600   26
7.126428+4 1.098402-3 8.971641+4 1.004696-3 1.129463+5 9.337621-4 725 3600   27
1.421909+5 8.875203-4 1.790078+5 8.692815-4 2.253574+5 8.851787-4 725 3600   28
2.837082+5 9.484470-4 3.165923+5 1.005389-3 3.173221+5 1.006882-3 725 3600   29
3.180536+5 1.008391-3 3.187868+5 1.009915-3 3.195217+5 1.011456-3 725 3600   30
3.202582+5 1.013013-3 3.209965+5 1.014586-3 3.217365+5 1.016177-3 725 3600   31
3.224782+5 1.017785-3 3.232215+5 1.019410-3 3.239666+5 1.021054-3 725 3600   32
3.247135+5 1.022716-3 3.254620+5 1.024396-3 3.262123+5 1.026096-3 725 3600   33
3.269643+5 1.027815-3 3.277180+5 1.029554-3 3.284735+5 1.031313-3 725 3600   34
3.292307+5 1.033093-3 3.299896+5 1.034894-3 3.307503+5 1.036716-3 725 3600   35
3.315128+5 1.038561-3 3.322770+5 1.040428-3 3.330430+5 1.042319-3 725 3600   36
3.338107+5 1.044232-3 3.345802+5 1.046170-3 3.353515+5 1.048133-3 725 3600   37
3.361246+5 1.050121-3 3.368994+5 1.052135-3 3.376761+5 1.054175-3 725 3600   38
3.384545+5 1.056242-3 3.392347+5 1.058337-3 3.400167+5 1.060460-3 725 3600   39
3.408005+5 1.062613-3 3.415862+5 1.064795-3 3.423736+5 1.067008-3 725 3600   40
3.431629+5 1.069252-3 3.439539+5 1.071528-3 3.447468+5 1.073838-3 725 3600   41
3.455416+5 1.076181-3 3.463381+5 1.078559-3 3.471365+5 1.080973-3 725 3600   42
3.479367+5 1.083423-3 3.487388+5 1.085912-3 3.495427+5 1.088438-3 725 3600   43
3.503485+5 1.091005-3 3.511562+5 1.093613-3 3.519657+5 1.096263-3 725 3600   44
3.527770+5 1.098956-3 3.535903+5 1.101693-3 3.544054+5 1.104477-3 725 3600   45
3.552223+5 1.107308-3 3.560412+5 1.110187-3 3.568620+5 1.113116-3 725 3600   46
3.576846+5 1.116097-3 3.585092+5 1.119132-3 3.593356+5 1.122221-3 725 3600   47
3.601640+5 1.125366-3 3.609942+5 1.128570-3 3.618264+5 1.131834-3 725 3600   48
3.626605+5 1.135161-3 3.634965+5 1.138551-3 3.643345+5 1.142007-3 725 3600   49
3.651744+5 1.145532-3 3.660162+5 1.149128-3 3.668599+5 1.152796-3 725 3600   50
3.677056+5 1.156540-3 3.685533+5 1.160362-3 3.694029+5 1.164265-3 725 3600   51
3.702545+5 1.168251-3 3.711080+5 1.172324-3 3.719635+5 1.176486-3 725 3600   52
3.728209+5 1.180741-3 3.736804+5 1.185092-3 3.745418+5 1.189542-3 725 3600   53
3.754052+5 1.194095-3 3.762706+5 1.198756-3 3.771380+5 1.203527-3 725 3600   54
3.780074+5 1.208413-3 3.788788+5 1.213419-3 3.797522+5 1.218549-3 725 3600   55
3.806276+5 1.223807-3 3.815050+5 1.229199-3 3.823845+5 1.234730-3 725 3600   56
```

```
3.832660+5 1.240405-3 3.841495+5 1.246231-3 3.850351+5 1.252213-3 725 3600   57
3.859227+5 1.258357-3 3.868123+5 1.264671-3 3.877040+5 1.271161-3 725 3600   58
3.885978+5 1.277835-3 3.894936+5 1.284700-3 3.903914+5 1.291765-3 725 3600   59
3.912914+5 1.299038-3 3.921934+5 1.306527-3 3.930975+5 1.314244-3 725 3600   60
3.940037+5 1.322197-3 3.949120+5 1.330397-3 3.958223+5 1.338856-3 725 3600   61
3.967348+5 1.347585-3 3.976494+5 1.356596-3 3.985660+5 1.365903-3 725 3600   62
3.994848+5 1.375519-3 4.004057+5 1.385460-3 4.013288+5 1.395740-3 725 3600   63
4.022539+5 1.406376-3 4.031812+5 1.417386-3 4.041106+5 1.428787-3 725 3600   64
4.050422+5 1.440601-3 4.059759+5 1.452846-3 4.069118+5 1.465546-3 725 3600   65
4.078498+5 1.478724-3 4.087900+5 1.492405-3 4.097324+5 1.506615-3 725 3600   66
4.106769+5 1.521383-3 4.116236+5 1.536738-3 4.125725+5 1.552714-3 725 3600   67
4.135236+5 1.569345-3 4.144769+5 1.586666-3 4.154323+5 1.604718-3 725 3600   68
4.163900+5 1.623543-3 4.173499+5 1.643185-3 4.183120+5 1.663693-3 725 3600   69
4.192763+5 1.685119-3 4.202428+5 1.707518-3 4.212116+5 1.730951-3 725 3600   70
4.221826+5 1.755481-3 4.231558+5 1.781178-3 4.241313+5 1.808118-3 725 3600   71
4.251090+5 1.836381-3 4.260890+5 1.866055-3 4.270712+5 1.897233-3 725 3600   72
4.280557+5 1.930020-3 4.290425+5 1.964526-3 4.300315+5 2.000873-3 725 3600   73
4.310228+5 2.039191-3 4.320165+5 2.079626-3 4.330123+5 2.122332-3 725 3600   74
4.340105+5 2.167482-3 4.350110+5 2.215262-3 4.360138+5 2.265878-3 725 3600   75
4.370190+5 2.319555-3 4.380264+5 2.376541-3 4.390362+5 2.437109-3 725 3600   76
4.400482+5 2.501559-3 4.410627+5 2.570227-3 4.420794+5 2.643480-3 725 3600   77
4.430985+5 2.721730-3 4.441200+5 2.805433-3 4.451438+5 2.895098-3 725 3600   78
4.461699+5 2.991293-3 4.471985+5 3.094659-3 4.482293+5 3.205910-3 725 3600   79
4.492626+5 3.325855-3 4.502983+5 3.455407-3 4.513363+5 3.595598-3 725 3600   80
4.523768+5 3.747605-3 4.534196+5 3.912769-3 4.544648+5 4.092620-3 725 3600   81
4.555125+5 4.288920-3 4.565625+5 4.503698-3 4.576150+5 4.739304-3 725 3600   82
4.586700+5 4.998463-3 4.597273+5 5.284361-3 4.607871+5 5.600733-3 725 3600   83
4.618493+5 5.951983-3 4.629140+5 6.343320-3 4.639811+5 6.780964-3 725 3600   84
4.650507+5 7.272355-3 4.661227+5 7.826492-3 4.671973+5 8.454277-3 725 3600   85
4.682743+5 9.169076-3 4.693538+5 9.987371-3 4.704357+5 1.092965-2 725 3600   86
4.715202+5 1.202164-2 4.726072+5 1.329601-2 4.736966+5 1.479456-2 725 3600   87
4.747886+5 1.657156-2 4.758831+5 1.869821-2 4.769801+5 2.126933-2 725 3600   88
4.780797+5 2.441303-2 4.791818+5 2.830517-2 4.802864+5 3.319117-2 725 3600   89
4.813936+5 3.941969-2 4.825033+5 4.749507-2 4.836156+5 5.815842-2 725 3600   90
4.847304+5 7.251254-2 4.858478+5 9.219929-2 4.869678+5 1.196009-1 725 3600   91
4.880904+5 1.578539-1 4.892156+5 2.098704-1 4.903433+5 2.742394-1 725 3600   92
4.914737+5 3.362746-1 4.926067+5 3.650803-1 4.937422+5 3.409174-1 725 3600   93
4.948804+5 2.820615-1 4.960213+5 2.191565-1 4.971647+5 1.674404-1 725 3600   94
4.983108+5 1.288978-1 4.994595+5 1.009718-1 5.006109+5 8.070056-2 725 3600   95
5.017649+5 6.577962-2 5.029216+5 5.459701-2 5.040810+5 4.605828-2 725 3600   96
5.052430+5 3.942107-2 5.064077+5 3.417660-2 5.075751+5 2.997058-2 725 3600   97
5.087452+5 2.655203-2 5.099179+5 2.374013-2 5.110934+5 2.140241-2 725 3600   98
5.122716+5 1.944031-2 5.134525+5 1.777942-2 5.146362+5 1.636284-2 725 3600   99
5.158225+5 1.514646-2 5.170116+5 1.409575-2 5.182034+5 1.318337-2 725 3600  100
5.193980+5 1.238748-2 5.205953+5 1.169044-2 5.217955+5 1.107795-2 725 3600  101
5.229983+5 1.053827-2 5.242040+5 1.006173-2 5.254124+5 9.640336-3 725 3600  102
5.266236+5 9.267383-3 5.278376+5 8.937271-3 5.290543+5 8.645292-3 725 3600  103
5.302739+5 8.387462-3 5.314963+5 8.160406-3 5.327216+5 7.961266-3 725 3600  104
5.339496+5 7.787609-3 5.351805+5 7.637368-3 5.364142+5 7.508789-3 725 3600  105
5.376508+5 7.400384-3 5.388902+5 7.310900-3 5.401325+5 7.239288-3 725 3600  106
5.413776+5 7.184676-3 5.426256+5 7.146354-3 5.438765+5 7.123757-3 725 3600  107
5.451303+5 7.116446-3 5.463869+5 7.124107-3 5.476465+5 7.146534-3 725 3600  108
5.489089+5 7.183627-3 5.501743+5 7.235385-3 5.514426+5 7.301906-3 725 3600  109
5.527138+5 7.383378-3 5.539879+5 7.480087-3 5.552650+5 7.592413-3 725 3600  110
5.565450+5 7.720825-3 5.578280+5 7.865900-3 5.591139+5 8.028310-3 725 3600  111
5.604028+5 8.208837-3 5.616947+5 8.408374-3 5.629895+5 8.627937-3 725 3600  112
5.642873+5 8.868673-3 5.655881+5 9.131861-3 5.668919+5 9.418944-3 725 3600  113
5.681988+5 9.731521-3 5.695086+5 1.007138-2 5.708214+5 1.044050-2 725 3600  114
```

```
5.721373+5 1.084109-2 5.734562+5 1.127560-2 5.747782+5 1.174674-2 725 3600  115
5.761032+5 1.225756-2 5.774313+5 1.281140-2 5.787624+5 1.341201-2 725 3600  116
5.800966+5 1.406354-2 5.814338+5 1.477065-2 5.827742+5 1.553849-2 725 3600  117
5.841176+5 1.637285-2 5.854641+5 1.728018-2 5.868138+5 1.826773-2 725 3600  118
5.881665+5 1.934357-2 5.895224+5 2.051682-2 5.908814+5 2.179766-2 725 3600  119
5.922435+5 2.319760-2 5.936087+5 2.472956-2 5.949772+5 2.640814-2 725 3600  120
5.963487+5 2.824979-2 5.977234+5 3.027307-2 5.991013+5 3.249901-2 725 3600  121
6.004824+5 3.495132-2 6.018667+5 3.765680-2 6.032541+5 4.064577-2 725 3600  122
6.046448+5 4.395233-2 6.060386+5 4.761494-2 6.074357+5 5.167673-2 725 3600  123
6.088359+5 5.618579-2 6.102395+5 6.119554-2 6.116462+5 6.676472-2 725 3600  124
6.130562+5 7.295700-2 6.144694+5 7.984030-2 6.158859+5 8.748516-2 725 3600  125
6.173057+5 9.596200-2 6.187287+5 1.053371-1 6.201551+5 1.156659-1 725 3600  126
6.215847+5 1.269846-1 6.230176+5 1.392976-1 6.244538+5 1.525628-1 725 3600  127
6.258933+5 1.666733-1 6.273361+5 1.814376-1 6.287823+5 1.965636-1 725 3600  128
6.302318+5 2.116476-1 6.316846+5 2.261788-1 6.331408+5 2.395625-1 725 3600  129
6.346003+5 2.511693-1 6.360632+5 2.604028-1 6.375295+5 2.667790-1 725 3600  130
6.389992+5 2.699968-1 6.404722+5 2.699809-1 6.419487+5 2.668864-1 725 3600  131
6.434285+5 2.610633-1 6.449118+5 2.529942-1 6.463984+5 2.432234-1 725 3600  132
6.478885+5 2.322912-1 6.493821+5 2.206874-1 6.508790+5 2.088240-1 725 3600  133
6.523795+5 1.970249-1 6.538834+5 1.855299-1 6.553907+5 1.745041-1 725 3600  134
6.569016+5 1.640519-1 6.584159+5 1.542302-1 6.599337+5 1.450613-1 725 3600  135
6.614550+5 1.365422-1 6.629798+5 1.286534-1 6.645081+5 1.213650-1 725 3600  136
6.660400+5 1.146407-1 6.675753+5 1.084415-1 6.691143+5 1.027278-1 725 3600  137
6.706567+5 9.746049-2 6.722028+5 9.260241-2 6.737523+5 8.811842-2 725 3600  138
6.753055+5 8.397591-2 6.768622+5 8.014483-2 6.784226+5 7.659766-2 725 3600  139
6.799865+5 7.330930-2 6.815540+5 7.025699-2 6.831252+5 6.742005-2 725 3600  140
6.846999+5 6.477977-2 6.862783+5 6.231928-2 6.878604+5 6.002324-2 725 3600  141
6.894461+5 5.787788-2 6.910354+5 5.587069-2 6.926284+5 5.399037-2 725 3600  142
6.942251+5 5.222670-2 6.958254+5 5.057039-2 6.974295+5 4.901306-2 725 3600  143
6.990372+5 4.754707-2 7.006487+5 4.616548-2 7.022638+5 4.486201-2 725 3600  144
7.038827+5 4.363090-2 7.055053+5 4.246690-2 7.071317+5 4.136525-2 725 3600  145
7.087618+5 4.032157-2 7.103956+5 3.933185-2 7.120333+5 3.839244-2 725 3600  146
7.136747+5 3.749996-2 7.153199+5 3.665134-2 7.169688+5 3.584372-2 725 3600  147
7.186216+5 3.507449-2 7.202782+5 3.434123-2 7.219386+5 3.364173-2 725 3600  148
7.236029+5 3.297392-2 7.252710+5 3.233591-2 7.269429+5 3.172593-2 725 3600  149
7.286187+5 3.114234-2 7.302983+5 3.058363-2 7.319818+5 3.004841-2 725 3600  150
7.336692+5 2.953535-2 7.353605+5 2.904324-2 7.370557+5 2.857095-2 725 3600  151
7.387548+5 2.811741-2 7.404578+5 2.768164-2 7.421647+5 2.726272-2 725 3600  152
7.438756+5 2.685979-2 7.455904+5 2.647204-2 7.473091+5 2.609871-2 725 3600  153
7.490318+5 2.573910-2 7.507586+5 2.539254-2 7.524892+5 2.505841-2 725 3600  154
7.542239+5 2.473612-2 7.559626+5 2.442513-2 7.577052+5 2.412491-2 725 3600  155
7.594519+5 2.383498-2 7.612026+5 2.355487-2 7.629574+5 2.328416-2 725 3600  156
7.647162+5 2.302244-2 7.664791+5 2.276932-2 7.682460+5 2.252443-2 725 3600  157
7.700169+5 2.228744-2 7.717920+5 2.205802-2 7.735712+5 2.183586-2 725 3600  158
7.753545+5 2.162068-2 7.771418+5 2.141219-2 7.789333+5 2.121013-2 725 3600  159
7.807290+5 2.101426-2 7.825287+5 2.082435-2 7.843326+5 2.064016-2 725 3600  160
7.861407+5 2.046150-2 7.879529+5 2.028817-2 7.897694+5 2.011996-2 725 3600  161
7.915900+5 1.995671-2 7.934148+5 1.979823-2 7.952438+5 1.964438-2 725 3600  162
7.970770+5 1.949500-2 7.989145+5 1.934993-2                       725 3600  163
      0.0        0.0           0          0          0          0 725 3   0  164
```

A.3 Kerma Factor for ICRU-33 tissue

Energy (eV)	k_f (Gy·cm^2)	Energy (eV)	k_f (Gy·cm^2)	Energy (eV)	k_f (Gy·cm^2)
$1.000 \cdot 10^{-4}$	$3.323 \cdot 10^{-12}$	$5.617 \cdot 10^{-3}$	$4.431 \cdot 10^{-13}$	0.3159	$5.914 \cdot 10^{-14}$
$1.121 \cdot 10^{-4}$	$3.137 \cdot 10^{-12}$	$6.302 \cdot 10^{-3}$	$4.183 \cdot 10^{-13}$	0.3544	$5.582 \cdot 10^{-14}$
$1.257 \cdot 10^{-4}$	$2.961 \cdot 10^{-12}$	$7.071 \cdot 10^{-3}$	$3.947 \cdot 10^{-13}$	0.3976	$5.270 \cdot 10^{-14}$
$1.411 \cdot 10^{-4}$	$2.794 \cdot 10^{-12}$	$7.934 \cdot 10^{-3}$	$3.726 \cdot 10^{-13}$	0.4462	$4.978 \cdot 10^{-14}$
$1.583 \cdot 10^{-4}$	$2.638 \cdot 10^{-12}$	$8.902 \cdot 10^{-3}$	$3.519 \cdot 10^{-13}$	0.5006	$4.701 \cdot 10^{-14}$
$1.776 \cdot 10^{-4}$	$2.492 \cdot 10^{-12}$	$1.000 \cdot 10^{-2}$	$3.323 \cdot 10^{-13}$	0.5617	$4.439 \cdot 10^{-14}$
$1.993 \cdot 10^{-4}$	$2.353 \cdot 10^{-12}$	$1.121 \cdot 10^{-2}$	$3.137 \cdot 10^{-13}$	0.6302	$4.191 \cdot 10^{-14}$
$2.236 \cdot 10^{-4}$	$2.221 \cdot 10^{-12}$	$1.257 \cdot 10^{-2}$	$2.961 \cdot 10^{-13}$	0.7071	$3.956 \cdot 10^{-14}$
$2.509 \cdot 10^{-4}$	$2.096 \cdot 10^{-12}$	$1.411 \cdot 10^{-2}$	$2.794 \cdot 10^{-13}$	0.7934	$3.737 \cdot 10^{-14}$
$2.815 \cdot 10^{-4}$	$1.978 \cdot 10^{-12}$	$1.583 \cdot 10^{-2}$	$2.638 \cdot 10^{-13}$	0.8902	$3.530 \cdot 10^{-14}$
$3.159 \cdot 10^{-4}$	$1.868 \cdot 10^{-12}$	$1.776 \cdot 10^{-2}$	$2.492 \cdot 10^{-13}$	1	$3.335 \cdot 10^{-14}$
$3.544 \cdot 10^{-4}$	$1.764 \cdot 10^{-12}$	$1.993 \cdot 10^{-2}$	$2.353 \cdot 10^{-13}$	1.121	$3.151 \cdot 10^{-14}$
$3.976 \cdot 10^{-4}$	$1.665 \cdot 10^{-12}$	$2.236 \cdot 10^{-2}$	$2.221 \cdot 10^{-13}$	1.257	$2.976 \cdot 10^{-14}$
$4.462 \cdot 10^{-4}$	$1.572 \cdot 10^{-12}$	$2.509 \cdot 10^{-2}$	$2.095 \cdot 10^{-13}$	1.411	$2.810 \cdot 10^{-14}$
$5.006 \cdot 10^{-4}$	$1.483 \cdot 10^{-12}$	$2.815 \cdot 10^{-2}$	$1.978 \cdot 10^{-13}$	1.583	$2.656 \cdot 10^{-14}$
$5.617 \cdot 10^{-4}$	$1.400 \cdot 10^{-12}$	$3.159 \cdot 10^{-2}$	$1.868 \cdot 10^{-13}$	1.776	$2.511 \cdot 10^{-14}$
$6.302 \cdot 10^{-4}$	$1.323 \cdot 10^{-12}$	$3.544 \cdot 10^{-2}$	$1.764 \cdot 10^{-13}$	1.993	$2.374 \cdot 10^{-14}$
$7.071 \cdot 10^{-4}$	$1.249 \cdot 10^{-12}$	$3.976 \cdot 10^{-2}$	$1.665 \cdot 10^{-13}$	2.236	$2.245 \cdot 10^{-14}$
$7.934 \cdot 10^{-4}$	$1.179 \cdot 10^{-12}$	$4.462 \cdot 10^{-2}$	$1.572 \cdot 10^{-13}$	2.509	$2.123 \cdot 10^{-14}$
$8.902 \cdot 10^{-4}$	$1.113 \cdot 10^{-12}$	$5.006 \cdot 10^{-2}$	$1.483 \cdot 10^{-13}$	2.815	$2.008 \cdot 10^{-14}$
$1.000 \cdot 10^{-3}$	$1.050 \cdot 10^{-12}$	$5.617 \cdot 10^{-2}$	$1.401 \cdot 10^{-13}$	3.159	$1.901 \cdot 10^{-14}$
$1.121 \cdot 10^{-3}$	$9.915 \cdot 10^{-13}$	$6.302 \cdot 10^{-2}$	$1.323 \cdot 10^{-13}$	3.544	$1.801 \cdot 10^{-14}$
$1.257 \cdot 10^{-3}$	$9.364 \cdot 10^{-13}$	$7.071 \cdot 10^{-2}$	$1.249 \cdot 10^{-13}$	3.976	$1.707 \cdot 10^{-14}$
$1.411 \cdot 10^{-3}$	$8.842 \cdot 10^{-13}$	$7.934 \cdot 10^{-2}$	$1.179 \cdot 10^{-13}$	4.462	$1.618 \cdot 10^{-14}$
$1.583 \cdot 10^{-3}$	$8.346 \cdot 10^{-13}$	$8.902 \cdot 10^{-2}$	$1.113 \cdot 10^{-13}$	5.006	$1.536 \cdot 10^{-14}$
$1.776 \cdot 10^{-3}$	$7.877 \cdot 10^{-13}$	0.1	$1.050 \cdot 10^{-13}$	5.617	$1.459 \cdot 10^{-14}$
$1.993 \cdot 10^{-3}$	$7.433 \cdot 10^{-13}$	0.1121	$9.923 \cdot 10^{-14}$	6.302	$1.388 \cdot 10^{-14}$
$2.236 \cdot 10^{-3}$	$7.020 \cdot 10^{-13}$	0.1257	$9.371 \cdot 10^{-14}$	7.071	$1.320 \cdot 10^{-14}$
$2.509 \cdot 10^{-3}$	$6.630 \cdot 10^{-13}$	0.1411	$8.848 \cdot 10^{-14}$	7.934	$1.260 \cdot 10^{-14}$
$2.815 \cdot 10^{-3}$	$6.259 \cdot 10^{-13}$	0.1583	$8.352 \cdot 10^{-14}$	8.902	$1.204 \cdot 10^{-14}$
$3.159 \cdot 10^{-3}$	$5.909 \cdot 10^{-13}$	0.1776	$7.882 \cdot 10^{-14}$	10	$1.153 \cdot 10^{-14}$
$3.544 \cdot 10^{-3}$	$5.576 \cdot 10^{-13}$	0.1993	$7.439 \cdot 10^{-14}$	11.21	$1.106 \cdot 10^{-14}$
$3.976 \cdot 10^{-3}$	$5.263 \cdot 10^{-13}$	0.2236	$7.027 \cdot 10^{-14}$	12.57	$1.065 \cdot 10^{-14}$
$4.462 \cdot 10^{-3}$	$4.971 \cdot 10^{-13}$	0.2509	$6.636 \cdot 10^{-14}$	14.11	$1.028 \cdot 10^{-14}$
$5.006 \cdot 10^{-3}$	$4.694 \cdot 10^{-13}$	0.2815	$6.266 \cdot 10^{-14}$	15.83	$9.960 \cdot 10^{-15}$

Energy (eV)	k_f (Gy·cm^2)	Energy (eV)	k_f (Gy·cm^2)	Energy (eV)	k_f (Gy·cm^2)
17.76	$9.688 \cdot 10^{-15}$	$1.000 \cdot 10^{3}$	$1.021 \cdot 10^{-13}$	$5.617 \cdot 10^{4}$	$4.260 \cdot 10^{-12}$
19.93	$9.468 \cdot 10^{-15}$	$1.121 \cdot 10^{3}$	$1.142 \cdot 10^{-13}$	$6.302 \cdot 10^{4}$	$4.645 \cdot 10^{-12}$
22.36	$9.295 \cdot 10^{-15}$	$1.257 \cdot 10^{3}$	$1.279 \cdot 10^{-13}$	$7.071 \cdot 10^{4}$	$5.054 \cdot 10^{-12}$
25.09	$9.184 \cdot 10^{-15}$	$1.411 \cdot 10^{3}$	$1.432 \cdot 10^{-13}$	$7.934 \cdot 10^{4}$	$5.485 \cdot 10^{-12}$
28.15	$9.123 \cdot 10^{-15}$	$1.583 \cdot 10^{3}$	$1.604 \cdot 10^{-13}$	$8.902 \cdot 10^{4}$	$5.943 \cdot 10^{-12}$
31.59	$9.120 \cdot 10^{-15}$	$1.776 \cdot 10^{3}$	$1.796 \cdot 10^{-13}$	$1.000 \cdot 10^{5}$	$6.420 \cdot 10^{-12}$
35.44	$9.183 \cdot 10^{-15}$	$1.993 \cdot 10^{3}$	$2.011 \cdot 10^{-13}$	$1.121 \cdot 10^{5}$	$6.921 \cdot 10^{-12}$
39.76	$9.310 \cdot 10^{-15}$	$2.236 \cdot 10^{3}$	$2.251 \cdot 10^{-13}$	$1.257 \cdot 10^{5}$	$7.449 \cdot 10^{-12}$
44.62	$9.505 \cdot 10^{-15}$	$2.509 \cdot 10^{3}$	$2.521 \cdot 10^{-13}$	$1.411 \cdot 10^{5}$	$8.003 \cdot 10^{-12}$
50.06	$9.783 \cdot 10^{-15}$	$2.815 \cdot 10^{3}$	$2.822 \cdot 10^{-13}$	$1.583 \cdot 10^{5}$	$8.578 \cdot 10^{-12}$
56.17	$1.014 \cdot 10^{-14}$	$3.159 \cdot 10^{3}$	$3.158 \cdot 10^{-13}$	$1.776 \cdot 10^{5}$	$9.177 \cdot 10^{-12}$
63.02	$1.059 \cdot 10^{-14}$	$3.544 \cdot 10^{3}$	$3.534 \cdot 10^{-13}$	$1.993 \cdot 10^{5}$	$9.799 \cdot 10^{-12}$
70.71	$1.114 \cdot 10^{-14}$	$3.976 \cdot 10^{3}$	$3.954 \cdot 10^{-13}$	$2.236 \cdot 10^{5}$	$1.045 \cdot 10^{-11}$
79.34	$1.179 \cdot 10^{-14}$	$4.462 \cdot 10^{3}$	$4.423 \cdot 10^{-13}$	$2.509 \cdot 10^{5}$	$1.113 \cdot 10^{-11}$
89.02	$1.257 \cdot 10^{-14}$	$5.006 \cdot 10^{3}$	$4.945 \cdot 10^{-13}$	$2.815 \cdot 10^{5}$	$1.184 \cdot 10^{-11}$
$1.000 \cdot 10^{2}$	$1.348 \cdot 10^{-14}$	$5.617 \cdot 10^{3}$	$5.527 \cdot 10^{-13}$	$3.159 \cdot 10^{5}$	$1.260 \cdot 10^{-11}$
$1.121 \cdot 10^{2}$	$1.453 \cdot 10^{-14}$	$6.302 \cdot 10^{3}$	$6.174 \cdot 10^{-13}$	$3.544 \cdot 10^{5}$	$1.345 \cdot 10^{-11}$
$1.257 \cdot 10^{2}$	$1.574 \cdot 10^{-14}$	$7.071 \cdot 10^{3}$	$6.893 \cdot 10^{-13}$	$3.976 \cdot 10^{5}$	$1.479 \cdot 10^{-11}$
$1.411 \cdot 10^{2}$	$1.713 \cdot 10^{-14}$	$7.934 \cdot 10^{3}$	$7.692 \cdot 10^{-13}$	$4.462 \cdot 10^{5}$	$1.734 \cdot 10^{-11}$
$1.583 \cdot 10^{2}$	$1.872 \cdot 10^{-14}$	$8.902 \cdot 10^{3}$	$8.578 \cdot 10^{-13}$	$5.006 \cdot 10^{5}$	$1.623 \cdot 10^{-11}$
$1.776 \cdot 10^{2}$	$2.053 \cdot 10^{-14}$	$1.000 \cdot 10^{4}$	$9.558 \cdot 10^{-13}$	$5.617 \cdot 10^{5}$	$1.689 \cdot 10^{-11}$
$1.993 \cdot 10^{2}$	$2.260 \cdot 10^{-14}$	$1.121 \cdot 10^{4}$	$1.065 \cdot 10^{-12}$	$6.302 \cdot 10^{5}$	$1.785 \cdot 10^{-11}$
$2.236 \cdot 10^{2}$	$2.493 \cdot 10^{-14}$	$1.257 \cdot 10^{4}$	$1.186 \cdot 10^{-12}$	$7.071 \cdot 10^{5}$	$1.881 \cdot 10^{-11}$
$2.509 \cdot 10^{2}$	$2.757 \cdot 10^{-14}$	$1.411 \cdot 10^{4}$	$1.319 \cdot 10^{-12}$	$7.934 \cdot 10^{5}$	$1.989 \cdot 10^{-11}$
$2.815 \cdot 10^{2}$	$3.056 \cdot 10^{-14}$	$1.583 \cdot 10^{4}$	$1.465 \cdot 10^{-12}$	$8.902 \cdot 10^{5}$	$2.124 \cdot 10^{-11}$
$3.159 \cdot 10^{2}$	$3.393 \cdot 10^{-14}$	$1.776 \cdot 10^{4}$	$1.626 \cdot 10^{-12}$		
$3.544 \cdot 10^{2}$	$3.773 \cdot 10^{-14}$	$1.993 \cdot 10^{4}$	$1.801 \cdot 10^{-12}$		
$3.976 \cdot 10^{2}$	$4.201 \cdot 10^{-14}$	$2.236 \cdot 10^{4}$	$1.996 \cdot 10^{-12}$		
$4.462 \cdot 10^{2}$	$4.683 \cdot 10^{-14}$	$2.509 \cdot 10^{4}$	$2.207 \cdot 10^{-12}$		
$5.006 \cdot 10^{2}$	$5.225 \cdot 10^{-14}$	$2.815 \cdot 10^{4}$	$2.436 \cdot 10^{-12}$		
$5.617 \cdot 10^{2}$	$5.834 \cdot 10^{-14}$	$3.159 \cdot 10^{4}$	$2.685 \cdot 10^{-12}$		
$6.302 \cdot 10^{2}$	$6.519 \cdot 10^{-14}$	$3.544 \cdot 10^{4}$	$2.956 \cdot 10^{-12}$		
$7.071 \cdot 10^{2}$	$7.288 \cdot 10^{-14}$	$3.976 \cdot 10^{4}$	$3.248 \cdot 10^{-12}$		
$7.934 \cdot 10^{2}$	$8.151 \cdot 10^{-14}$	$4.462 \cdot 10^{4}$	$3.563 \cdot 10^{-12}$		
$8.902 \cdot 10^{2}$	$9.119 \cdot 10^{-14}$	$5.006 \cdot 10^{4}$	$3.900 \cdot 10^{-12}$		

Appendix B

MCNP input of the Treatment Planning Simulations

B.1 MCNP input of the Treatment Planning

Here an example of the MCNP model for the Treatment Planning is shown, corresponding to the calculation of the Brain doses. Most of the data is retrieved from separate files of large size, and read from inside the mcnp input via the `READ` card. Some few lines of those files will also be shown below.

Main Input File

```
Treatment Planning Sim from DICOM file with BSA from UGR
C Simulation of BNCT treatment with beam from BSA (UGR) and GBM patient from HUVN
C Project within the frame of NeMeSis, led by: I. Porras https://doi.org/10.1016/j.apradiso.2020.109247
C BSA design from P. Torres-Sánchez, I. Porras et al. https://doi.org/10.1038/s41598-021-87305-9
C Patient data (DICOM files) from Hospital Universitario Virgen de las Nieves (HUVN), Granada:
C J. Expósito and J.M. Osorio-Ceballos
C Glioblastoma (GBM) case in frontal lobe - Close to chiasma and optic nerves
C MCNP Input by: P. Torres-Sánchez
C Subsequent data analysis with Dose Maps and Dose-Volume Histograms by: P. Torres-Sánchez (python3: GBM_analysis)
C
C CELL CARD
C Data identification from DICOM files by P. Torres-Sánchez
C (source: python3 ExtractContours.py then python3 IdentifyMaterials.py)
C Cell definition in file, containing a lattice-universe geometry design
C Content of each voxel of the lattice refer to a universe,
C filled with one cell with the material of the same number
C each universe corresponds to a material, namely:
C 1=air, 2=bone, 3=fat, 4=muscle, 5=brain, 6=skin, 7=eye and 8=lens
read file=./MatIdentification/CellCard.txt

C SURFACE CARD
C paralelepipeds defining the lattice
C 1 = first voxel of the lattice, at front,left,bottom corner
C 7 = limits of the latticed region
1 RPP -9.765625 -9.6875 -11.71875 -11.640625 0 0.125
7 RPP -9.765624 9.765624 -11.718749 11.718749 0.000001 26.999999
C Note from surface 7: parallelepiped limits are slightly less
C than the sum of voxels to avoid void regions in the limit
C Suggested by Randy Schwartz (MCNP instructor) at its web
99 SO 200 $ surrounding air to outside universe
301 PZ 0.0 $ surface needed for Source (SSR)

C DATA CARD
C MATERIAL CARD
C material content list as found from DICOM identification. Element composition from ICRP - Densities in g/cm3
```

```
m1 6000 -0.000124 7014 -0.755267 8016 -0.231781 18040 -0.012827 $ air d=1.29E-3 g/cm3
m2 1001 -0.047234 6000 -0.14433 7014 -0.004199 8016 -0.446096 12024 -0.0022
         15031 -0.104970 16032 -0.00315 20040 -0.20993 30064 -0.0001 $ cortical bone d=1.85
m3 1001 -0.119477 6000 -0.637240 7014 -0.007970 8016 -0.232333 11023 -0.0005 12024 -0.00002
         15031 -0.00016 16032 -0.00073 17035 -0.0009044 17037 -0.0002856 19039 -0.00032
         20040 -0.00002 26056 -0.00002 30064 -0.00002 $ adipose tissue d=0.92
m4 1001 -0.100637 6000 -0.107830 7014 -0.027680 8016 -0.754773 11023 -0.00075 12024 -0.00019
         15031 -0.0018 16032 -0.00241 17035 -0.0006004 17037 -0.0001896 19039 -0.000302
         20040 -0.00003 26056 -0.00004 30064 -0.00005 $ skeletal muscle d=1.04
m5 1001 -0.110667 6000 -0.125420 7014 -0.01328 8016 -0.737723 11023 -0.00184 12024 -0.00015
         15031 -0.00354 16032 -0.00177 17035 -0.0017936 17037 -0.0005664 19039 -0.0031
         20040 -0.00009 26056 -0.00005 30064 -0.00001 $ brain d=1.03
m6 1001 -0.100588 6000 -0.228250 7014 -0.04642 8016 -0.619002 11023 -0.00007
         12024 -0.0000474 12025 -0.000006 12026 -0.0000066 15031 -0.00033 16032 -0.0015105
         16034 -0.0000795 17035 -0.0020292 17037 -0.0006408 19039 -0.000792625 19041 -0.000057375
         20040 -0.00015 26056 -0.00001 30064 -0.00001 $ skin d=1.10
m7 1001 -0.112 6000 -0.004 7014 -0.001 8016 -0.883 $ vitreous humor as eye (vitreous is ~80% of eye) d=1.031
m8 1001 -0.099269 6000 -0.193710 7014 -0.053270 8016 -0.653751 $ eye lens d=1.10
C PHYSICS CARD
C nuclear reactions include neutron incident reactions
C neutrons and photons are created as secondaries and transported
phys:n
mode n p
C SOURCE CARD
C source from SSR file - 14 cm aperture diameter + 65 cm radius out of beam - BSA from UGR
C particles recorded at surface 13 in BSA input, loaded onto surface 301 in this input
C source distributed (TR=D1) into one or multiple independent beams as defined in the BeamOrientation.txt file
SSR OLD 13 NEW 301 TR=D1
read file=./SourceBSA/BeamOrientation.txt
C TALLY CARD
C Four tallies corresponding to thermal neutron, fast neutron, boron and gamma doses
C Tallies corresponding to cell 5 == Brain
C Kermas from own calculations based on ENDF-VIII database and NIST
C Kermas from 14N(n,p) derived from n_TOF Measurement
C Calculations by: P. Torres-Sánchez and I. Porras
read file=./KermaFactors/kerma_M5_Brain.txt
PRDMP 2J 1 1 $ produce mctal file as output for faster posterior data analysis
CTME 10000000.0 $ infinite simulation time, in practice limited to number of primaries recorded in SSR file
```

Cell Card File

```
998 0 -7 fill=999 (0 0 0) imp:n 1 imp:p 1
999 0 -1 u=999 lat=1  imp:n 1 imp:p 1 fill=0:250 0:299 0:216
       1 1 1 1 1 1 1 1 1 1 1 1 1 1 1 1 1 1 1 1 1 1 1 1 1 1 1 1 1 1 1
       1 1 1 1 1 1 1 1 1 1 1 1 1 1 1 1 1 1 1 1 1 1 1 1 1 1 1 1 1 1 1
       1 1 1 1 1 1 1 1 1 1 1 1 1 1 1 1 1 1 1 1 1 1 1 1 1 1 1 1 1 1 1
       1 1 1 1 1 1 1 1 1 1 1 1 1 1 1 1 1 1 1 1 1 1 1 1 1 1 1 1 1 1 1
       1 1 1 1 1 1 1 1 1 1 1 1 1 1 1 1 1 1 1 1 1 1 1 1 1 1 1 1 1 1 1
       1 1 1 1 1 1 1 1 1 1 1 1 1 1 1 1 1 1 1 1 1 1 1 1 1 1 1 1 1 1 1

                .
                .
                .

       1 1 1 1 1 1 1 1 1 1 1 1 1 1 1 3 1 1 1 1 1 1 1 1 1 1 1 1 1 1 3
       6 2 4 4 4 4 4 4 4 4 4 4 4 4 4 4 4 4 4 4 4 2 2 2 2 4 4 2 2 2 2 2
       2 2 2 2 2 2 2 5 5 5 5 5 5 5 5 5 5 5 5 5 5 5 5 5 5 5 5 5 5 5 5 5
       5 5 5 5 5 5 5 5 5 5 5 5 5 5 5 5 5 5 5 5 5 5 5 5 5 5 5 5 5 2 5 5
       5 5 5 5 5 5 5 5 5 5 5 5 5 5 5 5 5 5 5 5 5 5 5 5 5 5 5 5 5 5 5 5
       5 5 5 5 5 5 5 5 5 5 5 5 5 5 5 5 5 5 5 5 5 2 2 2 2 2 2 2 2 2 2 2
       2 2 2 2 2 4 4 2 4 4 4 4 4 4 4 4 4 4 4 4 4 4 4 4 2 3 1 1 1 1 1 1
       1 1 1 1 1 1 1 1 1 3 1 1 1 1 1 1 1 1 1 1 1 1 1 1 1 1 1 1 1 1 1 1
       1 1 1 1 1 1 1 1 1 1 1 3 1 1 1 1 1 1 1 1 1 1 1 1 1 1 1 6 6 4 4 4
       4 4 4 4 4 4 4 4 4 4 4 4 4 4 4 4 4 4 2 2 4 4 2 2 2 2 2 2 2 2 2 2
       2 2 5 5 5 5 2 5 5 5 5 5 5 5 5 5 5 5 2 5 5 5 2 5 5 5 5 5 5 5 5 5
       5 5 5 5 5 5 5 5 5 5 5 5 5 5 5 5 5 5 5 5 5 5 5 2 5 5 5 5 5 5 5 5
       5 5 5 5 5 5 5 5 5 5 5 5 5 5 5 5 5 5 5 5 5 5 5 5 5 5 5 5 5 5 5 5
       5 5 5 5 5 5 5 5 5 2 5 5 5 5 5 5 5 2 2 2 2 2 2 2 2 2 2 2 2 2 2 2
       4 4 4 4 4 4 4 4 4 4 4 4 4 4 4 4 4 4 6 6 2 3 1 1 1 1 1 1 1 1 1 1
       1 1 1 3 1 1 1 1 1 1 1 1 1 1 1 1 1 1 1 1 1 1 1 1 1 1 1 1 1 1 1 1

                .
                .
```

```
              .

       1 1 1 1 1 1 1 1 1 1 1 1 1 1 1 1 1 1 1 1 1 1 1 1 1 1 1 1 1 1 1
       1 1 1 1 1 1 1 1 1 1 1 1 1 1 1 1 1 1 1 1 1 1 1 1 1 1 1 1 1 1 1
       1 1 1 1 1 1 1 1 1 1 1 1 1 1 1 1 1 1 1 1 1 1 1 1 1 1 1 1 1 1 1
       1 1 1 1 1 1 1 1 1 1 1 1 1 1 1 1 1 1 1 1 1 1 1 1 1 1 1 1 1 1 1
       1 1 1 1 1 1 1 1 1 1 1 1 1 1 1 1 1 1 1 1 1 1 1 1 1 1 1 1 1 1 1
       1 1 1 1
1 1 -1.29E-3 -99  u=1  imp:n 1 imp:p 1 $ air
2 like 1 but mat=2 rho=-1.85 u=2  imp:n 1 imp:p 1 $ bone
3 like 1 but mat=3 rho=-0.92 u=3 imp:n 1 imp:p 1 $ fat
4 like 1 but mat=4 rho=-1.04 u=4  imp:n 1 imp:p 1 $ muscle
5 like 1 but mat=5 rho=-1.03 u=5 imp:n 1 imp:p 1 $ brain
6 like 1 but mat=6 rho=-1.10 u=6 imp:n 1 imp:p 1 $ skin
7 like 1 but mat=7 rho=-1.031 u=7 imp:n 1 imp:p 1 $ eyes
8 like 1 but mat=8 rho=-1.10 u=8 imp:n 1 imp:p 1 $ lens
1000 1 -1.29E-3 -99 7 imp:n 1 imp:p 1
9999 0 99  imp:n 0 imp:p 0
```

Source Orientation File

```
SI1 L 10 20
SP1 0.5 0.5
TR10 2.49615 -5.32346 18.32820 0.61132 0.67320 0.41603 0.67320 -0.16603 -0.72058 -0.41603 0.72058 -0.55470
TR20 -4.82219 0.29210 18.32820 -0.45056 0.38867 -0.80370 0.38867 0.89586 0.21535 0.80370 -0.21535 -0.55470
```

Kerma Factors and Tallies File

```
C TALLY CARD
C Brain tallies - M = 5 - CELL = 5
f514:n (5<999 [0:250 0:299 0:216]) $ Thermal Neutron Dose
f524:n (5<999 [0:250 0:299 0:216]) $ Fast Neutron Dose
f534:n (5<999[0:250 0:299 0:216])  $ Boron Dose
f544:p (5<999[0:250 0:299 0:216])  $ Gamma Dose
fm544 0.01 $ cGy to Gy
C Brain Kermas
c     Neutron Energy     Kerma (Gy cm2)
#           de514           df514
1.10535e-11 6.25732e-12
1.1079e-11 5.07085e-12
1.11045e-11 5.06538e-12
1.11301e-11 5.05991e-12
1.11558e-11 5.05442e-12
1.11815e-11 5.04891e-12
1.12073e-11 5.0434e-12
1.12331e-11 5.03787e-12
1.1259e-11 5.03233e-12
1.1285e-11 5.02678e-12

              .
              .
              .
```

Appendix C

The neutron beam of the NEAR Station at n_TOF

C.1 The NEAR Station

The n_TOF NEAR Station is a new experimental area designed very close to the spallation target, just outside of the shielding wall of the target-moderator assembly. This new station was presented as a Letter of Intent to the INTC recently [124], with the aim of characterizing the neutron beam during the Commissioning of the n_TOF Facility after the Long Shut-Down 2 (LS2). The NEAR Station is placed next to the spallation target with a lateral view with respect to the direction of proton beam impinging onto the target, at an approximate distance of 3 m. Figure C.1 shows the design o the n_TOF Target Area, with the location of the NEAR to the front. Figure C.2 shows the detail of the design of the new n_TOF Target together with the hole in the lateral shielding wall towards the NEAR Station.

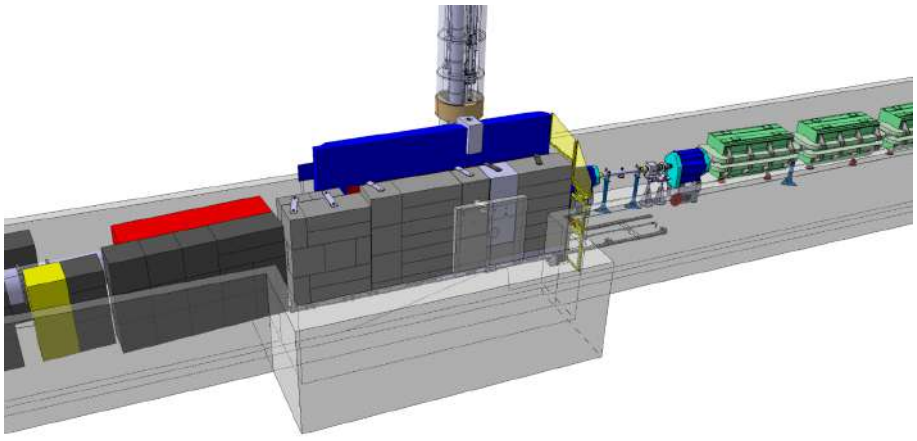

Figure C.1: Layout of the n_TOF Target Area, redesigned after LS2. The proton beam from the PS comes from the left and impinges onto the target, located at the center. Neutrons come out of the target towards EAR-1 in the forward direction, and towards EAR-2 in the upward direction. A hole in the shielding in the lateral direction allows neutrons to come out towards the NEAR Station.

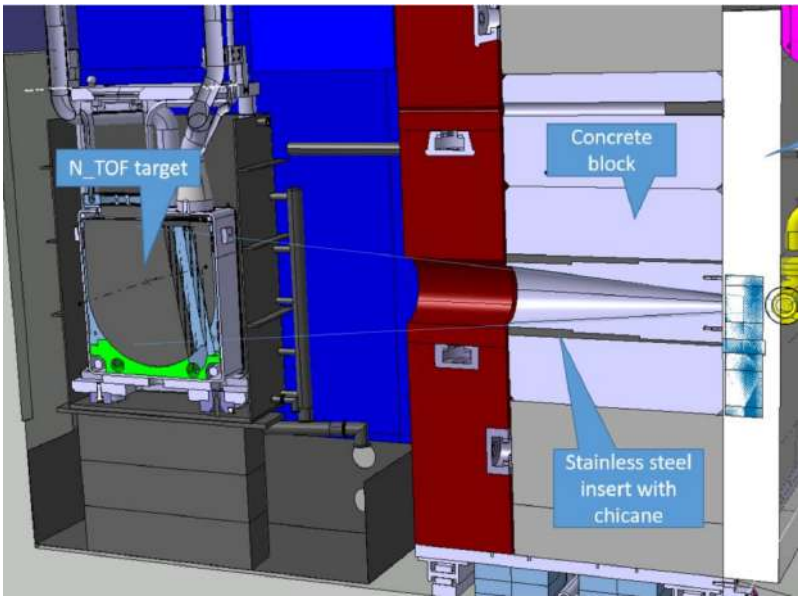

Figure C.2: Lateral cross-sectional view of the n_TOF Target and the shielding wall, including the collimator position. A final marble wall closes the shielding, with an aperture at the collimator position.

Due to the short distance and radiation conditions in the NEAR Station, this experimental area can not be accessed but for short interventions after few hours of cooling of the n_TOF Target (i.e. no beam). For this reason, and in order to profit from the high neutron flux exiting from the n_TOF Target, material irradiation and posterior activation analysis is the main experimental technique to be used at the NEAR. A list of possible applications for a physics program at NEAR is based on this, namely integral cross-section measurements (with the possible measurement of MACS if an appropriate neutron filter and/or moderator is used, e.g. filling the collimator volume). Measurement of short-lived isotopes will be possible given the high neutron flux. Other possibilities of this Station include neutron irradiation for various applications as energy production (fission and fusion), radiation damage in materials and electronic devices (SEEs).

The characterization of the neutron beam and experimental conditions at the NEAR can not make use of the TOF technique due to the short distance from the collimator, given the wide-energy spectrum covering from meV to over hundreds of MeV. To this aim, the Multi-foil Activation Technique, consisting of irradiating a set of materials with known cross-sections which then are used to extract information of the flux via an unfolding procedure, is a best candidate both for characterizing the neutron beam and testing the experimental capabilities and of work-flow of the NEAR Station.

C.2 The Multi-foil Activation Technique

The Multi-foil Activation Technique is based on the use of a set of materials whose response to neutrons is different depending on the energy range of the neutrons. A neutron beam is used to irradiate the foils, activating the material by producing a series of radioactive nuclides depending on the production reaction cross-section, whose activity can be subsequently measured by Gamma Spectroscopy. The produc-

tion of an isotope (N_j) after neutron irradiation is controlled by the overlap between the production reaction cross-section of the isotope (σ_j) and the fluence spectrum (total number of neutrons per unit surface, Φ), following the equation:

$$N_j = n_j \int \Phi(E)\sigma_j(E)dE \tag{C.1}$$

where n_j is the amount of parent nuclei in the sample, and index j runs over all the produced isotopes of interest (M).

In reality, the neutron fluence noticed by the foil is not the same as the neutron fluence under free-air conditions, due to the presence of effects that disturb the beam, mainly the neutron interaction within the foil itself, that attenuates and scatters along the foil, but also the beam changes provoked by surrounding materials (e.g. another foils present in the stack of samples, specially those upstream). The actual fluence inside the foil ($\tilde{\Phi}_j$) is then computable as the incident fluence (Φ) affected by a correction factor (κ_j) so that, $\tilde{\Phi}_j(E) = \Phi(E)\kappa_j(E)$:

$$N_j = n_j \int \tilde{\Phi}_j(E)\sigma_j(E)dE = n_j \int \Phi(E)\kappa_j(E)\sigma_j(E)dE \tag{C.2}$$

Likewise, the isotope production can be further normalized per unit mass or per unit nuclei in each sample, obtaining the specific number of activations during the irradiation, S_j, which will be the main input data from the experiment:

$$S_j = \int \Phi(E)\kappa_j(E)\sigma_j(E)dE \quad , \; S_j = \frac{N_j}{n_j} \tag{C.3}$$

In order to be useful for this technique, these isotopes have to live long enough so that they can be detected after the irradiation finishes. Another constraint for the selection of materials is that the produced isotope decays with subsequent emission of gamma radiation with enough intensity so that gamma lines can be seen over ambient background by means of Gamma spectroscopy.

Under these general conditions, the selection of materials is based on the shape of the production cross-sections, in a way that having different reactions peaking in well defined and separated energy ranges allows to determine the neutron fluence in each energy range.

For this reason, the neutron fluence can be divided in a set of "Neutron Energy Groups", which can be chosen arbitrarily on origin, but in general correspond to the shapes of the reactions under use, mainly defined by the presence of resonances or thresholds. To this aim, the fluence spectrum can be divided in group-wise fluences, Φ_i, with index i running over the total number of energy groups (N), where the sum of all group-wise fluences equates the total fluence:

$$\Phi_i = \int_{E_i}^{E_{i+1}} \Phi(E)dE \quad , \; \Phi = \sum_i \Phi_i \tag{C.4}$$

In the same way, the total isotope production can be divided in the portions corresponding to neutrons in each Energy Group and divided by the group-wise fluence, which are the number of activations in the foil per unit flux in the corresponding energy group, giving rise to the elements of the Response Matrix:

$$R_{ij} = \frac{1}{\Phi_i} \int_{E_i}^{E_{i+1}} \Phi(E)\kappa(E)(E)\sigma_j(E)dE \quad , \; S_j = \sum_i R_{ij}\Phi_i \tag{C.5}$$

The right-side equation shows that the total isotope production can be computed as the sum of the contributions from each energy range, as the group-wise fluence weighted with the elements of the Response Matrix. This can also be shown in matrix form:

$$\mathbf{S} = \hat{\mathbf{R}}\mathbf{\Phi} \tag{C.6}$$

where, $\mathbf{S}$ is the specific activation number vector, with $dim(\mathbf{S}) = M$, $\mathbf{\Phi}$ is the fluence vector, with $dim(\mathbf{\Phi}) = N$, and $\hat{\mathbf{R}}$ is the Response Matrix, with $dim(\hat{\mathbf{R}}) = N \times M$.

This matrix equation can be unfolded in order to solve for the fluence:

$$\mathbf{S} = \hat{\mathbf{R}}\mathbf{\Phi} \Rightarrow \hat{\mathbf{R}}^{-1}\hat{\mathbf{R}}\mathbf{\Phi} = \hat{\mathbf{R}}^{-1}\mathbf{S} = \mathbf{\Phi} \tag{C.7}$$

This is specially relevant since the matrix has the constraint of $M > N$ so that the linear system of equations is solvable when trying to find $\mathbf{\Phi}$. This way, the total number of Neutron Energy Groups, which define the energy resolution of the spectrum, are determined by the number of reaction products that can be found in the irradiated samples. In the same way, having a low number of reactions whose cross-section peaks in a certain part of the spectrum reduces the resolution in that region. In general, only a relatively small number of materials (hence produced isotopes) are available and adequate for being used in this technique, which causes this method to have lower energy resolution than other techniques.

In general, the production cross-sections of many reactions widely overlap and/or do not peak clearly at a single neutron energy, obstructing the choice of well defined reactions for each energy range. There are various strategies that can be used to overcome this, from the use cadmium covers to attenuate the thermal neutron influence, to using pairs of samples of a material with strong resonances so that the first foil acts as filter for the second foil, hence observing a so-called "black resonance" (e.g. ^{197}Au(n,γ) strong resonance at 4.9 eV), or by the use of materials with dominating resonances which produce a significant amount of the total isotope production, in the intermediate energy region, for instance ^{60}Co production. Also using reactions with no strong resonances is adequate to be used as a contrast with the others (e.g. ^{45}Sc(n,γ)). For the high energy region, the use of threshold reactions is paramount, as indicates the presence of neutrons of energy higher than the reaction threshold. In this range, most isotopes present (n,p), (n,α) or (n,xn) reactions with thresholds in the range of few to tens of MeV. A special feature of the (n,xn) reactions is that the threshold increases with the number of secondary neutrons, providing a set of well defined reactions to determine the flux at high energy. At energies

higher than several tens of MeV, the reaction cross-section data is scarce, and so the models, so only extrapolations can be used. In any case, the prior knowledge on the maximum energy of the neutrons of the beam under study does not fall above the hundreds of MeV, and the flux is expected to be much reduced in this region, which reduces the need of reaction cross-sections sensitive to this energy range. Figure C.3 shows a set of cross-sections of reactions used in this study, comprising reactions that provide information on the spectrum at low energy (below 1 MeV), such as (n,γ) from ^{197}Au, ^{59}Co and ^{45}Sc, and threshold reactions in the MeV range, as ^{27}Al(n,α)^{24}Na, ^{115}In(n,n')^{115m}In or several ^{59}Co(n,xn), ^{197}Au(n,xn) and ^{209}Bi(n,xn) reactions, among others.

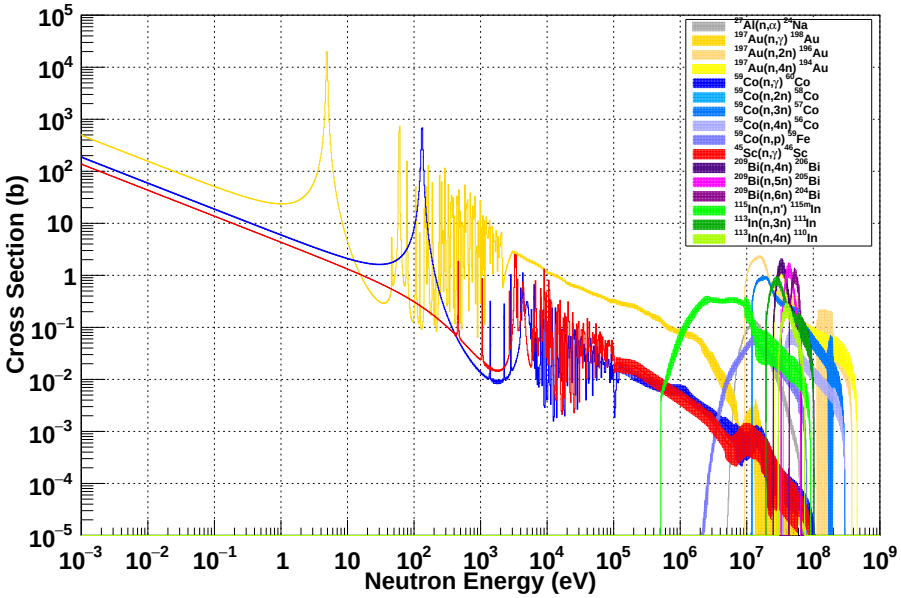

Figure C.3: Cross-sections of the reactions whose products were observed in the foils irradiated at NEAR. The foils were chosen so that a few reactions provided information at low energy (< 1 MeV) and a large set of threshold reactions provided details on the spectrum at high energy. Each set of colors correspond to a material, namely grey for Al, yellow for Au, blue for Co, red for Sc, violet for Bi and green for In. Uncertainty in the cross-section data are also shown as the shaded pattern filling. Data is extrapolated above 60 or 200 MeV (depending on the data) due to the lack of data above these energies. Cross-section data comes from ENDF-VIII for the (n,γ) reactions, and TENDL 2019 for the rest (threshold reactions).

C.3 Experimental Procedure

Two experiments were run in order to characterize and analyze possible applied configurations the neutron beam off the NEAR Station collimator. The first experiment aimed at characterizing the beam in free conditions, in order to measure the neutron spectrum coming from the n_TOF target and its spacial homogeneity. The second experiment aimed at testing the possibility of using some materials as filters that could be used to create different configurations for the future applications of the NEAR Station. In this case, a 70 cm aluminium bar was conceived as a filter between the collimator and the sample's irradiation position.

C.3.1 First Irradiation: Beam Characterization

The aim of the first irradiation was to measure the beam conditions, including the homogeneity of the beam and the spectrum. Samples were put in the central position aligned in front of the collimator, and extra samples were put around this position to check the possible variation in flux in all directions.

Set-up and Irradiation at NEAR

The set-up consisted of a sample holder with 9 "mini-holder" positions on it, where disk-shaped foils could be placed, as shown in Figure C.4.

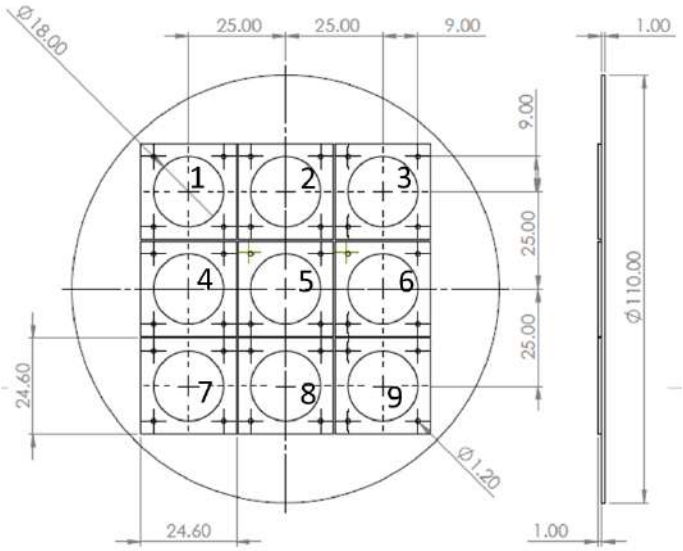

Figure C.4: Design of the sample holder with nine mini-holder positions for sample positioning and irradiation. The sample holder is made of Al. Dimensions are given in mm. Each mini-holder is 18 mm in diameter, which allows for using foils of 1 inch in diameter as the used ones from Shieldwerx [125]. The samples were held within the mini-holder positions with the help of a Cd capsule (only at the downstream position) and two mylar layers.

An Au sample was put in the first place from beam (upstream) in all mini-holder positions. This was made so that the homogeneity of the beam could be tested based on the same reactions in all positions. Au is a good candidate for this purpose due to the overall well known cross-sections and due to the 3 different isotopes produced during irradiation that could be measured later, namely ^{198}Au from the (n,γ) reaction, which provides information about the low energy part of the spectrum (mainly thermal and around the 4.9 eV resonance), and ^{196}Au and ^{194}Au from the (n,2n) and (n,4n) threshold reactions, which provide information above their production thresholds at 8.114 and 23.26 MeV, respectively.

At the central position, a full stack of samples was put so that a wide range information could be obtained from the irradiation. For this case, samples of Au, Co, Sc, In and Al were used in that order from the neutron beam. A second Au sample was put after all these in order to have a shadowed/attenuated beam to have extra information about the low energy range by comparing the first and last Au samples.

Material	Position	Diameter (mm)	Thickness (mm)	Mass* (g)
Au	5-u	12.7	0.0508	0.1268
Co	5	12.7	0.0508	0.0644
Sc	5	12.7	0.127	0.0503
In	5	12.7	0.127	0.1309
Al	5	12.7	0.762	0.2552
Au	5-d	12.7	0.0508	0.1283
Au	1	12.7	0.0508	0.1167
Au	2	12.7	0.0508	0.1213
Au	3	12.7	0.0508	0.1154
Au	4	12.7	0.0508	0.1214
Au	6	12.7	0.0508	0.1257
Au	7	12.7	0.0508	0.1250
Au	8	12.7	0.0508	0.1243
Au	9	12.7	0.0508	0.1222

Table C.1: Foil sizes, masses and positions for the set-up of the first irradiation at NEAR. Position stands for the mini-holder as in Figure C.4. 5-u and 5-d refer to the upstream and downstream Au samples in position #5, respectively. * The precision of the scaler was 0.0001 g. Dimensions correspond to the sheet provided by the supplier.

Table C.1 summarizes the sizes and masses of all the samples of this irradiation.

The holder with the samples on it was mounted onto a support and put in place at the NEAR Station for irradiation. The holder was left at 20 cm from the collimator and aligned so that the central position coincided with the center of the collimator. Figure C.5 shows the final position of the holder before irradiation.

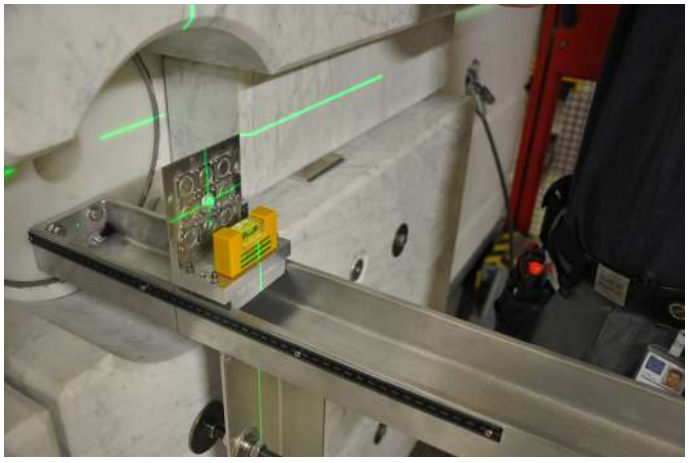

Figure C.5: Set-up of the first irradiation at NEAR. The sample holder was mounted onto a support and put on top of the rail. The samples were then positioned at 20 cm from the collimator position and aligned to the center of the collimator with the aid of the ruler, lasers and level.

Neutron irradiation took place between 15^{th} to 27^{th} September 2021. For this irradiation, a total amount of $7.0067 \cdot 10^{17}$ protons were delivered on the n_TOF target. Figure C.6 shows the irradiation history during the irradiation period, including all beam stops for interventions at the other Experimental Areas, and beam stops and instabilities of the proper functioning of the PS beam.

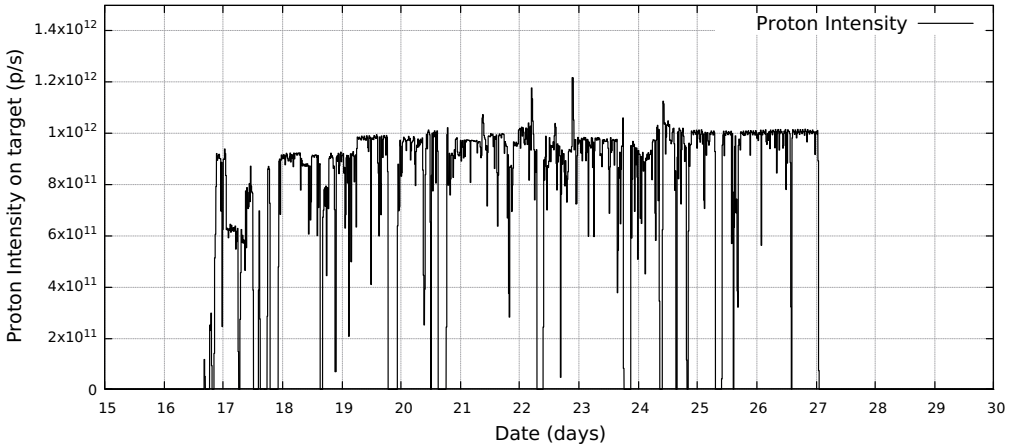

Figure C.6: Irradiation History for the first experiment. Time is shown as date, in days of the second half of the month of September 2021. Intensity is given as the intensity on the n_TOF target, in protons per second. The samples were mounted at NEAR on 15^{th} September, while irradiation started on late 16^{th} September due to a programmed stop of the beam to n_TOF.

After the end of irradiation at 01:01 h on 27^{th} September, the holder with the samples were left at their position for 13 hours of cooling time. Then the samples were extracted from the NEAR in a scheduled access to the n_TOF Target Area. The samples were then moved to the n_TOF Electronics Lab were the samples were collected from the holder and prepared for measurement. Figure C.7 shows the samples after they were taken out of the holder.

Figure C.7: Samples after being collected from the holder from the irradiation, ordered corresponding to their mini-holder position in the holder. Au samples can be seen in all positions. Cd capsules can also be seen as the last foil in all positions. The even positions were Cd-covered, hence the two pars of the capsules can be seen. Samples of other materials as Sc, Co, Al and In are also shown.

Gamma spectroscopy with HPGe detector

A series of scheduled measurements were made with the HPGe detector available at the n_TOF Electronics Lab. The HPGe detector is a P type coaxial Ge detector by Mirion Technologies, model EGPC 25 S/N 54035. Data acquisition was processed via a MCA Module AmpTek MCA8000D and the DPPMCA AmpTek display software. The HPGe detector was cooled via an electric cryo-cooling system by Camberra. A series of different holders and spacers were used to keep the samples at a fixed position with well defined distances to the detector. Figure C.8 shows the measurement set-up including the cryo-cooling system and the detector with the first spacer (labeled with "END", 3 cm from the detector) on top of it.

Figure C.8: HPGe Detector used at the n_TOF Electronics Lab, where the measurements took place. The detector together with the preamplifier and the electric cooling system are portrayed.

A total of 87 separate measurements were made during the period from 27$^{\text{th}}$ September to 19$^{\text{th}}$ October 2021. The general rule under the schedule was to complete at least 3-5 measurements of each sample at different times whenever possible. For short lived isotopes, at least 2 measurements were made and all those were kept within the first 2-3 days after irradiation. Due to the short half-life of some isotopes, two samples had to be put together in the detector for measurement. That was the case of Al and In samples. Some few background measurements were included within the schedule. Figure C.9 shows some representatives of the spectra from each type of material foil.

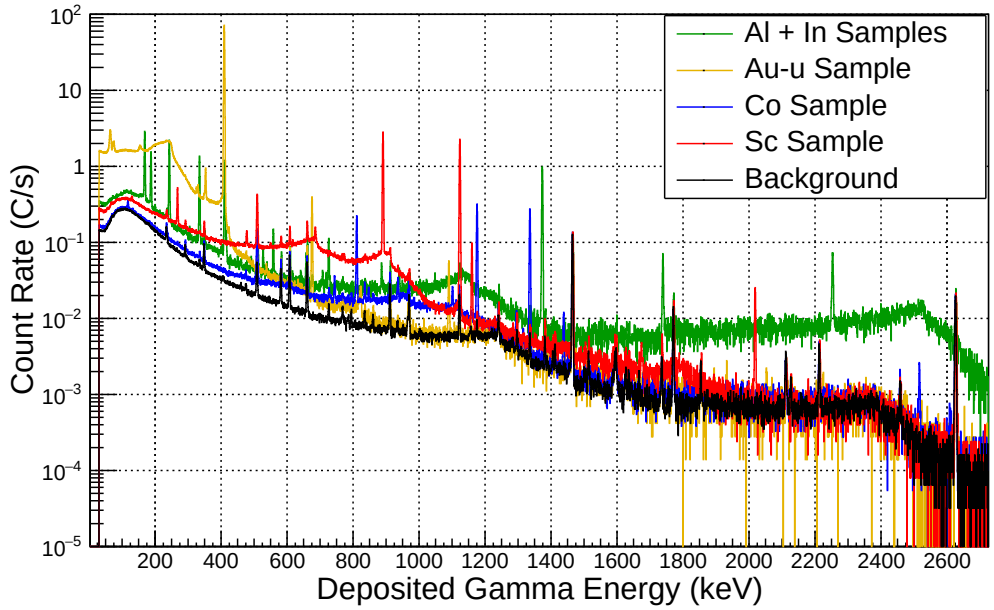

Figure C.9: Selection of a few Gamma spectra from the HPGe detector, from the measurements of the samples of the first irradiation at NEAR. The black line corresponds to the background measurement, made for a long run in the middle of the experiment, and provides reliable information on the ambient radiation and prevents from considering contaminated lines. The spectra from Au-u (golden-coloured) corresponds to the upstream Au sample, and also Co (blue) and Sc (red) contain the spectrum from a single foil. Contrarily, the green line corresponds to a joint measurement of the Al and In samples, which had to be measured at the beginning due to the presence of short-lived isotopes. A special remark can be also pointed regarding this spectrum, due to the presence of an intense line from ^{24}Na at 2754 keV, whose photopeak cannot be seen in this spectrum, but Compton interactions and single- and double-escape lines can be notably observed above the background in the 1500-2600 keV range.

C.3.2 Second Irradiation: Beam filtering with Al bar

The aim of the second irradiation was to test the possibility of filtering of the beam with an Aluminum filter.

An aluminium bar was placed between the collimator and the sample's position in order to test the filtering. The Al bar was 70 cm long and its diameter was large enough to cover the full area of the samples in the central position, but not covering the full collimator. Two polyethylene cylinders were used additionally at both ends of the Al bar, with 7.5 cm (close to the collimator) and 2.5 cm (far from the collimator) of thickness. Figure C.10 shows the setup prepared in place for irradiation at NEAR.

Material	Position	Diameter (mm)	Thickness (mm)	Mass* (g)
Au	5-u	12.7	0.0508	0.1271
Co	5	12.7	0.0508	0.0620
Sc	5	12.7	0.127	0.0523
Al	5	12.7	0.754	0.2503
Bi	5	12.7	0.254	0.3076
Au	5-d	12.7	0.0508	0.1219

Table C.2: Foil sizes, masses and positions for the set-up of the second irradiation at NEAR. Position stands for the mini-holder as in Figure C.4. 5-u and 5-d refer to the upstream and downstream Au samples in position #5, respectively. * The precision of the scaler was 0.0001 g. Dimensions correspond to the sheet provided by the supplier.

Figure C.10: Set-up of the second irradiation at NEAR. The sample holder was mounted onto a support and put on top of the rail, and aligned as in the previous case. In between the collimator and the samples, an Al bar of 70 cm in diameter was placed, also centered with the collimator. Two polyethylene blocks used to reduce thermal neutron fluence and hence activation of the Al bar were put at both ends of the bar.

For this second irradiation, the central position was used with a stack of samples similar to the one used in the first irradiation. In this case, the In sample was replaced by a Bi sample, which provides more detailed information on the high energy range (above 10 MeV). The aim was to check if such high energy neutrons were present after filtering with Al. The stack configuration in that case was Au, Co, Sc, Al, Bi, Au.

Table C.2 summarizes the sizes and masses of all the samples of this irradiation.

Neutron irradiation took place between 1st to 15th November 2021. For this irra-

diation, a total amount of $1.2 \cdot 10^{18}$ protons were delivered on the n_TOF target. Figure C.11 shows the irradiation history during the irradiation period.

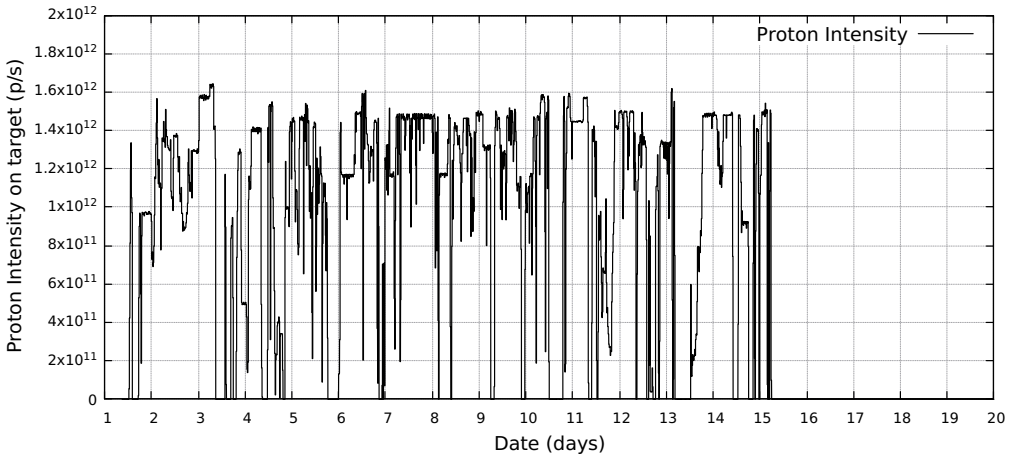

Figure C.11: Irradiation History for the second experiment. Time is shown as date, in days from the beginning of the month of November 2021. Intensity is given as the intensity on the n_TOF target, in protons per second. The samples were mounted at NEAR on the morning of 1$^{\text{st}}$ November, and irradiation begun shortly after. Irradiation ended on 15$^{\text{th}}$ at 6:00 h, coinciding with the Year-End Technical Stop (YETS) as scheduled.

After the end of irradiation at 06:00 h on 15$^{\text{th}}$ November, the holder with the samples were left at their position for 27 hours of cooling time. Then the samples were extracted from the NEAR in a scheduled access to the n_TOF Target Area. The samples were then moved to the n_TOF Electronics Lab and prepared for measurement.

For the gamma spectroscopy measurement, the experimental conditions were similar to those of the first irradiation. The measurement period took place from 16$^{\text{th}}$ November to 3$^{\text{rd}}$ December 2021. Figure C.12 shows some examples of the spectra taken for the different material foils.

C.4 Data Analysis

The experimental data from the gamma spectrometry was used to calculate the activity due to the different isotopes produced by neutron irradiation. The activity data was then used to compute the number of activations inside each sample, taking into account the irradiation history. The number of activations per atom in the samples was then the main input for the unfolding algorithm. The response function for the unfolding routine was the other main input data, which includes the corresponding isotope's production cross-section together with experimental corrections such as neutron attenuation along the stack of samples, the self-shielding of the sample and other scattering effects around the set-up. The result of the unfolding of the spectrum is the group-wise neutron flux.

C.4.1 Activity calculations

The experimental spectra from the gamma spectrometry were processed in order to extract data on the number of counts of each of the photopeaks of the gamma

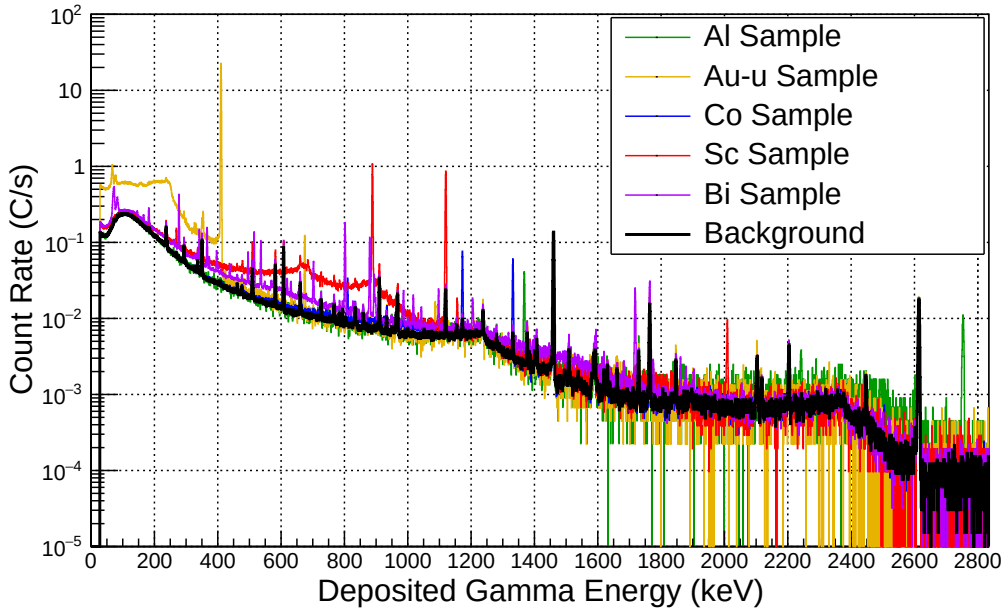

Figure C.12: Selection of a few Gamma spectra from the HPGe detector, from the measurements of the samples of the second irradiation at NEAR. The black line corresponds to the background measurement, made for a long run in the middle of the experiment, and provides reliable information on the ambient radiation and prevents from considering contaminated lines. The spectra from Au-u (golden-coloured) corresponds to the upstream Au sample, and also Co (blue), Bi (violet) and Sc (red) contain the spectrum from a single foil. In contrast with the measurements from the first irradiation, in this case the Al sample was also measured alone (green). A change in gain with respect to the measurements from the first irradiation allows to observe the intense line from ^{24}Na at 2754 keV. A noticeable change with respect to the measurements from the first irradiation is the lower count rates in all cases, consistent with a lower activation due to the presence of the 70 cm Al bar.

lines due to each isotope present in the sample. Separate measurements of ambient background together with the overall background (including the Compton-like background from higher energy lines present in the sample) was subtracted via a linear fit of the neighbourhood of the gamma line. Figure C.13 shows an example of a fit of a photopeak together with the neighbouring background.

The count rate, $\dot{C}$ was then computed from the total number of counts during the measuring time, t_M. Dead time was kept below 1 % during all the measurements and corrected in the count rate computation.

Subsequently, the activity of the sample $A(t_W)$, measured after a waiting time since the end of irradiation (EOI), can be computed following the equation:

$$A(t_W) = \frac{\dot{C}}{n_\gamma \varepsilon} \frac{\lambda t_M}{1 - e^{-\lambda t_M}} \tag{C.8}$$

where ε is the efficiency of the detector and n_γ is the absolute intensity of the gamma line of interest. The second factor in the equation is a correction factor for

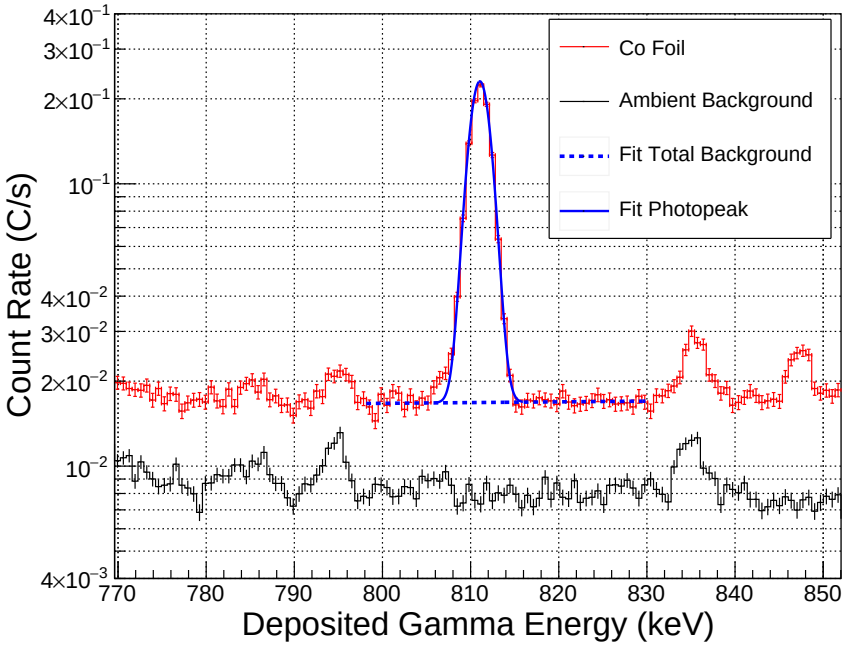

Figure C.13: Example of fitting of a photopeak from a gamma spectrum. The data corresponds to a measurement of the Co foil, and the observed line coincides with the 810.8 keV line from the decay of ^{58}Co, produced by the (n,2n) reaction. The ambient background is shown in black. Over that, the observed spectrum with the Co foil in place is shown in red. This spectrum shows an increased background, generated mainly by Compton interactions from the 1173 and 1332 keV lines from the decay of ^{60}Co, and other less intense lines of higher energy. The dashed blue line corresponds with a fit of the total background, by a linear fit of the counts in the vicinity of the line. The solid blue line corresponds to the fitting of the 810 keV line. The final count rate was computed by integrating the actual count rate data in the closest vicinity of the line (the same region as used for the fit of the line), and subtracting the integral of the background's fitting.

the reduction in activity of the sample during the measurement, which is also taken into account. This factor is typically small due to the relative large half-lives of most of the isotopes compared with the duration of the measurements (typically in the range of one to few hours), except for some cases of fast decaying isotopes such as ^{115m}In, ^{110}In with half-lives of 4.486 h and 4.92 h in the In sample, ^{24}Na with a half-life of 14.997 h in the Al sample, and to a lesser extent for the ^{194}Au with a half-live of 38.02 h in the Au samples.

The efficiency of the detector is computed based on a previous calibration by E. Stamati [126]. The efficiency calibration was computed at different distances from the sample position to the detector (namely 3, 6, 9, 12 and 15 cm) making use of the spacers and sample holder available for this detector. This efficiency estimation was computed with a calibrated radioactive source of ^{152}Eu, with a well measured initial activity determination and an uncertainty under 2 %.

Since the efficiency calibration, ε_0, was made using a point-like source with a size much smaller than the actual samples, additional correction factors, f_s, had to be considered in order to compute the actual efficiency for the measurements:

$$\varepsilon = \varepsilon_0 \cdot f_s \tag{C.9}$$

These correction factors were estimated via Monte Carlo simulations, using a MCNP6 model of the detector following the dimensions of the detector from the detector calibration. These correspond to the two main effects that reduce the efficiency in the actual samples when compared to the initial, ε_0 calibration. The sample extension in diameter reduces the solid angle at which the detector sees the sample, thus reducing the efficiency. The sample thickness reduces the efficiency due to the gamma attenuation inside the material. A couple of simulations were made for each of the lines observed in the spectra. The first simulation used a point-like isotropic source at the position in the center of the holder, with the energy of the gamma line. The second simulation included a model of the sample, including the sample dimensions, including diameter and thickness. From the ratio between counts in the photopeak from the second and the first simulation we can extract the correction factor. This correction factor is dependent on the energy of the gamma line, the material of which the sample is made, and the position (distance) of the sample to the detector. Figure C.14 shows the correction factor for the samples of the first irradiation.

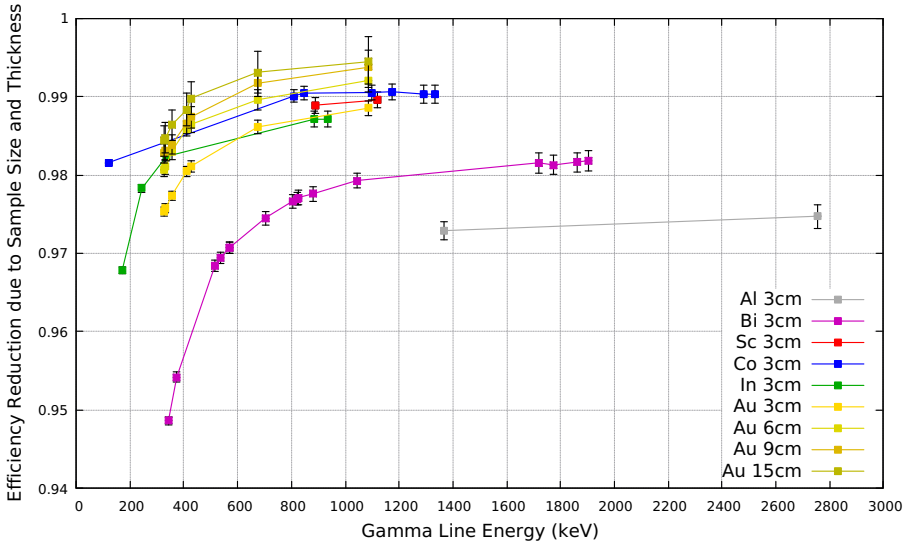

Figure C.14: Correction factors for the efficiency of the detector due to the sample size (attenuation inside material and reduction of solid angle due to sample extension). Correction as a function of gamma energy are shown, with data-points corresponding to the energy of the gamma lines observed from each sample. Each color correspond to a different foil (namely grey for Al, violet for Bi, red for Sc, blue for Co, green for In and yellow-ish for Au). The different shades of yellow correspond to the various sample-detector distances used for Au samples (for the purpose of count rate reduction to avoid large dead time losses). All other samples were always measured at 3 cm to increase statistics. Al and Bi samples exhibit a greater reduction due to the larger thicknesses of these foils, specially for Al.

Once the activity due to each of the isotopes present in the samples was measured by means of the various lines observed in the spectra, the activity at the End Of Irradiation (EOI) was computed via extrapolation from the decay equation:

$$A_{EOI} = \frac{A(t_W)}{e^{-\lambda t_W}} \tag{C.10}$$

An error estimation for all the activity calculations was assessed, including the statistical error from the number of counts in each photopeak of the spectra, the error due to the efficiency calibration (2 %) and the correction factors (0.1-0.5 %), and the uncertainty in the absolute intensity of the gamma lines (taken from the ENSDF database).

Each separate measurement of the same sample provided an additional data-point. The set of all activity estimations of the same isotope, from different lines and measurements, was weight-averaged according to their uncertainty via inverse-variance weighting. The compatibility of the measurements was assessed via a χ^2 test. Figure C.15 shows an example of all the independent activity estimations together with the weighted average, taken as the final estimation of the Activity at End of Irradiation for each observed isotope.

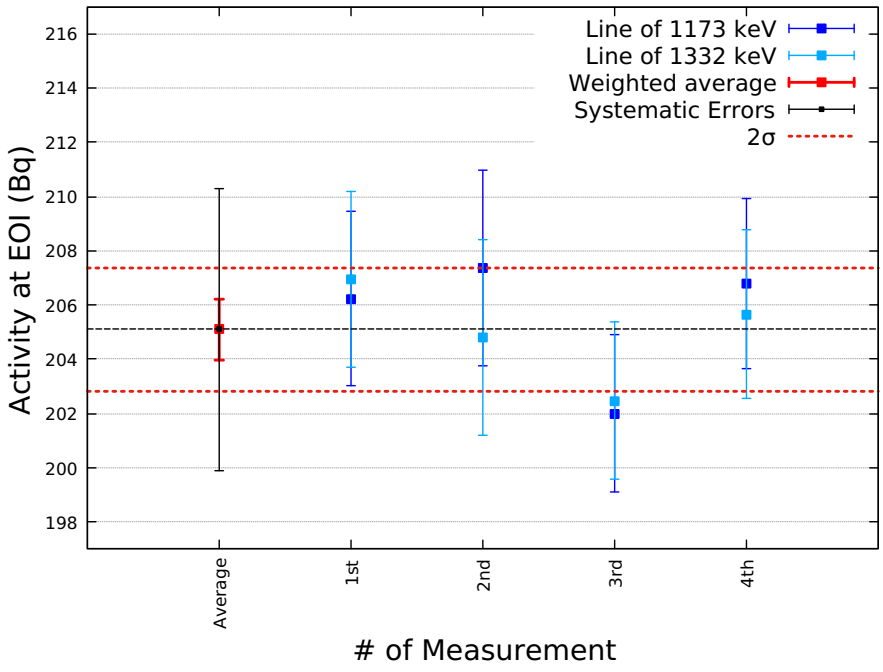

Figure C.15: Set of four successive measurements of the ^{60}Co activity in the Co foil of the first irradiation. Light and Dark blue colors correspond to the estimates via the 1173 and 1332 keV lines. The final weighted average is shown in red, with extended black error bars to account for additional systematic uncertainty (efficiency calibration).

The changing conditions of the proton beam that generates the neutron beam under study does not allow a straightforward definition of a saturation activity, due to the use of different average proton beam intensities, together with the multiple beam stops, during the time of irradiation. For this reason, an strategy based on the computation of the total number of activations during the irradiation was followed. This procedure aims at computing the total fluence of the beam during the irradiation, from which the actual flux for a given proton beam intensity can be easily derived by normalization.

This way, the activity at EOI has to be further used to compute the total number of activations in the sample during the irradiation, given the history of irradiation.

For such calculation, the conversion factor between activity (A_{EOI}) and number of activations during the irradiation (N_I), defined as in eq. C.11 has to be derived.

$$R = \frac{N_I}{A_{EOI}} \tag{C.11}$$

The total amount of activations depends on the total neutron fluence that impinges onto the sample, $\Phi(E)$, and the production cross-section, $\sigma(E)$, multiplied by the number of nuclei available for the neutron interaction, n:

$$N_I = n \int \Phi(E)\sigma(E)dE \tag{C.12}$$

The fluence can be interpreted as the sum of the instantaneous flux generated by a proton pulse, $\phi(E)$, multiplied by the number of proton pulses at any given time, $T(t)$:

$$\Phi(E) = \int_0^{t_{EOI}} T(t)\phi(E)dt \tag{C.13}$$

Taking these two expressions together and rearranging, we can separate the neutron-energy dependent variables with the time-dependent ones on two separate integrals:

$$N_{EOI} = n \int_0^{t_{EOI}} T(t)dt \int \phi(E)\sigma(E)dE \tag{C.14}$$

The activity at EOI can be computed from the number of active nuclei that remain active at the sample at that time, R_{EOI}, simply by multiplying by the corresponding decay constant λ, as $A_{EOI} = \lambda R_{EOI}$. The remaining active nuclei at the sample can be computed as from equation C.14, just including a convolution kernel $e^{-\lambda(t_{EOI}-t)}$. This accounts for the decay of part of the isotopes generated at time t and remain in the sample at t_{EOI}. Thus, after rearranging, the activity at EOI can be computed, as:

$$A_{EOI} = n\lambda e^{-\lambda t_{EOI}} \int_0^{t_{EOI}} T(t)e^{\lambda t}dt \int \phi(E)\sigma(E)dE \tag{C.15}$$

Finally, inserting C.15 and C.14 into C.11, we arrive at:

$$R = \frac{e^{\lambda t_{EOI}}}{\lambda} \frac{\int_0^{t_{EOI}} T(t)dt}{\int_0^{t_{EOI}} T(t)e^{\lambda t}dt} \tag{C.16}$$

This conversion factor has to be computed for each observed isotope with their corresponding decay constant. As can be observed from the equation, this factor

only depends on the evolution of the irradiation history ($T(t)$) and the half-life of the isotope.

After this conversion from activity at EOI to total number of activations during irradiation has been made, the normalization to the specific number of activations yields the final result which then can be used as input for the Unfolding Routine.

C.4.2 The Unfolding Routine

Several methods have been developed to unfold the spectrum from the response matrix and activation measurements, based on iterative computer codes. These codes provide a "best fit" using the set of data from activation of a list of isotopes, and an initial guess spectrum which serves as starting point for the iteration procedure. These methods are able to provide good resolution in terms of energy, such as the widely known 640-bin SAND-II code. However, those methods are highly dependent on the initial guess spectrum, and in addition, they do not typically include the uncertainty on cross-section data and experimental activation data into the computation of the final flux. Another aspect that is not well assessed by these methods is the uncertainty estimation of the final spectrum, together with correlation estimates. The use of Bayesian inference methods is able to overcome such problems, and is part of some statistical techniques with growing importance over the last decades, also in the case of multi-foil activation for spectrum measurements, such as the papers by Chiesa *et al.*, which are taken as reference for this study [127, 128].

Bayesian inference

Bayesian statistics is based on the Bayes theorem, expressed in the form of the following equation:

$$P(\theta|data) = \frac{P(data|\theta)}{P(data)} P(\theta) \tag{C.17}$$

Here θ is the set of parameters that we want to determine from the application of the model (in our case the set of Energy group-wise fluxes). Each term of the equation has a well defined meaning:

- $P(\theta)$ is the so-called *Prior* distribution, which reflects the knowledge on the value of the parameters before the measurement has taken place, i.e. the data is included into the model. It can go from completely uninformative distributions (any possible value is equally likely), through moderate restrictions on the possible values (i.e. general constraints as non-negative values only or limited to a range of few orders of magnitude around the expected value) to even well known distributions in case of the existence of previous measurements or data from reliable simulations, in whose case the new experimental data will serve as fine refinements of the knowledge on the parameters.
- $P(data|\theta)$ is the Likelihood distribution, determined via the model as the probability of finding some experimental data given a set of values for the parameters θ.

- $P(data)$ is a normalization factor, corresponding to the probability of getting some experimental data irrespective of the value of θ.
- $P(\theta|data)$, finally, is the so-called *Posterior* distribution, as the probability of finding the set of parameters θ given the experimental data. The *Posterior* summarizes all the information on the possible values of the parameters after doing the experiments, also including the *a priori* information given by the *Prior*.

The strategy followed when using Bayesian analysis consists of defining a model with rules between data and the parameters of interest, in which the analysis provides a mechanism to "update" the knowledge given by the *Prior* to the final results found in the *Posterior*. By using reasonably uninformative *Priors*, the *Posterior* distribution of parameters will be mostly determined by the actual data, specially if the information inside the Likelihood is dominant, i.e. enough experimental data is present.

Except for very simple models with few parameters, the *Posterior* distribution can only be determined through computational techniques. The most adequate for this aim are based on Markov Chain Monte Carlo (MCMC) simulations. MCMC is grounded on drawing a sequence of iterations on the set of parameters of interest, which tend to navigate around the parameter space with a likelihood equal to the one given by the probability distribution. Given an initial set of values for the parameters, θ_0, an algorithm such as the Metropolis-Hastings or the Gibbs sampler are able, after a few iterations of "thermalization" or "burn-in", to draw samples, θ_i, of the *Posterior* distribution with the only information given by the Likelihood functions $P(data|\theta)$. This procedure also overcomes one of the biggest problems on Bayesian inference, since the final parameters, sampled within the *Posterior* distribution, provide a good estimate of a kernel of actual joint *Posterior* distribution, without the need of complex normalization computations which would otherwise undermine this strategy. The final results from the MCMC simulations provide samples of the parameters from which the marginal distributions $P(\theta_i)$ can be obtained, and also conditional distributions $P(\theta_i|\theta_j)$. From these, the parameter uncertainties σ_{θ_i} and covariance matrix (and correlations) (θ_i, θ_j) can be easily extracted.

In order to make this process of MCMC to obtain the *Posterior* from the *Priors* and Likelihoods, the computational code JAGS (Just Another Gibbs Sampler) has been used [129]. This program is able to analyze data using a Bayesian statistics by using the Gibbs technique of sampling for the MCMC.

Bayesian Model

The statistical model for our flux unfolding is based on the matrix form of the equation for the total amount of isotopes production. In order to define the model on JAGS, the *Priors* and Likelihoods have to be described. For this work, uniform ($\mathbf{U}(x_{min}, x_{max})$) and Gaussian ($\mathbf{N}(\mu, \sigma)$) distributions will be used to model the *Priors* and Likelihoods. In this model, we will consider uncertainties coming from the experimental data (i.e. uncertainty in activity estimation), and also uncertainty in the Response Function. The response function is computed using nuclear cross-section data from standard libraries as ENDF-VIII and TENDL 2019, which provide uncertainty estimates for a broad number of reactions and also in a wide energy

range in most cases[1]. Additional uncertainty in the Response function comes from the simulations used to estimate the effects of beam interaction with the stack of material samples, as neutron scattering, beam attenuation, and self-absorption within the material samples. For this case, the experimental values for specific number of activations in each material sample ($S_{j,exp}$) are considered as random draws from a Gaussian distribution centered at the result from the folding of the flux vector with the response matrix ($\sum_i R_{s,ij}\Phi_i$), with an standard deviation equal to the experimental uncertainty ($\Delta S_{j,exp}$) in the determination of such quantity:

$$S_{j,exp} \sim \mathbf{N}\left(\mu = \sum_i R_{s,ij}\Phi_i, \sigma = \Delta S_{j,exp}\right) \tag{C.18}$$

Also, for each element of the Response Matrix, random draws, $R_{s,ij}$, are taken using a Gaussian distribution centered at the computed value, R_{ij} and with a standard deviation as discussed in the previous paragraph:

$$R_{s,ij} \sim \mathbf{N}\left(\mu = R_{ij}, \sigma = \Delta R_{ij}\right) \tag{C.19}$$

Since minimal information is wanted to be included in the *Priors* so as to minimize possible bias, only uniform distributions will be used in this case:

$$\Phi_i \sim \mathbf{U}\left(x_{min} = 0, x_{max} = M\right) \tag{C.20}$$

where M is an upper bound for the total fluence for this experiment, estimated as two orders of magnitude greater than the expected fluence from simulations. This is done so that any group-wise fluence will fall inside the range $[0, M]$. In case that after analysis, the *Posterior* distribution of each Φ_i approached this limit or was limited by it, this could be extended without altering the rest of the model.

After running the model with the experimental data ($S_{j,exp}$) and Response matrix R_{ij} as inputs (comprised also the uncertainty estimates), the output of the program is a list of samples of the joint *Posterior* distribution, $P(\mathbf{\Phi}|\mathbf{S_{exp}}, \mathbf{R_{ij}})$, from where the estimates (*i.e.* mean and standard deviation) of each group-wise fluence and the total fluence can be extracted. Special care has to be taken when adding up the contributions from each energy group to the total fluence, due to the presence of covariances that can be strong in some cases, specially if all response functions have similar shapes for two or more energy groups. For this reason, a separate marginal *Posterior* distribution can be computed from the sum of the group-wise components, by adding the contributions from the samples themselves instead of using the final estimates (*mean and standard deviation*) which lack that covariance information.

The result for the fluence can be further normalized to determine the nominal flux of the beam of the NEAR Station (neutron flux per nominal pulse of $7 \cdot 10^{12}$ protons on target).

[1]For those cases where uncertainty was not provided, a conservative estimate of 30 % relative error was used, following the same procedure as previous research. Where extrapolations had to be performed (specially the linear extrapolation of (n,xn) reactions over 60 or 200 MeV, where no cross-section data is available), a 50 % relative error was assumed.

Calculation of the Response Matrix

The elements of the Response Matrix can be computed following equation C.5, which is reproduced here:

$$R_{ij} = \frac{1}{\Phi_i} \int_{E_i}^{E_{i+1}} \Phi(E)\kappa_j(E)\sigma_j(E)dE \qquad \text{(C.5 revisited)}$$

The spectrum correction factor $\kappa(E)$ can be computed by means of MCNP6 simulations, which include the full geometry of the stack of samples. The result of this simulations can be observed in Figure C.16 which shows the product $\kappa_j(E)\sigma_j(E)$ for the foils in the first irradiation, where the effects of beam attenuation due to the presence of strong resonances is clearly observed in downstream foils.

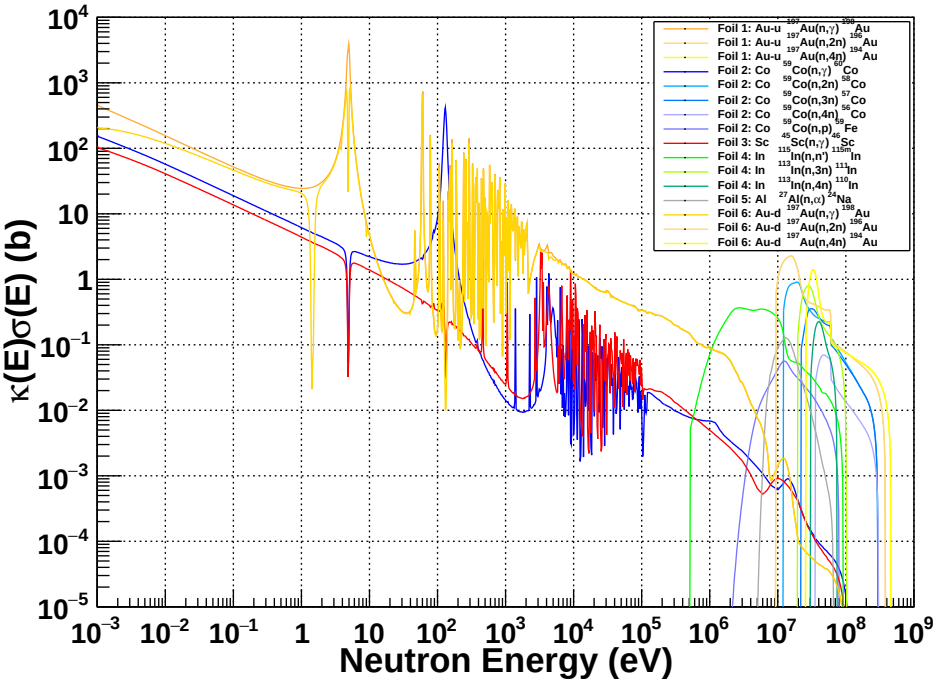

Figure C.16: Product of cross-section and the attenuation factor due to self-shielding and the presence of upstream foils, for the geometry of the first irradiation. The effect is small (negligible for the threshold reactions) in general except around the energy of strong absorption resonances, such as the ^{115}In(n,γ)^{116}In at 1.457 eV, ^{197}Au(n,γ)^{198}Au at 4.9 eV and ^{59}Co(n,γ)^{60}Co at 132 eV. The attenuation is also noticeably increasing through the foils at low energy in the 1/v region. The attenuation in the pair of Au samples is notable, specially the partially-black resonance effect. The 1.457 eV absorption dip, caused by the absorption in the In foil, is only observed in the last Au-d foil, and produces the radioactive isotope ^{116m}In, which could not be measured due to its shorter half-life of 54.29 min and had already fully decayed after 13 h of cooling time.

An additional factor that has to be carefully addressed is that of the shape of the intra-group fluence. The total fluence within the energy group is not relevant here, since it is already accounted as a normalization factor via the Φ_i on the denominator. However, the actual shape of the fluence within the group is relevant, since it works

as a weighting factor contributing to the integral. This way, the intra-group fluence shape can enhance some neutron energies at the expense of others, actually changing the overall effective cross-section in the energy group. This is a non-negligible effect that has to be overcome by using additional information for the shape of the spectrum, or alternatively, if this is not available, by a careful study of the uncertainty propagation due to the use of different realistic shapes. As a matter of fact, several previous details of the beam are known prior to the measurement and spectrum unfolding. These include the fact that the spectrum shows a maxwellian-like shape at low energies, specially around and below $kT = 25.3$ meV. In addition, by the way the neutrons are produced in a spallation source, high energy limits are known, and a neutron evaporation peak is also expected. A partially flat spectrum (relatively close to isolethargy) is expected at below MeV energies through the epithermal range. Overall, no sharp edges are expected in the spectrum, by no means at the arbitrary positions of the energy group edges.

For this reason, an initial shape, following all the previous key points, is used to perform the full analysis and extract a first estimate of the fluence. Subsequently, a series of small variations of the shape of the fluence are performed in order to iteratively converge towards a quasi-continuous shape for the fluence. These iterations are performed "by-hand", but always respecting the previous points. The iterative process is finished once the spectrum appears as quasi-continuous, within the uncertainties obtained via the bayesian inference procedure.

C.5 Results

Table C.3 shows the activity at EOI and specific number of activations for each sample in the stack of the central mini-holder in the first irradiation, Table C.4 does the same for the Au foils in the non-central positions, and similarly, Table C.5 does for the stack of samples of the second irradiation.

Foil	Reaction	Half-life	$A_{EOI}(Bq)$	$S(10^{-12}/atom)$
Au-u	^{197}Au(n,γ)^{198}Au	2.6941 d	187900 ± 5400	431 ± 18
	^{197}Au(n,2n)^{196}Au	6.1669 d	864 ± 32	2.79 ± 0.14
	^{197}Au(n,4n)^{194}Au	38.02 h	509 ± 30	1.066 ± 0.077
Co	^{59}Co(n,γ)^{60}Co	1925.28 d	205.1 ± 5.2	75.0 ± 3.4
	^{59}Co(n,2n)^{58}Co	70.86 d	99.0 ± 2.8	1.393 ± 0.068
	^{59}Co(n,3n)^{57}Co	271.74 d	7.04 ± 0.25	0.367 ± 0.021
	^{59}Co(n,4n)^{56}Co	77.236 d	4.95 ± 0.36	0.0757 ± 0.0070
	^{59}Co(n,p)^{59}Fe	44.490 d	13.56 ± 0.52	0.1231 ± 0.0073
Sc	^{45}Sc(n,γ)^{46}Sc	83.79 d	1435 ± 36	23.1 ± 1.2
In	^{115}In(n,n')^{115m}In	4.486 h	7135 ± 250	7.73 ± 0.37
	^{113}In(n,3n)^{111}In	2.8047 d	373 ± 14	0.489 ± 0.024
	^{113}In(n,4n)^{110}In	4.92 h	181 ± 15	0.196 ± 0.019
Al	^{27}Al(n,α)^{24}Na	14.997 h	1605 ± 51	0.2147 ± 0.0087
Au-d	^{197}Au(n,γ)^{198}Au	2.6941 d	111300 ± 3000	252 ± 10
	^{197}Au(n,2n)^{196}Au	6.1669 d	851 ± 34	2.71 ± 0.14
	^{197}Au(n,4n)^{194}Au	38.02 h	585 ± 31	1.212 ± 0.079

Table C.3: Activity and specific number of activations per atom due to each of the production reactions in the foils of the stack in the central position (#5) for the first irradiation. The half-life of each produced isotope is also given.

C.5.1 Homogeneity of the beam

In order to analyze the homogeneity of the beam, Au foils were placed in the nine miniholder positions. For each of them, the activity due to ^{194}Au, ^{196}Au and ^{198}Au was measured. Each of these isotopes provide information on the size and shape of the beam in different energy ranges, corresponding to their production cross-sections. The homogeneity at low energy is provided by ^{198}Au due to the strong resonance of the (n,γ) at 4.9 eV, but also a significant contribution comes from the thermal 1/v region. In the high energy region, ^{196}Au and ^{194}Au probe the beam shape in the range 9.4-25.5 MeV and 26.5-44.6 MeV, where the peaks of the cross-section are found, respectively.

Reaction	Foil	$A_{EOI}(Bq)$	$S(10^{-12}/atom)$
^{197}Au(n,γ)^{198}Au	5	187900 ± 5400	431 ± 18
	2	134400 ± 3700	323 ± 13
	4	125700 ± 3400	302 ± 12
	6	129800 ± 3500	301 ± 12
	8	124000 ± 3300	291 ± 12
	1	113100 ± 3000	282 ± 11
	3	115300 ± 3000	291 ± 12
	7	107500 ± 2900	251 ± 10
	9	113800 ± 3100	271 ± 11
^{197}Au(n,2n)^{196}Au	5	864 ± 32	2.79 ± 0.14
	2	790 ± 35	2.67 ± 0.15
	4	695 ± 32	2.34 ± 0.14
	6	744 ± 34	2.42 ± 0.14
	8	689 ± 31	2.27 ± 0.13
	1	549 ± 24	1.92 ± 0.11
	3	584 ± 27	2.07 ± 0.12
	7	468 ± 22	1.534 ± 0.092
	9	537 ± 25	1.80 ± 0.11
^{197}Au(n,4n)^{194}Au	5	509 ± 30	1.066 ± 0.077
	2	523 ± 30	1.146 ± 0.080
	4	517 ± 30	1.132 ± 0.082
	6	544 ± 32	1.151 ± 0.083
	8	523 ± 31	1.117 ± 0.082
	1	455 ± 25	1.037 ± 0.072
	3	455 ± 27	1.048 ± 0.076
	7	392 ± 25	0.833 ± 0.063
	9	432 ± 27	0.939 ± 0.071

Table C.4: Activity and specific number of activations per atom due to each of the production reactions in the Au foils in the nine positions for the first irradiation. Foils at the same distance to the central point are arranged together for an easier comparison (central, even positions at the edges and odd positions at the corners).

The activity at End of Irradiation provides a good estimate for the homogeneity of the beam, but it needs to be corrected for the mass of the samples, which even being in principle of the same dimensions and mass, showed differences up to 9 % in mass. For this reason, the specific number of activations per atom in the sample produced

Foil	Reaction	Half-life	$A_{EOI}(Bq)$	$S(10^{-12}/atom)$
Au-u	^{197}Au(n,γ)^{198}Au	2.6941 d	18540 ± 640	60.3 ± 2.9
	^{197}Au(n,2n)^{196}Au	6.1669 d	69.4 ± 3.3	0.272 ± 0.016
	^{197}Au(n,4n)^{194}Au	38.02 h	63.4 ± 7.9	0.206 ± 0.028
Co	^{59}Co(n,γ)^{60}Co	1925.28 d	40.3 ± 1.1	8.22 ± 0.75
	^{59}Co(n,2n)^{58}Co	70.86 d	10.54 ± 0.36	0.1570 ± 0.0086
	^{59}Co(n,4n)^{56}Co	77.236 d	0.711 ± 0.042	0.01148 ± 0.00092
	^{59}Co(n,p)^{59}Fe	44.490 d	1.049 ± 0.074	0.01020 ± 0.00093
Sc	^{45}Sc(n,γ)^{46}Sc	83.79 d	521 ± 13	8.22 ± 0.41
Al	^{27}Al(n,α)^{24}Na	14.997 h	100.9 ± 7.2	0.0230 ± 0.0018
Bi	^{209}Bi(n,4n)^{206}Bi	6.243 d	92.3 ± 2.6	0.1594 ± 0.0058
	^{209}Bi(n,5n)^{205}Bi	14.91 d	54.7 ± 1.8	0.1554 ± 0.0064
	^{209}Bi(n,6n)^{204}Bi	11.22 h	69.2 ± 9.4	0.078 ± 0.011
	^{209}Bi(n,7n)^{203}Bi†	11.76 h	61.2 ± 9.7	0.088 ± 0.015
Au-d	^{197}Au(n,γ)^{198}Au	2.6941 d	15200 ± 550	51.5 ± 2.6
	^{197}Au(n,2n)^{196}Au	6.1669 d	63.8 ± 3.4	0.261 ± 0.017
	^{197}Au(n,4n)^{194}Au	38.02 h	69.6 ± 4.9	0.235 ± 0.020

Table C.5: Activity and specific number of activations per atom due to each of the production reactions in the foils of the stack in the central position (#5) for the second irradiation. The half-life of each produced isotope is also given. † The amount of ^{203}Bi produced during the irradiation was measured and hence included in this table, though it was not further used due to the lack of reliable cross-section data above 60 MeV, where the production is expected to peak.

during the total duration of the irradiation is used to assess this issue. The activity and number of activations in each sample are detailed in Table C.4. Figure C.17 displays this information, normalized to the activations in the central foil for each reaction, for an easier comparison.

In total, a sample for the central position (miniholder #5), four samples for the edges (miniholders #2, #4, #6 and #8) and four for the corners (miniholders #1, #3, #7 and #9) were used. The support and sample holder were aligned with the center of the beam properly with the aid of lasers and a level, as shown in a previous figure (Figure C.5). In principle, an uniform beam should have produced the same level of irradiation in all samples in the same group, while the level of irradiation should decrease from the center to the edges and the corners. The observed activations show that this overall behavior is followed, with some remarks that have to be addressed. The beam dimensions vary with the neutron energy, being better collimated at low energy, with a sharp decrease ($\sim$ 30 %) in the activations from the center to the edges, which then do not show a further decrease to the corners. In addition, the irradiation appears to be slightly higher around the top part of the holder, decreasing towards the bottom. This same effect is observed in the activation of ^{196}Au, though

in this case the decrease of irradiation from the center to the edges is not as sharp ($\sim$ 5-20 %). A different behavior is found with the highest energy probe ^{194}Au, where a light increase in irradiation with respect to the center is found in the edges, compatible within uncertainty with an uniform spectrum. In this case, the bottom corners show less irradiation of around $\sim$ 20 %.

As a summary, the beam shows a sharper edge at lower energy, being not evident at high energy. Inhomogeneities in the beam are found, corresponding to a higher irradiation in the top part, with reduced flux at the bottom edge and bottom corners, which accounts up to 15 % in some cases. No relevant inhomogeneities are found in the lateral left-right axis.

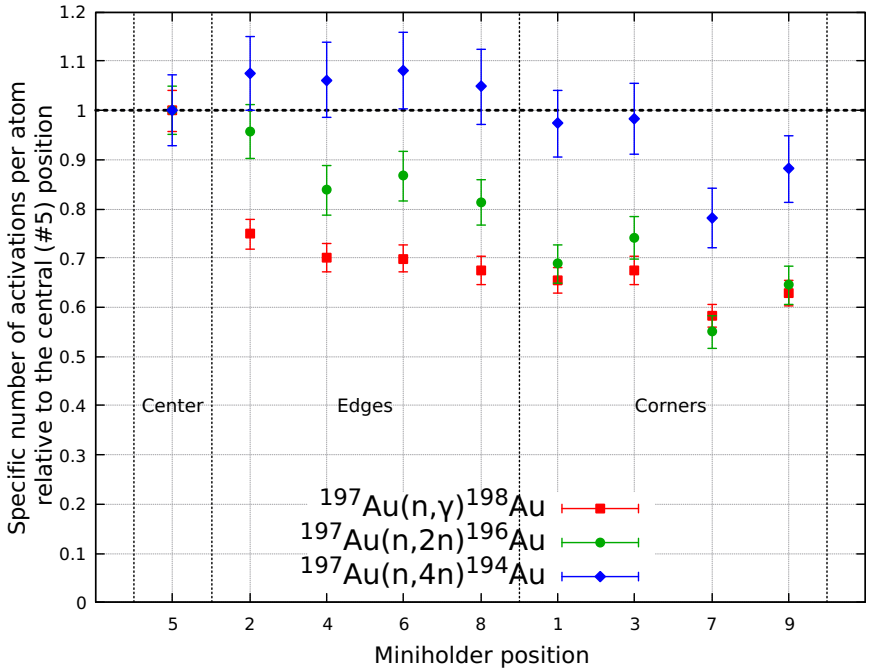

Figure C.17: Number of activations per atom relative to the central foil, in the Au foils used in the first irradiation to test the homogeneity of the beam. Color code corresponds to the three reactions that probe low energy (n,γ) red; 10-25 MeV (n,2n), green; and 25-45 MeV (n,4n), blue. Miniholder positions are separated by their distance to the central position, grouping them in "Center", "Edges" and "Corners". For a reminder of the numbering code, Figure C.4 shows the holder design.

C.5.2 The unfolded spectrum at the central position

The result of the process of unfolding with the bayesian routine yields a set of samples of the joint *Posterior* distribution, consisting of compatible values of each group-wise fluence, which are linked through the distribution. From them, we can extract the marginal *Posterior* distribution corresponding to each of the group-wise fluences, and also for the distribution-like sum of them, in order to compute the total fluence. Then, by normalizing taking into account the total number of protons during the irradiation, we obtain the group-wise flux and the total flux. The estimate and uncertainty (mean and standard deviation of the marginal *Posterior* distributions) of each group-wise flux and total flux for the first irradiation, are shown in Table C.6. The overall estimate for the total flux obtained from the characterization of the beam

is $(870 \pm 280) \cdot 10^6$ n/cm^2 per nominal pulse of $7 \cdot 10^{12}$ protons on the n_TOF target. Note that this value does not correspond to the sum of the group-wise fluxes, since the correlations between each group-wise flux are taken into account through the joint *Posterior* distribution. Likewise, the total flux has a slightly lower uncertainty than the sum of the components due mainly to strong negative correlations within some of the groups, which will be discussed later.

# Energy Group	E_i (eV)	E_{i+1} (eV)	$\phi_i(10^6$ n/cm$^2/(7 \cdot 10^{12}$ *ppp*$))$
0	10^{-3}	$1.25 \cdot 10^{-1}$	3.45 ± 0.76
1	$1.25 \cdot 10^{-1}$	$3.16 \cdot 10^{1}$	19.6 ± 2.1
2	$3.16 \cdot 10^{1}$	$2.14 \cdot 10^{3}$	40.1 ± 3.6
3	$2.14 \cdot 10^{3}$	$5.01 \cdot 10^{5}$	420 ± 280
4	$5.01 \cdot 10^{5}$	$3.72 \cdot 10^{6}$	307 ± 26
5	$3.72 \cdot 10^{6}$	$9.12 \cdot 10^{6}$	38.2 ± 7.0
6	$9.12 \cdot 10^{6}$	$1.23 \cdot 10^{7}$	4.4 ± 1.2
7	$1.23 \cdot 10^{7}$	$2.51 \cdot 10^{7}$	7.96 ± 0.79
8	$2.51 \cdot 10^{7}$	$3.47 \cdot 10^{7}$	2.27 ± 0.48
9	$3.47 \cdot 10^{7}$	10^{9}	23.6 ± 1.9
# Total flux	E_0 (eV)	E_N (eV)	$\phi = \sum_i \phi_i$ (n/cm$^2/(7 \cdot 10^{12}$ *ppp*$))$
-	10^{-3}	10^{9}	870 ± 280

Table C.6: Energy groups, including lower and upper energy limits of each group (in eV), and estimates of the flux within each energy group, normalized per nominal proton pulse. Total flux along the complete energy range is also given in the last row. The estimate and uncertainty for the flux is taken from the marginal *Posterior* distribution of each parameter (group-wise flux) as mean and standard deviation.

The choice of the energy groups was driven by the available isotopes detected in the irradiated material, by analyzing the production cross sections. Three different reactions provided information below 600 keV, with additional information due to two Au upstream and downstream samples, where the second provided a quasi-black resonance case, and hence extra information in the region near the 4.9 eV Au resonance. For this reason, four energy groups were used in this range, loosely corresponding to thermal, Au resonance, Co resonance and keV range (no strong resonances were present in ^{45}Sc(n,γ)^{46}Sc, so overall baseline structure was obtained through this reaction). For the rest of the energy group, their limits were defined by the presence of a threshold in one of the reactions, being the first above 500 keV, from the ^{115}In(n,n')^{115m}In reaction. No relevant structures or data is available above 60 MeV, hence a large energy group covers this range.

The unfolded spectrum is displayed in Figure C.18, compared to previous FLUKA simulations of the flux at the same point where the irradiated foils were placed. The spectrum follows the expected shape with a strong evaporation peak, and a magnitude higher than that of simulations, which is larger in the epithermal range

and also in the 5-20 MeV range, where reaches a factor of 4 in some cases. The flux in Figure C.18 is displayed in two different ways, where the first (red) corresponds to the flux in each energy group taken as a single value. The second way (purple), includes the information of the intra-group flux shape, which is relevant for the calculation of the Response Matrix. These shapes were defined so that the general structure of the spectrum corresponded to a sum of spallation and evaporation peak, a flat isolethargic component in the epithermal range and a maxwellian distribution around the thermal range. The last case, however, was mostly overstepped by the epithermal component leading only to a maxwellian decrease in flux below the thermal range. An iterative process was made in order to obtain a quasi-continuous shape for the flux, with no sharp changes in flux at the energy group edges, which was achieved within uncertainties across the spectrum.

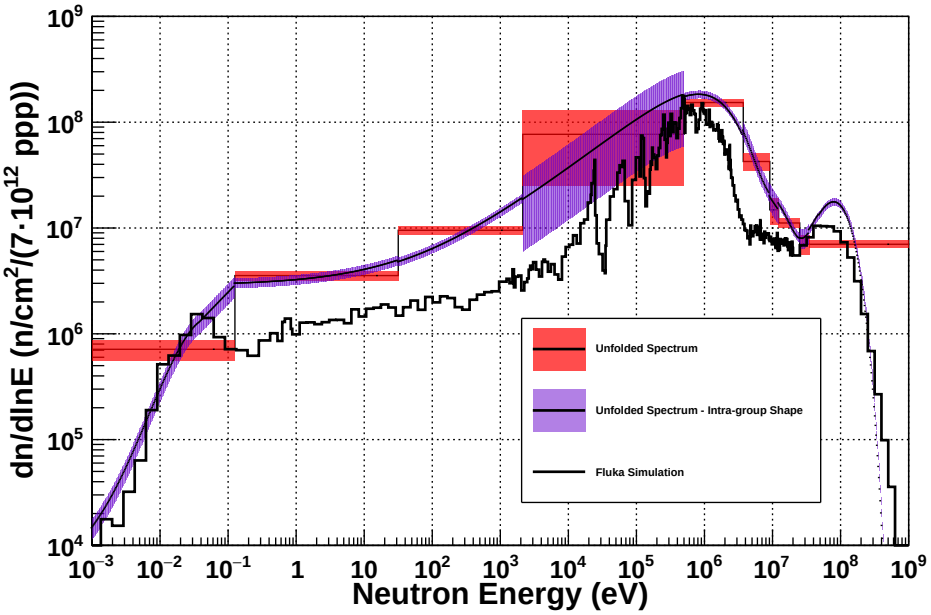

Figure C.18: Unfolded Spectrum of the NEAR Station at the central position for the first irradiation, normalized per nominal flux of $7 \cdot 10^{12}$ protons on target. Group-wise fluxes from the unfolding are given in red and scaled accordingly per unit lethargy. Same fluxes, but shaped as with the intra-group flux shape used in response function computations are shown in violet, also normalized so that total area equals the flux. Uncertainty is marked as the width of the rectangles (one standard deviation).

Apart from obtaining estimates of group-wise fluxes from the joint *Posterior* distribution, a dedicated analysis on the covariances and correlations between each pair of energy groups was carried out. This analysis provides information on the adequacy on the choice of the number and limits of the energy groups. In this regard, a large number of energy groups, which would be convenient in order to increase the energy resolution, would contribute to large correlations between groups and not provide actual information but increase group-wise uncertainty. For instance, any energy group could arbitrarily be divided into two separate energy groups in order to increase energy resolution. In case that there is no significant difference among the response functions between the two new groups, the neutron flux would

not be better known due to that splitting. Thus, the sum of the two energy group fluxes would have a lower uncertainty than the sum of the individual uncertainties, leading to a strong negative correlation. Conversely, where sharp differences are present in at least one response function, the group splitting would increase the energy resolution compared to the non-separated group due to the absence or small correlation between groups. The correlation matrix for the unfolding (scaled to energy group sizes) is shown in Figure C.19. Examples of both of the previously discussed situations are present here. For example, there is negligible correlation between low energy and high energy energy groups, shown by pale yellow coloring in these cases, clearly revealing independent sources of information to compute the low energy fluxes ((n,γ) reactions) and high energy fluxes (threshold reactions). Likewise, only adjacent energy groups in the high energy part show some amount of negative correlation, which is due to reactions contributing strongly to both groups. At low energy, a different situation is observed, with a small number of groups (due to a small number of reactions in this energy range), and also similar shapes for all the reactions. That is the case specially for the first and fourth energy groups, where all response functions show clearly the same pattern, namely 1/v at the first energy group and the Resolved and Unresolved Resonance Region (RRR and URR) at the fourth, leading to same ratios of effective cross sections and hence similar ratios of response function matrix elements, driving the system of equations to lower discrimination between these groups.

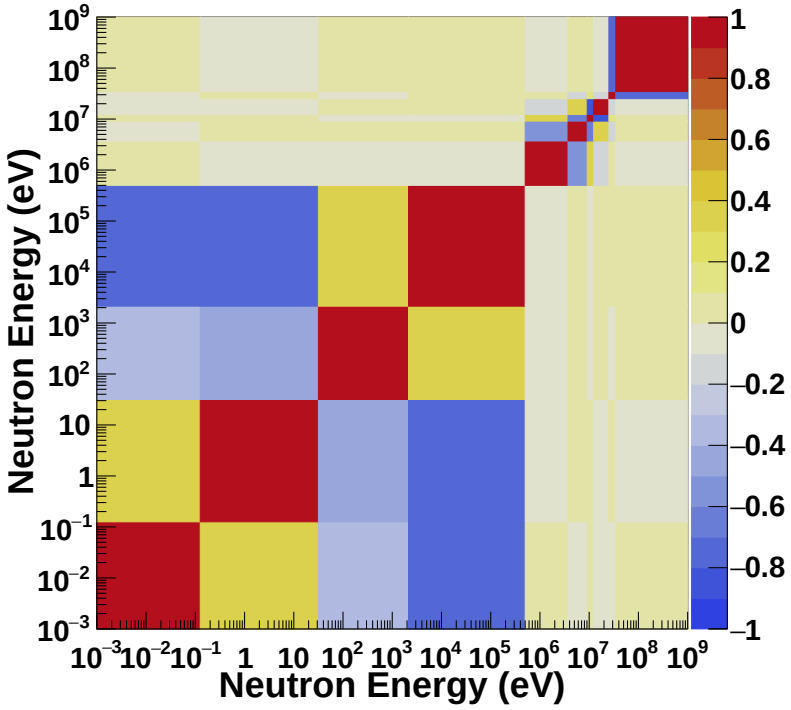

Figure C.19: Correlation matrix ($\frac{cov(i,j)}{\sigma_i \sigma_j}$) for the unfolding of the flux of the characterization of the NEAR Station beam. The energy group sizes are scaled to their sizes in eV. Color corresponds to correlation, being red fully correlated and blue fully anti-correlated, with pale yellow uncorrelated. Red squares corresponding to the main diagonal correspond actually to self-correlation which equals to 1.

C.5.3 The unfolded spectrum of the filtered configuration

The unfolding of the spectrum for the Al-filtered beam was in general similar to the previous case, with two main changes to remark. The first one is the use of a Bi foil instead of an In foil, which changes the response function and hence the choice of the limits of the energy groups. The second is the change in the intra-group flux shape to adapt to the additional knowledge provided by the fact of using an Al filter. By swapping In for Bi, we add extra information on the high energy region (n,xn) with $n \geq 4$ at the expense of losing the In reactions, one of which provided relevant information due to a low energy threshold below 600 keV. This change motivates the choice of new energy limits for the high energy groups to account for the Bi-related thresholds, and manifests for example on the addition of a second-to-last group from 34.7 to 44.7 MeV. The total number of groups remains the same as in the first irradiation, as well as the limits of the low energy groups. Regarding the intra-group flux shapes that were used to define the response functions, in this case a stronger thermal contribution was found, hence low weight of the epithermal-shaped contribution in this part compared to the previous unfolding. More importantly, since the beam in this case is measured after a 70 cm Al filter, a reduction in the spectrum is expected as compared to the previous case, except in the range around 25 keV where a dip in the total cross-section of Al is present. For this reason, a peak in this energy is added to the overall shape of the spectrum, with the additional restriction that the maximum height of that peak should not exceed the observed flux with no filtration, within uncertainties.

# Energy Group	E_i (eV)	E_{i+1} (eV)	$\phi_i(10^6$ n/cm$^2/(7 \cdot 10^{12}$ *ppp*$))$
0	10^{-3}	$1.25 \cdot 10^{-1}$	1.38 ± 0.14
1	$1.25 \cdot 10^{-1}$	$3.16 \cdot 10^{1}$	0.76 ± 0.35
2	$3.16 \cdot 10^{1}$	$2.14 \cdot 10^{3}$	3.29 ± 0.71
3	$2.14 \cdot 10^{3}$	$1.58 \cdot 10^{6}$	146 ± 81
4	$1.58 \cdot 10^{6}$	$3.72 \cdot 10^{6}$	1.8 ± 1.6
5	$3.72 \cdot 10^{6}$	$9.12 \cdot 10^{6}$	1.54 ± 0.63
6	$9.12 \cdot 10^{6}$	$2.45 \cdot 10^{7}$	0.564 ± 0.043
7	$2.45 \cdot 10^{7}$	$3.47 \cdot 10^{7}$	0.364 ± 0.082
8	$3.47 \cdot 10^{7}$	$4.47 \cdot 10^{7}$	0.491 ± 0.087
9	$4.47 \cdot 10^{7}$	10^{9}	1.18 ± 0.19
# Total flux	E_0 (eV)	E_N (eV)	$\phi = \sum_i \phi_i$ (n/cm$^2/(7 \cdot 10^{12}$ *ppp*$))$
-	10^{-3}	10^{9}	174 ± 82

Table C.7: Energy groups, including lower and upper energy limits of each group (in eV), and estimates of the flux within each energy group, normalized per nominal proton pulse. Total flux along the complete energy range is also given in the last row. The estimate and uncertainty for the flux is taken from the marginal *Posterior* distribution of each parameter (group-wise flux) as mean and standard deviation. Note that the energy groups are not the same as in the previous case, because of the different reactions utilized for this unfolding.

Provided these observations, the unfolding routine was used in the same manner as in the first case and then the intra-group shapes were adjusted by iteration so as to achieve a quasi-continuous shape for the flux between groups, within uncertainties. The results of the unfolding of the spectrum, including the group-wise fluxes together with the total flux, all normalized per nominal pulse are shown in Table C.7. The total flux of the filtered configuration is $(174 \pm 82) \cdot 10^6$ n/cm^2 per nominal pulse of $7{\cdot}10^{12}$ protons on the n_TOF target, which corresponds to a reduction of a factor of 5 compared with the non-filtered beam.

The unfolded spectrum is displayed in Figure C.20 in blue and green, in this case also in comparison with the characterization flux. The results show good agreement in terms of a strong reduction of the beam flux, though not enough to eliminate high energy neutrons from the beam. The reduction is stronger for high energy neutrons, above 10 MeV, and less intense around the evaporation peak. Also strong reduction of the flux is observed in the epithermal range, specially around the eV. This could already be noticed simply by observing the smaller reduction of the activation between the two Au samples when compared to the first irradiation, remarking the smaller contribution of the 4.9 eV resonance to the total Au activation. On the contrary, the thermal flux is only slightly reduced, most probably due to the effect of over-moderation through Al but more importantly by the close polyethylene cylinder in the set-up. A special mention is deserved by the 25 keV window that left neutrons travel through Al, and is represented with an adequate weight compared to the close fall of the evaporation peak so that the top of the peak does not surpass the characterized flux from the previous irradiation as was previously discussed.

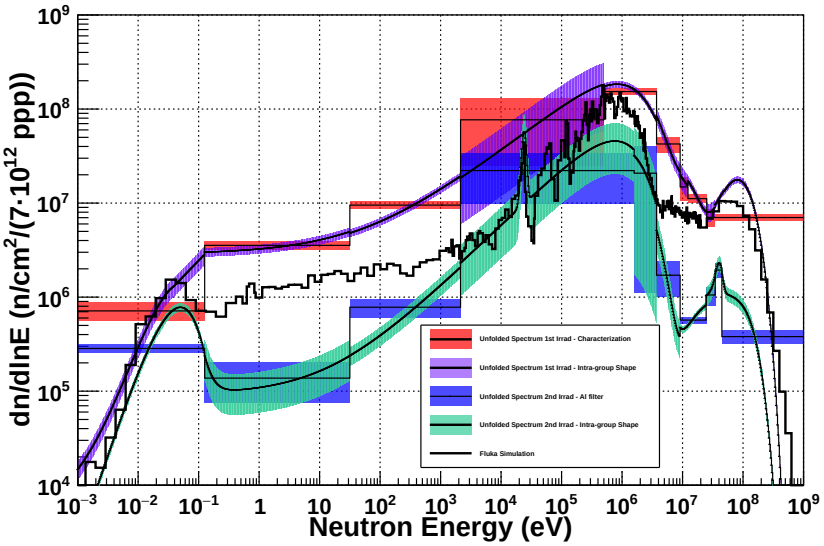

Figure C.20: Unfolded Spectrum of the NEAR Station at the central position for the second irradiation compared to the first one, normalized per nominal flux of $7{\cdot}10^{12}$ protons on target. The spectrum of the characterization is given in red and violet as in Figure C.18. For the second irradiation, Group-wise fluxes from the unfolding are given in blue and scaled accordingly per unit lethargy. Same fluxes, but shaped as with the intra-group flux shape used in response function computations are shown in green, also normalized so that total area equals the flux. Uncertainty is marked as the width of the rectangles (one standard deviation).

In the same way as for the first case, a correlation analysis was assessed in this case. The correlation matrix is shown in Figure C.21. The general features of the correlation matrix are the same, portraying small correlation between low and high energy groups as expected from the use of the same type of reactions. In this case, however, in two cases larger values of correlation (first and second groups) and anti-correlation (second and third groups) are found. A small remark can be added for case of larger positive correlation, revealing the fact that the difference between the two group-wise fluxes is better known than the separate groups themselves.

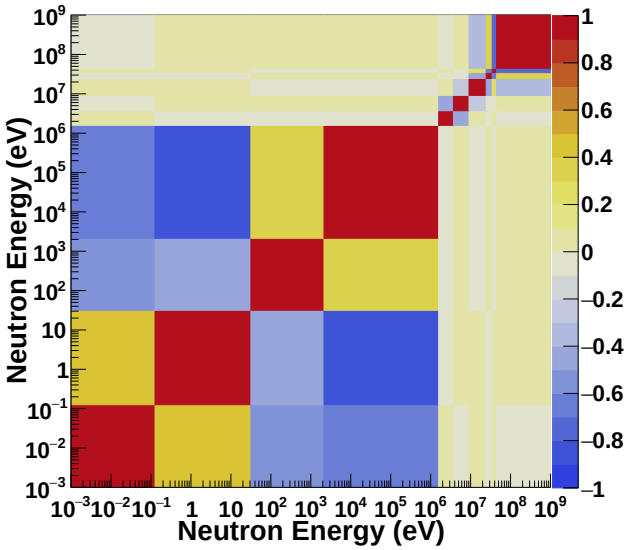

Figure C.21: Correlation matrix ($\frac{cov(i,j)}{\sigma_i \sigma_j}$) for the unfolding of the flux of the Al-filtered beam. The energy group sizes are scaled to their sizes in eV. Color corresponds to correlation, being red fully correlated and blue fully anti-correlated, with pale yellow uncorrelated. Red squares corresponding to the main diagonal correspond actually to self-correlation which equals to 1.

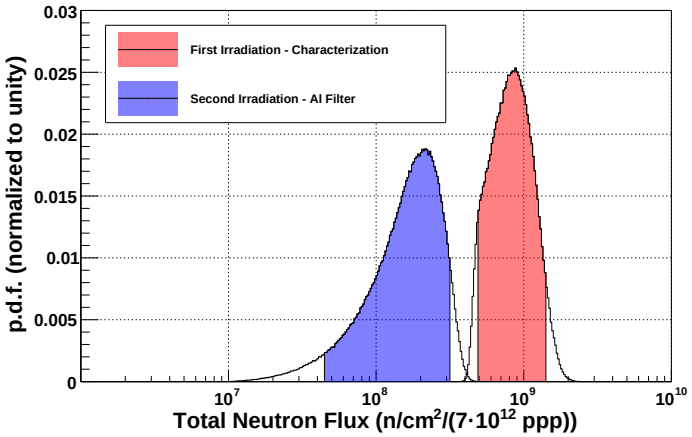

Figure C.22: Marginal distributions of the total flux characterization and Al-filtered beams, extracted from sampling the joint *Posterior* distribution obtained through the unfolding routine. 2σ credible intervals are displayed in color for each distribution, being red for the first irradiation and blue for the second.

Finally, in order to show the possible values for the total flux for the first and second irradiations, the marginal distributions of the sum of group-wise fluxes are displayed in Figure C.22. These distributions correspond to a set of samples from the joint *Posterior* distribution obtained by the unfolding using the bayesian inference procedure, and allow to closely estimate the likelihood of each possible flux value, together with the 2σ credible intervals, displayed in color (red for the characterization and blue for the Al-filtered beam), that constitute the final result of this study.

Bibliography

[1] National Cancer Institute of the National Institutes of Health. What is cancer, 2021.

[2] Jacques Ferlay, Murielle Colombet, Isabelle Soerjomataram, Donald M. Parkin, Marion Piñeros, Ariana Znaor, and Freddie Bray. Cancer statistics for the year 2020: An overview. *International Journal of Cancer*, 149(4):778–789, 2021.

[3] Sergey V. Gudkov, Natalya Yu. Shilyagina, Vladimir A. Vodeneev, and Andrei V. Zvyagin. Targeted radionuclide therapy of human tumors. *International Journal of Molecular Sciences*, 17(1), 2016.

[4] Deborah E. Citrin. Recent developments in radiotherapy. *New England Journal of Medicine*, 377(11):1065–1075, 2017. PMID: 28902591.

[5] Jérôme Doyen, Alexander Tuan Falk, Vincent Floquet, Joël Hérault, and Jean-Michel Hannoun-Lévi. Proton beams in cancer treatments: Clinical outcomes and dosimetric comparisons with photon therapy. *Cancer Treatment Reviews*, 43:104–112, 2016.

[6] Timothy D. Malouff, Anita Mahajan, Sunil Krishnan, Chris Beltran, Danushka S. Seneviratne, and Daniel Michael Trifiletti. Carbon ion therapy: A modern review of an emerging technology. *Frontiers in Oncology*, 10, 2020.

[7] Bleddyn Jones. Clinical radiobiology of fast neutron therapy: What was learnt? *Frontiers in Oncology*, 10, 2020.

[8] J. Chadwick. Possible existence of a neutron. *Nature*, 129:312, 1932.

[9] Gordon L. Locher. Biological effects and therapeutic possibilities of neutrons. *Am. J. Roentgenol. Radium Ther.*, 36:1 – 13, 1936.

[10] I. Porras. Sulfur-33 nanoparticles: A monte carlo study of their potential as neutron capturers for enhancing boron neutron capture therapy of cancer. *Applied Radiation and Isotopes*, 69(12):1838–1841, 2011. Special Issue: 14th International Conference on Neutron Capture Therapy.

[11] *Current Status of Neutron Capture Therapy*. Number 1223 in TECDOC Series. International Atomic Energy Agency, Vienna, 2001.

[12] Mitsunori Kirihara, Tsuguhiro Morimoto, and Itsuo Ichimoto. A Simple and Improved Synthesis of p-Boronophenylalanine, a Boron Carrier for the Boron-Neutron Capture Therapy. *Bioscience, Biotechnology, and Biochemistry*, 57(11):1940–1941, 01 1993.

[13] Front-matter. In Greg T. Hermanson, editor, *Bioconjugate Techniques (Third Edition)*, pages i–iii. Academic Press, Boston, third edition edition, 2013.

[14] Krishna R. Pulagam, Kiran B. Gona, Vanessa Gómez-Vallejo, Jan Meijer, Carolin Zilberfain, Irina Estrela-Lopis, Zuriñe Baz, Unai Cossío, and Jordi Llop. Gold nanoparticles as boron carriers for boron neutron capture therapy: Synthesis, radiolabelling and in vivo evaluation. *Molecules*, 24(19), 2019.

[15] Rolf F. Barth, Peng Mi, and Weilian Yang. Boron delivery agents for neutron capture therapy of cancer. *Cancer Communications*, 38(35), 2018.

[16] Sauli Savolainen, Mika Kortesniemi, Marjut Timonen, Vappu Reijonen, Linda Kuusela, Jouni Uusi-Simola, Eero Salli, Hanna Koivunoro, Tiina Seppälä, Nadja Lönnroth, Petteri Välimäki, Heini Hyvönen, Petri Kotiluoto, Tom Serén, Antti Kuronen, Sami Heikkinen, Antti Kosunen, and Iiro Auterinen. Boron neutron capture therapy (BNCT) in Finland: Technological and physical prospects after 20 years of experiences. *Physica Medica*, 29(3):233 – 248, 2013.

[17] Jeffrey A. Coderre and Gerard M. Morris. The radiation biology of boron neutron capture therapy. *Radiation Research*, 151(1):1–18, 1999.

[18] Sara J. González and Gustavo A. Santa Cruz. The Photon-Isoeffective Dose in Boron Neutron Capture Therapy. *Radiation Research*, 178(6):609 – 621, 2012.

[19] William H. Sweet. The uses of nuclear disintegration in the diagnosis and treatment of brain tumor. *New England Journal of Medicine*, 245(23):875–878, 1951. PMID: 14882442.

[20] Hiroshi Hatanaka. A revised boron-neutron capture therapy for malignant brain tumors. *Journal of Neurology*, 209:81–94, 1975.

[21] Yutaka Mishima. First human clinical trial of melanoma neutron capture. diagnosis and therapy. *Strahlentherapie und Oncologie*, 165:251, 1989.

[22] Tiina Seppälä. *FIR 1 Epithermal neutron beam model and dose calculation for treatment planning in Neutron Capture Therapy.* PhD thesis, University of Helsinki, 2002.

[23] Iiro Auterinen, Pekka Hiismäki, Petri Kotiluoto, Rolf J. Rosenberg, Seppo Salmenhaara, Tiina Seppälä, Tom Serén, Vesa Tanner, Carita Aschan, Mika Kortesniemi, Antti Kosunen, Juha Lampinen, Sauli Savolainen, Matti Toivonen, and Petteri Välimäki. *Metamorphosis of a 35 Year-Old TRIGA Reactor into a Modern BNCT Facility*, pages 267–275. Springer US, Boston, MA, 2001.

[24] S. Bortolussi, N. Protti, M. Ferrari, I. Postuma, S. Fatemi, M. Prata, F. Ballarini, M.P. Carante, R. Farias, S.J. González, M. Marrale, S. Gallo, A. Bartolotta, G. Iacoviello, D. Nigg, and S. Altieri. Neutron flux and gamma dose measurement in the bnct irradiation facility at the triga reactor of the university of pavia. *Nuclear Instruments and Methods in Physics Research Section B: Beam Interactions with Materials and Atoms*, 414:113–120, 2018.

[25] H. Kumada, A. Matsumura, H. Sakurai, T. Sakae, M. Yoshioka, H. Kobayashi, H. Matsumoto, Y. Kiyanagi, T. Shibata, and H. Nakashima. Project for the development of the linac based nct facility in university of tsukuba. *Applied Radiation and Isotopes*, 88:211–215, 2014. 15th International Congress on Neutron Capture Therapy Impact of a new radiotherapy against cancer.

[26] Yoshinori Sakurai, Hiroki Tanaka, Takushi Takata, Nozomi Fujimoto, Minoru Suzuki, Shinichiro Masunaga, Yuko Kinashi, Natsuko Kondo, Masaru Narabayashi, Yosuke Nakagawa, Tsubasa Watanabe, Koji Ono, and Akira Maruhashi. Advances in boron neutron capture therapy (BNCT) at kyoto university - From reactor-based BNCT to accelerator-based BNCT. *Journal of the Korean Physical Society*, 67(1):76–81, Jul 2015.

[27] W Sauerwein and A Zurlo. The eortc boron neutron capture therapy (bnct) group: achievements and future projects. *European Journal of Cancer*, 38:31–34, 2002.

[28] Valerio Giusti, Per M. Munck af Rosenschöld, Kurt Sköld, Bruno Montagnini, and Jacek Capala. Monte Carlo model of the Studsvik BNCT clinical beam: Description and validation. *Medical Physics*, 30(12):3107–3117, 2003.

[29] Y.-W.H Liu, T.T Huang, S.H Jiang, and H.M Liu. Renovation of epithermal neutron beam for BNCT at THOR. *Applied Radiation and Isotopes*, 61(5):1039 – 1043, 2004. Topics in Neutron Capture Therapy: Proceedings of the Eleventh World Congress on Neutron Capture Therapy (ISNCT-11).

[30] Manjeet Chadha, Jacek Capala, Jeffrey A Coderre, Eric H Elowitz, Jun ichi Iwai, Darrel D Joel, Hungyuan B Liu, Lucian Wielopolski, and Arjun D Chanana. Boron neutron-capture therapy (bnct) for glioblastoma multiforme (gbm) using the epithermal neutron beam at the brookhaven national laboratory. *International Journal of Radiation Oncology*Biology*Physics*, 40(4):829–834, 1998.

[31] Rolf F. Barth, MGraca H Vicente, Otto K. Harling, W. S. Kiger III, Kent J. Riley, Peter J. Binns, Franz M. Wagner, Minoru Suzuki, Teruhito Aihara, Itsuro Kato, and Shinji Kawabata. Current status of boron neutron capture therapy of high grade gliomas and recurrent head and neck cancer. *Radiation Oncology*, 7, 2012.

[32] A Zonta, U Prati, L Roveda, C Ferrari, S Zonta, Am Clerici, C Zonta, T Pinelli, F Fossati, S Altieri, S Bortolussi, P Bruschi, R Nano, S Barni, P Chiari, and G Mazzini. Clinical lessons from the first applications of BNCT on unresectable liver metastases. *Journal of Physics: Conference Series*, 41:484–495, may 2006.

[33] S. Bortolussi and S. Altieri. Thermal neutron irradiation field design for boron neutron capture therapy of human explanted liver. *Medical Physics*, 34(12):4700–4705, 2007.

[34] *Nuclear Physics for Medicine*. Nuclear Physics European Collaboration Committee (NuPECC), 2014.

[35] Ling-Wei Wang, Yen-Wan Hsueh Liu, Fong-In Chou, and Shiang-Huei Jiang.

Clinical trials for treating recurrent head and neck cancer with boron neutron capture therapy using the tsing-hua open pool reactor. *Cancer Communications*, 38(1):37, 2018.

[36] S.J González, M.R Bonomi, G.A Santa Cruz, H.R Blaumann, O.A.Calzetta Larrieu, P Menéndez, R.Jiménez Rebagliati, J Longhino, D.B Feld, M.A Dagrosa, C Argerich, S.G Castiglia, D.A Batistoni, S.J Liberman, and B.M.C Roth. First bnct treatment of a skin melanoma in argentina: dosimetric analysis and clinical outcome. *Applied Radiation and Isotopes*, 61(5):1101–1105, 2004. Topics in Neutron Capture Therapy: Proceedings of the Eleventh World Congress on Neutron Capture Therapy (ISNCT-11).

[37] Andres Juan Kreiner, Javier Bergueiro, Daniel Cartelli, Matias Baldo, Walter Castell, Javier Gomez Asoia, Javier Padulo, Juan Carlos Suárez Sandín, Marcelo Igarzabal, Julian Erhardt, Daniel Mercuri, Alejandro A. Valda, Daniel M. Minsky, Mario E. Debray, Hector R. Somacal, María Eugenia Capoulat, María S. Herrera, Mariela F. del Grosso, Leonardo Gagetti, Manuel Suarez Anzorena, Nicolas Canepa, Nicolas Real, Marcelo Gun, and Hernán Tacca. Present status of Accelerator-Based BNCT. *Reports of Practical Oncology Radiotherapy*, 21(2):95 – 101, 2016. 7th Young BNCT meeting.

[38] I. Porras, J. Praena, F. Arias de Saavedra, M. P. Sabariego, M. Pedrosa, F. Ogállar, P. Torres-Sánchez, C. Ruiz-Ruiz, and M. J. Ruiz-Magaña. *Proceedings of the 15th International Conference on Nuclear Reaction Mechanisms*, chapter Perspectives on Neutron Capture Therapy of Cancer, pages 295–304. CERN, Geneva, 2018.

[39] Takahiro Kato, Katsumi Hirose, Hiroki Tanaka, Toshinori Mitsumoto, Tomoaki Motoyanagi, Kazuhiro Arai, Takaomi Harada, Akihiko Takeuchi, Ryohei Kato, Satoru Yajima, and Yoshihiro Takai. Design and construction of an accelerator-based boron neutron capture therapy (AB-BNCT) facility with multiple treatment rooms at the Southern Tohoku BNCT Research Center. *Applied Radiation and Isotopes*, 156:108961, 2020.

[40] Liisa Porra, Tiina Seppälä, Lauri Wendland, Hannu Revitzer, Heikki Joensuu, Paul Eide, Hanna Koivunoro, Noah Smick, Theodore Smick, and Mikko Tenhunen. Accelerator-based boron neutron capture therapy facility at the helsinki university hospital. *Acta Oncologica*, 61(2):269–273, 2022. PMID: 34569418.

[41] Ian Postuma. *Clinical application of accelerator-based Boron Neutron Capture Therapy*. PhD thesis, University of Pavia, 2015.

[42] Chiara Magni. *Experimental and computational studies for an Accelerator-Based Boron Neutron Capture Therapy clinical facility: a multidisciplinary approach*. PhD thesis, University of Pavia, 2021.

[43] S. Yu. Taskaev. Development of an accelerator-based epithermal neutron source for boron neutron capture therapy. *Physics of Particles and Nuclei*, 50:569–575, 2019.

[44] D.E. Cartelli, M.E. Capoulat, M. Baldo, J.C. Suárez Sandín, M. Igarzabal, M.F. del Grosso, A.A. Valda, N. Canepa, M. Gun, D.M. Minsky, G. Conti,

J. Erhardt, H.R. Somacal, A.A. Bertolo, J. Bergueiro, P.A. Gaviola, and A.J. Kreiner. Status of low-energy accelerator-based bnct worldwide and in argentina. *Applied Radiation and Isotopes*, 166:109315, 2020.

[45] H. Tanaka, Y. Sakurai, M. Suzuki, S. Masunaga, T. Mitsumoto, K. Fujita, G. Kashino, Y. Kinashi, Y. Liu, M. Takada, K. Ono, and A. Maruhashi. Experimental verification of beam characteristics for cyclotron-based epithermal neutron source (C-BENS). *Applied Radiation and Isotopes*, 69(12):1642 – 1645, 2011. Special Issue: 14th International Conference on Neutron Capture Therapy.

[46] H. Tanaka, Y. Sakurai, M. Suzuki, S. Masunaga, Y. Kinashi, G. Kashino, Y. Liu, T. Mitsumoto, S. Yajima, H. Tsutsui, A. Maruhashi, and K. Ono. Characteristics comparison between a cyclotron-based neutron source and KUR-HWNIF for boron neutron capture therapy. *Nuclear Instruments and Methods in Physics Research Section B: Beam Interactions with Materials and Atoms*, 267(11):1970 – 1977, 2009.

[47] Katsumi Hirose, Akiyoshi Konno, Junichi Hiratsuka, Seiichi Yoshimoto, Takahiro Kato, Koji Ono, Naoki Otsuki, Jun Hatazawa, Hiroki Tanaka, Kanako Takayama, Hitoshi Wada, Motohisa Suzuki, Mariko Sato, Hisashi Tamaguchi, Ichiro Seto, Yuji Ueki, Susumu Iketani, Shigeki Imai, Tatsuya Nakammura, Takashi Ono, Himoasa Endo, Yusuke Azami, Yasuhiro Kikuchi, Masao Murakami, and Yoshihiro Takai. Boron neutron capture therapy using cyclotron-based epithermal neutron source and borofalan (10B) for recurrent or locally advanced head and neck cancer (JHN002): An open-label phase II trial. *Radiotherapy and Oncology*, 155, 2021.

[48] Shinji Kawabata, Minoru Suzuki, Katsumi Hirose, Hiroki Tanaka, Takahiro Kato, Hiromi Goto, Yoshitaka Narita, and Shin-Ichi Miyatake. Accelerator-based BNCT for patients with recurrent glioblastoma: a multicenter phase II study. *Neuro-Oncology Advances*, 3(1), 05 2021. vdab067.

[49] I. Porras, J. Praena, F. Arias de Saavedra, M. Pedrosa-Rivera, P. Torres-Sánchez, M.P. Sabariego, J. Expósito-Hernández, J.M. Llamas-Elvira, A. Ramírez-Navarro, A. Rodríuez-Fernández, J.M. Osorio-Ceballos, C. Ruiz-Ruiz, and M.J. Ruiz-Magaña. BNCT research activities at the Granada group and the project NeMeSis: Neutrons for medicine and sciences, towards an accelerator-based facility for new BNCT therapies, medical isotope production and other scientific neutron applications. *Applied Radiation and Isotopes*, 165:109247, 2020.

[50] J. T. Goorley, W. S. Kiger III, and R. G. Zamenhof. Reference dosimetry calculations for neutron capture therapy with comparison of analytical and voxel models. *Medical Physics*, 29(2):145–156, 2002.

[51] María Pedrosa-Rivera, Javier Praena, Ignacio Porras, María José Ruiz-Magaña, and Carmen Ruiz-Ruiz. A simple approximation for the evaluation of the photon iso-effective dose in boron neutron capture therapy based on dose-independent weighting factors. *Applied Radiation and Isotopes*, 157:109018, 2020.

[52] M.J. Berger, J.S. Coursey, M.A. Zucker, and J. Chang. *NIST Standard Reference Database 124*. National Institute of Standards and Technology, Gaithersburg, MD, 2017.

[53] Leena Kankaanranta, Tiina Seppälä, Hanna Koivunoro, Petteri Välimäki, Annette Beule, Juhani Collan, Mika Kortesniemi, Jouni Uusi-Simola, Petri Kotiluoto, Iiro Auterinen, Tom Serèn, Anders Paetau, Kauko Saarilahti, Sauli Savolainen, and Heikki Joensuu. l-boronophenylalanine-mediated boron neutron capture therapy for malignant glioma progressing after external beam radiation therapy: A phase i study. *International Journal of Radiation Oncology, Biology, Physics*, 80:369–376, 2011.

[54] C. J. Werner, J. S. Bull, C. J. Solomon, F. B. Brown, G. W. McKinney, M. E. Rising, D. A. Dixon, R. L. Martz, H. G. Hughes, L. J. Cox, A. J. Zukaitis, J. C. Armstrong, R. A. Forster, and L. Casswell. *MCNP6.2 Release Notes - report LA-UR-18-20808*. Los Alamos National Laboratory (LANL), 2018.

[55] A. Wallner, M. Bichler, K. Buczak, I. Dillmann, F. Käppeler, A. Karakas, C. Lederer, M. Lugaro, K. Mair, A. Mengoni, G. Schätzel, P. Steier, and H. P. Trautvetter. Accelerator mass spectrometry measurements of the $^{13}C(n,\gamma)^{14}C$ and $^{14}N(n,p)^{14}C$ cross sections. *Phys. Rev. C*, 93:045803, Apr 2016.

[56] C. Abia, K. Cunha, S. Cristallo, , and P. de Laverny. The origin of fluorine: abundances in agb carbon stars revisited. *Astronomy and Astrophysics*, 581(A88):8, 2015.

[57] Herbert J. Kouts and Luke C. L. Yuan. The production rate of cosmic-ray neutrons and c^{14}. *Phys. Rev.*, 86:128–129, Apr 1952.

[58] George S. Burr. *Bomb Carbon*, pages 1–1. Springer Netherlands, Dordrecht, 2021.

[59] N. Otuka, E. Dupont, V. Semkova, B. Pritychenko, A.I. Blokhin, M. Aikawa, S. Babykina, M. Bossant, G. Chen, S. Dunaeva, R.A. Forrest, T. Fukahori, N. Furutachi, S. Ganesan, Z. Ge, O.O. Gritzay, M. Herman, S. Hlavač, K. Katō, B. Lalremruata, Y.O. Lee, A. Makinaga, K. Matsumoto, M. Mikhaylyukova, G. Pikulina, V.G. Pronyaev, A. Saxena, O. Schwerer, S.P. Simakov, N. Soppera, R. Suzuki, S. Takács, X. Tao, S. Taova, F. Tárkányi, V.V. Varlamov, J. Wang, S.C. Yang, V. Zerkin, and Y. Zhuang. Towards a more complete and accurate experimental nuclear reaction data library (exfor): International collaboration between nuclear reaction data centres (nrdc). *Nuclear Data Sheets*, 120:272–276, 2014.

[60] R Batchelor and B H Flowers. Thermal neutron capture in nitrogen. atomic energy research establishment report. 7 1949.

[61] J. H. Coon and R. A. Nobles. Disintegration of he^3 and n^{14} by thermal neutrons. *Phys. Rev.*, 75:1358–1361, May 1949.

[62] P.Cuer, J-P.Longchamp, and S.Gorodetzky. Determination of the cross section for reactions of thermal neutrons on nitrogen. *Journal de Physique*, 12:6S, 1951.

[63] G. C. Hanna, D. B. Primeau, and P. R. Tunnicliffe. Thermal neutron cross sections and resonance integrals of the reactions o17(n,)c14, ar36(n,)s33, and n14(n,p)c14. *Canadian Journal of Physics*, 39(12):1784–1806, 1961.

[64] Y. M. Gledenov, V. I. Salatski, and P. V. Sedyshev. The14n(n, p)14c reaction cross section for thermal neutrons. *Zeitschrift für Physik A Hadrons and Nuclei*, 346:307–308, 1993.

[65] J. Wagemans, C. Wagemans, G. Goeminne, and P. Geltenbort. Experimental determination of the $^{14}\mathrm{N}(n,p)^{14}\mathrm{C}$ reaction cross section for thermal neutrons. *Phys. Rev. C*, 61:064601, Apr 2000.

[66] R Kitahara, K Hirota, S Ieki, T Ino, Y Iwashita, M Kitaguchi, J Koga, K Mishima, A Morishita, N Nagakura, H Oide, H Otono, Y Seki, D Sekiba, T Shima, H M Shimizu, N Sumi, H Sumino, K Taketani, T Tomita, T Yamada, S Yamashita, M Yokohashi, and T Yoshioka. Improved accuracy in the determination of the thermal cross section of $^{14}N(n,p)^{14}C$ for neutron lifetime measurement. *Progress of Theoretical and Experimental Physics*, 2019(9), 09 2019. 093C01.

[67] P. E. Koehler. $^{14}\mathrm{N(n,p)}^{14}\mathrm{C}$ cross section near thermal energy. *Phys. Rev. C*, 48:439–440, Jul 1993.

[68] M. Chadwick, P. Young, G. M. Hale, and et al. Technical report no. la-ur-99-1222. Technical report, Los Alamos National Laboratory (LANL), 1999.

[69] P. E. Koehler and H. A. O'Brien. $^{14}\mathrm{N(n,p)}^{14}\mathrm{c}$ cross section from 61 mev to 34.6 kev and its astrophysical implications. *Phys. Rev. C*, 39:1655–1657, Apr 1989.

[70] F. Ajzenberg-Selove. Energy levels of light nuclei a = 1315. *Nuclear Physics A*, 449(1):1–155, 1986.

[71] Y. M. Gledenov, V. I. Salatski, P. V. Sedyshev, M. V. Sedysheva, V. A. Pshenichnyj, and J. Andrzejewski. Cross sections of the 14N(n, p)14C reaction at 24.5, 53.5 and 144 keV. *Zeitschrift für Physik A Hadrons and Nuclei*, 348:199–200, 1994.

[72] Toshiya Sanami, Mamoru Baba, Isamu Matsuyama, Shigeo Matsuyama, Takehide Kiyosumi, Yasushi Nauchi, and Naohiro Hirakawa. Measurement of 14n(n,p)14c cross section for kt = 25.3 kev maxwellian neutrons using gridded ionization chamber. *Nuclear Instruments and Methods in Physics Research Section A: Accelerators, Spectrometers, Detectors and Associated Equipment*, 394(3):368–373, 1997.

[73] T. Shima, T. Kii, T. Kikuchi, F. Okazaki, T. Kobayashi, T. Baba, Y. Nagai, and M. Igashira. Experimental Studies of keV Energy Neutron-Induced Reactions Relevant to Astrophysics and Nuclear Physics. *JAERI Conference 97*, 1997.

[74] C. H. Johnson and H. H. Barschall. Interaction of fast neutrons with nitrogen. *Phys. Rev.*, 80:818–823, Dec 1950.

[75] G. L. Morgan. Cross sections for the 14n(n,p0), (n,0), and (n,1) reactions from 0.5 to 15 mev. *Nuclear Science and Engineering*, 70(2):163–176, 1979.

[76] Fletcher Gabbard, H. Bichsel, and T.W. Bonner. The disintegration of nitrogen by fast neutrons. *Nuclear Physics*, 14(2):277–294, 1959.

[77] H. H. Barschall and M. E. Battat. On the disintegration of nitrogen by fast neutrons. *Phys. Rev.*, 70:245–248, Sep 1946.

[78] R. J. deBoer, Q. Liu, Y. Chen, M. Couder, J. Görres, E. Lamere, A.M. Long, S. Lyons, K. Manukyan, L. Morales, D. Robertson, C. Seymour, G. Seymour, E. Stech, B. Vande Kolk, and M. Wiescher. Global r-matrix analysis of the sup11/supb(,n)sup14/supn reaction. *Journal of Physics: Conference Series*, 1668(1):012011, oct 2020.

[79] G. A. Bartholomew, F. Brown, H. E. Gove, A. E. Litherland, and E. B. Paul. Capture radiation and neutrons from the bombardment of c14 with protons. *Canadian Journal of Physics*, 33(8):441–456, 1955.

[80] Richard M. Sanders. Study of the $c^{14}(p,n)n^{14}$ and $c^{14}(\alpha,n)o^{17}$ reactions. *Phys. Rev.*, 104:1434–1440, Dec 1956.

[81] J. H. Gibbons and R. L. Macklin. Total neutron yields from light elements under proton and alpha bombardment. *Phys. Rev.*, 114:571–580, Apr 1959.

[82] M. Niecke, M. Niemeier, R. Weigel, and H. Wirzba-Lorenz. Angular distributions of neutron polarization from the 14C(p,n)14N and 11B(α,n)14N reactions and R-matrix analysis of 15N in the excitation-energy range between 11.5 and 12.5 MeV. *Nuclear Physics A*, 289(2):408–424, 1977.

[83] Recommended thermal cross sections, resonance properties, and resonance parameters for z = 1–60. In S.F. Mughabghab, editor, *Atlas of Neutron Resonances (Sixth Edition)*, pages 89–822. Elsevier, Amsterdam, sixth edition edition, 2018.

[84] Praena J., Porras I., Sabaté-Gilarte M., Ogállar F., Torres-Sánchez P., Lederer-Woods C., Davinson T., Dietz M., Lonsdale S.J., Woods P.J., Barbagallo M., Andrzejewski J., Perkowski J., Cristallo S., Abia C., Arias de Saavedra F., Domínguez I., Fernández B., and Macías M. The ^{14}n(n,p)^{14}c and ^{35}cl(n,p)^{35}s reactions at n_TOF-EAR2: dosimetry in BNCT and astrophysics. Technical report, n_TOF Collaboration (CERN), 2017.

[85] Chiaveri, E., Aberle, O., Alcayne, V., Amaducci, S., Andrzejewski, J., Audouin, L., Babiano-Suarez, V., Bacak, M., Barbagallo, M., Bennett, S., Berthoumieux, E., Bosnar, D., Brown, A.S., Busso, M., Caamaño, M., Caballero, L., Calviani, M., Calviño, F., Cano-Ott, D., Casanovas, A., Cerutti, F., Colonna, N., Cortés, G.P., Cortés-Giraldo, M.A., Cosentino, L., Cristallo, S., Damone, L.A., Davies, P.J., Diakaki, M., Dietz, M., Domingo-Pardo, C., Dressler, R., Ducasse, Q., Dupont, E., Durán, I., Eleme, Z., Fernández-Domíngez, B., Ferrari, A., Ferro-Gonçalves, I., Finocchiaro, P., Furman, V., Garg, R., Gawlik, A., Gilardoni, S., Göbel, K., González-Romero, E., Guerrero, C., Gunsing, F., Heinitz, S., Heyse, J., Jenkins, D.G., Jericha, E., Jiri, U., Junghans, A., Kadi, Y., Käppeler, F., Kimura, A., Knapová, I., Kokkoris,

M., Kopatch, Y., Krticka, M., Kurtulgil, D., Ladarescu, I., Lederer-Woods, C., Lerendegui-Marco, J., Lonsdale, S.-J., Macina, D., Manna, A., Martínez, T., Masi, A., Massimi, C., Mastinu, P.F., Mastromarco, M., Maugeri, E., Mazzone, A., Mendoza, E., Mengoni, A., Michalopoulou, V., Milazzo, P.M., Millán-Callado, M.A., Mingrone, F., Moreno-Soto, J., Musumarra, A., Negret, A., Ogállar, F., Oprea, A., Patronis, N., Pavlik, A., Perkowski, J., Petrone, C., Piersanti, L., Pirovano, E., Porras, I., Praena, J., Quesada, J.M., Ramos Doval, D., Reifarth, R., Rochman, D., Rubbia, C., Sabaté-Gilarte, M., Saxena, A., Schillebeeckx, P., Schumann, D., Sekhar, A., Smith, A.G., Sosnin, N., Sprung, P., Stamatopoulos, A., Tagliente, G., Tain, J.L., Tarifeño-Saldivia, A.E., Tassan-Got, L., Thomas, B., Torres-Sánchez, P., Tsinganis, A., Urlass, S., Valenta, S., Vannini, G., Variale, V., Vaz, P., Ventura, A., Vescovi, D., Vlachoudis, V., Vlastou, R., Wallner, A., Woods, P.J., Wright, T.J., and Zugec, P. Status and perspectives of the neutron time-of-flight facility n_TOF at CERN. *EPJ Web Conf.*, 239:17001, 2020.

[86] M. Barbagallo, A. Musumarra, L. Cosentino, E. Maugeri, S. Heinitz, A. Mengoni, R. Dressler, D. Schumann, F. Käppeler, N. Colonna, P. Finocchiaro, M. Ayranov, L. Damone, N. Kivel, O. Aberle, S. Altstadt, J. Andrzejewski, L. Audouin, M. Bacak, J. Balibrea-Correa, S. Barros, V. Bécares, F. Bečvář, C. Beinrucker, E. Berthoumieux, J. Billowes, D. Bosnar, M. Brugger, M. Caamaño, M. Calviani, F. Calviño, D. Cano-Ott, R. Cardella, A. Casanovas, D. M. Castelluccio, F. Cerutti, Y. H. Chen, E. Chiaveri, G. Cortés, M. A. Cortés-Giraldo, S. Cristallo, M. Diakaki, C. Domingo-Pardo, E. Dupont, I. Duran, B. Fernandez-Dominguez, A. Ferrari, P. Ferreira, W. Furman, S. Ganesan, A. García-Rios, A. Gawlik, T. Glodariu, K. Göbel, I. F. Gonçalves, E. González-Romero, E. Griesmayer, C. Guerrero, F. Gunsing, H. Harada, T. Heftrich, J. Heyse, D. G. Jenkins, E. Jericha, T. Katabuchi, P. Kavrigin, A. Kimura, M. Kokkoris, M. Krtička, E. Leal-Cidoncha, J. Lerendegui, C. Lederer, H. Leeb, S. Lo Meo, S. J. Lonsdale, R. Losito, D. Macina, J. Marganiec, T. Martínez, C. Massimi, P. Mastinu, M. Mastromarco, A. Mazzone, E. Mendoza, P. M. Milazzo, F. Mingrone, M. Mirea, S. Montesano, R. Nolte, A. Oprea, A. Pappalardo, N. Patronis, A. Pavlik, J. Perkowski, M. Piscopo, A. Plompen, I. Porras, J. Praena, J. Quesada, K. Rajeev, T. Rauscher, R. Reifarth, A. Riego-Perez, P. Rout, C. Rubbia, J. Ryan, M. Sabate-Gilarte, A. Saxena, P. Schillebeeckx, S. Schmidt, P. Sedyshev, A. G. Smith, A. Stamatopoulos, G. Tagliente, J. L. Tain, A. Tarifeño Saldivia, L. Tassan-Got, A. Tsinganis, S. Valenta, G. Vannini, V. Variale, P. Vaz, A. Ventura, V. Vlachoudis, R. Vlastou, J. Vollaire, A. Wallner, S. Warren, M. Weigand, C. Weiß, C. Wolf, P. J. Woods, T. Wright, and P. Žugec. $^{7}\mathrm{Be}(n,\alpha)^{4}\mathrm{He}$ reaction and the cosmological lithium problem: Measurement of the cross section in a wide energy range at n_TOF at CERN. *Phys. Rev. Lett.*, 117:152701, Oct 2016.

[87] L. Damone, M. Barbagallo, M. Mastromarco, A. Mengoni, L. Cosentino, E. Maugeri, S. Heinitz, D. Schumann, R. Dressler, F. Käppeler, N. Colonna, P. Finocchiaro, J. Andrzejewski, J. Perkowski, A. Gawlik, O. Aberle, S. Altstadt, M. Ayranov, L. Audouin, M. Bacak, J. Balibrea-Correa, J. Ballof, V. Bécares, F. Bečvář, C. Beinrucker, G. Bellia, A. P. Bernardes,

E. Berthoumieux, J. Billowes, M. J. G. Borge, D. Bosnar, A. Brown, M. Brugger, M. Busso, M. Caamaño, F. Calviño, M. Calviani, D. Cano-Ott, R. Cardella, A. Casanovas, D. M. Castelluccio, R. Catherall, F. Cerutti, Y. H. Chen, E. Chiaveri, J. G. M. Correia, G. Cortés, M. A. Cortés-Giraldo, S. Cristallo, M. Diakaki, M. Dietz, C. Domingo-Pardo, A. Dorsival, E. Dupont, I. Duran, B. Fernandez-Dominguez, A. Ferrari, P. Ferreira, W. Furman, S. Ganesan, A. García-Rios, S. Gilardoni, T. Glodariu, K. Göbel, I. F. Gonçalves, E. González-Romero, T. D. Goodacre, E. Griesmayer, C. Guerrero, F. Gunsing, H. Harada, T. Heftrich, J. Heyse, D. G. Jenkins, E. Jericha, K. Johnston, Y. Kadi, A. Kalamara, T. Katabuchi, P. Kavrigin, A. Kimura, N. Kivel, U. Köster, M. Kokkoris, M. Krtička, D. Kurtulgil, E. Leal-Cidoncha, C. Lederer-Woods, H. Leeb, J. Lerendegui-Marco, S. Lo Meo, S. J. Lonsdale, R. Losito, D. Macina, J. Marganiec, B. Marsh, T. Martínez, A. Masi, C. Massimi, P. Mastinu, F. Matteucci, A. Mazzone, E. Mendoza, P. M. Milazzo, F. Mingrone, M. Mirea, A. Musumarra, A. Negret, R. Nolte, A. Oprea, N. Patronis, A. Pavlik, L. Piersanti, M. Piscopo, A. Plompen, I. Porras, J. Praena, J. M. Quesada, D. Radeck, K. Rajeev, T. Rauscher, R. Reifarth, A. Riego-Perez, S. Rothe, P. Rout, C. Rubbia, J. Ryan, M. Sabaté-Gilarte, A. Saxena, J. Schell, P. Schillebeeckx, S. Schmidt, P. Sedyshev, C. Seiffert, A. G. Smith, N. V. Sosnin, A. Stamatopoulos, T. Stora, G. Tagliente, J. L. Tain, A. Tarifeño Saldivia, L. Tassan-Got, A. Tsinganis, S. Valenta, G. Vannini, V. Variale, P. Vaz, A. Ventura, V. Vlachoudis, R. Vlastou, A. Wallner, S. Warren, M. Weigand, C. Weiß, C. Wolf, P. J. Woods, T. Wright, and P. Žugec. ^{7}Be$(n,p)^{7}$Li reaction and the cosmological lithium problem: Measurement of the cross section in a wide energy range at n_TOF at CERN. *Phys. Rev. Lett.*, 121:042701, Jul 2018.

[88] V. Vlachoudis, M. Sabaté-Gilarte, V. Alcayne, F. Gunsing, E. Mendoza, F. Ogallar, I. Rejwan, M. Bacak, C. Guerrero, C. Massimi, and A. Stamatopoulos. On the resolution function of the n_tof facility: a comprehensive study and user guide. Technical report, n_TOF Collaboration (CERN), 2021.

[89] C. Weiß, E. Chiaveri, S. Girod, V. Vlachoudis, O. Aberle, S. Barros, I. Bergström, E. Berthoumieux, M. Calviani, C. Guerrero, M. Sabaté-Gilarte, A. Tsinganis, J. Andrzejewski, L. Audouin, M. Bacak, J. Balibrea-Correa, M. Barbagallo, V. Bécares, C. Beinrucker, F. Belloni, F. Bečvář, J. Billowes, D. Bosnar, M. Brugger, M. Caamaño, F. Calviño, D. Cano-Ott, F. Cerutti, N. Colonna, G. Cortés, M.A. Cortés-Giraldo, L. Cosentino, L. Damone, K. Deo, M. Diakaki, C. Domingo-Pardo, E. Dupont, I. Durán, R. Dressler, B. Fernández-Domínguez, A. Ferrari, P. Ferreira, P. Finocchiaro, R. Frost, V. Furman, S. Ganesan, A. Gheorghe, T. Glodariu, K. Göbel, I.F. Gonçalves, E. González-Romero, A. Goverdovski, E. Griesmayer, F. Gunsing, H. Harada, T. Heftrich, S. Heinitz, A. Hernández-Prieto, J. Heyse, D.G. Jenkins, E. Jericha, Y. Kadi, F. Käppeler, T. Katabuchi, P. Kavrigin, V. Ketlerov, V. Khryachkov, A. Kimura, N. Kivel, M. Kokkoris, M. Krtička, E. Leal-Cidoncha, C. Lederer, H. Leeb, J. Lerendegui, M. Licata, S. Lo Meo, D. López, R. Losito, D. Macina, J. Marganiec, T. Martínez, C. Massimi, P.F. Mastinu, M. Mastromarco, F. Matteucci, E. Mendoza, A. Mengoni, P.M. Milazzo, F. Mingrone, M. Mirea, S. Montesano, A. Musumarra, R. Nolte,

R. Palomo Pinto, C. Paradela, N. Patronis, A. Pavlik, J. Perkowski, I. Porras, J. Praena, J.M. Quesada, T. Rauscher, R. Reifarth, A. Riego-Perez, M.S. Robles, C. Rubbia, J. Ryan, A. Saxena, P. Schillebeeckx, S. Schmidt, D. Schumann, P. Sedyshev, G. Smith, A. Stamatopoulos, P. Steinegger, S.V. Suryanarayana, G. Tagliente, J.L. Tain, A. Tarifeño-Saldivia, L. Tassan-Got, S. Valenta, G. Vannini, V. Variale, P. Vaz, A. Ventura, R. Vlastou, A. Wallner, S. Warren, M. Weigand, T. Wright, and P. Žugec. The new vertical neutron beam line at the cern n_tof facility design and outlook on the performance. *Nuclear Instruments and Methods in Physics Research Section A: Accelerators, Spectrometers, Detectors and Associated Equipment*, 799:90–98, 2015.

[90] M. Sabaté-Gilarte, M. Barbagallo, N. Colonna, F. Gunsing, P. Žugec, V. Vlachoudis, Y. H. Chen, A. Stamatopoulos, J. Lerendegui-Marco, M. A. Cortés-Giraldo, A. Villacorta, C. Guerrero, L. Damone, L. Audouin, E. Berthoumieux, L. Cosentino, M. Diakaki, P. Finocchiaro, A. Musumarra, T. Papaevangelou, M. Piscopo, L. Tassan-Got, O. Aberle, J. Andrzejewski, V. Bécares, M. Bacak, R. Baccomi, J. Balibrea, S. Barros, F. Bečvář, C. Beinrucker, F. Belloni, J. Billowes, D. Bosnar, M. Brugger, M. Caamaño, F. Calviño, M. Calviani, D. Cano-Ott, R. Cardella, A. Casanovas, D. M. Castelluccio, F. Cerutti, E. Chiaveri, G. Cortés, K. Deo, C. Domingo-Pardo, R. Dressler, E. Dupont, I. Durán, B. Fernández-Domínguez, A. Ferrari, P. Ferreira, R. J. W. Frost, V. Furman, K. Göbel, A. R. García, A. Gawlik, I. Gheorghe, T. Glodariu, I. F. Gonçalves, E. González, A. Goverdovski, E. Griesmayer, H. Harada, T. Heftrich, S. Heinitz, A. Hernández-Prieto, J. Heyse, D. G. Jenkins, E. Jericha, F. Käppeler, Y. Kadi, T. Katabuchi, P. Kavrigin, V. Ketlerov, V. Khryachkov, A. Kimura, N. Kivel, M. Kokkoris, M. Krtička, E. Leal-Cidoncha, C. Lederer, H. Leeb, M. Licata, S. Lo Meo, S. J. Lonsdale, R. Losito, D. Macina, J. Marganiec, T. Martínez, C. Massimi, P. Mastinu, M. Mastromarco, F. Matteucci, E. A. Maugeri, E. Mendoza, A. Mengoni, P. M. Milazzo, F. Mingrone, M. Mirea, S. Montesano, R. Nolte, A. Oprea, F. R. Palomo-Pinto, C. Paradela, N. Patronis, A. Pavlik, J. Perkowski, J. I. Porras, J. Praena, J. M. Quesada, K. Rajeev, T. Rauscher, R. Reifarth, A. Riego-Perez, M. S. Robles, P. C. Rout, C. Rubbia, J. A. Ryan, A. Saxena, P. Schillebeeckx, S. Schmidt, D. Schumann, P. Sedyshev, A. G. Smith, S. V. Suryanarayana, G. Tagliente, J. L. Tain, A. Tarifeño-Saldivia, A. Tsinganis, S. Valenta, G. Vannini, V. Variale, P. Vaz, A. Ventura, R. Vlastou, A. Wallner, S. Warren, M. Weigand, C. Wolf, P. J. Woods, C. Weiss, and T. Wright. High-accuracy determination of the neutron flux in the new experimental area n_tof-ear2 at cern. *The European Physical Journal A*, 53, 2017.

[91] P. Žugec, C. Weiß, C. Guerrero, F. Gunsing, V. Vlachoudis, M. Sabate-Gilarte, A. Stamatopoulos, T. Wright, J. Lerendegui-Marco, F. Mingrone, J.A. Ryan, S.G. Warren, A. Tsinganis, and M. Barbagallo. Pulse processing routines for neutron time-of-flight data. *Nuclear Instruments and Methods in Physics Research Section A: Accelerators, Spectrometers, Detectors and Associated Equipment*, 812:134–144, 2016.

[92] S. Andriamonje, M. Calviani, Y. Kadi, R. Losito, V. Vlachoudis, E. Berthoumieux, F. Gunsing, A. Giganon, Y. Giomataris, C. Guerrero,

R. Sarmento, P. Schillebeeckx, and P. Siegler. A Transparent Detector for n_TOF Neutron Beam Monitoring. *J. Korean. Phys. Soc.*, 59:1597–1600, 2011.

[93] J. Praena, M. Sabaté-Gilarte, I. Porras, J. M. Quesada, S. Altstadt, J. Andrzejewski, L. Audouin, V. Bécares, M. Barbagallo, F. Bečvář, F. Belloni, E. Berthoumieux, J. Billowes, V. Boccone, D. Bosnar, M. Brugger, F. Calviño, M. Calviani, D. Cano-Ott, C. Carrapiço, F. Cerutti, E. Chiaveri, M. Chin, N. Colonna, G. Cortés, M. A. Cortés-Giraldo, M. Diakaki, M. Dietz, C. Domingo-Pardo, R. Dressler, I. Durán, C. Eleftheriadis, A. Ferrari, K. Fraval, V. Furman, K. Göbel, M. B. Gómez-Hornillos, S. Ganesan, A. R. García, G. Giubrone, I. F. Gonçalves, E. González-Romero, A. Goverdovski, E. Griesmayer, C. Guerrero, F. Gunsing, T. Heftrich, A. Hernández-Prieto, J. Heyse, D. G. Jenkins, E. Jericha, F. Käppeler, Y. Kadi, D. Karadimos, T. Katabuchi, V. Ketlerov, V. Khryachkov, N. Kivel, P. Koehler, M. Kokkoris, J. Kroll, M. Krtička, C. Lampoudis, C. Langer, E. Leal-Cidoncha, C. Lederer-Woods, H. Leeb, L. S. Leong, J. Lerendegui-Marco, R. Losito, A. Mallick, A. Manousos, J. Marganiec, T. Martínez, C. Massimi, P. Mastinu, M. Mastromarco, E. Mendoza, A. Mengoni, P. M. Milazzo, F. Mingrone, M. Mirea, W. Mondelaers, C. Paradela, A. Pavlik, J. Perkowski, A. J. M. Plompen, T. Rauscher, R. Reifarth, A. Riego-Perez, M. Robles, C. Rubbia, J. A. Ryan, R. Sarmento, A. Saxena, P. Schillebeeckx, S. Schmidt, D. Schumann, P. Sedyshev, G. Tagliente, J. L. Tain, A. Tarifeño Saldivia, D. Tarrío, L. Tassan-Got, A. Tsinganis, S. Valenta, G. Vannini, V. Variale, P. Vaz, A. Ventura, M. J. Vermeulen, V. Vlachoudis, R. Vlastou, A. Wallner, T. Ware, M. Weigand, C. Weiss, T. Wright, and P. Žugec. Measurement and resonance analysis of the ^{33}S$(n,\alpha)^{30}$Si cross section at the CERN n_TOF facility in the energy region from 10 to 300 keV. *Phys. Rev. C*, 97:064603, Jun 2018.

[94] J. Praena, F.J. Ferrer, W. Vollenberg, M. Sabaté-Gilarte, B. Fernández, J. García-López, I. Porras, J.M. Quesada, S. Altstadt, J. Andrzejewski, L. Audouin, V. Bécares, M. Barbagallo, F. Bečvář, F. Belloni, E. Berthoumieux, J. Billowes, V. Boccone, D. Bosnar, M. Brugger, F. Calviño, M. Calviani, D. Cano-Ott, C. Carrapiço, F. Cerutti, E. Chiaveri, M. Chin, N. Colonna, G. Cortés, M.A. Cortés-Giraldo, M. Diakaki, M. Dietz, C. Domingo-Pardo, R. Dressler, I. Durán, C. Eleftheriadis, A. Ferrari, K. Fraval, V. Furman, K. Göbel, M.B. Gómez-Hornillos, S. Ganesan, A.R. García, G. Giubrone, I.F. Gonçalves, E. González-Romero, A. Goverdovski, E. Griesmayer, C. Guerrero, F. Gunsing, T. Heftrich, A. Hernández-Prieto, J. Heyse, D.G. Jenkins, E. Jericha, F. Käppeler, Y. Kadi, D. Karadimos, T. Katabuchi, V. Ketlerov, V. Khryachkov, N. Kivel, P. Koehler, M. Kokkoris, J. Kroll, M. Krtička, C. Lampoudis, C. Langer, E. Leal-Cidoncha, C. Lederer, H. Leeb, L.S. Leong, J. Lerendegui-Marco, R. Losito, A. Mallick, A. Manousos, J. Marganiec, T. Martínez, C. Massimi, P. Mastinu, M. Mastromarco, E. Mendoza, A. Mengoni, P.M. Milazzo, F. Mingrone, M. Mirea, W. Mondelaers, C. Paradela, A. Pavlik, J. Perkowski, A.J.M. Plompen, T. Rauscher, R. Reifarth, A. Riego-Perez, M. Robles, C. Rubbia, J.A. Ryan, R. Sarmento, A. Saxena, P. Schillebeeckx, S. Schmidt, D. Schumann, P. Sedyshev, G. Tagliente, J.L. Tain, A. Tarifeño-Saldivia, D. Tarrío, L. Tassan-Got, A. Tsinganis, S. Valenta, G. Vannini, V. Variale, P. Vaz, A. Ventura, M.J. Vermeulen, V. Vlachoudis,

R. Vlastou, A. Wallner, T. Ware, M. Weigand, C. Weiss, T. Wright, and P. Žugec. Preparation and characterization of ^{33}S samples for $^{33}S(n,\alpha)^{30}Si$ cross-section measurements at the n_TOF facility at CERN. *Nuclear Instruments and Methods in Physics Research Section A: Accelerators, Spectrometers, Detectors and Associated Equipment*, 890:142–147, 2018.

[95] *Ion Beam Analysis Nuclear Data Library (IBANDL).* IAEA, 2014.

[96] M. Mayer. *SIMNRA User's Guide, Report IPP 9/113.* Max-Planck-Institut für Plasmaphysik, Garching, Germany, 1997.

[97] M.S. Moore. Rate dependence of counting losses in neutron time-of-flight measurements. *Nuclear Instruments and Methods*, 169(1):245–247, 1980.

[98] F.-J. Hambsch and I. Ruskov. The 10b(n,0)7li and 10b(n,1)7li alpha-particle angular distributions for en ¡ 1 mev. *Nuclear Science and Engineering*, 163(1):1–16, 2009.

[99] Nancy M. Larson. *Updated users' guide for SAMMY: Multilevel R-Matrix fits to neutron data using Bayes' equations.* Oak Ridge National Laboratory, 2008.

[100] A. C. Kahler. *The NJOY Nuclear Data Processing System, Version 2016.* Los Alamos National Laboratory, 2019.

[101] P. Torres-Sánchez, I. Porras, F. Arias de Saavedra, M.P. Sabariego, and J. Praena. On the upper limit for the energy of epithermal neutrons for Boron Neutron Capture Therapy. *Radiation Physics and Chemistry*, 156:240 – 244, 2019.

[102] Pablo Torres-Sánchez, Ignacio Porras, Fernando Arias de Saavedra, and Javier Praena. Study of the upper energy limit of useful epithermal neutrons for boron neutron capture therapy in different tissues. *Radiation Physics and Chemistry*, 185:109490, 2021.

[103] Tim Goorley. MCNP Medical Physics Geometry Database. Technical report, 2008.

[104] C.L. Lee and X.-L. Zhou. Thick target neutron yields for the $^7Li(p,n)^7Be$ reaction near threshold. *Nuclear Instruments and Methods in Physics Research Section B: Beam Interactions with Materials and Atoms*, 152(1):1 – 11, 1999.

[105] Horst Liskien and Arno Paulsen. Neutron production cross sections and energies for the reactions $^7Li(p,n)^7Be$ and $^7Li(p,n)^7Be*$. *Atomic Data and Nuclear Data Tables*, 15(1):57 – 84, 1975.

[106] T E Blue, N Gupta, and J E Woollard. A calculation of the energy dependence of the RBE of neutrons. *Physics in Medicine and Biology*, 38(12):1693–1712, dec 1993.

[107] A. J. Kreiner. Private communication.

[108] P. Torres-Sánchez, I. Porras, N. Ramos-Chernenko, F. Arias de Saavedra, and J. Praena. Optimized beam shaping assembly for a 2.1-MeV proton-accelerator-based neutron source for boron neutron capture therapy. *Scientific reports*, 11(1):7576, April 2021.

[109] Hanna Koivunoro. *Dosimetry and dose planning in boron neutron capture therapy: Monte Carlo studies*. PhD thesis, University of Helsinki, 2012.

[110] H.W. Koay, M. Fukuda, H. Toki, R. Seki, H. Kanda, and T. Yorita. Feasibility study of compact accelerator-based neutron generator for multi-port BNCT system. *Nuclear Instruments and Methods in Physics Research Section A: Accelerators, Spectrometers, Detectors and Associated Equipment*, 899:65 – 72, 2018.

[111] Yoshikai Kiyanagi, Kenji Asano, Akihiro Arakawa, Shin Fukuchi, Fujio Hiraga, Kenju Kimura, Hitoshi Kobayashi, Michio Kubota, Hiroaki Kumada, Hiroshi Matsumoto, Akira Matsumoto, Takeji Sakae, Kimiaki Saitoh, Tokushi Shibata, and Masakazu Yoshioka. A Project of Boron Neutron Capture Therapy System based on a Proton Linac Neutron Source. *Physics Procedia*, 26:223 – 230, 2012. Proceedings of the first two meetings of the Union of Compact Accelerator-Driven Neutron Sources.

[112] Akihiko Masuda, Tetsuro Matsumoto, Kenta Takada, Takahiro Onishi, Kohei Kotaki, Hidenori Sugimoto, Hiroaki Kumada, Hideki Harano, and Takeji Sakae. Neutron spectral fluence measurements using a bonner sphere spectrometer in the development of the iBNCT accelerator-based neutron source. *Applied Radiation and Isotopes*, 127:47 – 51, 2017.

[113] O.E Kononov, V.N Kononov, M.V Bokhovko, V.V Korobeynikov, A.N Soloviev, A.S Sysoev, I.A Gulidov, W.T Chu, and D.W Nigg. Optimization of an accelerator-based epithermal neutron source for neutron capture therapy. *Applied Radiation and Isotopes*, 61(5):1009 – 1013, 2004. Topics in Neutron Capture Therapy: Proceedings of the Eleventh World Congress on Neutron Capture Therapy (ISNCT-11).

[114] L. Zaidi, M. Belgaid, S. Taskaev, and R. Khelifi. Beam shaping assembly design of $^{7}Li(p,n)^{7}Be$ neutron source for boron neutron capture therapy of deep-seated tumor. *Applied Radiation and Isotopes*, 139:316 – 324, 2018.

[115] Jeffrey A. Coderre, Arjun D. Chanana, Darrel D. Joel, Eric H. Elowitz, Peggy L. Micca, Marta M. Nawrocky, Manjeet Chadha, Jan-Olaf Gebbers, Magdy Shady, Nancy S. Peress, and Daniel N. Slatkin. Biodistribution of Boronophenylalanine in Patients with Glioblastoma Multiforme: Boron Concentration Correlates with Tumor Cellularity. *Radiation Research*, 149(2):163–170, 1998.

[116] P.J. Binns, K.J. Riley, and O.K. Harling. Dosimetric comparison of six epithermal neutron beams using an ellipsoidal water phantom. In W. Sauerwein, R. Moss, and A. Wittig, editors, *Research and development in Neutron Capture Therapy*, pages 405–409. Monduzzi Editore, Bologna, Italy, 2002. Proceedings Paper: 10th International Congress on Neutron Capture Therapy.

[117] D. L. Bleuel, R. J. Donahue, B. A. Ludewigt, and J. Vujic. Designing accelerator-based epithermal neutron beams for boron neutron capture therapy. *Medical Physics*, 25(9):1725–1734.

[118] Kyung-O Kim, Jong Kyung Kim, and Soon Young Kim. Optimized therapeutic neutron beam for accelerator-based BNCT by analyzing the neutron

angular distribution from $^{7}li(p,n)^{7}be$ reaction. *Applied Radiation and Isotopes*, 67(7):1173 – 1179, 2009. 6th International Conference on Isotopes.

[119] D.M. Minsky and A.J. Kreiner. Beam shaping assembly optimization for $^{7}li(p,n)^{7}be$ accelerator based BNCT. *Applied Radiation and Isotopes*, 88:233 – 237, 2014. 15th International Congress on Neutron Capture Therapy Impact of a new radiotherapy against cancer.

[120] Sebastiaan Breedveld, David Craft, Rens van Haveren, and Ben Heijmen. Multi-criteria optimization and decision-making in radiotherapy. *European Journal of Operational Research*, 277(1):1–19, 2019.

[121] Søren M. Bentzen, Louis S. Constine, Joseph O. Deasy, Avi Eisbruch, Andrew Jackson, Lawrence B. Marks, Randall K. Ten Haken, and Ellen D. Yorke. Quantitative analyses of normal tissue effects in the clinic (quantec): An introduction to the scientific issues. *International Journal of Radiation Oncology*Biology*Physics*, 76(3, Supplement):S3–S9, 2010. Quantitative Analyses of Normal Tissue Effects in the Clinic.

[122] Charles Mayo, Mary K. Martel, Lawrence B. Marks, John Flickinger, Jiho Nam, and John Kirkpatrick. Radiation dose–volume effects of optic nerves and chiasm. *International Journal of Radiation Oncology*Biology*Physics*, 76(3, Supplement):S28–S35, 2010. Quantitative Analyses of Normal Tissue Effects in the Clinic.

[123] Yaacov Richard Lawrence, X. Allen Li, Issam el Naqa, Carol A. Hahn, Lawrence B. Marks, Thomas E. Merchant, and Adam P. Dicker. Radiation dose–volume effects in the brain. *International Journal of Radiation Oncology*Biology*Physics*, 76(3, Supplement):S20–S27, 2010. Quantitative Analyses of Normal Tissue Effects in the Clinic.

[124] Alberto Mengoni and the n_TOF Collaboration. The new n_TOF NEAR station. Technical report, 2020.

[125] Shieldwerx, a division of Bladewerx LLC. Activation foils.

[126] Maria Elisso Stamati. Feasibility study for neutron inelastic cross section measurements at n_TOF/CERN using HPGe detectors. Master's thesis, University of Ioannina, 2020.

[127] Davide Chiesa, Ezio Previtali, and Monica Sisti. Bayesian statistics applied to neutron activation data for reactor flux spectrum analysis. *Annals of Nuclear Energy*, 70:157–168, 2014.

[128] Davide Chiesa, Massimiliano Nastasi, Carlo Cazzaniga, Marica Rebai, Laura Arcidiacono, Ezio Previtali, Giuseppe Gorini, and Christopher D. Frost. Measurement of the neutron flux at spallation sources using multi-foil activation. *Nuclear Instruments and Methods in Physics Research Section A: Accelerators, Spectrometers, Detectors and Associated Equipment*, 902:14–24, 2018.

[129] Martyn Plummer. *JAGS Version 4.3.0 user manual*, 2017.